Tuning the Structure and Dynamics of Hybrid Perovskite Photovoltaic Materials

Jake Lee Minns

School of Physical Sciences
University of Kent

This dissertation is submitted for the degree of
Doctor of Philosophy

October 2021

I would like to dedicate this thesis to my loving parents

Declaration

The work described in this thesis except where specific reference is made, has not been submitted in whole or in part for consideration for any other degree or qualification in this, or any other university. This work is original and has been carried out solely under the supervision of Professor Mark A. Green or in collaboration with others, as specified below, in the text and in the acknowledgements:

Chapter 3 The sample synthesis and powder neutron diffraction experiment on BT1 at NIST was carried out by Professor Mark A Green, initial analysis of this data including, initial model refinement and initial interpretation of maximum entropy analysis was presented and accepted for the award of a Master of Physics honours (MPhys (Hons)) degree at the University of Kent. Variable temperature synchrotron powder diffraction measurements were carried out by Dr Wouter Van Beek and Dr Dmitry Chernyshov at the Swiss-Norwegian beamline (SNBL) at the ESRF, France.

Chapter 4 Sample synthesis was carried out by Rhianna Day at the University of Kent. TOF powder neutron diffraction measurements conducted on POWGEN at Oak Ridge National Laboratory were carried out by Professor Mark A. Green.

Chapter 5 Sample synthesis was carried out by Rhianna Day at the University of Kent.

Jake Lee Minns
October 2021

Acknowledgements

At every stage of writing this thesis I found myself constantly reminded that without the collaboration and support of others, not only would this research not have been possible but working with others made the process truly enjoyable.

First of all, I would like to thank Professor Mark A Green for his supervision, for his expertise and experience which enabled this interesting and exciting research. His continued mentoring has been invaluable and open discussion was insightful and motivating. I'd also like to thank my second supervisor Dr George Dobre for his support throughout. Special thanks goes to past and present members of my research group, working with you all was a pleasure. I'd also like to thank Rhianna Day for her significant efforts towards synthesising many of the samples discussed in this work.

There are a number of people that have helped me with both experiments and analysis throughout my research that I would like to thank. Firstly, I am indebted to Dr Pawel Zajdel for his expertise, passion and help towards the analysis of single crystal and maximum entropy analysis of diffraction data, it was a joy to work with you and I can't thank you enough for your patience and time. I'd also like to thank Dr Wouter Van Beek and Dr Dmitry Chernyshov at the Swiss-Norwegian beamline (SNBL), ESRF, France, for assistance with both synchrotron single crystal and powder diffraction experiments.

I am grateful to the University of Kent for the financial support received through the Vice-Chancellors scholarship.

To my friends and loved ones, you kept me sane throughout. To my parents, I owe everything to your loving support throughout my life, you gave me the confidence to push myself throughout my PhD, I can never thank both of you enough.

Abstract

Hybrid organic-inorganic halide perovskites (HOIHPs) are a new class of material that combine molecular and valence solids to form a disordered material that exhibits flexible bonding and is susceptible to structural distortions. With applications in optoelectronics and as light-harvesters in solar cell devices, HOIHPs have been extensively researched. This thesis focuses on understanding the structure and dynamics of the archetypal HOIHP, methylammonium lead iodide ($MAPbI_3$), developing new methods for tuning the structure of the material and characterising new structural phases.

This research started with a detailed study of the structure and dynamics of $MAPbI_3$ at ambient temperature, the temperature most critical to the operation of HOIHP based solar cell devices. For this purpose, traditional analysis of X-ray single crystal and neutron powder diffraction measurements were combined with maximum entropy method (MEM) analysis. This revealed the structure to be significantly more disordered than previously realised. Following the observation of interstitial iodine sites the PbI_6 framework was found to exhibit distortions that when combined with analysis of variable temperature synchrotron powder diffraction data allowed a mechanism for iodine diffusion to be proposed. Bond distance analysis of both migrating and distorted iodines were consistent with the formation of neutral I_2 and suggests the redox couple $2I^- \rightarrow I_2 + 2e^-$. The proposed mechanism for iodine diffusion describes the population of interstitial iodide sites only through the collective motion of MA^+ cations in a gate opening type mechanism.

Following the significant structural disorder observed for $MAPbI_3$ at ambient temperature, a series of experiments aimed at characterising subtle changes to the average structure of $MAPbI_3$ following a number of post synthesis thermal treatments were conducted. Some of these treatments are consistent with those described in the literature for the processing of HOIHP based solar cell devices. Analysis of variable temperature synchrotron powder diffraction measurements revealed low temperature (<80 °C) annealing in air to result in subtle distortions to the structure consistent

with the incorporation of interstitial oxygen. Low temperature (<80 °C) vacuum annealing was found to have little effect, however at higher temperatures (≥80 °C) subtle changes to the tilting of the PbI_6 octahedral framework were observed. This was followed by a series of X-ray single crystal and neutron powder diffraction measurements on $MAPbI_3$ samples annealed at high temperature and under a vacuum. This research demonstrates precise control of both the framework tilting and bond lengths of the PbI_6 octahedral framework as well as disorder that is dependent on annealing temperature. This treatment was found to have no significant effect on the thermal stability of the material. The changes observed are attributed to the loss of MA^+ that results in a change in the interaction between the organic A-site cation and inorganic framework, demonstrating the flexible nature of the structure that allows for a range of structures to be stabilised.

After demonstrating precise control of principle structural features of $MAPbI_3$ following high temperature vacuum annealing, a post synthesis thermal iodine treatment was devised that resulted in the stabilisation of a new structural phase $MAPbI_{3+x}$. The structural characterisation of this phase was investigated between 100 K and 400 K through a combination of variable temperature X-ray powder and single crystal diffraction measurements. Between the measured temperature range this compound was found to exhibit four structural phases that are stabilised through the incorporation of additional interstitial iodine positioned at the centre face of the perovskite framework. At ambient temperature this phase exhibits ordering of the MA^+ cations, a reduction in both PbI_6 framework tilting and Pb-I bond lengths, and a decrease in the disorder of the framework that demonstrates increased rigidity of the structure. Below ambient temperature, ordering of the interstitial iodine sites is observed to correlate with tilting of the framework and ordering of the MA^+. This research provides experimental evidence for intrinsic doping of $MAPbI_3$ and demonstrates the porous nature of HOIHPs, whilst presenting a new route for synthesising novel variants of HOIHP photovoltaic materials.

This thesis demonstrates HOIHPs to be flexible, highly disordered materials. Most surprisingly, the structure of these materials is shown be highly dependent on the synthesis method and post synthesis thermal treatment undertaken. Through demonstrating precise control of the structure of these compounds, this thesis contributes towards producing more stable, highly efficient photovoltaic devices through the development of new structural phases for $MAPbI_3$.

List of Publications

Below details publications that have been published, and were produced throughout the duration of the work contained within this thesis:

- JL Minns, P Zajdel, D Chernyshov, W Van Beek, MA Green: **Structure and interstitial iodide migration in hybrid perovskite methylammonium lead iodide**. – *Nature communications*, 8 (1), 1-5
- M Songvilay, Nathan Giles-Donovan, M Bari, Z-G Ye, JL Minns, MA Green, Guangyong NMN Xu, Peter M Gehring, K Schmalzl, William D Ratcliff, Craig Brown, D Chernyshov, W van Beek, Sandy Cochran, Christopher Stock: **Anharmonic Acoustic Phonons and A-site Critical Fluctuations in the Lead Halide Perovskite $CsPbBr_3$**. – *Physical review materials*, 3 (9), 093602

"X-rays will prove to be a hoax."

– Sir William Thomson

Table of contents

List of figures

List of tables

1

Introduction

1.1 Motivation

In just 90 minutes the earth is exposed to more energy from the sun (6.45×10^{20} J) than humanity uses in a single year (5.72×10^{20} J as of 2001) [1]. Considering this, and that as of 2019 solar power makes up just 0.46% of global energy production the solar resource is drastically under utilised [2]. The under representation of solar power as a clean energy resource is set against a backdrop of increased global energy demands and the reality of climate change, which is thought to be a result of greenhouse gases released through the burning of coal, oil and gas. These processes currently dominate the global energy market.

For the purpose of developing new solar power technology, photovoltaics are now a thriving area of materials research, where reducing the cost and efficiency of materials that exhibit photovoltaic properties is a key goal. First discovered by Edmond Becquerel in 1839 the photovoltaic effect is the mechanism by which solar cells generate electrical power through exposure to light. The basic process involves incident photons exciting valence electrons to the conduction band of semiconducting materials allowing them to propagate through the material. Typically excited electrons will relax back to a ground state, but in a solar cell a characteristic asymmetry results in the flow of excited electrons that are then used in an external circuit [3].

A series of recent discoveries have demonstrated that a class of semiconducting materials refereed to as hybrid organic-inorganic halide perovskites (HOIHPs) can be used to produce low cost cells that already demonstrate efficiencies competitive with silicon [4–6]. The functional properties of these materials extends beyond

light-harvesting for solar cell devices, with applications in optoelectronics [7, 8], transistors [9, 10] and X-ray detection [11]. Currently, the underlying mechanism by which these properties are exhibited is largely unknown, and therefore fundamental studies of these materials are required if a commercial HOIHP based solar cell is to be realised. This provided an exciting opportunity for a rewarding study, for which this thesis intends to contribute through the characterisation, and study of the structure and dynamics of HOIHPs.

1.2 Development of Solar Cell Technology

The potential advantages of HOIHP based solar cells is best understood through considering the development of solar cell technology and the underpinning fundamental materials research. The advancement of solar cell technology over the past 70 years can be categorised into first (I), second (II) and third (III) generation, each distinguishable by the materials technology, and how they balance efficiency with production costs. To summarise, first generation solar cells are based on silicon wafers that form a p-n junction. Despite their high costs these cells show relatively low efficiencies [12]. Second generation thin films are defined by cheap and simple manufacturing processes with thin photoactive layers, these cells exhibit even lower efficiency. However, commercial potential lies in the opportunity for mass production and the ability to integrate these cells into small electronic devices at low cost [13]. The industry now looks to be on the verge of a third revolution in solar cell technology that aims to produce low cost high efficiency solar cells.

1.2.1 First Generation Solar cells

Developed in 1954 at Bell labs, first generation solar cells are currently the most widely adopted solar cell technology, a result of their high power efficiencies. However, these devices are expensive to manufacture and mainly comprised of monocrystalline Silicon (c-Si) or multi-crystalline Silicon (mc-Si) wafers.

Mono-Crystalline Silicon

Mono-crystalline solar cells are comprised of single crystal silicon square wafers generally between 125 mm and 156 mm in size. Columns of single crystal ingots are grown by the Czochralski method from which the silicon wafers are cut [12]. This process involves melting high-purity silicon in a quartz crucible, into which a seed crystal mounted rod is submerged. Through careful control of the temperature

gradients a single-crystal ingot is pulled from the melt. The float zone method is also a common method of producing higher purity silicon but at a greater cost.

Multi-Crystalline Silicon

Multi-crystalline silicon is prepared by a simpler casting method that results in the growth of polycrystalline ingots. The process was refined for photovoltics by Wacker Chemitronic in the 1970's and involves solidifying molten silicon from the bottom up producing large grains typically 0.1 cm to 10 cm in size. The large ingots are then cut into wafers to be used in constructing solar cells. This manufacturing process is less rigorous than those used for mono-crystalline Silicon with lower tolerances. It is therefore cheaper than the Czochralski method, but results in a reduction by up to 20% in cell efficiency [14].

Constructing a Silicon Solar Cell

A basic silicon solar cell consists of a single p-n junction formed at the contact point between two adjacent layers of p and n type doped silicon wafers. The p type wafer is placed above a metal contact forming the base of the solar cell. This is generally the thickest component of the cell at around between 300–500 μm and is used to absorb as much light as possible. The doping is dilute for increased diffusion lengths increasing the probability that photogenerated electrons reach the p-n junction. The n-type layer is thin to insure as much light as possible reaches the p-type base, this layer is heavily doped increasing electron-hole recombination and therefore less charge carriers are produced. The final layer consists of a top contact and anti-reflection (AR) coating that is typically deposited from liquid or vapour. For silicon the AR coating is around 80 nm to 100 nm thick and usually made from titanium dioxide [15].

The Limitations of Silicon Solar Cells

First generation silicon based solar cells make up the vast majority of the solar cell market. It benefits from the fact that the silicon manufacturing industry is incredibly well developed, a result of its massive application across micro-electronics. The growth of high quality single crystal silicon on an industrial scale has existed for many years. Although there has been progress towards so called 'dirty silicon' referring to low purity silicon for use in solar cell applications, the growth of high purity silicon still makes up a large portion of the cost in producing current devices.

As a photovoltaic material silicon has some significant drawbacks. For instance, silicon poorly absorbs sunlight meaning silicon solar cells have to be much thicker than alternative photovoltaic materials, this limits commercial solar cells to bulky rigid form factors. For terrestrial based solar cells the optimum band gap for photovoltaic applications is 1.34 eV for a single junction solar cell, which is demonstrated by the Shockley-Queisser limit with a maximum possible efficiency of 33% [16]. Silicon falls short of this ideal with a band gap of 1.1 eV and is therefore not ideal as a photovoltaic. The growth of large single crystal silicon ingots requires a large amount of energy input to produce, this means although the end result is a clean energy source the industrial process is extremely energy consuming.

1.2.2 Second Generation Solar Cells

Second generation solar cells are a group of photovoltaic devices based on thin films. Thin films are much cheaper to produce compared with first generation silicon devices, and can be incorporated into an ultra thin flexible form factors, a result of the reduced raw material cost and low temperature chemical deposition manufacturing methods. The thin-film devices are primarily comprised of three materials, amorphous silicon (α-Si), copper indium gallium selenide (CIGS) and cadmium telluride (CdTe).

Amorphous Silicon (α-Si)

The first thin-film solar cell was constructed from α-Si by Carlson and Wronski in 1976, demonstrating a power conversion efficiency of 2.4% [17]. These thin film cells are most commonly found at the top of scientific calculators, and their popularity originates from their abundance and non-toxicity. Low temperature processing allows for the manufacturing of flexible and cheap substrates with a high absorption coefficient relative to crystalline silicon, allowing layers to be as thin as 1-2 μm. This high absorption coefficient is the most attractive property of α-Si and stems from the inherent high disorder and abundance of dangling bonds present within the amorphous structure. Unfortunately, the disorder in α-Si promotes recombinations, and drastically reduces charge carrier lifetime, but more importantly the high defect concentration makes n- or p-type doping difficult. This problem was solved by incorporating 10% hydrogen into the film. The hydrogen bonds contain an unpaired electron (dangling bond) and thereby remove the ability to trap an electron or hole, reducing the defect density from 10^{19} cm^{-3} to 10^{16} cm^{-3}. The resulting material, α-Si:H, has significantly enhanced electrical properties, and possesses a

well defined direct band gap of 1.75 eV where doping is now possible allowing for the manufacturing of junction devices [18].

The primary downside of α-Si:H as a photovoltaic is the degradation resulting from the Staebler Wronski effect. Over a period of time the defect density can increase with light exposure, which increases recombinations that can reduce efficiency by up to 30% over a 6 month time span. The root cause is believed to be the breaking of Si-H bonds. However, degraded α-Si:H can be restored by annealing at a few hundred degrees Celsius and means α-Si:H based solar cells perform better at high temperatures [19].

Constructing a Amorphous Silicon Solar Cell

An α-Si:H based solar cell consists of a p-i-n junction, where the p and n doped regions are consistent with a typical p-n junction but an intrinsic (i) undoped region is placed between the two increasing the area in which photons are absorbed [19]. The i region is the thickest part of the cell often 250-500 nm and is responsible for the majority of photon absorption allowing for the doped p- and n-type regions to be much thinner. The built-in bias remains but the electric field is extended across the i region, which drives charge separation and increases the short charge carrier life time present in α-Si. The photocarriers are collected by drift and not diffusion in contrast to a p-n junction. A thicker *i* region maximises photon absorption but the electric field is reduced by charge defects. At a certain width the *i* region will exceed the space charge width resulting in a layer that does not contribute to the photocurrent. Therefore, the depletion width is greater than the *i* region, and in general the limit is approximately 0.5 μm.

The first layer in an amorphous silicon solar cell is normally a glass substrate onto which a transparent conducting oxide is coated usually made up of tin oxide or indium tin oxide [19]. The p-type, undoped and n-type α-Si:H layers are sequentially deposited at 240–400 °C in a design type known as "superstrate". A large number of deposition techniques exist but the most commonly used are plasma decomposition of silane and sputtering. Finally a rear contact usually zinc oxide is deposited onto the n-type layer and then sealed with a metal layer.

Evolution of the Amorphous Silicon Solar Cell

Optimising the design of α-Si based solar cells has seen the efficiency rise from 2.4% (Carlson and Wronski, 1976) [17] to 13.6% [20]. These improvements stem from a series of incremental design iterations starting with the discovery of hydrogenated

α-Si:H by Tawada *et al*. in 1982 pushing the efficiency to 8.04% [21]. The next key iteration came in the form of multi-junction cells. These cells have multiple band gaps as a result of layered junctions such that the cell responds to a larger proportion of the solar spectrum. Through alloying each junction, the device can be tuned to a specific band gap where the top layer junction has the highest band gap, this sequentially reduces with each layer of the cell. This allows for the capture of photons that would normally be lost in a single junction cell [22].

Copper Indium Gallium Diselenide

As a photovoltaic, copper indium diselenide ($CuInSe_2$) is ideal. It has a direct band gap of 1 eV and is an excellent light absorbing material allowing for extremely thin cell layers (1.2–4.04 μm) [18, 19]. Interestingly, structural defects do not impede the electrical behaviour of $CuInSe_2$ meaning that solar cell performance is less dependent on impurities and crystal defects [18]. Often $CuInSe_2$ is alloyed with Ga producing $CuInGaSe_2$ (CIGS), which has the effect of raising the band gap as well improved electronic behaviour at the contacts.

The most effective CIGS based solar cells follow a hetrojunction structure. These devices employ different base compounds for the p- and n-type layers, typically an n-type CdS emitter layer is used on a doped p-type CIGS base [19]. The CdS layer is highly doped with a band gap of 2.5 eV [18], thereby acting as a window to reduce collection losses and transport electrons from the p-n junction to the front contact with minimal resistance. The use of a heterojunction introduces a number of new problems at the interface that impede performance, such as unwanted new compounds forming at the junction. For example, at the $CuInSe_2$ - CdS interface the compounds $CuSe_2$ and CuS_2 form [19]. Differences in the lattice constants of the two compounds result in intra-band gap defect states at the junction, which increase Shockley-Read-Hall recombination, this increases dark currents and reduces the open circuit voltage of the cell. Variations in the band gap of the two materials can introduce a narrow barrier or spike in the conduction or valence band at the interface. This means that the photogenerated charge carriers crossing the p-n junction must tunnel across the spike before collection. If the step is much less than 0.5 eV the effect is minimal but for $Cu(In,Ga)Se_2$-CdS this barrier is 0.5 eV in the conduction band and disrupts collection [19].

Constructing a $CuInGaSe_2$ Solar Cell

To construct a $CuInGaSe_2$ based solar cell CIGS is deposited onto a molybdenum coated substrate. Two methods can be employed for CIGS deposition, either copper

indium gallium and selenium are vapour co-deposited or the selenisation of Cu/In films is used. The layer is then annealed in oxygen. The n-type CdS layer is formed through a chemical bath followed by the application of a zinc oxide conducting layer that doubles as an anti reflection coating. This manufacturing process, and the costly raw materials makes CIGS based solar cells expensive to manufacture compared with other thin film devices [19]. Development of CIGS based solar cells began in 1976 by Kazmerski *et al*. with a cell efficiency of 4.5% [23]. As of 2015 the highest recorded efficiency of CIGS based solar cells was 22.3%.

Cadmium Telluride

Belonging to the II-VI group of materials in theory cadmium telluride (CeTe) is an ideal photovoltaic semiconductor. It has a direct band gap of 1.4 eV and an excellent photon absorption coefficient [18]. CdTe can be doped both p- and n- type, one of only two II-VI compounds for which this is possible [19]. Growth of both single crystal and polycrystalline CdTe is possible. However for thin films polycrystalline is of most interest and so far has produced the most efficient solar cells. CdTe forms a wurtzite crystal structure. The strong chemical bonding means that the compound has a high chemical and thermal stability. However, it tends to suffer from excess Te atoms at grain boundaries that form defect states deep in the band gap [19].

CdTe based solar cells follow the same heterojunction design a CIGS. They use a n-Cds emitter layer with a p-CdTe base layer. The most effective deposition technique for CdTe layers is close space vapour transport although gas phase evaporation and spray pyrolysis can also be implemented. Typically CdTe layers are between 3 and 5 μm thick for good optical absorption [19]. CdTe dominates the thin-film solar cell market, with a record efficiency of 22.1% [24].

Are Second Generation Solar Cells the Future?

Stability and reliability are two key areas where thin film solar cells perform poorly, especially when compared to crystalline silicon. As discussed previously the Staebler-Wronski effect is prevalent in the degradation of α-Si thin film technology. Although it has been shown that thinner intrinsic layers show reduced performance loss as a result of decreased recombination of photocarriers, this still poses a significant stability issue [25].

High operating temperatures pose a serious obstacle to the reliability of thin film solar cells. As shown by Figure 1.1, increased temperatures result in a reduction of fill factor, this represents a decrease in maximum power output for CIGS and CdTe

thin films with the exception of α-Si. The annealing effect discussed previously that counters the Staebler-Wronski effect is responsible for α-Si high temperature performance [26].

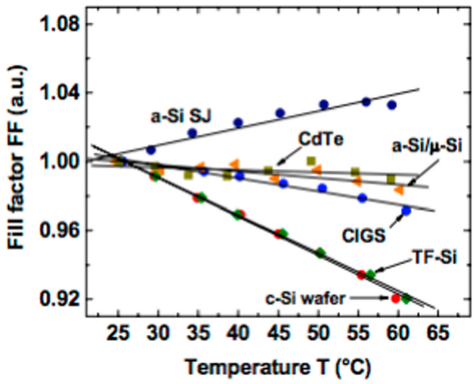

Fig. 1.1 Comparison of fill factor for a variety of thin-film cell materials as a function of temperature [26].

Abundance of raw materials is an important factor to consider when looking at emergent solar cell technologies. For instance in order for CdTe and CIGS photovoltaics to become the dominant solar technology we would require 75 times more gallium and tellurium than has ever been produced for all other applications combined. This combined with the relative availability of silicon being 20,000 and 300,000,000 times more abundant than gallium and tellurium, respectively. This makes the complete adoption of either of these thin-film technologies difficult [27].

The toxicity of compounds found in CdTe and CIGS solar cells pose a significant health risk throughout the life cycle of the solar cell. Both cell types utilise an n-type CdS emitter layer. Cadmium presents the most significant health and environmental risk as it has been demonstrated to cause pulmonary inflammation and fibrosis [28]. Significant leaching of the compounds occurs through roof-top acidic runoff and disposal in an aquatic environment and waste dump sites [29, 30]. Clearly the toxicity of the materials used in thin-film CdTe and CIGS solar cells should be considered when arguing for widespread adoption of these technologies.

Commercial solar cells are sold in modules where the reported efficiencies are often significantly lower than the those achieved by research lab cells. By comparing a number of commercially available solar cell modules in Table 1.1 it becomes clear that thin-film solar cells significantly under perform when compared with traditional crystalline silicon. Although CdTe has come the closest to rivalling the efficiencies of crystalline silicon, the toxic properties of cadmium pose a significant issue [26].

Material	PCE (%)
α-Si	9.8
CdTe	19.0
CIGS	19.0
Crystalline Silicon	21.5

Table 1.1 Comparison of solar cell module efficiency for a number of solar cell materials as of 2020 [31].

When comparing power conversation efficiency (PCE) alone, crystalline silicon clearly dominates. However this is not the only metric by which a solar cell technology should be judged. Price per watt is cited as an important metric for a solar cell systems characteristic. When considering the large amount of investment required to meet global energy demands, this metric should be at minimum considered along side power conversion efficiency. It is here that thin-films excel, being the first to brake the $1/Watt landmark [32]. This is in part a result of the thin photoactive layers and simple manufacturing techniques. Thin-film solar cells are able to target areas of the market where cost is everything and space is irrelevant.

1.2.3 Third Generation Solar Cells

Third generation solar cells look to achieve the high efficiency of first generation devices whilst maintaining the low cost deposition techniques of second generation devices. These technologies are currently less commercially viable and therefore considered 'emerging' technology. Examples of these include organic photovoltaics, copper zinc tin sulfide (CZTS), dye-sensitised solar cells (DSSCs) and the subject of this thesis HOIHP based solar cells.

Dye-Sensitised Solar Cells (DSSCs)

After the invention of the dye-sensitised solar cells by Oregan and Grätzel in 1991, it became apparent that this configuration defined a new class of solar cells (third generation) with instantaneous commercially viable efficiencies of 7.1%, whilst utilising low to medium purity materials and a low cost manufacturing process [33].

The key innovation of the dye-sensitised solar cell was to separate the charge carrier transport and light absorption functions carried out by the n-type semiconductor into a dye and electrolyte layer respectively. A layer of charge transfer dye is covalently bonded onto a mesoporous oxide layer usually made up of TiO_2 nano-particles.

Charge carriers are generated through photon electron interactions in the dye layer which is ideally a single molecule thick due to the short lifetime of the carriers. The photogenerated electrons are transferred to the TiO_2 conduction band where they diffuse to the anode.

The large band gap of TiO_2 makes the regeneration of the dye unlikely, as such regeneration is facilitated through a redox mediator. Typically the iodide and triiodide (I^- I_3^-) redox couple is used in the liquid electrolyte [34]. The dye sensitizer is extremely poor at harvesting light, a smooth monomolecular layer will absorb less than 1% of monochromatic light. The solution uses TiO_2 nanoparticles where the entire free surface of the particles is coated and arranged in an extremely porous structure. The large pore size allows for an electrolyte to diffuse through the structure.

In 2009, a new class of quantum dot materials, HOIHPs, were reported by Miyasaka *et al*. to exhibit photovoltaic performance equal to the best chalcogenides-based cells at the time [35]. Later developments allowed for HOIHPs to be incorporated as the sensitised layer in a DSSC cell [36]. More recently the use of a solid hole transporting material, replacing the unstable liquid iodine redox electrolyte allowed hybrid perovskite based solar cells to emerge as highly efficient [37], low cost devices that are already competitive with their silicon counterpart, with efficiencies surpassing 24% [38]. The continued increase in performance is now faster than that any previous photovoltaic technology, this is combined with low cost raw materials and low temperature solution processing [39].

1.3 Hybrid Perovskites

1.3.1 Perovskite Structure

Since the discovery of calcium titanium oxide ($CaTiO_3$), by Lev Alekseevich Perovski in 1839, any compound that shares its chemical formula (ABX_3) and structure are given the classification of perovskite. This perovskite aristotype is comprised of a B site metal cation bonded to six X site anions. At the cuboctahedral intercises of the resulting framework of corner-sharing BX_6 octahedra sits a large A-site cation. The resulting simple cubic ($Pm\bar{3}m$) structure is shown in Figure 1.2.

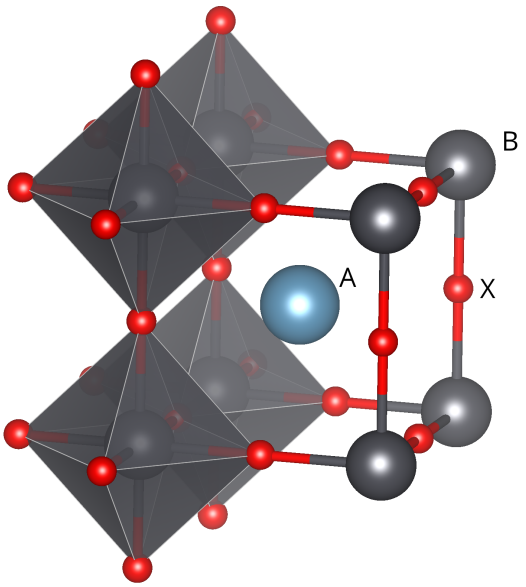

Fig. 1.2 Atomic coordination of the perovskite structure ABX_3.

The versatility of the perovskite structure is evidenced by the abundance of possible atomic substitutions into the structure. This has made it ideal for studying the effect of different elements on the bonding, crystal structure and properties of solid-state materials. As a result of the extensive range of chemical compositions and structures, perovskites have become a staple of functional materials research, owing to the large range of functional properties they exhibit. Specifically the well-known properties of oxide based perovskites such as $BaTiO_3$, that display both ferromagnetism and ferroelectricity and the superconductivity of layered perovskites such as $Ba_2YCu_3O_7$. Oxide based perovskites also show excellent magnetic, electrical and structural properties that are often governed by distortions resulting from collective Jahn-Teller effects and tilting of the corner sharing octahedral framework. For example the transport properties of ruthenates and manganites are influenced by the B-O-B octahedral

tilt angle. For this purpose, structural distortions from the simple cubic perovskite structure ($Pm\bar{3}m$) through octahedral tilting have been extensively described, most notably by Goldschmidt (1926 [40]), Glazer (1972 [41]) and Woodward (1997 [42]). In order to predict the likelihood of a tilted structure and the stability of a perovskite compound the Goldschmidt tolerance factor, τ was devised:

$$\tau = \frac{R_A + R_X}{\sqrt{2}(R_B + R_X)} \tag{1.1}$$

Here, the perovskite lattice is treated as a series of close-packed hard spheres. According to Equation 1.1, the ideal perovskite forms when the ionic radii of the A site cation (R_A) results in a B-X bond length that is twice the size of the unit cell edge and the A-X bond length is twice the length of the face diagonal. For this formulation a value for τ between $1.05 > \tau > 0.78$, predicts the formation of the archetypal cubic perovskite (described by the space group $Pm\bar{3}m$).

The majority of perovskite compounds exhibit distortions that deviate from the simple cubic structure though octahedral tilting. This is often temperature dependent where the ideal perovskite structure is only found at high temperature, typically above 1000 K for oxide perovskites. Upon temperature decrease lower symmetry phase transitions are displayed that exhibit octahedral tilting. For a tilted perovskite structure, the coordination of the A-site cation changes dramatically compared with that of the B-site cation. Octahedral tilting about the crystallographic axes optimises the anion coordination of the A-site cation. Therefore, octahedral tilting is driven by a mismatch in the size of the A-site cation and X site anion resulting in structural phase transitions, and can lead to the formation of nonperovskite structures. The possible tilting of perovskite structures and the associated space groups have been extensively studied by Glazer (1972 [41]), Woodward (1997 [42]), Howard and Stokes (2002 [43]). The resulting first and second order phase transitions that are made possible are identified in Figure 1.3 where the tilt systems and respective space-group relationships are shown.

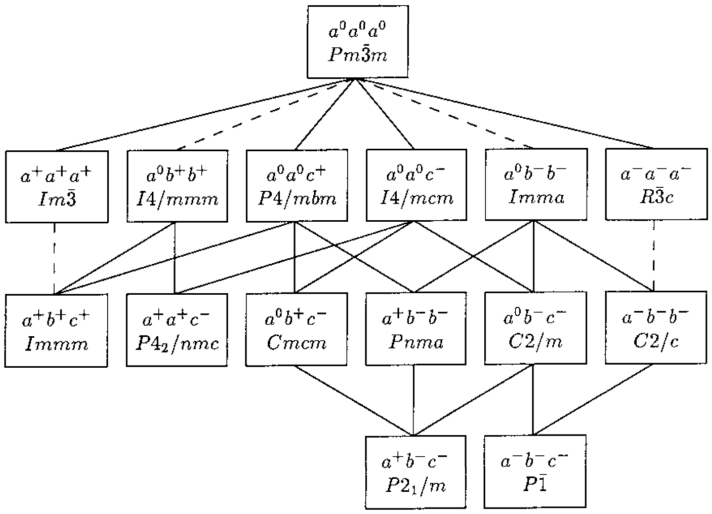

Fig. 1.3 Perovskite group-subgroup relationships derived by Howard and Stokes [43].

Beyond oxide based perovskites, inorganic halide perovskites were first reported by Wells in 1893, in the form of $CsPbX_3$ (X = Br, Cl, I). They were later characterised by Moller in 1958 as exhibiting a black perovskite phase for $CsPbBr_3$ and $CsPbCl_3$ at ambient temperature. The range of inorganic perovskites $CsPbX_3$ (X = Br, Cl, I) exhibit a photo-active cubic perovskite phase. However, for $CsPbI_3$ this phase only exists above 315 °C below which the structure reverts to a nonperovskite orthorhombic phase, despite possessing a tolerance factor value of 0.89. In general, compared to oxide based perovskites the tolerance factor does not generalise well as an indicator for the formation of halide based perovskite compounds as shown in Figure 1.4. Considering 576 oxide and halide based perovskites experimentally characterised under ambient conditions [44]. τ correctly predicts 62.87% and 77.27% of oxide and fluoride based perovskites respectively, whilst on average only 20% of Cl^-, Br^- and I^- based systems. The increased covalency of metal-halide bonds compared with metal-oxide perovskites results in larger observed atomic radii of metal halide perovskites beyond those described by Shannon's tables and therefore leads to values of τ outside of the range considered for stable perovskite compounds.

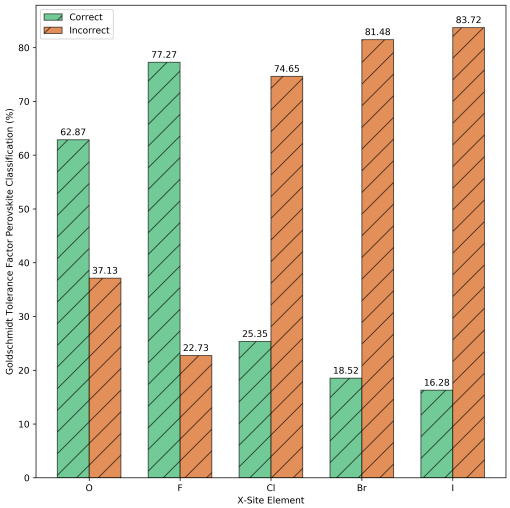

Fig. 1.4 The number of correctly classified perovskites based on a tolerance factor value $0.825 < t < 1.059$ from a data set of 576 experimentally characterised ABX_3 compounds containing X = O^-, F^-, Cl^-, Br^-, I^-. Plotted from data reported by Bartel et. al. [44].

1.3.2 Hybrid Perovskite Structure

The classification of materials according to the nature of their chemical bonding serves as a useful distinction for studying materials and their properties. For this purpose, functional materials can traditionally be categorised as being one of the following: a metal, ionic crystal, a valence or covalent crystal, a molecular crystal or a semi-conductor. This type of categorisation is useful in developing theories and methodologies to better understand fundamental material properties, and develop new technology. For instance, studying the physical properties of metals and semi-conductors has resulted in the development of modern electronic components such as transistors, photovoltaic cells and diodes. The study of ionic and covalent crystals, has lead to an understanding of magnetic ordering and electrical polarisation that emerges from ionic shifts, enabling the development of both magnetic and ferro-electric materials respectively. More recently, molecular solids have shown potential in functional electronics with the development of molecular semiconductors and optoelectronics [45].

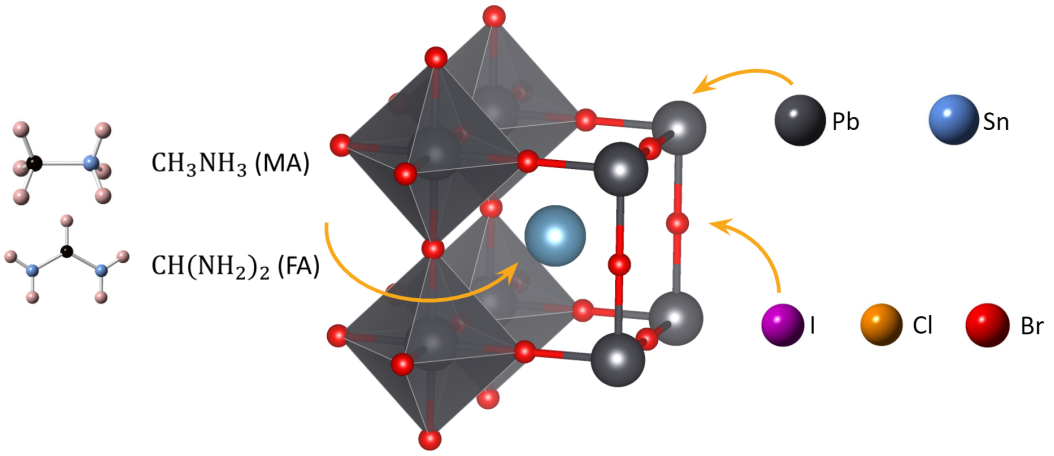

Fig. 1.5 A number of possible atomic substitutions are shown for each of the A, B and X sites for which the hybrid perovskite can be synthesised.

In searching for new material properties scientists now look to blur the lines between these distinct classes of materials. The development of hybrid organic-inorganic halide perovskites (HOIHPs), a class of material that combines molecular and valence solids, provides an exciting opportunity for new exciting research with potential applications in optoelectronics. The incorporation of an organic A-site cation into the perovskite structure, defined by the chemical formula ABX_3 and here consisting of a post transition metal (B-site) halide (X-site) framework were first reported in 1978 by Weber, where a simple cubic perovskite structure for the compound $CH_3NH_3PbX_3$ (X = Cl, Br, I) was described. The substitution of a large organic ammonium cation, in this case methylammonium onto the A-site and has been shown to extend the functionality and flexibility of purely organic perovskite compounds. With respect to photovoltaic applications, atomic substitution onto the B-site of HOIHPs has been restricted to IVA group metals (Pb^{2+} and Sn^{2+}) whilst combined with X-site halides Cl^-, Br^- and I^-. The resulting BX_6 octahedral framework is typically populated by the organic cations methylammonium (MA) and formamidinium (FA). Incorporation of organic linkers onto the X-site such as azides, formates, dicyanamides, cyanides and dicyanometallates have also been successfully synthesised.

The series of hybrid perovskites that has received the most attention from the academic community, and the subject of this thesis, $MAPbX_3$ (MA = CH_3NH_3 and X = Cl, Br and I) has lattice constants in the range of 5.7 Å to 6.3 Å. This is considerably larger than the 4 Å of conventional lead oxide based perovskites such as $PbTiO_3$. In addition, the relatively low bulk and Young modulus of between 10–25 GPa for HOIHP materials, is in contrast to 144 GPa for $PbTiO_3$. These distinctions

point towards relatively flexible bonds, and makes HOIHPs susceptible to structural distortions.

As with oxide based perovskites, HOIHPs exhibit temperature dependent phase transitions. Many of which, upon cooling follow phase transitions from cubic to tetragonal to orthorhombic driven by changes to symmetry. The temperature dependent structural phase transitions for the first synthesised hybrid perovskite $MAPbI_3$, which is the focus of this thesis, were first reported in 1978 by Weber as an analog to the inorganic perovskite $CsPbI_3$ [46]. It was reported that $MAPbI_3$ exhibits three structural phases, the first above 330 K, where the compound is described by the archetypal simple cubic perovskite space group $Pm\bar{3}m$ and is denoted as phase I. Between 160 K and 330 K the structure is tetragonal and was described by the space group *I4/mcm*, which is denoted II. Below 160 K the structure transitions to an orthorhombic *Pnma* phase, labelled III. More recent studies conducted by Weller *et al*. [47] and Whitefield *et al*. [48] aimed to derive a complete structure solution for $MAPbI_3$. These were based on powder diffraction measurements and synchrotron total scattering, on both hydrogenous and deuterated samples. For these studies, solutions for each of the temperature dependant structural phases (I, II and III) were reported including hydrogen and deuterium atomic parameters respectively [47, 48].

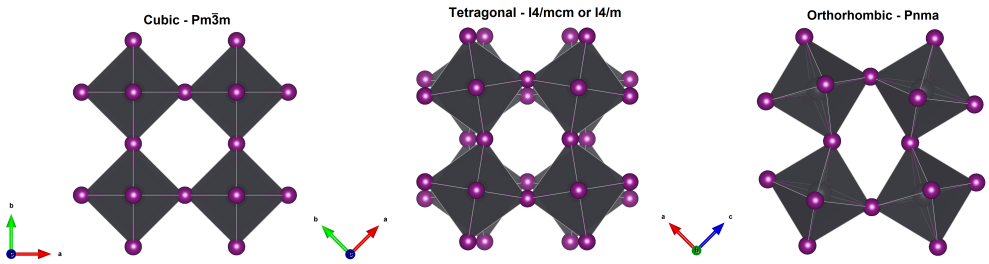

(a) (b) (c)

Fig. 1.6 The rotations of the PbI_6 octahedra for the (a) cubic, (b) tetragonal and (c) orthorhombic phases of $MAPbI_3$ as derived by Weber [46].

For the high temperature cubic $Pm\bar{3}m$ phase I, the MA^+ cation has C_{3v} point group symmetry and therefore completely orientationally disordered at the centre cavity of the surrounding PbI_6 framework, as shown in Figure 1.7a. The Pb-I bonds that form the octahedra sit along each of the crystallographic axis and are O_{d^-} symmetric. This zero tilt system is described by Glazer notation $a^0a^0a^0$.

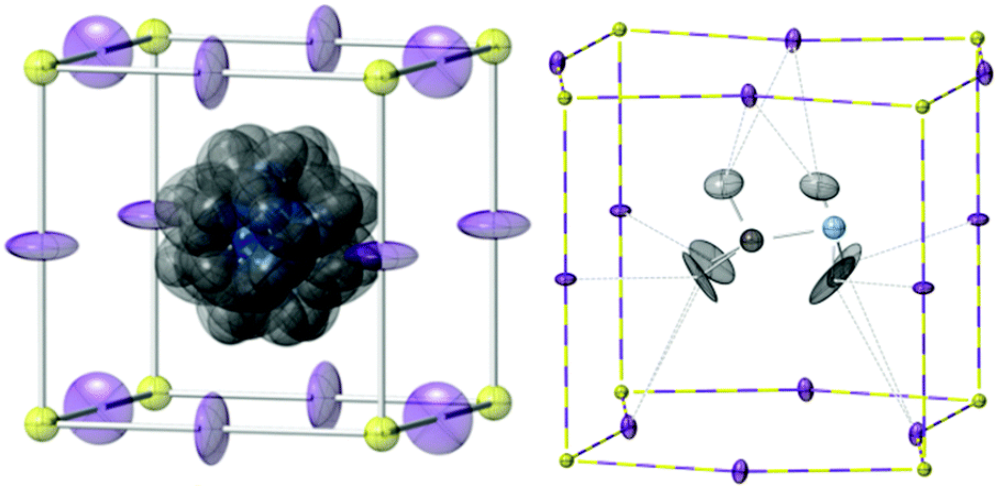

(a) (b)

Fig. 1.7 The structure of $MAPbI_3$ at (a) 352 K and (b) 180 K as reported by Weller *et al*. [47]. For this figure the ellipsoids describe; lead yellow, iodine purple, carbon black, nitrogen blue and hydrogen grey.

As the temperature is reduced and the structure transitions to tetragonal (phase II) with lattice parameters $\sqrt{2}a \times \sqrt{2}a \times 2a$, a drop in symmetry results, with out-of phase tilting of the PbI_6 octahedra about the crystallographic c-axis, denoted by Glazer notation $a^0a^0c^-$ and shown in Figure 1.7b. This notation form was originally designed with inorganic mineral perovskites in mind, and the linear MA^+ cations adopts a relaxed disordered configuration according to their site symmetry. With the $-NH_3$ ends pointed towards the centre face of the perovskite PbI_6 framework.

The transition from the tetragonal phase II to the orthorhombic phase III at 160 K with lattice parameters $\sqrt{2}a \times \sqrt{2}a \times 2a$ corresponds with head-to-tail anti-ferroelectric orientational ordering of the MA^+ cations. The tilting of the PbI_6 octahedra is found to conform with the ordering of the MA^+ cations and characterised by Glazer notation $a^-b^+a^-$ as shown in Figure 1.8.

Unlike inorganic based perovskites, such as $PbTiO_3$, the non-spherical symmetry of organic cations, such as MA^+, means the material is not characterised by a highly periodic array of atoms. Instead, for the high temperature simple cubic phase, the MA^+ sits on the A-site described by $m\bar{3}m$ symmetry, and has been shown to be completely orientational disordered through inelastic neutron scattering experiments in order to stabilise the structural phase [49]. The principal interaction between the inorganic BX_3^- framework and the organic cation is electrostatic. However, unlike organic perovskites, hydrogen bonding (N–H$\cdots$H for MA and FA) between the organic cation and surrounding inorganic framework influences structural distortions

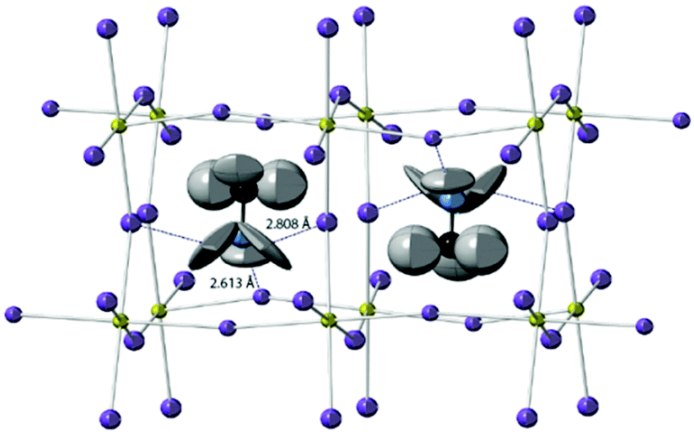

Fig. 1.8 The structure of $MAPbI_3$ at 100 K as reported by Weller *et al*. [47]. For this figure the ellipsoids describe; lead yellow, iodine purple, carbon black, nitrogen blue and hydrogen grey.

of the octahedral framework exhibited at ambient temperature [47]. The dynamics of the PbX_3 framework are therefore strongly coupled with the molecular cation, the result is a highly disordered framework [50]. The combination of flexible chemical bonding and considerable disorder point towards a new class of dynamic solids that is the focus of this work.

1.3.3 Evolution of the Perovskite Solar Cell

With respect to photovoltaics, the potential of HOIHP compounds was first realised in 2006 when Kojima et. al used the HOIHP $CH_3NH_3PbBr_3$ as a light sensitizer layer in an otherwise typical dye-sensitized solar cell (DSSC) [51]. These cells demonstrated an efficiency of 2.2%. Further work by the same group found that substitution of the bromide component with iodide resulted in a jump in efficiency to 3.8% [52].

The perovskite demonstrated an order of magnitude better light absorption than the common dye N719 used in typical DSSC devices. However the perovskite rapidly dissolved in the electrolyte component, with 80% degradation over 10 minutes [53]. This motivated a search for an alternative electrolyte material, specifically research focused on solid-state hole transport materials (HTM). In 2012 the originator of the DSSC configuration Michael Grätzel demonstrated spiro-MeOTAD (2,2',7,7'-tetrakis(N,N-di-p-methoxyphenylamine)-9,9'-spirobifluorene) as an effective HTM that boosted stability as well as further increasing photovoltaic efficiency to 9.7% [37].

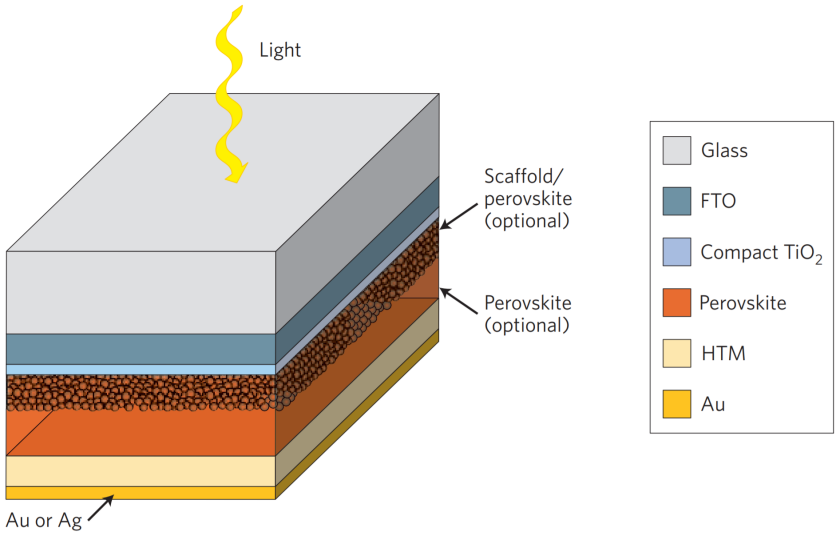

Fig. 1.9 The architecture of a simple perovskite solar cell [54].

In 2012 and 2013 key improvements to both stability and efficiency were made by Snaith *et al*. that moved hybrid perovskites into the photovoltaic spotlight [55, 56]. The first being the use of a mixed halide perovskite absorber, specifically $CH_3NH_3PbI_{3-x}Cl_x$, which improved stability but also increased diffusion lengths to 1 μm [57]. Next, by replacing the conducting TiO_2 layer with the non-conducting Al_2O_3 it was found that both open-circuit voltage (V_{oc}) and efficiency increased. This was a key finding as it demonstrated the ambipolar nature of the hybrid perovskite, here the material transfers both holes between the perovskite and spiro-OMeTAD layers and electrons to the respective electrical contact better than the original TiO_2 layer. The resulting device was no longer "sensitised", instead it was a two-component hybrid cell with a Al_2O_3 meso-scale scaffold.

Electron beam induced current (EBIC) measurements on perovskite based devices later confirmed that charge carriers are collected by both electrodes on the device [58]. Charge carrier life times of hundreds of nanoseconds and diffusion lengths of 1 μm have been measured for perovskite devices [57].

Additional improvements were made by coating the nonporous scaffold with an extremely thin absorber perovskite layer, the scaffolding could also be entirely removed to form simple planar cells that exploited the electron-hole transport properties of the perovskite [59]. The basic configuration of these solid-state perovskite solar cells is shown in Figure 1.9.

As shown in Figure 1.10, a series of incremental improvements has seen the efficiency of perovskite based solar cells increase rapidly compared with competing

technologies over the same time period. As of early 2020 the efficiency record for a perovskite solar cell device stands at 25.5% making it competitive with the industry standard silicon based devices [38], alone this sets perovskite apart from other emerging solar cell technologies.

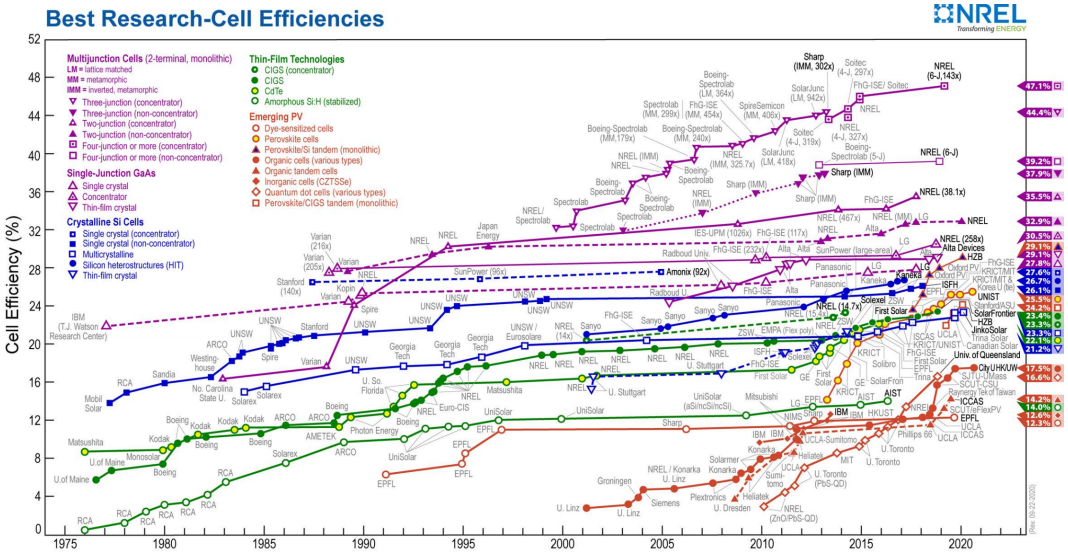

Fig. 1.10 The increased efficiency of a number of solar cell technologies over time [38].

Year	Device Structure	PCE (%)
2009	FTO/bl-TiO_2/mp-TiO_2/$CH_3NH_3PbI_3$/Redox Liquid electrolyte/Pt	3.8 [52]
2011	FTO/bl-TiO_2/mp-TiO_2/$CH_3NH_3PbI_3$/Redox Liquid electrolyte/Pt	6.5 [53]
2012	FTO/bl-TiO_2/mp-TiO_2/$CH_3NH_3PbI_3$/Spiro-OMeTAD/Au	9 [37]
March 2013	FTO/bl-TiO_2/mp-Al_2O_3/$CH_3NH_3PbI_{3-x}Cl_x$/Spiro-OMeTAD/Ag	12.3 [60]
July 2013	FTO/bl-TiO_2/mp-TiO_2/$CH_3NH_3PbI_3$/Spiro-OMeTAD/Au	15 [61]
2013	FTO/Graphene-TiO_2/mp-Al_2O_3/$CH_3NH_3PbI_{3-x}Cl_x$/Spiro-OMeTAD/Au	15.6 [62]
December 2013	ITO/np-ZnO/$CH_3NH_3PbI_3$/Spiro-OMeTAD/Ag	15.7 [63]
August 2014	1 ITO-PEIE/Y-TiO_2/$CH_3NH_3PbI_{3-x}Cl_x$/Spiro-OMeTAD/Au	19.3 [64]
June 2015	FTO/bl-TiO_2/mp-TiO_2/$(FAPbI_3)_{1-x}(MAPbBr_3)_x$/PTAA/Au	20.1 [65]
March 2016	1 FTO/bl-TiO_2/mp-TiO_2/$Cs_x(MA_{0.17}FA_{0.83})_{1-x}Pb(I_{0.83}Br_{0.17})_3$/Spiro-OMeTAD/Au	21.1 [66]

Table 1.2 Incremental changes to the architecture of the most efficient perovskite solar cells.

These high performance solar cells focus on mixed cation and halide hybrid perovskites, in particular a mixture of the standard perovskite compounds $MAPbX_3$, $FAPbX_3$ and $CsPbX_3$ (X = Br or I). Each of these compounds demonstrate photovoltaic properties, however, they each have their own drawbacks. The ability to swap cations and halides highlights the versatility of the perovskite structure to tune material properties, such as a band gap range of 1.1 to 3.3 eV as well as stability [67–69] . This versatility is also evident in the wide range of processing techniques available including spin coating, dip coating, 2-step interdifussion, chemical vapour

deposition, spray pyrolysis, atomic layer deposition, ink-jet printing or thermal evaporation.

Device Architecture

A strong absorption coefficient across the visible spectrum, ambipolar properties (the diffusion of both positive and negative species) and a high power conversion efficiency has meant that hybrid perovskite solar cells have gathered a considerable amount of interest from the photovoltaic community. This has resulted in the development of a large number of device architectures. These devices largely fall under one of two structures, mesoscopic (as shown in Figure 1.11a and Figure 1.11b) and planar (as shown in Figure 1.12a and Figure 1.12b).

Mesoscopic Architecture

Mesoscopic configurations shown on Figure 1.11a and Figure 1.11b are defined by the presence of an oxide scaffold onto which a layer of perovskite absorber is coated. This architecture can be further divided into conductive and non conductive scaffolds. It is unclear if the scaffold is necessary for obtaining perovskite cells of high performance.

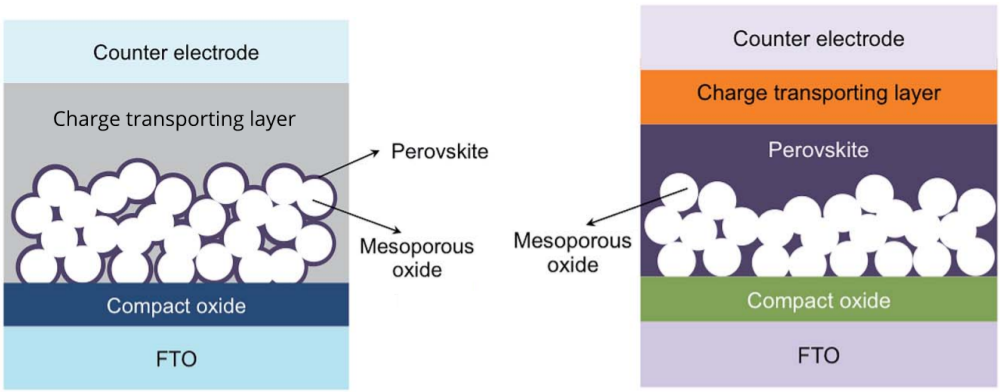

(a) (b)

Fig. 1.11 Mesocopic heterojunction perovskite solar cell device architectures with (a) no perovskite overlay and (b) with a perovskite overlay. Figures adapted from [70].

TiO_2 is the most studied conductive scaffold, the thickness of which has a varied effect on efficiency. For instance Kim *et al*. showed that for excellent performance only a submicron thick mesoporous TiO_2 layer is required compared to the $\approx 3\ \mu$m

thick layer required for regular DCCS cells [71]. Cell performance dependency on the presence of the mesoporous TiO_2 layer has been attributed to a perovskite pore filling effect. Enhanced performance of devices containing TiO_2 has also been ascribed to the high electron density in TiO_2 improving charge collection and transport.

As discussed previously replacing the TiO_2 with the non conducting AlO_2 demonstrated the ambipolar nature of the hybrid perovskite. This passive scaffold also drastically reduced the temperature of solution processing during deposition. TiO_2 requires high temperature (500 °C) sintering in order to remove organic binders from within the thin film. In contrast, Al_2O_3 requires <150 °C processing temperature where nanoparticles free of any binder are sintered [60]. This reduces the cost of producing the devices as well as making them compatible with flexible substrates. Improvements in the V_{oc} also occur when replacing TiO_2 with Al_2O_3 scaffolds, the result was an increase from 0.8 to 0.98 V respectively [59]. This can be attributed to a lack of surface and sub-band gap states that significantly decrease the chemical capacitance of the solar cell.

Planar Architecture

A planar solar cell is constructed with the exclusion of an oxide scaffold, and typically employ n-i-p or p-i-n configurations. Although <150 °C processing is possible for mesoscopic perovskite solar cells through the use of nanoparticles, the majority of high performance mesoporous films are incompatible with these processing methods. Hence removal of the scaffold allows for the low-temperature processing of planar heterojunction perovskite solar cells. The benefits of this architecture is integration with flexible polythylene terephlate (PET) substrates, the possibility of incorporating them into tandem cells and the increased versatility in deposition technique.

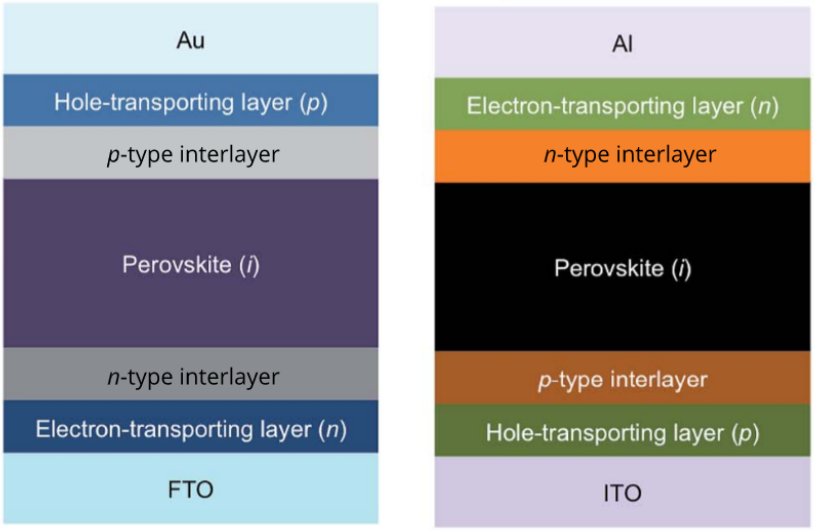

(a) (b)

Fig. 1.12 Two planar perovskite device architectures with (a) "n-i-p" and (b) inverted "p-i-n" configurations. Figures adapted from [70].

The n-i-p configuration often denoted "conventional" is most comparable to the most commonly used mesoscopic perovskite device (FTO/TiO_2/perovskite/spiro-OMeTAD/Au). Here an n-type layer is deposited onto a transparent conductive substrate, a perovskite layer is subsequently coated followed by a p-type layer and finally a metal contact. For this configuration the mesoscopic layer is replaced by a single metal n-type layer opposed to both.

A p-i-n configuration often referred to as "inverted" are comprised of solution-processable organolead halide perovskite placed between an n-type fullerene derivative ($PC_{61}BM$) and a p-type conducting polymer (PEDOT:PSS), here the p-type layer is coated onto the transparent conductive substrate first. This architecture type has seen a massive increase in performance over a short period of time, where PCE has risen from 3.9% to greater than 15% [70].

A Comparison of Mesoscopic and Planar Architectures

Both planar and mesoscopic devices architectures have demonstrated a commercially viable PCE of greater than 15%. A further comparison is therefore required. To start, the planar configuration is much simpler to process making it better for large-scale manufacturing. Charge carrier mobility is also greater in planar films, although these cells do suffer from photovoltage loss [72]. The use of a mesoporous scaffold often results in a more extensive heterogeneous nucleation and smaller crystallites [60].

The larger crystal sizes of planar films often improves charge transport, although producing excellent films on planar substrates is difficult. A common issue with hybrid perovskite films is decomposition. This results in the formation of PbI_2 which tends to be more pronounced in mesoporous architectures [73]. The wide bandgap of PbI_2 (E_g = 2.3 eV) and its poor optical absorption makes it an unwanted impurity in photovoltaic devices.

1.3.4 Challenges to Overcome in Perovskite Solar Cells

In terms of photovoltaics, excellent progress has been made with HOIHP materials given the relatively short time they have been studied. However, a number of challenges remain before a commercial product can realised.

Stability

Perovskite solar cells are highly sensitive to air and water vapour, and degrade quickly in the mildest of environmental conditions into products of PbI_2 and I_2 for $CH_3NH_3PbI_3$. In humid conditions, degradation is evident from a decrease in film absorption between 530 and 88 nm. Degradation resulting from exposure to moisture results in a reduction in crystallinity and the formation of PbI_2 and I_2 (although I_2 only forms in the presence of moisture and light) [74]. The PbI_2 product is highly soluble in water and toxic to humans.

In terms of currently commercialised solar cells, perovskite based cells most resemble CIGS. Without encapsulated CIGS solar cells degrade under environmental conditions similar to those based on perovskite. Preventing moisture penetration is possible through double glass layers. However, this drastically restricts the design of the cells and removes the possibility of flexible form factors. Recent approaches such as the incorporation of a moisture barrier like Al_2O_3 may free up the design of perovskite solar cells. Perovskite solar cells also suffer from degradation under ultraviolet light that is most severe for TiO_2 scaffold device architectures, although ultraviolet filters may mitigate this problem.

Environmental Impact

Thus far the most promising cells have been based on lead based HOIHP perovskites. Lead is highly toxic and a carcinogenic element, it is therefore associated with health and environmental concerns. As discussed above, PbI_2 is a common product of degradation in these perovskite cells, thus a number of possible candidates for replacing lead have been highlighted including Sn, Cu and Fe. However success

in producing an efficient solar cell has been limited. This problem is shared with the successfully commercialised CdTe based thin-film solar cells where sufficient encapsulation prevents contamination. However the environmental impact at the end of life disposal of these cells remains unclear. The commercialisation of CdTe solar cells was possible as photovoltaic modules are exempt from the European Restriction on Hazardous Substances (RoHS) [75], with a limit of 0.01% Cd by weight for any homogeneous layer, no CdTe module would be commercially feasible. Although the limits outlined by the RoHS for lead are ten times higher than that of Cd, this limit is still breached even if it was acceptable to consider the scaffold as a homogenous layer.

1.3.5 Compositional Engineering

In aiming to solve the problems posed in section 1.3.4, research has primarily focused on compositional engineering of the perovskite system in order to improve the power conversion efficiency (PCE), stability and environmental toxicity of hybrid perovskite solar cell devices.

For this approach, the traditional indicator for determining stable perovskite structures is the Goldschmidt tolerance factor (τ), as shown in section 1.3.1 for halide based perovskites the prediction power of τ is poor. As a result, with respect to photovoltaic applications the range of atomic species used in compositional engineering has remained relatively limited. For each of the sites A, B and X the atomic species MA or FA for the A-site, Pb^{2+}, Sn^{2+} or Ge^{2+} for the B-site and Cl^{-}, Br^{-} or I^{-} for the X-site have been reported as successful atomic substitutions.

In terms of PCE, A-site substitution has seen the state of the art move beyond the pristine $MAPbI_3$ and towards the so-called triple cation $MA_xFA_{0.95-x}Cs_{0.05}Pb(I_{1-y}Br_y)_3$ that has displayed the highest efficiency perovskite based solar cell device [66]. In principle A-site substitution aims to produce a more stable cubic phase. The larger radius of FA^{+} compared with MA^{+} causes the structure of the material to move from the tetragonal $MAPbI_3$ to the cubic $FAPbI_3$, this results in indirect changes to the electronic structure. As well as cation size, the structural changes observed when substituting MA^{+} for FA^{+} are effected by increased hydrogen bonding that alters the covalent/ionic nature of the Pb-I bonds, and may explain the observed increased thermal stability of $FAPbI_3$ [76, 77]. The favourable band gap of $FAPbI_3$ (1.47 eV) sits closer to the Shockley-Queisser optimum and has driven the mixed cation approach compared with pristine $MAPbI_3$ (1.57 eV) [78, 69]. However, the practicality of producing a highly crystallised photo-active phase thin film of $FAPbI_3$

has proven difficult. Therefore, significant work surrounding A-site substitution looks to compromise the band gap for stability and crystallinity.

In recognising the toxicity of Pb^{2+} based perovskite solar cells, efforts to substitute Pb^{2+} for both Sn^{2+} and Ge^{2+} is vital for commercialisation. $ASnI_3$ and $AGeI_3$ based systems show increased octahedral tilting of the perovskite framework, observed through a deviation from 180° for the bond angle X-A-X that correlates with a reduction in the observed band gap [79]. For $MAPbI_3$ based perovskites this moves the band gap towards a more desirable value. However, a relatively low number of reports on Ge^{2+} based systems combined with reduced stability has meant B site substitution has not yet proved viable.

The influence of X-site halide substitution, specifically Cl^-, Br^- or Br^- has been studied extensively for $MAPbX_3$. With respect to pristine $MAPbI_3$, the favourable band gap (1.5 eV) means a high current density, however it results in a relatively low open circuit voltage ($V_{oc} \approx 0.85$ V). In general $MAPbI_3$ based solar cells have reported the highest PSCs, primarily this is attributed to rapid charge extraction, high light absorption and efficient ambipolar charge transport [80–82]. The poor stability of $MAPbI_3$ has proven problematic, for which the structure is tetragonal under operating conditions and prone to degradation [83], this intensifies the toxicity concerns. Moving towards bromide based $MAPbBr_3$, the large band gap (2.2 eV) means much higher open circuit voltage ($V_{oc} \approx 1.2 - 1.5$ V) combined with good charge transport this has meant bromide based hybrid perovskites have gathered significant attention [84, 85]. The stability of Br^- is also improved compared with I^-, where the smaller anion size means the structure adopts a pseudocubic structure [86]. They do however exhibit poor light absorption hindering solar cell device performance. Chloride based devices, $MAPbCl_3$, have the highest band gap (3.1 eV) making them the least appropriate for solar cell applications due to the resulting poor light absorption [87, 88]. The complementary properties of the pristine compounds $MAPbX_3$ (X = Cl^-, Br^- or I^-) makes a mixed halide based perovskite an obvious approach for improving the PSCs. In this regard there has been great success in dictating the band gap of $MAPbI_3$ based solar devices through halide substitution of Cl^- and Br^- where a range 0.6 eV can be achieved. This relationship is consistent for $FAPbI_3$, where upon substitution of I^- for Br^- results in a drop in band gap from 2.23 to 1.48 eV [89].

2

Experimental & Theory

2.1 Diffraction Geometry

2.1.1 X-ray Scattering

X-rays describe the region of the electromagnetic spectrum with a wavelength around 1 Å. This is within the order of a crystals atomic spacing, and means X-rays are ideal for investigating the geometry of a crystal structure. In most laboratory based diffractometers X-rays are generated in a sealed high vacuum tube. A beam of electrons are accelerated towards an anode (typically made of Copper (Cu) or Molybdenum (Mo)), by the application of a large voltage (between 30 kV and 60 kV). The incident electrons ionise the target atoms, specifically the K-shell. When the resulting hole in the electron shell is filled from an electron in a higher level an X-ray with a well defined wavelength is released. The selection rules that govern the allowed transitions between an upper level (typically L-shells) and lower K-shell mean that a high energy doublet is emitted denoted $K_{\alpha 1}$ and $K_{\alpha 2}$ (λ = 1.54056 Å and λ = 1.54439 Å for Cu respectively). These are the characteristic wavelengths used to study the atomic structure of crystalline materials in most laboratory based diffractometers. Synchrotron facilitates offer an alternative source of radiation that benefits from very high intensity, tuneable wavelengths, low divergence and a high degree of polarisation.

X-ray scattering is a phenomenon that results from the interaction between an incident X-ray and the electrons bound to atoms that make up a material. A single electron will oscillate when interacting with the electric field of an incident X-ray, the resulting acceleration causes the X-ray to be scattered through the emission of an electromagnetic plane wave. When considering the scattering of a beam of incident radiation ($\vec{k}$) by a pair of atoms separated by a distance $\vec{r}$, the phase of the waves scattered by the two atoms ($\vec{k'}$) will shift due to the different path lengths. For an elastic process where $|\vec{k}| = |\vec{k'}|$, the resulting change in wave vector, referred to as the scattering vector ($\vec{Q}$) is defined by:

$$\vec{Q} = \vec{k'} - \vec{k} \tag{2.1}$$

As shown on Fig.2.1, the scattering angle 2θ can be related to the scattering vector $\vec{Q}$ by:

$$|\vec{Q}| = Q = \frac{4\pi \sin(\theta)}{\lambda} \tag{2.2}$$

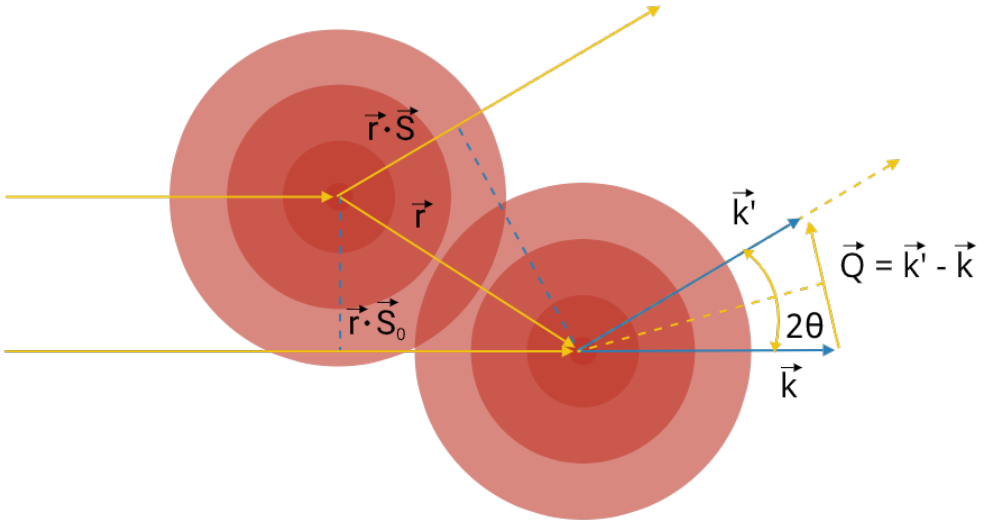

Fig. 2.1 The geometry of X-rays scattered by neighbouring atoms.

For a many particle system the scattering amplitude can be described by the sum of phase shifts for each particle in the system at a distance $\vec{r}$ from a defined origin:

$$F(\vec{Q}) = \sum_{i=1}^{N} f_i e^{-i\vec{Q}\cdot\vec{r}_i} \tag{2.3}$$

Here, the scattering of different particle types has been accounted for by weighting each component of the amplitude. In terms of X-rays, f_i is refereed to as the X-ray atomic scattering factor.

For an atom defined by a continuous distribution of particles, where an origin is defined by the center of the atom. The scattering of incident radiation by a small area of the distribution at a distance $\vec{r}$ from the origin and with a density $\rho(\vec{r})$ can be used to calculate the scattering across the whole distribution of particles by integrating across the entire volume:

$$f(\vec{Q}) = \int_0^\infty \rho(\vec{r}) e^{-i\vec{Q}\cdot\vec{r}} dr \tag{2.4}$$

This equation is essential to our understanding of observed scattering as it allows us to describe diffraction in terms of a Fourier transform. Specifically, the amplitude of scattering from incident X-rays by an atom is the Fourier transform of the electron density. This is especially useful when it comes to the analysis of our diffraction results through the use of convolution. This is because we can describe the crystal structure as the convolution of the atomic coordinates of the unit cell, the lattice and

the thermal motion of the atoms, and therefore the Fourier transform of the crystal structure corresponds to the product of the Fourier transform of each component. In this way the Fourier transform of the crystal structure, and therefore the observed scattering, can be constructed through treatment of each component of the structure and its Fourier transform separately, simplifying the structure determination process.

2.1.2 Neutron Scattering

Neutrons have zero charge and negligible dipole moment, such that they only interact with atoms through the nuclear force and the intrinsic magnetic moment of an atom. Therefore neutrons will penetrate deep within a material making neutron scattering ideal for studying the position of nuclei within a crystal structure. The different interaction mechanisms of X-ray and neutron scattering makes the information gathered by the respective techniques complimentary. For example hydrogen does not interact strongly with X-rays but has a large negative neutron scattering length in contrast to most other elements.

The wavelength (λ) of a neutron is related to its velocity ($\vec{v}$) according to the De Broglie relation. In terms of the wavevector $\vec{k}$ pointing in the direction travelled this relationship is expressed as:

$$\vec{k} = \frac{2\pi m\vec{v}}{h} \tag{2.5}$$

Where h represents Planck's constant and m represents the mass of a neutron. An incident neutron is described by the wavefunction $e^{i\vec{k}\vec{r}}$ (r being the position of the neutron) where the neutron has exact momentum $\frac{h\vec{v}}{2\pi}$ but is equally likely to be found at all positions r. A nucleus will scatter a passing neutron when the neutron passes through an associated scattering cross section (σ) defined by the interaction distance. This area is small compared to the wavelength of a neutron and therefore the scattering is uniform (isotropic). The wavefunction of an isotropic scattered neutron is $\frac{-b}{r}e^{i\vec{k}\vec{r}}$, where b represents the strength of the interaction and is known as the scattering length. The incident and scattered neutron is represented by the parallel and spherical wavefronts on Figure 2.2 respectively.

This is an example of elastic scattering and is a result of the fixed position of the nucleus, neither the energy of the neutron or nucleus changes. The relationship be-

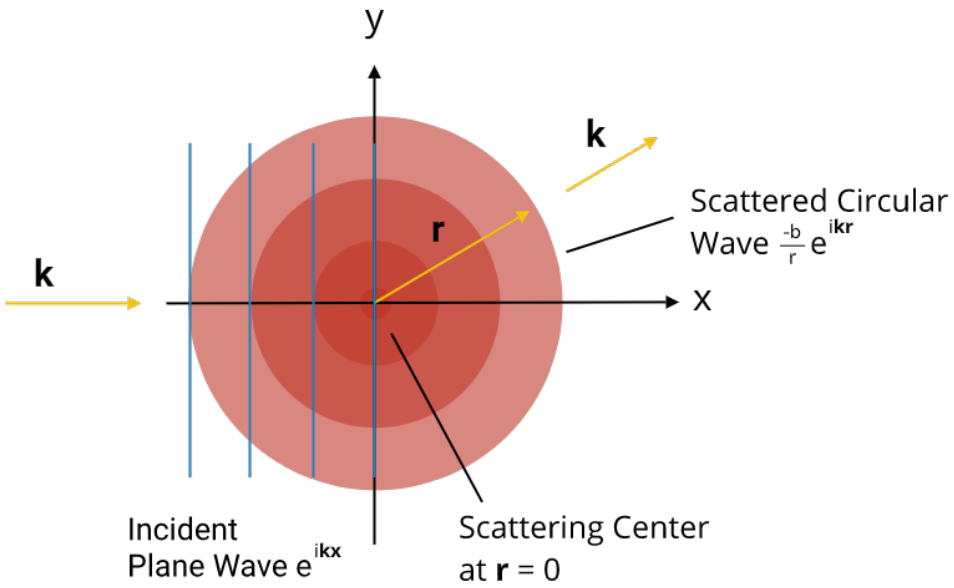

Fig. 2.2 An incident neutron wave and scattered isotropic scattering neutron wave.

tween the incident and scattered neutron wave vector is represented by the scattering vector ($\vec{Q}$) and is defined as:

$$\vec{Q} = \vec{k'} - \vec{k} \tag{2.6}$$

The angle between the incident and scattered neutron is defined as the scattering angle (2θ) and is illustrated on Figure 2.3.

For elastic scattering $|\vec{k}| = |\vec{k'}|$ and the scattering vector can be defined in terms of the scattering angle:

$$Q = \frac{4\pi \sin(\theta)}{\lambda} \tag{2.7}$$

In practice it is the intensity of scattered neutrons that is measured as a function of $\vec{Q}$ for elastic scattering experiments. Neutron diffraction is an example of coherent scattering where neutrons that are scattered by neighbouring atoms interfere. The atom at which scattering occurs becomes the origin of a spherical wavefront that has a definite phase compared to waves scattered by neighbouring atoms. At specific directions waves scattered by different atoms constructively interfere, which is dependent on the distance between atoms meaning structural information can be determined. The elastic nature of the scattering measured in this project means the equilibrium position of atoms is measured. Any incoherent scattering observed

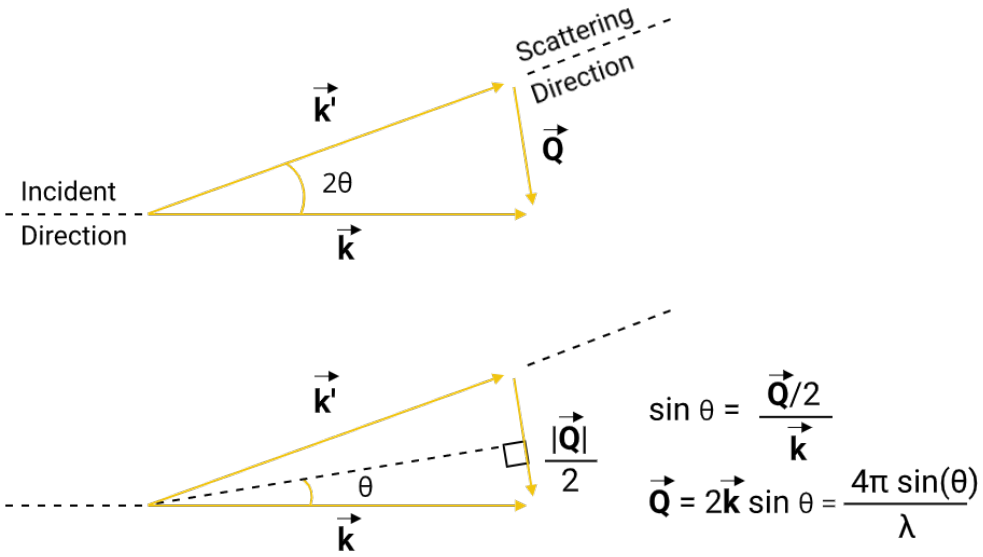

Fig. 2.3 The geometry of elastic neutron scattering.

during an elastic scattering measurement, such as quasielastic contributions to an observed Bragg peak are sufficiently small that it can be considered as background. Unlike X-ray scattering, for neutrons the coherent scattering length that describes the probability of a scattering interaction is independent of the scattering angle.

2.1.3 The Bragg Equation

A crystal structure is most often described by a unit cell containing many atoms. When describing the conditions required for diffraction to occur it is useful to consider each atom in the unit cell individually and as an isolated set of lattice points that extend throughout the crystal in three dimensions. The crystal is therefore made up of a number of these individual lattices that represent each atom in the unit cell. In order to understand how the geometry of a crystal results in a diffraction pattern it is useful to begin with the simple example of a crystal made up of a single atom that extends along a single direction spaced periodically. An incident wave will be scattered by this array of atoms at the same angle of incident. For the waves to be reflected in phase the path difference (or atom spacing) must be an integer number of wave lengths.

$$OQ - PR = m\lambda \tag{2.8}$$

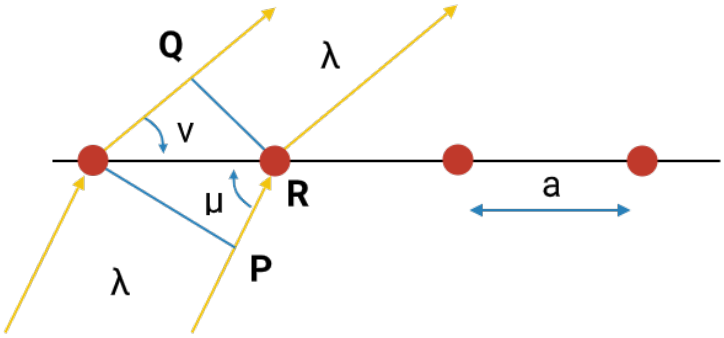

Fig. 2.4 Bragg scattering geometry.

We can use the two assertions described above to derive a condition required for the reflected wave to be observed, this is illustrated in Figure 2.5.

$$\cos(v) = \frac{OQ}{a}\sin(\mu) = \frac{PR}{a}a(\cos(v) - \cos(\mu)) = m\lambda \tag{2.9}$$

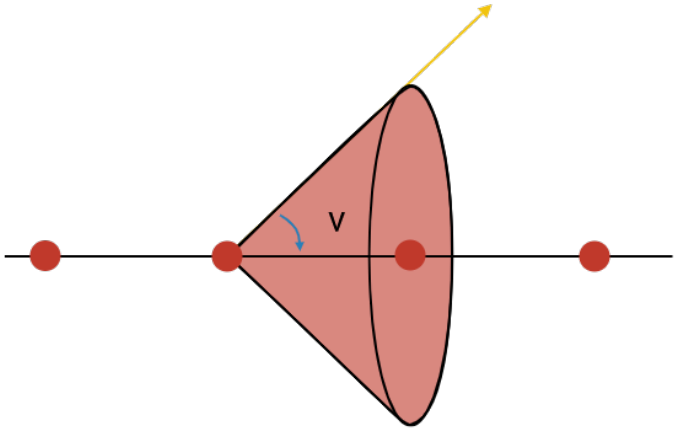

Fig. 2.5 Laue scattering geometry for a single dimension.

For a two dimensional array of atoms the above condition can be applied along two directions, the resulting condition for the reflected wave to be observed is therefore the common point between the two cones, as shown in Figure 2.6.

At this point it is simple to extend these conditions to three dimensions. The result is a set of Laue equations that describe the conditions of scattering for which a reflection will be observed in a diffraction experiment. It is the restrictive nature of these conditions that means for a single crystal diffraction experiment the crystal must be rotated around all possible angles for the respective crystal lattice to be constructed. For a powder diffraction experiment the scattering is measured along a

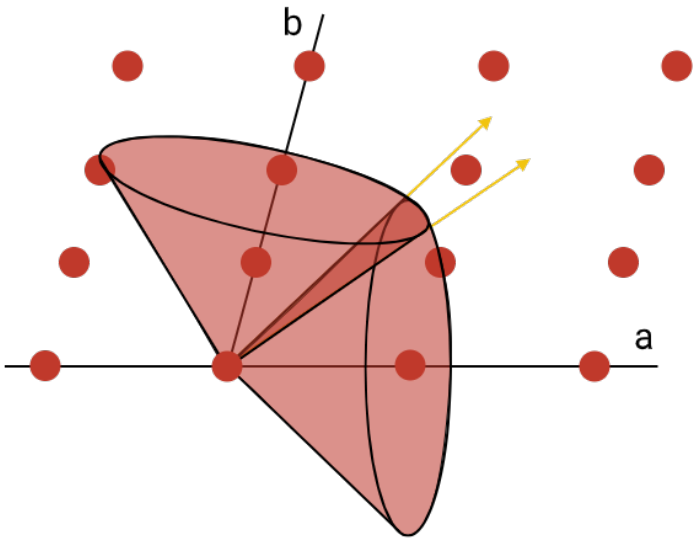

Fig. 2.6 Laue scattering geometry for two dimensions.

single angle, it is therefore convenient to simplify the Laue equations and describe the angle for which diffraction will occur in terms of the path difference between a wave reflected by a lattice plane and a wave reflected by a lattice plane immediately adjacent. This relationship was derived by W.L. Bragg and is hence known as the Bragg equation:

$$2dsin(\theta) = n\lambda (n = 1,2,3...) \tag{2.10}$$

For a wave with wavelength λ incident on a set of lattice planes with spacing d, the angle θ defines the order of diffraction n.

2.1.4 Reciprocal Lattice

For every real (or direct space) lattice defined by a set of axes and angles $a, b, c, \alpha, \beta, \gamma$, there corresponds a reciprocal lattice set $a^*, b^*, c^*, \alpha^*, \beta^*, \gamma^*$ whoes dimensions are reciprocally related. The reciprocal lattice is populated by a set of points with spacing defined by a^*, b^*, c^* and correspond to a set of direct lattice planes.

2.1.5 Ewald Construct

In order to relate the reciprocal lattice to the conditions of a diffraction experiment the Ewald sphere is introduced. This is particularly useful in describing the geometry of single crystal diffraction experiments. The Ewald sphere is a geometric sphere constructed in reciprocal space such that the sample crystal is situated at the origin,

as shown on Figure 2.7. The incident X-ray ($\vec{k}$) passes through both the centre of the Ewald sphere and the origin of the reciprocal lattice (corresponding to a (000) reflection), which lies on the surface of the sphere. The radius of the sphere is $\frac{1}{\lambda}$, where λ is the wavelength of the incident X-ray. The geometry of the Ewald sphere is such that any reciprocal lattice point that lies on the surface of the sphere describes a lattice plane that meets the Bragg condition (Equation 2.10). The angle between the incident radiation and a vector that joins the centre of the Ewald sphere to a reciprocal lattice point on the surface of the sphere is 2θ. Hence the distance between the reciprocal lattice origin and the diffraction lattice point on the surface of the sphere is $\frac{1}{d_{hkl}}$. By rotating a crystal sample the centre of the Ewald sphere rotates about the origin of the reciprocal lattice passing through the reciprocal lattice. For a single crystal X-ray diffraction measurement lattice points that intersect the surface of the Ewald sphere are projected onto a 2-dimensional plane in front of the sphere, by placing a CCD area-detector between the X-ray source and the sample the projected diffraction points of the reciprocal lattice can be recorded as points of intensity. The points of intensity therefore describe the lattice planes that diffract within a sample. The design of single crystal diffractometers allow for the rotation of a sample at all angles with respect to the X-ray beam using a 4-circle goniometers, each goniometer has a respective degree of freedom defined by the angles ϕ, 2θ, ω and κ. A set of spatial axis (x, y , z) are defined with respect to the diffraction instrument, it must be determined how these axis relate to the reciprocal axis (a^*, b^*, c^*) in order to calculate the h, k, l of a diffraction pattern. The orientation matrix describes this relationship:

$$\vec{x} = \mathbf{A}\vec{h} \rightarrow \begin{bmatrix} x \\ y \\ z \end{bmatrix} = \begin{bmatrix} a_x^* & b_x^* & c_x^* \\ a_y^* & b_y^* & c_y^* \\ a_z^* & b_z^* & c_z^* \end{bmatrix} \begin{bmatrix} h \\ k \\ l \end{bmatrix} \tag{2.11}$$

Where **A** is defined as the orientation matrix and describes the magnitude of the components of the reciprocal cell axes (a^*, b^*, c^*) with respect to x, y and z. The orientation matrix is determined by measuring a small region of the reciprocal space, this is a quick process and allows for an initial unit cell to be calculated at the start of a single crystal diffraction experiment. A comprehensive diffraction pattern is then measured.

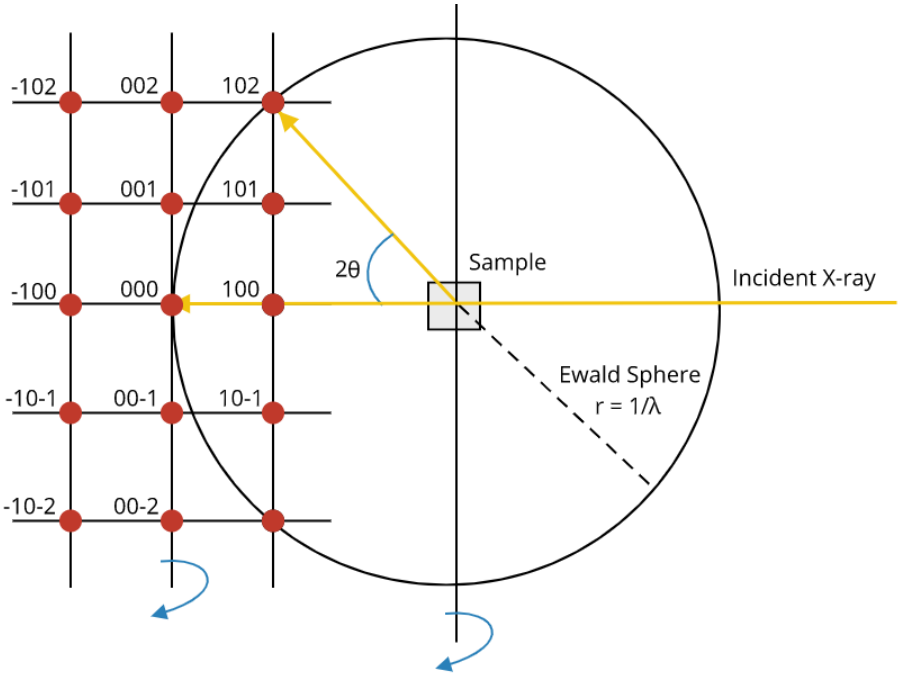

Fig. 2.7 Geometry of an Ewald sphere.

2.1.6 Structure Factor

So far the elastic scattering processes for incident X-rays and neutrons by electrons and nuclei respectively has been described. It has been shown that for a crystalline material this will result in diffraction if Bragg's equation conditions are met. For a diffraction experiment this leads to the measurement of a series of reciprocal lattice points from which the reciprocal lattice is constructed through the Ewald construct. Where the measured intensity of reciprocal lattice points, known as the structure amplitude F_{hkl}, are then related to the atomic structure of the crystalline material. This is the primary objective of most material characterisation studies and diffraction experiments.

For a unit cell made up of n atoms of different scattering factors and lengths for incident X-ray and neutrons respectively, the total scattering amplitude of each Bragg reflection (F_{hkl}) is calculated through the summation of the scattering contributions for each atom in the unit cell:

$$F_{hkl} = \sum_{j=1}^{n} g^j t^j(s) f^j(s) e^{2\pi i(hx^j + ky^j + lz^j)} \tag{2.12}$$

For each reflection the scattering contribution from each atom in the unit cell is defined in terms of its atomic co-ordinates x, y and z, the occupancy of the atomic

site (g^j), the atomic displacement parameter t^j (describing the thermal motion of the atom) and the atomic scattering $f^j(s)$ factor. The occupancy term describes the time averaged occupation of a given atomic site, typically this is expressed as a fraction of a fully occupied site with a value of 1, and depends on the amount of disorder in the average structure of the material and the symmetry of the site. The interpretation of the temperature factor (t^j) and atomic form factor ($f^j(s)$) are less obvious and worth exploring in more detail.

Atomic Displacement Factor - t^j

Crystal lattice excitations result in the oscillation of atoms about an equilibrium position defined by the atomic coordinates x, y, z. The temperature factor is introduced into the structure amplitude equation in order to account for this thermal motion and the resulting spread in scattering. In material characterisation there are two levels of approximation made about the thermal motion of atoms. The simplest isotopic description assigns a single atomic displacement parameter to each atom in the unit cell, for which the temperature factor is defined as:

$$t^j = e^{-B_j \frac{sin^2(\theta)}{\lambda^2}} \tag{2.13}$$

Where B_j is the displacement parameter of the j^{th} atom, θ describes the Bragg angle of the reflection for which the structure amplitude is being calculated and λ is the incident wavelength. During analysis of diffraction data B_j is typically the parameter that is determined, from which the root mean square deviation (u^2) from the equilibrium position (Å^2) can be calculated using:

$$B_j = 8\pi^2 (u^2)^j \tag{2.14}$$

Often the isotropic model is not sufficient to describe more complex atomic thermal motion, for this case the anisotropic model is used, where the thermal motion is described by an ellipsoid centred at the equilibrium position of a specific atom. This model uses 6 anisotropic atomic displacement parameters β^j_{11}, β^j_{22}, β^j_{33}, β^j_{12}, β^j_{13}, β^j_{23} to describe the shape of the ellipsoid, the corresponding temperature factor is defied as:

$$t^j = e^{-(\beta^j_{11}h^2 + \beta^j_{22}k^2 + \beta^j_{33}l^2 + \beta^j_{12}hk + \beta^j_{13}hl + \beta^j_{23}kl)} \tag{2.15}$$

It should be noted that like the atomic coordinates the anisotropic displacement parameters are subject to the symmetry requirements of the subject atom. As such the appropriate restraints should be applied such that the symmetry requirements are accounted for.

Atomic Form Factor - $f^j(s)$

In section 2.1.1 and section 2.1.2 the scattering geometry for both electrons and nuclei by X-rays and neutrons respectively was described, we showed that for X-rays a characteristic scattering factor results in a drop in the measured scattering intensity as a function of Bragg angle. This scattering factor was also shown to drop as a function of the number of electrons for the scattering nuclei. For neutrons the scattering length does not vary as function of Bragg angle. The atomic form factor $f^j(s)$ is the general term given to describe the scattering factor for X-rays and scattering length for neutrons. The functional dependency of scattering factor on scattering angle θ has a general form across the periodic table. As such it is common for the relevant scattering factor of an element to be calculated from the general equation:

$$f_0^i(sin(\frac{\theta}{\lambda})) = c_0^j + \sum_{i=1}^{4} a_i^j e^{-b_i^j sin(\frac{\theta}{\lambda})} \tag{2.16}$$

This describes the scattering factor as a function of 9 coefficients: c_0, $a_1 - a_4$, $b_1 - b_4$ and $\sin(\frac{\theta}{\lambda})$, which can be found in the International Tables for Crystallography, vol. C [90]. So far we have restricted our discussion of the scattering capability of atoms with respect to the element type and scattering angle dependency. However, for the majority of elements anomalous scattering contributions must be accounted for. These contributions are most notable close to the absorption edge of a given element and results from the promotion of electronic transition by incident radiation. Including anomalous scattering contributions our equation for the atomic form factor becomes:

$$f^j(s) = f_0^j(s) + \delta f^{j\prime} + i\delta f^{j\prime\prime} \tag{2.17}$$

Where $f^{j\prime}$ and $\delta f^{j\prime\prime}$ are the real and imaginary anomalous scattering components and can be looked up in the International Tables for Crystallography [90].

2.2 Single Crystal Diffraction

2.2.1 Data Collection

Crystal Selection

The quality of a structural solution derived from any single crystal diffraction measurement is subject to the quality of the crystal measured. Hence the procedure for proper crystal selection is worth outlining. The size and shape of a selected crystal is an important consideration when performing single crystal diffraction measurements, especially when measuring on in house laboratory based diffractometers such as the Rigaku Supernova (section 2.2.6) that provide limited intensity. Typically a crystal between 30 and 300 μm is acceptable for the collection of high-resolution data. For microfocus beam-lines such as those at the ESRF (section 2.2.7) high quality data acquisition is possible for smaller crystals. Crystal shape is often a prerequisite of the crystal structure and crystal growth technique employed during sample preparation. This makes selecting the ideal crystal, that is one whose dimensions are uniform in all directions, is often impractical. Plate or needle like crystals pose the biggest problems during data collection but can often be cut to a more appropriate shape. In general data collection is possible for most crystal shapes given proper treatment of absorption correction.

A polarising stereo microscope is helpful for effective crystal selection. The optical examination of a crystal can allow for satellite crystals and various other imperfections to be spotted. A set of polarising filters placed in front and behind the crystal specimen and rotated such that they are cross polarised allows for the isotropic, uniaxial or biaxial nature of the crystal to be determined when rotating the crystal between the two filters. This serves two main purposes, firstly it provides an initial assessment of the crystal lattice type. Secondly, if a crystal is made up of more than one fragment then the crystal will appear to be comprised of bright and dark regions and the specimen can be rejected. This type of examination is also useful for spotting twinning before preliminary measurements.
The best test for a crystals quality is through a series of short screening measurements where reflections can be manually inspected for signs of satellites, tails, streaks and powder rings.

Crystal Mounting

Once a crystal thought to be of sufficient quality has been selected it is ready to be mounted onto the diffractometer goniometer head. A goniometer is made up of

two perpendicular slides that can be adjusted in-order to centre the crystal through the rotational axis of the diffractometer circles. The crystal is mounted to either a small loop or capillary and held in place by either a viscous oil or amorphous glue depending on the temperature range being measured. Once secured the loop or capillary can be mounted onto the goniometer head and secured to the diffractometer. As mentioned above after mounting the crystal it must be centred within the path of the beam for all rotations of the goniometer. This is often aided through the use of a high magnification video camera which also enables the recording of a crystal movie so that a crystal shape model can be generated and used for numerical absorption correction during data reduction. For a four-circle diffractometer such as those commonly found at beamlines and the Rigaku Supernova the ϕ-axis is orientated perpendicular to the microscope axis. From this position the goniometer slides can be used to centre the crystal whilst rotating the crystal along the ϕ-axis for multiple full rotations.

Collection of X-ray Intensities

After successful mounting and centring of the crystal the data collection process can begin. A data collection strategy must be decided, that is often based upon a pre-experiment where small regions of reciprocal space can be measured, from which an initial unit cell and orientation matrix can be established. Based on this a collection strategy that reaches an appropriate level of completeness and redundancy is calculated along with a reasonable exposure level for the diffractometer CCD.

2.2.2 Data Processing

Once the data has been collected the data processing routines can begin. This includes all data handling processes up until the structural refinement procedure. In this thesis, all data processing has been carried out using the CrysAlisPro program.

Peak hunting

The purpose of the peak hunting routine is to search each diffraction image recorded during data collection for Bragg peaks above a given threshold. There are a number of options for carrying out this process, each option aims to find an appropriate balance between distinguishing background noise and Bragg peaks.

Indexing and Unit Cell Determination

Reflection indexing and unit cell determination finds the most appropriate unit cell for a given set of reflections by determining an orientation matrix that relates the experiment coordinates system to the samples unit cell. After this process, manual inspection of the fit is required. Here alignment between the lattice and reflections can be assessed along each of the directions a^*, b^* and c^*. A distribution histogram is useful for determining if any reflections are not accounted for by the current unit cell. For example, it is common that low intensity reflections have not been accounted for that sit between the centre and edge peaks on the histogram for a given axis. In this case doubling of the unit cell along the given axis is required.

Data Reduction

Once an orientation matrix has been determined, the process of extracting reflection intensities and formatting them ready to be used by the structure refinement program can begin.

The first step is to decide if a lattice centring filter should be applied to the list of observed reflections, if the structure is unknown it is recommended that no filter is applied. Next an algorithm used for predicting the position of reflections based on the orientation matrix is chosen. Following this the method used for background evaluation is decided.

The next step is to choose whether outlier rejection is to be applied. In the case that an unknown structure is measured then no outlier rejection is used. This allows for outliers to be assessed.

Space Group Determination

Once the measured reflection files are prepared the process of determining the space group begins. This process is carried out using GRAL, a space group determination module which has an interactive mode in CrysAlisPro. The first step involves determining if a centred crystal lattice is present. This involves comparing the number of missing reflections or systematic absences you would expect to find if a specific centring, with the number of these systematic absences that are present in the measured data. The number of absence violations that exist are then compared with the intensity of the violations in order to asses if the centring conditions are violated. It should be noted that if a centring filter is applied in the data reduction process then 0 violations will be recorded for that given centring, but this is only because they are not counted for in the data reduction process. Next a Niggli reduction routine is

applied to the unit cell in order to find if a standard reduced form of the current cell exists.

At this point the space group selection begins. To start, the E-value statistics are used as a cautious hint for if the structure is non-centrosymmetric. These values are based on the normalised structure factors scaled such that the mean value of E^2 is 1 in all resolution shells. It has been shown that for centrosymmetric space groups it is statistically more likely that E values are either very large or very small. For observed data the value $< E^2 - 1 >$ can be used to judge this statistical occurrence [91]. For centrosymmetric and non-centrosymmetric space groups this value is likely to be closer to 0.97 and 0.74 respectively.

Finally a list of possible space group are generated based on systematic absences generated by the occurrence of either screw axes and glide planes. This analysis was performed along three axial directions of the reciprocal lattice and varies according to the crystal system. At this point either a single space group option becomes apparent or a series of space groups with identical reflection conditions are given.

2.2.3 Data Finalisation

The data finalisation process was used to apply frame scaling and absorption corrections to the reflection intensities obtained in the data reduction process. After the data reduction process an automatic finalisation process is run by default, however for unknown structures and data collected at beam-line facilities the full data finalisation process is run. This allows for inspection of the data reduction output and individual data quality indicators. The R_{int} value is used as the final indicator for accessing the quality of the data collection, when this value is sufficiently large (>15%) then accurate structural refinement is not possible.

Once the data finalisation process is complete the software package SHELX is used for structure solution and refinement.

Observed and Calculated Structure Factors

The observed structure factors F_o^2 are determined during the data reduction process from the intensities measured (I_o) during the data collection process. A series of experimental corrections were made, these include: the application of a scale factor (k), Lorentz-polarisation correction (Lp) and a transmission factor.

$$F_o^2 = \frac{I_o}{k \times Lp \times A} \tag{2.18}$$

The basis for the structure solution and refinement processes is the calculation of the structure factors (F_c) based on a crystallographic structural model. The structure factor describes the Bragg scattering of an incident wave by a family of crystal lattice planes for a given crystalline sample. The scattering contribution of each atom in the unit cell is calculated for each reflection (hkl) using the equation:

$$F_c = \sum_{hkl}\sum_{i} f_i \exp\left[-B_i(\frac{\sin\theta}{\lambda})^2\right] exp\left[2\pi i(hx_i + ky_i + lz_i)\right] \tag{2.19}$$

This equation describes a scattering model for each atom in the unit cell dependant on the atomic form factor (f_i) of a given element, the mean-square isotropic thermal contribution (B_i), the atomic coordinates x_i, y_i and z_i and the scattering angle (θ) of the scattered X-ray with a wavelength λ. A more complicated equation is used for describing anisotropic thermal contributions. From the calculated structure factor both the amplitude (the square of which gives the measured intensity) and phase angle can be determined. However, the phase of a measured structure factor is not experimentally observable, and constitutes the famous phase problem. If the phases were experimentally observable the electron density (p_{xyz}) of a structures unit cell would be directly accessible by the inverse Fourier transform of the structure factors over the volume (V) of the unit cell:

$$p_{xyz} = \frac{1}{V}\sum_{hkl} F_{hkl} exp[-2\pi i(hx + ky + lz)] \tag{2.20}$$

However as this is not possible a number of methods have been derived that serve to obtain a structural model from the measured diffraction data. This is known as structure solution. The choice of method depends on a variety of experimental factors such as atom types, anomalous scattering contributions and the maximum resolution of the measurement and are described below.

2.2.4 Structure Solution

After data finalisation is carried out the process of solving and refining the structure is performed. At this point in the process the following is obtained: a set of integrated reflection intensities, lattice constants, a space group and an idea about the chemical composition of the sample. The next step is to generate a starting model for the structure that is to be used for structural refinement. This is done with the program SHELXS which has the options of implementing either Patterson or direct methods for generating a solution. These programs are relatively self contained and run with

little to no input from the user and therefore a complete description of these methods is beyond the scope of this work. For this work, the direct methods were found to be sufficient. This step results in the generation of initial phase angles for the measured structure factors from which an initial electron density map of the structure's unit cell can be calculated. The model generated at this stage typically only contains the positions of a few heavy atoms, these positions are often not correct and often the wrong atom type has been assigned. The refinement process is therefore required in order to obtain a model that more accurately describes the measured data.

2.2.5 Structure Refinement

The program SHELXL was used to refine crystal structure models against diffraction data obtained in single crystal X-ray diffraction measurements. In order to use SHELXL two input files are required, a reflection data file (*.hkl) containing h, k, l, F^2 and $\sigma(F^2)$ data columns and a measurement/structure model file (*.ins) that provides a number of instructions to the program through four-letter keywords along with information describing the crystal structure. The program merges equivalent reflections and removes systematic absences by default. A general description of the refinement workflow is as follows. The *.ins and *.hkl files are read by the SHELXL program using the command "shelxl name.ins", the program then performs the crystal structure refinement routine and outputs a series of files including a *.res file. Here more accurate phase angles have been calculated and an updated electron density map is generated, from this more accurate atom positions are derived for the current model. Peaks and holes in the electron density map allow for new atom positions to be found as well as identifying positions where atoms are already located and should be removed. The updated structural information found in the *.res file is then copied into the *.ins ready to be refined again by SHELXL. This process is repeated until reasonable agreement parameters have been reached, this entire process is known as refinement.

Least-Squares Refinement

The principal method used for determining changes to a structural model during structural refinement of diffraction data is known as least squares. The general principle of this method is simple, a set of structure factors are obtained from a structural model by Fourier transformation. A function that relates the observed (F_o) and calculated (F_c) structure factors is then minimised, the two equations used for this purpose are:

$$\sum_{hkl} w\Delta_1^2 = \sum_{hkl} w(|F_o| - |F_c|)^2 = min \tag{2.21}$$

$$\sum_{hkl} w\Delta_2^2 = \sum_{hkl} w'(|F_o|^2 - |F_c|^2)^2 = min \tag{2.22}$$

Here the symbols Δ_1 and Δ_2 refer to minimisation based on F_o and F_o^2, both of which can be used in structure determination. The parameter w refers to the weights applied to each observation, this allows for the errors that relate to more accurately observed data to be counted as more important than errors associated with less accurately recorded data. Although both F_o and F_o^2 can be used for minimisation, in practise the use of F_o^2 has been shown to be more beneficial. This is because during the data reduction process weak data may result in the recording of negative F^2 values, where the background model has been determined to be stronger than a peak. For this case negative reflections are given an arbitrary value when F_o is used for refinement. This affects the structure determination as the resulting bias ignores the structural information contained within these weak reflections.

The process of minimising the squared difference of observed and calculated structure factors involves calculating the partial derivative of each structure factor with respect to the parameters (p_i) used to calculate the structure factor. The parameters used to calculate the structure factors vary depending on if anisotropic or isotropic thermal parameters are refined for each atom:

$$\sum_{hkl} w(|F_o| - |F_c|)\frac{\partial F_c}{\partial p_i} = 0 \tag{2.23}$$

$$\begin{aligned} Anisotropic : p_i = {} & x_1, y_1, z_1, U_{11(1)}, U_{22(1)}, U_{33(1)}, U_{23(1)}, U_{13(1)}, U_{12(1)}, \\ & x_2, y_2, z_2, U_{11(2)}, U_{22(2)}, U_{33(2)}, U_{23(2)}, U_{13(2)}, U_{12(2)}, ... \end{aligned} \tag{2.24}$$

$$Isotropic : p_i = x_1, y_1, z_1, U_{iso(1)}, x_2, y_2, z_2, U_{iso(2)}, ...x_i, y_i, z_i, U_{iso(i)} \tag{2.25}$$

This process requires that over a single cycle only small changes (Δp_i) are made to each parameter (p_i) that describes the current structural model. The calculated structure factors (F_c) are calculated using the equation:

$$F_c = F_{c(0)} + \frac{\partial F_c}{\partial p_1}\Delta p_1 + \frac{\partial F_c}{\partial p_2}\Delta p_2 + ...\frac{\partial F_c}{\partial p_n}\Delta p_n \tag{2.26}$$

A starting structural model ($F_{c(0)}$) that is close to correct is required so that the shifts made to each parameter are small. The small shift requirement means that a Taylor series expansion can be used for determination of each partial derivative. The result is a series of normal equations for each parameter from which parameter shifts can be calculated and the model improved.

R-Factors

The validity of a structural model obtained through the methods described above can be assessed by a number of residual factors (R-factors). These factors are g iven for any published structure and in general used as a merit for the validity of a model. The most commonly reported of these is the R-factor:

$$R = \frac{\sum_{hkl} ||F_o| - |F_c||}{\sum hkl|F_o|} \tag{2.27}$$

This describes the average deviation between the observed and calculated structure factors. It does not however, account for the weights used during the refinement process, which if accounted for generally give a worse value. This weighted R-factor (wR) is calculated as follows for F_o and F_o^2 respectively:

$$wR = \sqrt{\frac{\sum_{hkl} w\Delta^2}{\sum_{hkl} wF_o^2}} \tag{2.28}$$

$$wR_2 = \sqrt{\frac{\sum_{hkl} w(F_o^2 - F_c^2)^2}{\sum_{hkl} w(F_o^2)^2}} \tag{2.29}$$

This quantity is most useful in illustrating if changes to the structural model are significant to the validly of the model. Finally a further indicator, the goodness of fit (S, GooF or GoF) is also used:

$$S = \sqrt{\frac{\sum_{hkl} w\Delta^2}{N_R - N_P}} \tag{2.30}$$

This calculation uses the number of independent reflections (N_R) and number of refined parameters (N_P). This value is subject to manipulation from an improper weighting scheme, but if used correctly should give a value close to 1. This is useful for determining if a structural model is overfitted (S<1) or underfitted (S>1) and gives an indication as to if the absorption correction was not carried out correctly or

if model has been assigned the the wrong space group. As a rule of thumb values for wR_2 and R-value below 0.15 and 0.05 respectively are reasonable for a complete structure.

2.2.6 Single Crystal Diffractometer - Rigaku Oxford Diffraction Supernova

Variable temperature single crystal diffraction measurements were performed using a dual wavelength (Cu/Mo) microfocus Rigaku Oxford Diffraction Supernova Diffractometer. Operating at 0.8 kV and 50 mA, with multi-layer focusing optics diffraction images are recorded using an Atlas S3 CCD area detector. The sample is held using a MiTeGen microloop and experimental temperature is maintained using a Oxford Cryosystem cryo cooling system allowing for data to be collected between 80 K and 500 K.

2.2.7 Multipurpose Diffractometer - PILATUS@SNBL

Variable temperature single crystal and powder synchrotron diffraction experiments were conducted using the PILATUS@SNBL based single-crystal diffractometer located at the Swiss-Norwegian Beam Lines (SNBL), European Synchrotron Radiation. An X-ray wavelength of λ = 0.956910 Å was used for all measurements focused using a pair of collimating and vertically focusing rhodium-coated X-ray mirrors and a sagittally focusing double-crystal Si(111) monochromator. Samples are mounted to a flexible kappa-goniometer. Diffraction images are recorded using the large area detector, Pilatus 2M detector as shown on Figure 2.8. Primarily the diffractometer was developed for single-crystal diffraction. However, powder diffraction measurements are made possible through azimuthal integration of raw area detector images. An Oxford Cryostream 700+ nitrogen blower is used to maintain experimental temperatures between 80 K and 500 K. The non standard wavelength (0.9569 Å) used for these experiments required the anomalous absorption factors f' and f" to be calculated for each element during analysis, this was done using the software package Hephaestus.

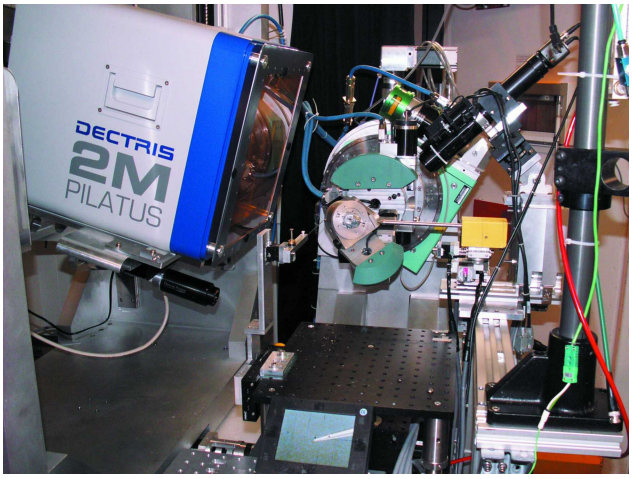

Fig. 2.8 Photograph of the PILATUS@SNBL based single-crystal diffractometer including Pilatus 2m detector and the Huber mini-kappa goniometer located at the Swiss-Norwegian Beam Lines (SNBL) [92].

2.3 Powder Diffraction

2.3.1 Powder Diffraction Pattern

As discussed in section 2.1.4 and section section 2.1.5 the diffraction pattern observed for a single crystal can be understood in terms of a three dimensional array of reflections (reciprocal space) constructed from the geometry of the diffraction experiment using the Ewald sphere. The situation is very different when studying powders. Typically a powder is a collection of identical single crystals, crystallites or grains, these are measured in a similar way to single crystals, through irradiation by an incident monochromatic beam. For an ideal experiment the crystallites are large in quantity and randomly orientated such that the resulting diffraction pattern is made up of many identical reciprocal lattices randomly orientated with respect to one another. Importantly each reciprocal lattice shares a common origin, meaning that common reflections (or simply identical reciprocal lattice vectors) across all the reciprocal lattices will be equidistant from the origin. If we construct an Ewald sphere in the same maner as discussed in section 2.1.5 then identical lattice vectors will form a ring across the surface of the Ewald sphere. The scattering vector will form a cone thats apex corresponds to the centre of the Ewald sphere that passes through the ring formed by the spread of identical lattice vectors. The assumption made in a powder diffraction experiment is that the number of crystallites approaches infinity, this means the density of the scattering vector ring is constant and therefore a flat detector only has to measure along a narrow plane that passes through the centre of the Ewald sphere. As the detector follows this arc of measurement the angle the detector makes with the incident scattering vector is known as 2θ. This means that a powder diffraction measurement can be represented as a series of intensities (total number of counts) along a single axis (2θ) and is referred to as the diffraction pattern in this work.

2.3.2 Components of Powder Diffraction

Compared with a single crystal experiment a powder diffraction pattern contains the information described by the reciprocal lattice of a large number of randomly orientated crystallites compressed along a single axis. Despite this loss of information a large amount of information about the crystal structure of the sample, the macroscopic properties of the sample crystallites and the instrument used for measurement can be analysed. In some cases powder diffraction offers significant benefits over its single crystal counter part. For instance it is not possible to synthesise single crystals of some compounds of sufficient size or quality for a single crystal experiment. It is

also a better study of the average structure of a material where stoichiometry and structural variations from crystal to crystal for the same sample mean only powder diffraction offers the ability to study the bulk properties of a material.

In order to understand a powder diffraction pattern it is useful to separate the pattern into a number of components each of which contain different structural information. The first component is a continuous background, this contains information about the crystallinity of the sample, the information contained within the background is often discarded during analysis. Overlaid onto the background is a discrete set of observed peaks that arise from the Bragg diffraction described above, as such they are often referred to as Bragg peaks. The peaks of a diffraction pattern contain all the structural information to be analysed and are comprised of the following components: position, intensity and shape, all of which encode separate information about the crystal structure, sample properties and the instrument used for the measurement. Details of each of the contributing components are discussed below.

The data recorded during a powder diffraction experiment takes the form of a series of discrete intensities recorded at regular step sizes. The measured intensity $Y(i)$ of the i^{th} data point can be considered as the sum of all contributions, y_k, from m overlapping Bragg peaks. Therefore all that is required to describe the diffraction pattern is to calculate $Y(i)$ for the total number of measured data points.

$$Y(i) = \sum_{k=1}^{m} I_k[y_k(x_k) + 0.5y_k(x_k + \delta x_k)] \tag{2.31}$$

Peak Position

The peaks that make up a diffraction pattern arise from Bragg scattering by a periodic lattice. The measured 2θ angle at which each peak appears is a function of the lattice plane (described by Miller indices h,k and l) from which the diffraction occurs. The dimensions of the samples unit cell and the wavelength of the incident radiation. The quadratic form of the Bragg equation describes this relationship:

$$\begin{aligned}\sin^2(\theta) = \frac{2}{4}[&h^2a^{*2} + k^2b^{*2} + l^2c^{*2} + \\ &2klb^*c^*cos(\alpha^* + 2lhc^*a^*cos(\beta^*) + 2hka^*b^*cos(\gamma^*)]\end{aligned} \tag{2.32}$$

The complexity of this equation is reduced when considering different crystal system types (for instance if $\alpha = \beta = \gamma = 90°$). For an ideal crystal and diffractometer setup

this formula completely describes the angle at which each reflection is measured. However in reality a number of sample and instrumental factors result in a shift in the measured angle. The most common corrections required are displacement parameters arising from a shift in the measured sample and improper alignment of the diffraction axes in relation to the radiation source and detector. These are known as specimen displacement and zero shift respectively. Typically these are the only corrections considered during analysis.

Peak Intensity

The structure factor is the primary contributing factor to the measured intensity of a Bragg reflection, it derives from the atomic structure of the sample is therefore most important for material characterisation. However, for a powder diffraction experiment there are a number of other factors that are not directly related to the atomic structure of the measured sample but never-the-less required in understanding the measured Bragg peak intensity. We will see later that a number of sample and instrumental factors mean that for a powder diffraction experiment the measured peaks are not sharp delta functions as you might expect from our understanding of the structure factor but instead these instrumental and sample factors result in peak broadening. This means for powder diffraction the intensity of a Bragg peak is defined as the total area under a given peak. The term profile intensity (y_i) is given to the experimentally measured intensity for a discrete set of scattering angles (T_i) and are typically measured with a fixed step size. Including both sample and instrumental factors the integrated intensity can be calculated as follow:

$$I_{hkl} = KxP_{hkl}xL_{\theta}xP_{\theta}xA_{\theta}xT_{hkl}xE_{hkl}x|F_{hkl}|^2 \tag{2.33}$$

The factors included in this equation will be discussed in detailed below but for reference: K is the scale factor, P_{hkl} is the multiplicity factor, L_{θ} is the Lorentz multiplier, P_{θ} is the polarisation factor, A_{θ} is the absorption correction, T_{hkl} is the preferred orientation function, E_{hkl} is the extinction factor and F_{hkl} is the structure factor.

Scale Factor - K

The scale factor is a simple multiplier applied to each structural phase considered in the analysis. This factor accounts for the fact that the atomic structure contributions to the intensity such as the structure factor are typically calculated for a single unit cell, in order to calculate the resulting measured intensity a large number of known

experimental and sample factors would be required including the intensity of the incident beam and the volume of the sample measured. In practice this is not possible and therefore the scale factor is introduced in order to normalise the calculated intensity with respect to the measured intensity.

Multiplicity Factor - P_{hkl}

As previously discussed a powder diffraction experiment measures the reciprocal lattice of a large number of randomly orientated crystallites along a single axis. This means that Bragg reflections where the magnitude of the reciprocal lattice vector is the same will be observed at the same Bragg scattering angle. For certain symmetry the Bragg reflections that share the same reciprocal lattice vector will also share the same intensity. Therefore when modelling the measured intensity it is only required that a single intensity is calculated for a group of reflections and then a multiplier can be applied to obtain the total measured intensity.

Lorentz-Polarisation Factor - L_θ and P_θ

Two adjustments to our calculated Bragg reflection intensity are required that account for the geometry of a diffraction experiment. The first known as the Lorentz factor has two components. The first results from the fact that different reflections will fulfil the conditions of diffraction longer than others. This can be derived from the Ewald construction. Here a reciprocal lattice rotating with a constant angular velocity will result in shorter scattering vectors spending shorter periods of time intersecting with the surface of the Ewald sphere and therefore fulfil the conditions for diffraction less than longer scattering vectors. This results in a smaller measured intensity and is relevant to both single crystal and powder diffraction experiments. From this explanation it is simple to see that this correction is θ dependent and proportional to $\frac{1}{sin(\theta)}$. The other component arises from the fixed length of the detector slit (and therefore only relevant to powder diffraction). This means that a fixed length of each Debye ring will be measured for all Bragg angles. For each ring the total scattering intensity is evenly distributed across its entire circumference, the length of which is dependent on Bragg angle. This means that the portion of the total scattering intensity for each ring measured by the detector is proportional to $\frac{1}{sin(2\theta)}$. Both of these contributions are combined into a single Lorentz factor defined as:

$$L = \frac{1}{sin(2\theta)} \tag{2.34}$$

The second correction to be made to our peak intensities results from the partial polarisation of a scattered electromagnetic wave. Here the electric vector of an incident electromagnetic wave can be separated into two components. The first component is that where the wave amplitude is parallel to the reflected plane, for this component the reflected amplitude is unperturbed by the scattering interaction. For the second component the amplitude is perpendicular to the reflection plane, for which the reflected wave is reduced by a factor of $cos^2(2\theta)$. The total polarisation factor (p) is calculated as:

$$p = \frac{1+\cos^2(2\theta)}{2} \tag{2.35}$$

Absorption correction - A_θ

In powder diffraction the absorption correction required varies depending on the sample measured and the geometry of the diffractometer. In general the intensity of an incident X-ray beam (I_o) will be reduced when passing through a material due to inelastic (Compton) scattering, elastic (Raleigh) scattering and ionisation. Considering this the absorption of an incident beam can be calculated in terms of the linear absorption coefficient (μ) using the equation:

$$I = I_o e^{\mu l} \tag{2.36}$$

Here l is the total path length travelled by the incident beam through the material resulting in a measured intensity of the transmitted beam as I. For a diffraction experiment the effect of absorption (A) can be calculated by integrating over the entire volume (V) of the sample that contributes to scattering (in the path of the incident beam):

$$A = \frac{1}{V}\int_V e^{-\mu_{\text{eff}} l} dV \tag{2.37}$$

Here the effective linear absorption coefficient (μ_{eff}) is introduced to account for the reduced density of a packed powder.

Preferred Orientation - T_{hkl}

A powder diffraction pattern arises from the measurement of a large number of randomly orientated crystallites. This assumption implies that the same number of crystallites are orientated such that the scattering contributions are equal for each

Bragg reflection. However certain experimental factors can reduce how random the orientation of each crystallite is for a measured sample, the most notable of which is the crystallite size and shape.

For a sample made up of a large number of isotropic crystallites, achieving a random distribution of orientations is easy. However, for crystallites that deviate from this ideal, such as plate-like or needle-like crystals the natural packing of crystallites introduces a bias into the orientations of the crystallites. The effect of this is an adjustment in the scattering intensities for families of reflections and is known as preferred orientation.

The preferred orientation factor aims to counter the effects of preferred orientation in a set of measured Bragg peaks. However, it is important to not that proper sample preparation is the best way to reduce any of the effects outline above.

Extinction Factor - E_{hkl}

Two types of extinction effects (primary and secondary) are relevant to the reduction of measured intensity for both powder and single crystal diffraction experiments. Primary extinction results from the back-reflection of a scattered wave back into the crystallite of origin. Here the reflected wave is usually out-of phase with the incident wave and therefore results in destructive interference. Secondary extinction occurs in crystals with low mosaicity, here a scattered beam is re-scattered by a different neighbouring block that happens to fulfil the conditions of diffraction for the scattered beam.

Peak Shape - $\Omega(T_{hkl})$

As discussed above the powder diffraction pattern describes the collapse of a 3d dimensional reciprocal space across a single axis. This inevitably results in a significant overlap of Bragg peaks, meaning that the process of analysing a diffraction pattern requires the modelling of a peak shape with a function from which individual peak positions and intensities can be extracted. The peak shape function describes the observed peak shape and is constructed from the convolution of instrument broadening contributions, wavelength dispersion and a sample related function. The background contributions are also linearly added.

The instrument contributions relate to the geometry of the diffractometer and the wavelength dispersion function describes any variation in the wavelength of the source and is therefore dependent on the source type and monochromator used. These contributions are inconsequential to material characterisation and are typically

determined through the measurement of a standard material that does not contain any broadening from the sample. The sample function however, is directly related to the properties of the sample being measured and therefore useful in the structural analysis process. The predominant sample related properties that give rise to peak broadening are the average crystallite size (τ) and microstrain (ε). The additional broadening (β) contribution for each Bragg peak resulting from sample size and strain is calculated from:

$$\beta_{size} = \frac{\lambda}{\tau \cos(\theta)} \tag{2.38}$$

and

$$\beta_{strain} = k\varepsilon \tan(\theta) \tag{2.39}$$

The constant k is dependent on the nature of the microstrain. In order to calculate the additional sample related broadening β a peak shape function is required from which the extra width β can be extracted. For this purpose two basic peak shape functions are defined, the Gaussian and Lorentzian distributions:

$$\begin{aligned} G(x) &= a_G exp(-b_G x^2) \\ a_G &= \frac{2}{H\sqrt{\frac{ln2}{\pi}}}, b_G = \frac{4ln2}{H^2} \end{aligned} \tag{2.40}$$

$$\beta_G = \frac{1}{a_G} \tag{2.41}$$

$$\begin{aligned} L(x) &= \frac{a_L}{1 + b_L z^2} \\ a_L &= \frac{2}{\pi H}, b_L = \frac{4}{H^2} \end{aligned} \tag{2.42}$$

$$\beta_L = \frac{1}{a_L} \tag{2.43}$$

The Lorentzian distribution can be described simply as a sharp peak with a long tail where as the Gaussian distribution does not have a tail but has a rounded tip. In

practice a powder diffraction peak is often described as a mix of both Gaussian and Lorentzian components. Ideally a convolution of the two would be used, however traditionally the computational complexity required to perform these calculations over a number of cycles was not available and therefore a linear combination of the two has become standard. This function is known as the psudo-Voigt function:

$$\Omega(x) = \eta L(x) + (1-\eta)G(x) \tag{2.44}$$

Here η is a mixing parameter describing the ratio of the Gaussian and Lorentzian contributions. As noted above, the width of the peak is an important parameter in material characterisation. This is denoted as H above and is known as the Caglioti formula [93], this describes the full width half maximum (FWHM) as a function of θ [94]. The parameters U, V and W are free variables refined during structure determination.

$$H = \sqrt{U\tan^2(\theta) + V\tan(\theta) + W} \tag{2.45}$$

In practice this formula for H is rarely used. This is because the Gaussian and Lorentzian separately describe the instrument and sample broadening contributions respectively. Therefore separate definitions of H for both Gaussian (H_G) and Lorentzian (H_L) distributions are desirable. This is achieved through the Thompson-Cox Hastings modified pseudo-voigt, for which the separate Lorentzian and Gaussian components are defined as:

$$H_G^2 = (U + D_{ST}^2)\tan^2(\theta) + V\tan(\theta) + W + \frac{I_G}{\cos^2(\theta)} \tag{2.46}$$

$$H_L = X\tan(\theta) + \frac{Y + F(S_z)}{cos(\theta)} \tag{2.47}$$

Here the free parameters (U, X) and (Y, I_G) relate to sample broadening resulting from strain and size respectively. The parameters D_{ST} and $F(S_z)$ also refer to strain and size broadening and there meaning is dependent on strain/size model used.

2.3.3 Rietveld Refinement

The primary purpose of a powder diffraction measurement is material characterisation through the determination of a correct crystal structure model. The loss of information

that results from the 1 dimensional nature of a powder diffraction pattern means that generating a solution from scratch is impractical for all but the simplest cases. However, if an approximate structural model is known the analysis of powder diffraction data proves a powerful technique for the optimisation and refinement of a crystal structure model and when appropriately implemented is comparable to its single crystal diffraction counterpart. This is primarily due to the contributions made by Rietveld in the development of the the Rietveld refinement method.

Rietveld refinement aim is to minimise the weighted difference between the calculated (Y^{calc}) and measured (Y^{obs}) profiles of a powder diffraction pattern:

$$\Psi = \sum_{i=1}^{n} w_i (Y_i^{obs} - Y_i^{calc})^2 \tag{2.48}$$

For a set of n measured data points the weight w_i is assigned to every data point and minimised through a non-linear least squares routine. Therefore the task is to generate a calculated profile that best describes the crystal structure of the measured sample taking into account both instrumental and sample scattering contributions. Using the concepts described earlier in the chapter the calculated profile can be defined as:

$$Y_i^{calc} = \sum_{\phi} S_{\phi} \sum_{hkl} I_{\phi,hkl} \Omega(T_i - T_{\phi,hkl}) + b_i \tag{2.49}$$

Here $I_{\phi,hkl}$ is defined by equation 2.33. The model is therefore a summation over the number of refined structural phases ϕ that contribute to the measured Bragg scattering. As the name implies the Rietveld refinement method involves the refinement of the following parameters related to the structural and instrumental scattering contributions:

- The parameters that describe the background function (b_i), either defined as a set of discrete intensities as a function of 2θ with refined shifts or a 1 to 24 Chebychev polynomial.
- Zero-shift and other parameters related to the geometry of the experimental setup (described in section 2.3.2).
- Parameters associated with describing the peak shape function $\Omega(T_i - T_{\phi,hkl})$ (described in section 2.3.2).

- The lattice parameters of the unit cell (described in relation to peak position in section 2.3.2).
- Any preferred orientation, absorption or extinction parameters (described in section 2.3.2).
- The scale factor of each structural phase S_{phi} (described in section 2.3.2).
- The atomic coordinates of the atomic sites assigned to the structural model
- The occupancy of each atomic site (described in section 2.1.6).
- The thermal displacement parameters describing the thermal motion of each atom, where the number of parameters depends on the use of an isotropic or anisotropic model (described in section 2.1.6).

It is unusual that from the start of a refinement all of these parameters are allowed to refine. The complexity of the problem and number of refined parameters mean that typically the parameters are allowed to refine sequentially allowing the least-squares routine to minimise before the next parameter is refined. The order in which these parameters are allowed to refine is dependent on the data quality, the accuracy of the starting structural model and how well the instrument/profile contributions are defined.

2.3.4 Agreement Factors

The agreement between the measured and calculated profile gives an indication of the quality of a refinement. For this purpose a number of statistical agreement factors are used for both comparing crystal structure models and determining when the refinement process is finished. For this purpose the R-factors, R_p and R_{wp}, are used to directly compare the difference in observed and calculated intensities:

$$R_p = 100\frac{\sum_{i=1,n}|Y_i^{obs} - Y_i^{calc}|}{\sum_{i=1,n} Y_i^{obs}} \tag{2.50}$$

$$R_{wp} = 100[\frac{\sum_{i=1,n} w_i|Y_i^{obs} - Y_i^{calc}|^2}{\sum_{i=1,n} w_i Y_i^{obs2}}]^{\frac{1}{2}} \tag{2.51}$$

These values directly relate to the quantity minimised during the Rietveld optimisation process. Looking at our definitions for R_p and R_{wp} it is clear that for an ideal model the average value for $(Y_i^{obs} - Y_i^{calc})^2$ is equal to the statistical error for each data point ($\sigma^2[Y_i^{obs}]$). Given that the weights (w_i) for our definition of R_{wp} are for

most circumstances defined as $\frac{1}{\sigma^2[Y_i^{obs}]}$ this ideal model would give a value of 1 for $w_i(Y_i^{obs} - Y_i^{calc})^2$ and the resulting value for R_{wp} is the best possible value we could obtain. As such for a given data set the best possible R_{wp} is a useful parameter, this is known as the expected R-factor (R_{exp}):

$$R_{exp} = 100[\frac{n-p}{\sum_i w_i Y_i^{obs2}}]^{\frac{1}{2}} \tag{2.52}$$

Here n is the number of data points and p is the number of refined parameters. Using the above definitions we can define our final agreement parameter for powder diffraction, the statistical value χ^2 known as Chi-squared:

$$\chi^2 = \sqrt{\frac{R_{wp}}{R_{exp}}} \tag{2.53}$$

For least-squares refinement the value of χ^2 should decrease for every cycle, if this is not the case it is an indicator that there is a problem with the refinement or several of the refined parameters are correlated. Given our definition for χ^2 it is clear that it's value should never go below 1 and an ideal value is one that is close to 1.

2.3.5 Powder Diffractometer - Empyrean Panalytical

For the purpose of determining phase purity and initial structure refinement powder X-ray diffraction measurements were performed on ground polycrystalline samples mounted to a zero-background silicon sample holder using a Empyrean Panalytical with Cu $K_{\alpha 1}$ radiation. The Empyrean Panalytical diffractometer typically operates at 4.6 kW (40 kV and 40 mA) generating high resolution monochromatic incident X-rays from Cu X-ray tubes. The zero-background sample holder is secured to a reflection-transmission spinner, and variable angles measured with a θ-2θ goniometer, typically between 5-160 2θ in increments of 0.05° steps. Scattered X-rays are detected with an X'Celerator detector.

2.3.6 High Resolution Powder Diffractometer - BT1

The constant wavelength powder neutron diffraction measurements described in Chapter 3 were carried out using the BT1 diffractometer at the NIST Center for Neutron Research (NCNR) Gaithersburg, Maryland, USA. Neutrons are generated from a uranium fuel cell reactor at a flux of 4×10^4 neutrons/cm^{2}s. Scattered neutrons are detected using a set of 32 ^{3}He detectors placed at 5° intervals, detectors are

shifted such that a 2θ range of 0 to 165 degrees can be measured. Low angle detectors are partially masked to minimise Bragg peak shifting, broadening and asymmetry resulting from finite detector slits. Three different monochromators allowing for a choice of three incident neutron wavelengths Ge(311), Cu(311) and Ge(733) with respective take off angles of 75°, 90° and 120°, along with two different incident Soller collimators, the resulting flexibility allows for a range of experimental setups.

2.3.7 High Resolution Powder Diffractometer - POWGEN

The time-of-flight (TOF) neutron diffraction measurements described in Chapter 4 were collected using the powder diffractometer POWGEN located at the Spallation Neutron Soruce (SNS), Oak Ridge National Laboratory. POWGEN is unique as a TOF powder diffractometer, the 360° radial collimator design allows for all detected scattered neutrons to be focused to a single diffraction pattern allowing for a high count rate with varying resolution as a function of d-spacing. For this, a resolution of Δd/d of 0.0015 at a d-spacing of 1 Å. The instrument allows for a variety of incident wavelengths over a wide range through adjustment of bandwidth-limiting choppers and pulse repetition rates.

2.4 Maximum-Entropy Based Whole-Pattern Fitting

The maximum entropy method (MEM) is an iterative procedure that aims to estimate the average structure of a compound based on limited information. Here, information entropy is maximised under a number of constraints consistent with observed physical quantities. First described in 1990, Sakata *et al*. analysed X-ray powder diffraction data by converting measured diffraction intensities to electron scattering density maps for CeO_2 [95]. Sakata *et al*. later extended the technique (1993) for determining nuclear scattering densities based on neutron diffraction data. For this purpose, the negative scattering length of atoms such as Ti and H are treated separately from positive scattering atomic species [96].

Traditional analysis of diffraction data, particularly single crystal diffraction, involves repeatedly determining the difference between modelled and real structures. For this purpose calculation of Fourier difference maps based on the difference between the Fourier transform of observed and calculated structure factors ($F_o(h_k)$ and $F(h_k)$ respectively) is carried out. Although sufficient for most practical applications, it is often difficult to interpret any physical meaning from the resulting residual density with the appearance of a high significant to noise ratio. This is a result of the termination effect, where high-Q structure factors are not experimentally measured. As well as this, for powder diffraction data the collapse of 3D reciprocal space onto a single dimension means observed structure factors are difficult to observe accurately when reflections are heavily overlapped.

MEM analysis poses a solution to both of these problems. For Fourier synthesis observed structure factors are fit based upon a model function using Rietveld refinement. For MEM analysis, within the errors of observed diffraction data, a scattering density of a sample's unit cell is estimated that maximises the information entropy. The Fourier transform of which then provides a series of calculated structure factors (F_{MEM}) that a diffraction pattern can be fit against, in essence the reverse process of Fourier synthesis.

2.4.1 Maximum Entropy Method

In general, the principle of the maximum entropy method (MEM) is to maximise the information entropy (S) under a series of constraints through an iterative process. The first method for such a process was devised by Jaynes in 1957, where a method for describing a probability distribution from an incomplete set of discrete testable data was proposed. The theory is derived from Claude Shannon's description of

information entropy (S) as a measure of the uncertainty in a probability distribution [97, 98]:

$$S = -\sum_{i}^{N} \rho_i ln(\rho_i) \tag{2.54}$$

Here, ρ_i describes the probability of outcome i from a discrete number of possible outcomes N. Jaynes demonstrated that by maximising entropy, an equal distribution of probability is given to those outcomes we have no information about. Therefore, the probability distribution that maximises entropy (S) results in the least biased distribution. With respect to MEM analysis of diffraction data, the probability distributions are represented by scattering densities for a given unit cell are represented by a $N_a \times N_b \times N_c = N_{pix}$ grid of voxels. The information entropy of a scattering density grid is then described:

$$S = -\sum_{r}^{N_{pix}} p'(\mathbf{r}) ln\left(\frac{p'(\mathbf{r})}{\tau'(\mathbf{r})}\right) \tag{2.55}$$

Here, $p'(\mathbf{r})$ represents the normalised scattering density at each position $\mathbf{r}_k$ for a given scattering density grid. $\tau'(\mathbf{r})$ describes the normalised scattering density derived from prior information. MEM is an iterative process for determining a final solution for $p'(\mathbf{r})$, where the value for $\tau'(\mathbf{r})$ is initialised as a uniform distribution across the scattering grid cell. For subsequent iterations the value for $\tau'(\mathbf{r})$ is taken from the scattering density of the previous iteration. The prior probability ($\tau'(\mathbf{r})$) and probability ($p'(\mathbf{r})$) scattering densities are defined in terms of the scattering density distributions $\tau(\mathbf{r})$ and $\rho(\mathbf{r})$ respectively:

$$p'(\mathbf{r}) = \frac{\rho(\mathbf{r})}{\sum_{\mathbf{r}} \rho(\mathbf{r})} \tag{2.56}$$

$$\tau'(\mathbf{r}) = \frac{\tau(\mathbf{r})}{\sum_{\mathbf{r}} \tau(\mathbf{r})} \tag{2.57}$$

For the purposes of diffraction analysis, the value for S represents the uncertainty of a given scattering density. When S is maximised the subsequent scattering density is the most 'uncertain' distribution of scattering densities for all possible distributions given the information available. For the MEM process the value of S is maximised by a method of undetermined Lagrange multipliers under a number of constraints C.

The value M_F is the total number of reflections where the respective phases are known. For a given reflection, h_K, $F_c(h_k)$ is the calculated structure factor, $F_o(h_K)$ is the observed structure factor and $\sigma(|F_o(h_K)|)$ is the standard uncertainty of $|F_o(h_K)|$. As stated above, the density grid described by the grid $N_a \times N_b \times N_c = N_{pix}$ that maximises S is iteratively derived by the method of undetermined Lagrange multiplier by maximising Q with respect to p_K and two Lagrange multipliers λ and μ using the equation:

$$Q = S - \lambda C - \mu(\sum_{K=1}^{N} p_K - 1) \tag{2.58}$$

For neutron diffraction data, a modification to the above is required for MEM analysis when dealing with elements of negative coherent scattering length such as Ti and H. As there is often negligible overlap of nuclear densities an approximate value for the entropy S is described as the sum of positive (S_+) and negative (S_-) scattering densities:

$$S = S_+ + S_- \tag{2.59}$$

This is extended to the calculation of scattering factors ($F_c(h_k)$) from nuclear scattering density (p_j):

$$F_c(h_k) = \sum_{j=1}^{N_{pix}} (p_j^+ + p_j^i) e^{2\pi i h_k \dot{r}_j} \tag{2.60}$$

From the above the final MEM solution for neutron diffraction data is the given as the sum of positive and negative scattering densities.

2.4.2 MEM based Whole Pattern Fitting

The process of MEM based whole pattern fitting starts with a Rietveld refinement using an initial structural model, from which estimated structure factors (denoted $F_o(Rietveld)$) are calculated. Rietveld based structure factors are then used to estimate the observed integrated intensity ($I_o(Rietveld)$) based on the profile intensity of overlapping reflections determined during Rietveld Analysis. For powder diffraction the standard uncertainty of the observed structure factor $\sigma(|F_o(Rietveld)|)$ are then calculated from the equation:

$$\sigma(|F_o(Rietveld)|) = \frac{|F_o(Rietveld)|}{2}(\frac{1}{EI_o(Rietveld)} + (\frac{\sigma(s)}{s})^2)^{\frac{1}{2}} \tag{2.61}$$

Here, E is a factor to adjust $\sigma(|F_o(Rietveld)|)$. s is the scale factor for which $\sigma(s)$ is the standard uncertainty. Using the real and imaginary components of $F_o(Rietveld)$ (where X-ray dispersion contributions are subtracted) and the values for $F_o(Rietveld)$ and $\sigma(|F_o(Rietveld)|)$ the MEM process is carried out to generate a set of 3D scattering densities, $\rho(x,y,z)$. A set of MEM based structure factors are also calculated by the Fourier transform of $\rho(x,y,z)$ for a unit cell of a given volume V:

$$F_c(MEM) = V\int\int\int \rho(x,y,z)e^{2\pi i(hx+ky+lz)}\text{dxdydz} \tag{2.62}$$

In calculating values for $F_c(MEM)$, the bias towards any structural model is minimised. The scattering densities generated ($\rho(x,y,z)$) are then analysed visually and the structural model is modified accordingly, if necessary then the above steps are repeated.

The observed diffraction data is then fit using values for $F_c(MEM)$ obtained above. The structure factors fit during this refinement are fixed at $F_c(MEM)$ where only parameters not relevant to crystal structure are refined such as scale-factor, lattice parameters and background, in a process refereed to as whole pattern fitting (w.p.f.).

Values for integrated intensity are then calculated ($I_o(w.p.f.)$), from which $F_o(w.p.f.)$ is obtained resulting in a set of real and imaginary components for $F_o(w.p.f.)$ (where X-ray dispersion effects are again subtracted). The MEM process is then repeated using values for $\sigma(|F_o(w.p.f.)|)$ and $F_o(w.p.f.)$ for which a new set of scattering densities, $\rho(x,y,z)$, are generated. Subsequently values for $F_c(MEM)$ are generated using equation 2.62.

The process of calculating $F_c(MEM)$ from $\rho(x,y,z)$ as illustrated in Figure 2.9, calculating new values for $I_o(MEM)$ through the whole pattern fitting and then feeding $I_o(MEM)$ into the MEM process generating new values for $\rho(x,y,z)$ is repeated until convergence. These cycles are refereed to as Remedy cycles. As the MEM process is carried out, the derivation of additional structural information in the calculated scattering densities ($\rho(x,y,z)$) alters the contributions of individual scattering factors ($F(w.p.f.)$) to the integrated intensity ($I_o(w.p.f.)$) for heavily overlapping peaks. This serves to reduce the bias towards any structural model in the generated scattering densities following the initial Rietveld refinement.

Compared with Rietveld refinement, the reduced bias of MEM based whole pattern fitting and generation of scattering density maps allow for a better representation of chemical bonding, anharmonic thermal motion and static/dynamic disorder.

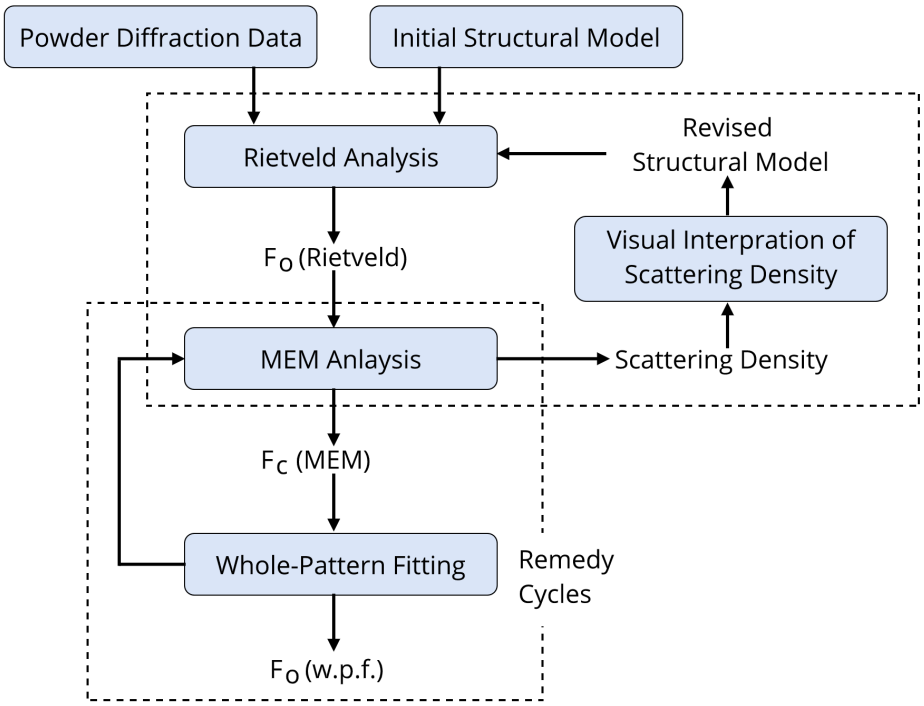

Fig. 2.9 The steps involved in MEM based whole pattern fitting.

2.5 Other Characterisation Techniques

2.5.1 SEM and EDX

Scanning electron microscopes (SEM) and Energy Dispersive X-ray spectroscopy (EDX) enable the elemental composition and surface topology of a sample to be determined. This is particularly useful for determining changes to the B-site and X-site composition of organic-inorganic hybrid perovskites due to the population of heavy atoms on these sites. All SEM and EDX measurements described in this work were performed at ambient temperature using a Hitachi S-3400N.

2.5.2 TGA and DSC

Thermogravimetric analysis (TGA) and Differential Scanning Calorimetry (DSC) allow the thermal stability of a compound to be determined by measuring the mass loss and heat absorption of a sample as a function of temperature.

The TGA and DSC measurements described in this work were conducted in air with samples placed in an aluminium crucible. Initial measurements were carried out using an empty crucible and then subtracted in order to isolate the sample contribution. A Netzsch STA 409 PC TGA-DSC was used for all measurements and conducted between 20 °C and 500 °C, with a heating rate of 10 °C/min. Data was analysed using Netzsch Proteus.

2.5.3 Raman Spectroscopy

Through measurement of the inelastic (Raman) scattering of monochromatic light by the polarisable electron density of a sample, Raman spectroscopy allows a materials vibrational modes to be probed from which bonding types can be identified. The Raman measurements reported in chapter 3 were carried out at the university of Kent, Canterbury. For the measurements reported a Horiba “LabRam HR” was used, this implements a 180° collection system. A range of four lasers are available at the University of Kent’s Raman system that allows for a choice of excitation wavelength that is best suited for the sample being measured and one that limits fluorescence. The range of lasers available are: a 472.98 nm blue laser (4.87 mW); a 532.00 nm green laser (6.29 mW); a 632.81 nm red laser (1.65 mW); and a 784.15 nm infrared laser (20.10 mW).

2.6 Materials Synthesis

The excitement surrounding hybrid perovskites and their applications in photovoltaics lies in the potential for manufacturing highly efficient, low cost and low temperature solution processed materials. For this purpose, perovskite layers are typically deposited through precursor chemistry using organic polar solvents such as dimethylformamide (DMF), dimethyl sulfoxide (DMSO) and γ-butyrolactone. The experimental techniques used in this work required both bulk powder and single crystal samples of $CH_3NH_3PbI_3$, for which several techniques have been used to successfully synthesis samples. A detailed outline of the two methods used here are given below along with the synthesis methods for precursor materials. Both methods involve decreasing the solubility of precursor solution to the point that it becomes saturated, upon which nucleation occurs and crystal growth follows. Primarily, the two methods differ in the length of time taken for crystal growth, the first uses slow evaporation of a solvent over a number of weeks to grow large single crystals. The second method produces a powder and small single crystals through fast precipitation from solution.

2.6.1 CH_3NH_3I Precursor Synthesis

The precursor material methylammonium iodide (CH_3NH_3I or MAI) was used in all sample preparation methods for the synthesis of $CH_3NH_3PbI_3$ and all its derivatives. To begin the synthesis of CH_3NH_3I, 30ml of hydroiodic acid (57 wt% in water, Sigma Aldrich) and 27.8 ml of methylamine (40% in methanol, Sigma Aldrich) were cooled to 0 °C in a water-ice bath. These were slowly mixed in a conical flask and stirred with a magnetic stirrer at 0 °C for 2 hours in the water-ice bath. The solvent is evaporated by placing the solution in a hot water bath at 80 °C over several days. The resulting precipitate is recovered and purified by washing in diethyl ether (anhydrous $\leq$ 99.0%, Sigma Aldrich) and filtered using a vacuum filtration system, the precipitate is then dried in a furnace overnight producing CH_3NH_3I in a white powdered form.

2.6.2 $MAPbI_3$ Slow Evaporation

In order to synthesis single crystals (<1 mm) of $CH_3NH_3PbI_3$ ($MAPbI_3$) the precursor CH_3NH_3I (1.9923 g) was mixed with PbI_2 (5.7776 g, 99%, Sigma Aldrich) at a 1:1 molar ration with the solvent γ-butyrolactone (15 ml to 20 ml). The γ-butyrolactone solution was contained within a conical flask and placed in a vacuum oven at 120 °C.

The solvent was slowly evaporated off over the course of a week, this allowed for crystallisation to occur producing single crystal samples of $CH_3NH_3PbI_3$.

2.6.3 $MAPbI_3$ Solution Synthesis

The rapid precipitation of $CH_3NH_3PbI_3$ ($MAPbI_3$) from solution starts with dissolving PbO powder (5 mmol) in a boiling solution of HI (38 mmol) and H_3PO_2 (7.75 mmol) while magnetic stirring for 5 minutes, the result is a bright yellow liquid. The precursor MAI (5 mmol) is then added to the solution, immediately precipitating a black powder that redissolved into a yellow solution with continued stirring. The stirring is then stopped and the solution is left to cool down to ambient temperature resulting in black crystals at the bottom of the solution as shown in Figure 2.10.

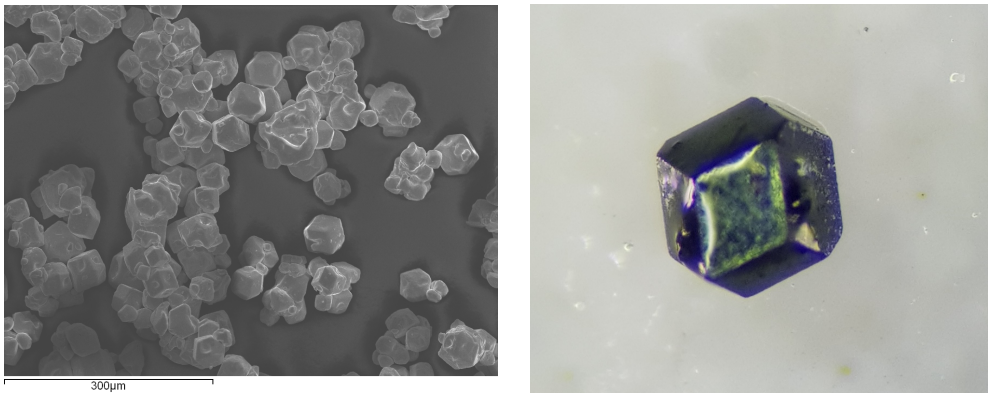

(a) (b)

Fig. 2.10 Scanning electron microscope (a) and optical microscope (b) images of $MAPbI_3$ crystals grown through solution synthesis outlined in section 2.6.3.

2.6.4 Sample IDs

This thesis describes the synthesis and characterisation of a number of $MAPbI_3$ samples synthesised under different conditions and subsequently treated differently post synthesis. For the purpose of clarity each sample has been given a unique ID that makes it distinguishable based on both the synthesis method and post processing routine followed. Table 2.1 provides a reference for each sample and the respective treatment. In addition to the denotations described in Table 2.1 this work also makes reference to "prototypical $MAPbI_3$", this refers to $MAPbI_3$, its properties and structure as typically reported in the literature, and outlined in section 1.3.2.

Sample ID	Description	Section
SE-$MAPbI_3$	Evaporated slowly from solution, no post processing.	2.6.2
SS-$MAPbI_3$	Solution processed, no post processing.	2.6.3
AA80-$MAPbI_3$	Solution processed, annealed in air at 80°C.	2.6.3
AV80-$MAPbI_3$	Solution processed, annealed under vacuum at 80°C.	2.6.3
AV200-$MAPbI_3$	Solution processed, annealed under vacuum at 200°C.	2.6.3
AV300-$MAPbI_3$	Solution processed, annealed under vacuum at 300°C.	2.6.3
AV280-$MAPbI_3$	Solution processed, annealed under vacuum at 280°C.	2.6.3
AV285-$MAPbI_3$	Solution processed, annealed under vacuum at 285°C.	2.6.3
AV290-$MAPbI_3$	Solution processed, annealed under vacuum at 290°C.	2.6.3
AV295-$MAPbI_3$	Solution processed, annealed under vacuum at 295°C.	2.6.3
AV300-$MAPbI_3$	Solution processed, annealed under vacuum at 300°C.	2.6.3
AV305-$MAPbI_3$	Solution processed, annealed under vacuum at 305°C.	2.6.3
AV310-$MAPbI_3$	Solution processed, annealed under vacuum at 310°C.	2.6.3
AV315-$MAPbI_3$	Solution processed, annealed under vacuum at 315°C.	2.6.3
AV320-$MAPbI_3$	Solution processed, annealed under vacuum at 320°C.	2.6.3
AI200-$MAPbI_3$	Solution processed, annealed in I2 a to 260°C.	2.6.3

Table 2.1 A description of each $MAPbI_3$ sample described in this thesis, the corresponding sample ID and the thesis section the synthesis method is described.

3

Structural Dynamics and Disorder of $MAPbI_3$

Hybrid perovskites have emerged as prominent candidates for the next generation of solar cell devices. However, the excellent optical and electronic properties these materials exhibit is undermined by a lack of understanding of the photovoltaic mechanism. This in part, stems from a lack of clarity on their structure and dynamics. In this chapter the application of maximum entropy method analysis on neutron powder and single crystal X-ray diffraction measurements in conjunction with Rietveld refinement of variable temperature synchrotron X-ray diffraction measurements are reported for $MAPbI_3$. Following this, characterisation of the ambient temperature tetragonal phase was carried out, for which considerable structural disorder has been observed including the presence of interstitial iodide sites above 280 K. This allowed for a mechanism for ambient temperature iodine migration to be proposed that is facilitated through the collective motion of MA^+ cations.

3.1 Introduction

3.1.1 Ambient temperature Average Structure Studies

Observation of low exciton binding energy and strong light absorption [99–101], coupled with a low recombination rate of photogenerated charge carriers [102], makes hybrid perovskites a promising candidate for the photoactive layer in the next generation of solar cells. For this purpose, understanding their photovoltaic mechanism is essential, which in part relies on a complete understanding of their crystal structure. Although it was only in 2009 that hybrid perovskites was first used for photovoltaic applications, studies on organic-inorganic post transition metal halide based perovskites dates back to the 1980's. The first detailed study on the characterisation of hybrid perovskites were on methylammonium lead iodide ($CH_3NH_3PbI_3$ or $MAPbI_3$), and was conducted by D. Weber and A. Poglistich [46] in 1987. In this work the ambient temperature structure, most relevant for photovoltaic applications, was determined through single crystal X-ray diffraction where the compound was ascribed the tetragonal crystal system with space groups *I4/m* or *I4/mcm*. The perovskite framework of PbI_6 octahedral was found to tilt along the crystallographic c-axis (Glazer notation $a^-a^-c^+$) to form a cuboctahedral, the interstices of which are populated by methylammonium (MA^+) cations. Hydrogen bonding was shown to play an important role, weak N-H$\cdots$I bonds and a coordination of 12 iodide atoms restricts the rotational dynamics of the linear cation, and therefore significant cation disorder is expected over a number of orientations.

Compared with traditional semiconductors, that are typically described by a rigid crystal structure with a highly periodic array of atoms, hybrid perovskites exhibit a flexible crystal structure, significant rotational and positional freedom of the organic cation [49]. The breaking of average long-range order makes determining a reliable average crystal structure challenging. For this purpose a number of structural studies have been conducted, that report a number of alternative space groups for the ambient temperature phase of $MAPbI_3$. These include *I4/mcm* [103, 104, 47], I4cm [105, 106], *I422* [107], *I4/m* [108] and *Fmmm* [109]. Correct space group assignment, especially the choice of a centrosymmetric or non-centrosymmetric space group for example, has important implications for the predicted properties of the material. The ferroelectric nature of $MAPbI_3$ being a primary example for which the generally accepted centrosymmetric space group *I4/mcm* would not allow. This is despite experimental reports of such behaviour [110]. Ferroelectric properties have been suggested as a reason for the exceptional power conversion efficiency of hybrid perovskite solar cell devices, these properties cannot be inferred from the

polar nature of the $CH_3NH_3^+$ cation alone due to the significant dynamic disorder exhibited at ambient temperature, evidenced by quasielastic neutron diffraction studies [111, 112]. The dynamic disorder of the MA^+ complicates refinement of the tetragonal phase II, where a four-fold model of the MA^+ has typically been used for structural refinements [47, 113]. However, at temperatures closer to the orthorhombic-tetragonal structural phase transitions NMR [114, 115] and heat capacity [116] measurements suggest the MA^+ has 8-fold symmetry. Average structure modelling of the MA^+, including the assignment of hydrogen positions has been studied through a number of powder neutron diffraction measurements [47, 48].

3.1.2 Ion Migration

High ionic conductivity of hybrid perovskite compounds is not a recent observation. Before their excellent light harvesting and charge carrier collection properties were reported, halide conductivity was observed by Yamada *et al*. in Ge-based perovskite compounds such as $MAGeCl_3$ [117]. However, it is only recently that the migration of charged species has been observed for $MAPbI_3$ [73, 118]. Hybrid perovskites such as $MAPbI_3$ are now considered mixed conductors [119], and therefore consideration of their ionic conduction is important. Especially as ion migration has important implications for both the operating performance and stability of hybrid perovskite solar cell devices. Materials that exhibit both electronic and ionic conductivity will form stoichiometric gradients across the material when placed between ion-blocking materials [120]. This type of architecture is typical for perovskite based solar cell devices and therefore an inherent source of instability. There are also reports that ion migration near device interfaces contributes to anomalous observations of I-V hysteresis [121, 122]. Practical uses for ion migration have been found, with interesting applications in perovskite resistance-switching memory devices [123, 124] and through manipulation under an electric field, fast response photodetectors can be produced [125, 126]. Therefore highlighting the benefit of better understanding the ion migration process for developing new hybrid perovskite based devices.

For typical semiconductors, an abundance of defects is associated with shorter charge carrier diffusion lengths and faster charge carrier recombination, therefore lessening photovoltaic performance. However, for hybrid perovskites, despite significantly higher defect densities in polycrystalline hybrid perovskite thin films (10^{16} cm^{-3} [127]) compared with inorganic semiconductors such as Si (10^{13} - 10^{14} cm^{-3} [128]) and CdTe/Cds (10^{11} - 10^{13} cm^{-3} [129]), a high defect density is found to have little effect on charge carrier transport properties [82, 55]. This has made determining the origin and nature of ion migration in hybrid perovskites such as $MAPbI_3$ the subject

of conflicting reports. With respect to $MAPbI_3$, extensive studies having been carried out on all possible migrating candidates MA^+, Pb^{2+} and I^-.

There have been a number of theoretical studies that aimed to determine the most likely mobile ion within $MAPbI_3$ from first principle calculations. Here, the activation energy for all possible mobile ions is calculated. Eames *et al*. calculated the lowest activation energy to be associated with I^- ions (0.58 eV) that migrate along a curved edge across the I–I edge of the PbI_6 octahedron [130]. This is compared to Pb^{2+} and MA^+ with activation energies of 2.31 eV and 0.84 eV respectively. Further calculations carried out by Azpiroz *et al*. calculated the activation energy of MA^+, Pb^{2+} and Pb^{2+} to be 0.46 eV, 0.80 eV and 0.08 eV respectively [131]. The calculated value for I^- is significantly lower than those calculated by Eames *et al*., however both studies do agree that I^- are the most likely mobile ions, although only Schottky defects were considered in this report. For Frenkel defects, Wan-Jian *et al*. have calculated the interstitial formation energies of I^- and MA^+ to be between 0.23–0.83 eV and 0.20–0.93 eV respectively, and therefore comparable to the activation energies of vacancy defects [132].

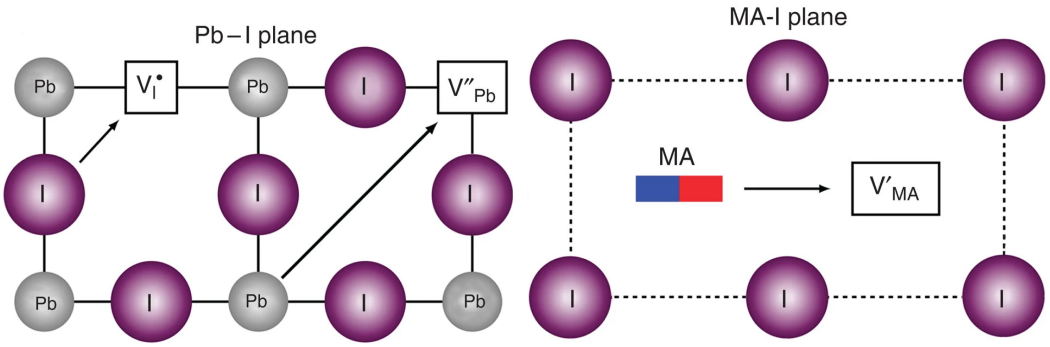

Fig. 3.1 Illustration published by Eames *et al*. describing the ionic transport mechanism involving conventional vacancy hoping for (a) I^- migration along an octahedron edge and Pb^{2+} migration along the diagonal direction <110> [130]. (b) $CH_3NH_3^+$ migration between neighbouring vacant A-site perovskite cavity.

Based on theoretical calculations, there is a consensus for I^- ions as the candidate for ion conductivity in $MAPbI_3$, experimental evidence has been far less consistent. The first direct experimental evidence for mobile ions within $MAPbI_3$ was provided by Yuan *et al*., where the migration of MA^+ ions was reported [133]. This study used photothermal induced resonance (PTIR) microscopy to measure the depletion of MA^+ ions from the anode side of a $MAPbI_3$ based solar cell device, with an access of MA^+ ions measured at the cathode end following the application of an

electric field. Further experiments carried out by Leijtens *et al*. aimed to measure ion migration under ambient conditions for thin films of $MAPbI_3$. For this purpose, Auger electron spectroscopy mapping was able to observe significantly more MA^+ migration compared to I^- when in the presence of moisture. Following this, at the point where degradation was apparent Pb^{2+} migration was also observed around the cathode. Importantly, these experiments do not exclude I^- migration.

At the time the work described in this chapter was carried out, experimental observations of MA^+ migration were clear, less so was experimental observations of mobile I^-. At least at ambient temperature, work carried out by Yang et a. reported the observation of possible I^- migration at elevated temperatures [119]. Through the construction of an electrochemical cell consisting of Pb | $MAPbI_3$ | AgI | Ag layers, it was reported that upon long term current flow a PbI_2 phase forms at the Pb | $MAPbI_3$ interface. It was suggested that I^- migration could be responsible. Further evidence of I^- has been reported by Bastiani *et al*., where a $MAPbI_3$ solar cell device was constructed with Ag electrodes. After continued biasing the anodes were found to be damaged, following a reaction with I^- [134]. For the purpose of ion migration within hybrid perovskite thin films, theoretical work has focused on the ion migration within the bulk, whilst experimental observations primarily probe ion migration at the grain boundary of the polycrystalline films. These results indicate that under normal operating conditions Pb^{2+} migration is unlikely with both MA^+ and I^- preferred as the dominate contributors to ion conductivity in $MAPbI_3$. What was apparent though, was the need for experimental clarification on the topic.

3.1.3 Purpose of Present Study

Hybrid perovskites, composed of an organic cation, inside a post transition metal halide framework, have emerged since 2009 as simple, low cost solar cell materials, with power conversion efficiencies that are competitive with silicon. Advances in cell efficiency have been made despite an incomplete understanding of the materials photovoltaic mechanism and poor long term thermal stability, which is in part, due to a lack of clarity on there structure. Observations of significant ion mobility complicates the structural dynamics of hybrid perovskites such as $MAPbI_3$. The purpose of this study is to characterise the average structure and structural dynamics of $MAPbI_3$ through the application of complementary powder neutron diffraction, single crystal X-ray diffraction and powder synchrotron X-ray diffraction measurements on bulk samples of $MAPbI_3$. For this purpose traditional structure determination techniques such as Rietveld refinement, were combined with the maximum entropy method (MEM) analysis.

3.2 Synthesis

For the purposes of manufacturing perovskite solar cell devices, hybrid perovskites are often synthesised through low temperature solution based methods, where the sample is rapidly precipitated from a solution. This is often proposed as a benefit for these materials as it means low cost and efficient fabrication methods. It does however result in a relatively high defect concentration, a high defect concentration has been shown to have little effect on the optoelectronic properties of the materials [135]. For the purpose of this study a slow crystal growth synthesis method was chosen in order to limit the defect concentration in bulk samples of $MAPbI_3$ for the detailed structural analysis intended for this study. The synthesis method for this sample is detailed in section 2.6.2 and has been given the denotation SE-$MAPbI_3$. The sample discussed in this chapter was synthesised by Professor Mark A Green, University of Kent.

3.3 Ambient Temperature Characterisation

3.3.1 Neutron Powder Diffraction

Crystals of the sample SE-$MAPbI_3$ grown via the methods described in section 3.2 were ground to a powder and measured on the BT1 diffractometer at NCNR at the National Institute of Standards and Technology, Gaithersburg, MD. Powder neutron diffraction data were collected using a Cu(311) monochromator ($\lambda = 1.5401(1)$ Å). The extensive incoherent scattering contribution resulting from the presence of hydrogen (here non-deuterated samples were measured) meant that data were collected over a 3-day period to ensure sufficient data quality.

The initial aim of this measurement was to determine a structural model for the MA^+ cation at room temperature. For this purpose, Maximum Entropy Analysis (MEM) was used to generate nuclear scattering density maps of the samples unit cell that was not biased towards a structural model. This analysis was carried out in collaboration with Dr Pawel Zajdel, University of Silesia. Initial analysis of the data described in the current section 3.3.1 including, modelling of the MA^+ cation and identification of the interstitial iodide site I2A based on maximum entropy analysis was presented and accepted for the award of a Master of Physics honours (MPhys (Hons)) degree at the University of Kent.

To begin, an initial Rietveld refinement was carried out using the software package RIETAN, from which a set of initial calculated structure factors and the respective

phases were generated. A structural model described by the space group *I4/mcm* was input into the refinement. Only atomic coordinates of the PbI_6 framework were included in the structure model, this was adapted from structure characterisation work carried out by Weller *et al*. [47]. The generated nuclear scattering density map that results from the MEM analysis using the software packages RIETAN and PRIMA was therefore unbiased towards an initial structural model for the MA^+ cation and the symmetry of the space group.

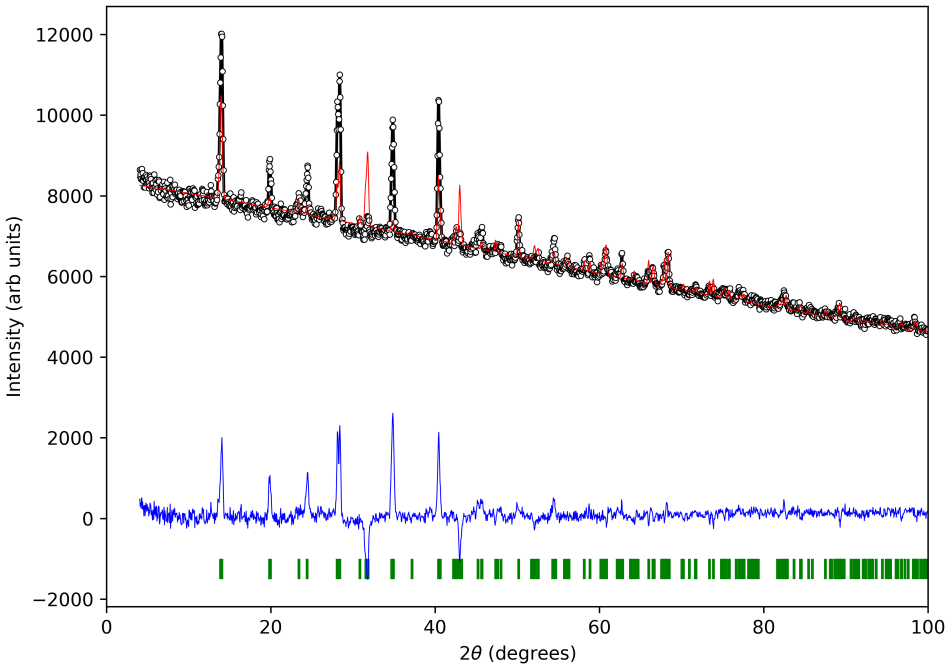

Fig. 3.2 Preliminary Rietveld refinement of powder neutron diffraction data based on a structural model that only describes the PbI_6 framework of SE-$MAPbI_3$ at 300 K. The observed (black), calculated (red) and difference (blue) intensities are shown as a function of two-theta. Fit factors for this refinement are R_{wp} = 2.899 %, R_p = 1.884 % and S = 2.0921.

Figure 3.2 shows a Rietveld refinement fit based on the simplified structural model described above, the resulting fit is poor, a result of not modelling the MA^+. MEM analysis was then carried out based on the structure factors obtained from the initial Rietveld refinement.

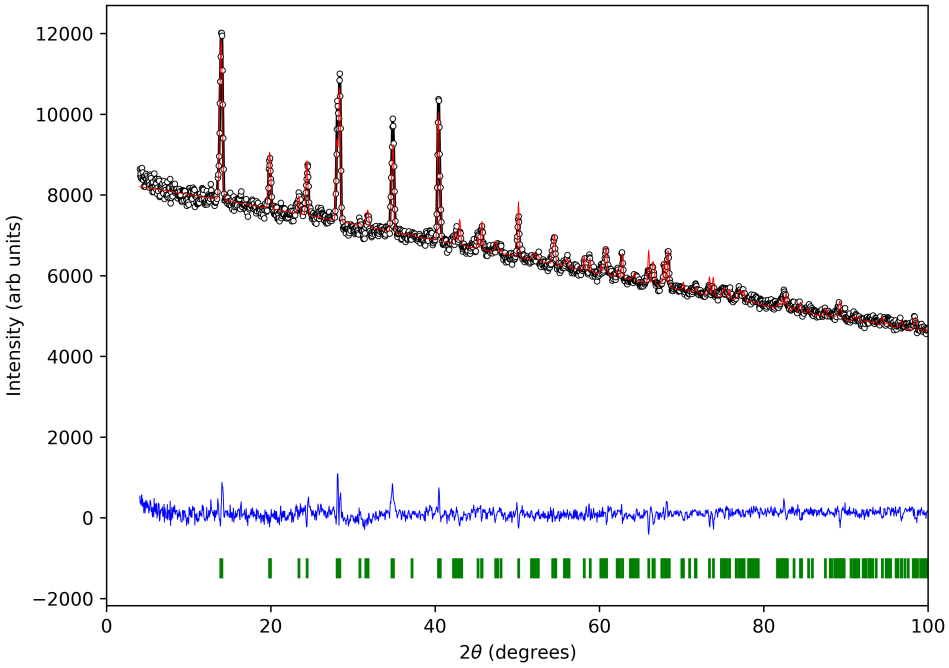

Fig. 3.3 Powder diffraction pattern and fit generated from structure factors obtained from MEM analysis based on a simplified structural model (the Rietveld refinement for which is shown in Figure 3.2). The observed (black), calculated (red) and difference (blue) intensities are shown as a function of two-theta. Fit factors for this refinement are R_{wp} = 1.741 %, R_p = 1.386 % and S = 1.2565.

From the nuclear scattering density map generated through MEM analysis a set of structure factors are obtained and fit to the observed data for comparison against the initial simplified Rietveld refinement fit (Figure 3.2). The resulting fit displayed in Figure 3.3 shows an improved fit of the observed data compared with Figure 3.2 with reduction in the fit factor Rwp from 2.899 % to 1.740 %.

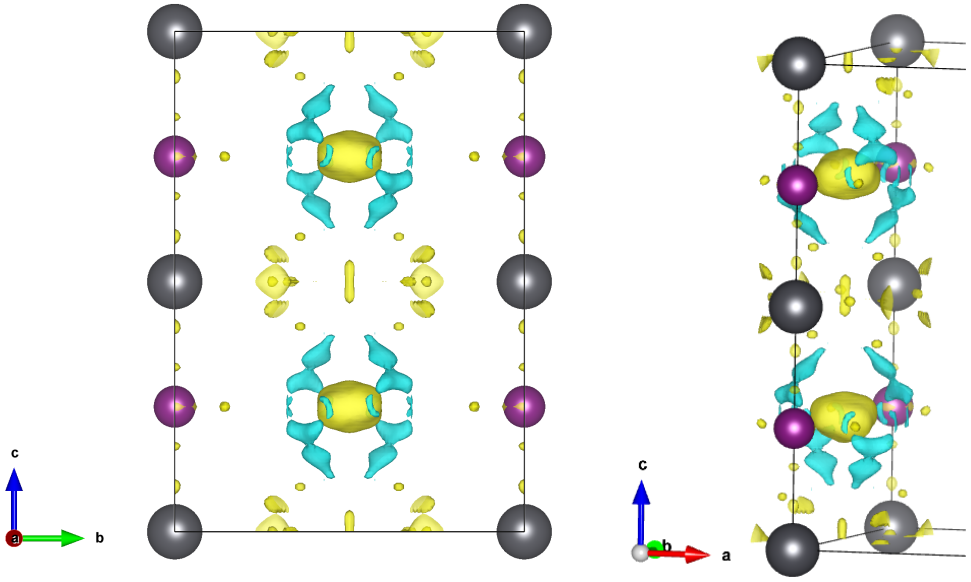

(a) (b)

Fig. 3.4 (a) and (b) lead (grey spheres) and iodide positions (purple spheres) derived from initial structure determination for the *I4/mcm* space group. For both (a) and (b) the nuclear scattering density maps are overlaid onto the structural model with both positive (yellow) and negative (blue) nuclear density shown (isosurface 1.5 fmÅ^{-3}).

As shown on Figure 3.5, the nuclear scattering density maps showed distinctive areas of positive localised scattering at the centre of the perovskite void, consistent with the expected location of the MA^+ cation derived from previous structure determination carried out in section 3.3.2. The shape of the positive density is best described by a tetrahedron unit. The centre of mass of the tetrahedron unit sits at the the centre of the A-site perovskite void. Areas of significant negative scattering were found to be located at the ends of the tetrahedron unit associated with hydrogen scattering of the MA^+ cation. This density was significantly disordered and attributed to the hydrogen scattering associated with the MA^+ cation.

From the positions of maxima located in the nuclear scattering density maps a crystallographic structural model for the A site MA^+ cation was derived, including positions for carbon, nitrogen and hydrogen atomic sites (referred to as C1, N1, H1, H2 and H3 in the structural model respectively) for the space group *I4/m*. The resulting location of the carbon and nitrogen atoms gave bond distances of 1.25 Å and C–H and N–H bond distances of 1.24 Å and 1.36 Å. The MA^+ cation can adopt two orientations, one along the (220) plane and the other orientated along the $(2\bar{2}0)$ plane. These orientations are such that the NH_3 and CH_3 ends point exactly towards the distorted I2 site.

The MEM analysis allows for the separation of positive and negative scattering of the hydrogen from the other compositional elements for SE-$MAPbI_3$ allowing for distinct hydrogen sites to be identified. Typically samples that contain hydrogen would be deuterated. However for the measurements described here, considerable coherent hydrogen scattering allowed for the refinement of hydrogen positions despite a considerable background and signal to noise ratio resulting from significant incoherent scattering of hydrogen. In the reconstructions, six areas of localised negative scattering were identified and assigned as distinct hydrogen sites located approximately 1 Å from the carbon and nitrogen positions of the methylammonium cation. It should be noted the negative scattering density distribution was not as distinctly localised as other sites, this is associated with both liberation and rotational disorder consistent with the disorder determined by inelastic neutron scattering.

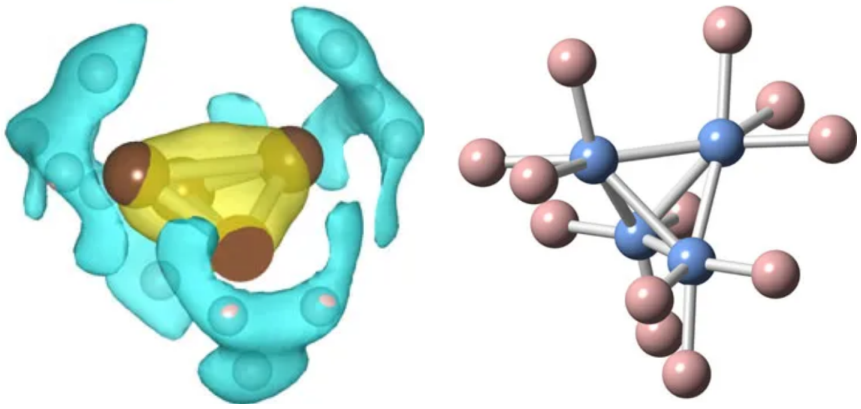

(a) (b)

Fig. 3.5 (a) Nuclear scattering density map of the methylammonium cation (isosurface level of 1.0 fmÅ^{-3}), showing carbon, nitrogen (brown and blue) and hydrogen scattering (pink). With positive (yellow) and negative (blue) scattering density. (b) Crystallographic structure extracted from the maxima in the scattering density maps of the methylammonium cation.

Following the success of the MEM analysis in identifying accurate positions for the atomic sites associated with the MA^+ cation as shown in Figure 3.5, further MEM analysis was carried out with a more detailed initial structural model. Here, a simplified representation of the MA^+ cation was added to the structure used for the previous MEM analysis and a Rietveld refinement was carried out as shown in Figure 3.6.

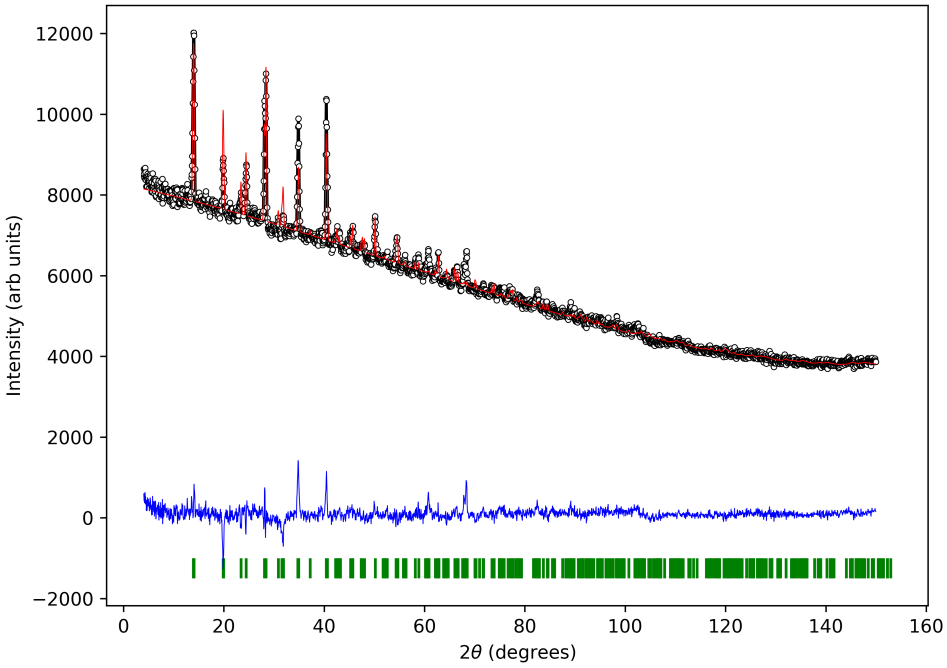

Fig. 3.6 Rietveld refinement of powder neutron diffraction data based on a structural model that describes the PbI_6 framework of SE-$MAPbI_3$ and a simplified model of the MA^+ cation at 300 K. The observed (black), calculated (red) and difference (blue) intensities are shown as a function of two-theta. Fit factors for this refinement are R_{wp} = 2.089 %, R_p = 1.567 % and S = 1.5075.

MEM analysis and corresponding remedy cycles were carried out based upon initial structure factors and phases obtained from the Rietveld refinement shown in Figure 3.6. Following the MEM analysis, structure factors were obtained from the resulting nuclear scattering density map. This was then fit against the observed data (Figure 3.7) for which a better fit of the observed data was obtained.

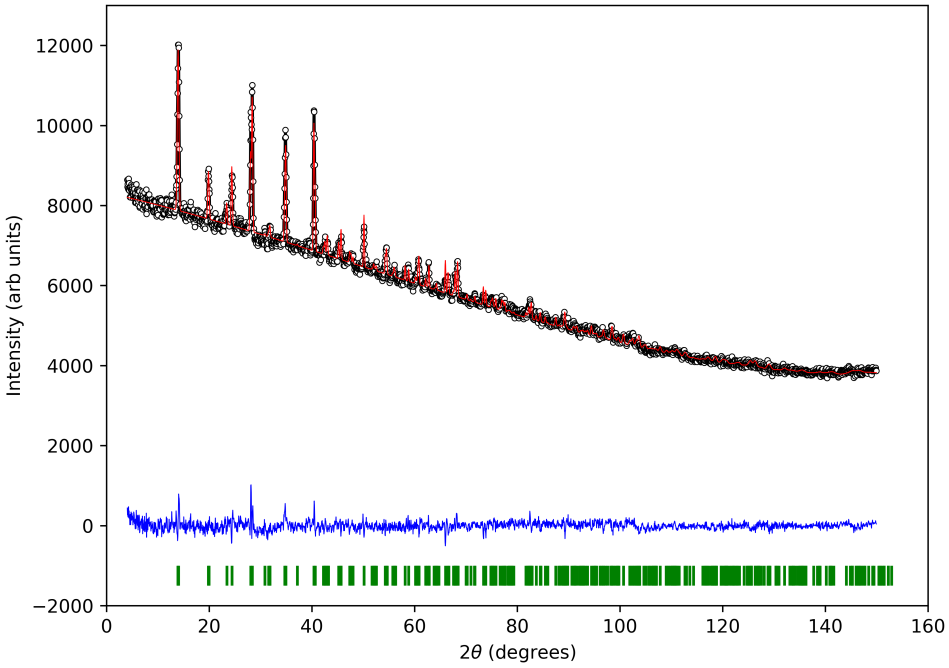

Fig. 3.7 Powder diffraction pattern and fit generated from structure factors obtained from MEM analysis based on a simple structural model for SE-$MAPbI_3$, the Rietveld refinement for which is shown in Figure 3.6). The observed (black), calculated (red) and difference (blue) intensities are shown as a function of two-theta. Fit factors for this refinement are R_{wp} = 1.694 %, R_p = 1.357 % and S = 1.2220.

The nuclear scattering density maps generated through the MEM analysis (corresponding to Figure 3.7) revealed a significantly more disordered structure than the simple perovskite structure described above. Areas of nuclear scattering associated with the iodide site that describes the tilting of the perovskite framework (I2) were found to be localised within levels typical for the thermal distributions expected at room temperature. However, two areas of localised scattering were identified close to the I2 site ($\approx$ 0.8 Å) and assigned as interstitial iodide positions in the structural model (I2A) as shown in Figure 3.8, representing a static disorder of the I2 site.

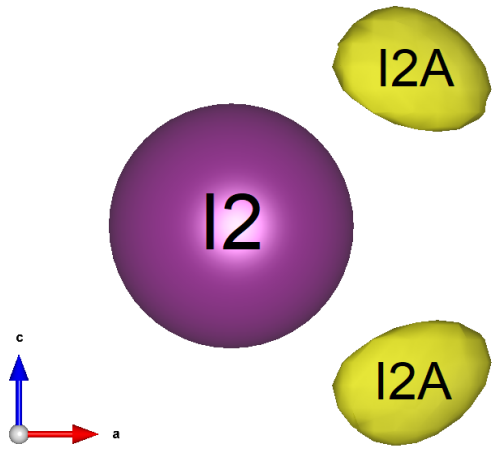

Fig. 3.8 A section of the (100) projection of the nuclear scattering density (yellow) at room temperature (isosurface level of 1.2 fmÅ^3) showing the main iodide position (assigned the label I2 in the structural model, purple sphere) is accompanied by two additional scattering densities (labelled I2A in the subsequent structural model).

The atomic positions of the atoms associated with the MA^+ cation (including carbon, nitrogen and hydrogen) that were extracted from maxima in the nuclear density maps were added to the structural model used in the initial PbI_6 structural model. The interstitial iodide site I2A and an additional interstitial site, denoted I3, derived from the single crystal experiment described below in section 3.3.2, were later added to the final structural model. A Rietveld refinement was then carried out using the software package FullProf. The resulting atomic coordinates of the structural model are described in Table 3.1. The tilting of the PbI_6 framework were found to be consistent with previous studies reported in the literature, with out of phase tilting along a single crystallographic axis and described by the Glazer notation $a^0a^0c^-$.

Neutron Powder Diffraction Refined Atomic Coordinates - 300 K					
Atom	x	y	z	U_{iso} (^{3})	Occupancy
Pb1	0.5	0.5	0.5	0.036(2)	1.0
Pb2	0.5	0.5	0.0	0.036(2)	1.0
I1	0.5	0.5	0.75(3)	0.092(6)	0.92(3)
I2	0.21(4)	0.29(4)	0.5	0.092(6)	0.90(4)
I2A	0.27(7)	0.24(7)	0.449(3)	0.092(6)	0.06(2)
I3	-0.21(4)	-0.31(4)	0.25(4)	0.092(6)	0.004(3)
C1/N1	0.55(1)	-0.04(1)	0.278(6)	0.25(4)	1.0
H1	0.15(2)	0.55(2)	0.70(1)	0.089(7)	1.0
H2	-0.03(2)	0.35(2)	0.29(1)	0.089(7)	1.0
H3	0.44(3)	-0.05(3)	0.851(3)	0.089(7)	1.0

Table 3.1 Atomic coordinates of SE-$MAPbI_3$ obtained from Rietveld refinement of powder neutron diffraction data using the space group *I4/m* shown in Figure 3.9. Cell parameters were refined to be $a = b = 8.8618(4)$ Å and $c = 12.6588(8)$ Å with a volume of 994.11(9) Å^3

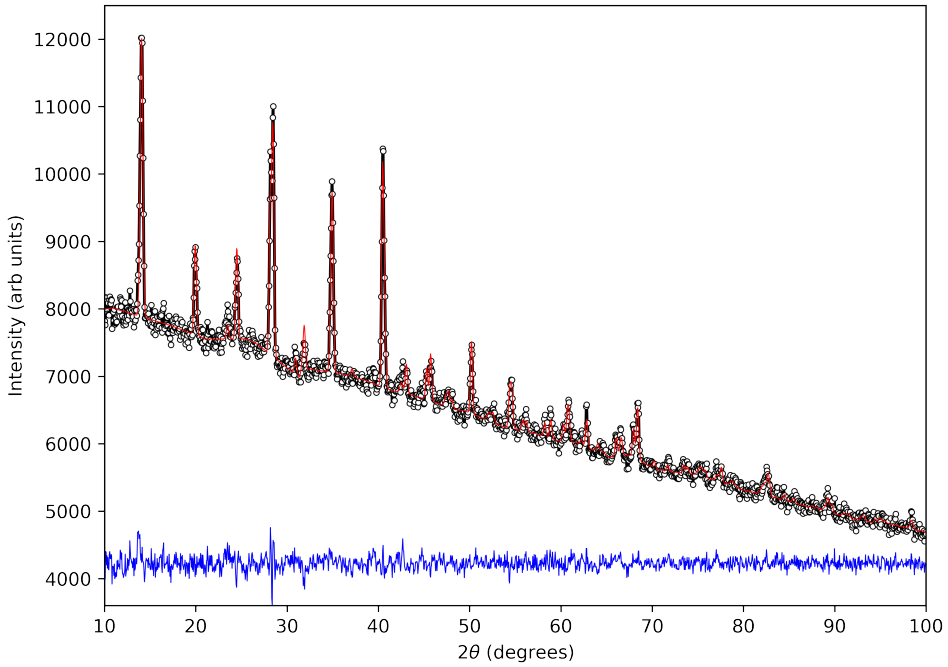

Fig. 3.9 Rietveld refinement of powder neutron diffraction data based on a structural model described in Table 3.1 for the sample SE-$MAPbI_3$ at 300 K. The observed (black), calculated (red) and difference (blue) intensities are shown as a function of two-theta.

3.3.2 X-ray Single Crystal Diffraction

A single crystal was selected from the sample SE-$MAPbI_3$, synthesised via the method described in section 3.2. Two single crystal X-ray diffraction measurements were then performed using Mo-K_α radiation on an in-house dual-source Rigaku Oxford Diffraction Supernova diffractometer located at the University of Kent. Both measurements were collected at 300 K, the first measurement upon cooling the sample from 350 K and the second upon heating from 250 K. The data was then analysed using SHELXL software in collaboration with Dr Pawel Zajdel, University of Silesia.

The data reduction process was carried out with two absorption correction types:

1. Standard empirical spherical harmonics (SADABS), 4/m Laue class and Friedel mates were treated as equivalent.
2. Multifaced crystal with Gaussian integration + SADABS, P-1 Laue class and Friedel mates were treated as in equivalent.

The merging of Friedel mates and the choice of $4/m$ Laue class filter for the first absorption correction type means the resulting solution is biased towards a centrosymmetric space group choice and tetragonal crystal system type. Following automatic space group assignment using the software routine GRAL, *I4/mmm* and *I4/m* were given as possible space group choices. There has been considerable debate in the literature over the proper space group assignment for the ambient temperature phase for $MAPbI_3$, with reports of both centrosymmetric and non-centrosymmetric options *I4/mcm* [113] and *I4cm* [136, 48] respectively. Neither of which have been determined as possible options with multiple violations of the -c- extinction conditions observed. Despite the observation of -c- extinctions, structure determination was carried out with *I4/mcm* for comparison against *I4/m* due to the frequency at which it is assigned in the literature. *I4/mmm* was eliminated due to the generation of high R factors (>20%) at the beginning of the structure determination process.

	Warming		Cooling					
Abs. Corr.	Shape, P-1, No Friedel		Shape, P-1, No Friedel				Empi. 4/m, Friedel	
a, c (Å)	8.8756(1), 12.6517(3)		8.8801(1), 12.56575(5)					
Reflections	21947		10648				10649	
I>3σ	7874		7636				7560	
<I>	11.5		23.7				24.4	
<I/σ>	6.4		11.5				11.2	
-c- violations	704		690				688	
-c- viol.I>3σ	233		227				229	
-c- <I>	1.1		1.4				1.4	
-c- <I/σ>	3.4		3.8				3.6	
Space Group	*I4/m*	*I4/mcm*	*I4/m*	*I4/mcm*	*I4/m*	*I4/mcm*	*I4/m*	*I4/mcm*
Extra Sites	2 (I2A, I3)		2 (I2A, I3)		Multiple		2 (I2A, I3)	
R1 (%)	3.92	2.96	4.41	3.30	4.35	3.02	4.52	3.38
R1all (%)	4.62	3.35	4.96	3.55	4.88	3.26	5.1	3.64
wR2(%)	9.93	6.74	11.16	7.42	11.76	6.86	11.51	7.87
S	1.400	1.218	1.437	1.210	1.284	1.210	1.428	1.189
N unique	947	521	943	521	943	521	943	521
N I>4σ	801	472	809	476	809	476	800	473

Table 3.2 Reflection statistics derived from a data reduction process carried out using the CrysAlisPro program based on single crystal X-ray diffraction measurements performed at 300 K upon cooling and heating SE-MAPbI$_3$. The structure refinement fit parameters are given for a number of structure refinements.

For both space groups the structure determination was carried out with the software package SHELXS. This process generated initial atomic positions for the PbI_6 framework. Two distinct iodide sites (labelled I1 and I2) are assigned for both space groups and a single lead site (Pb1) for *I4/mcm* and two lead sites (Pb1 and Pb2) for *I4/m* as shown in Figure 3.10. Further structure refinement was carried out with the software package SHELXL, through electron peaks identified in the difference Fourier maps generated by SHELXL. Atomic coordinates for both carbon and nitrogen atoms that constitute the centre A-site perovskite cation, MA^+, were located. The positions of both carbon and nitrogen atoms were restricted to the same crystallographic site in the structure model (referred to as C1 and N1) as the respective X-ray scattering form factors do not allow separate sites to be distinguished.

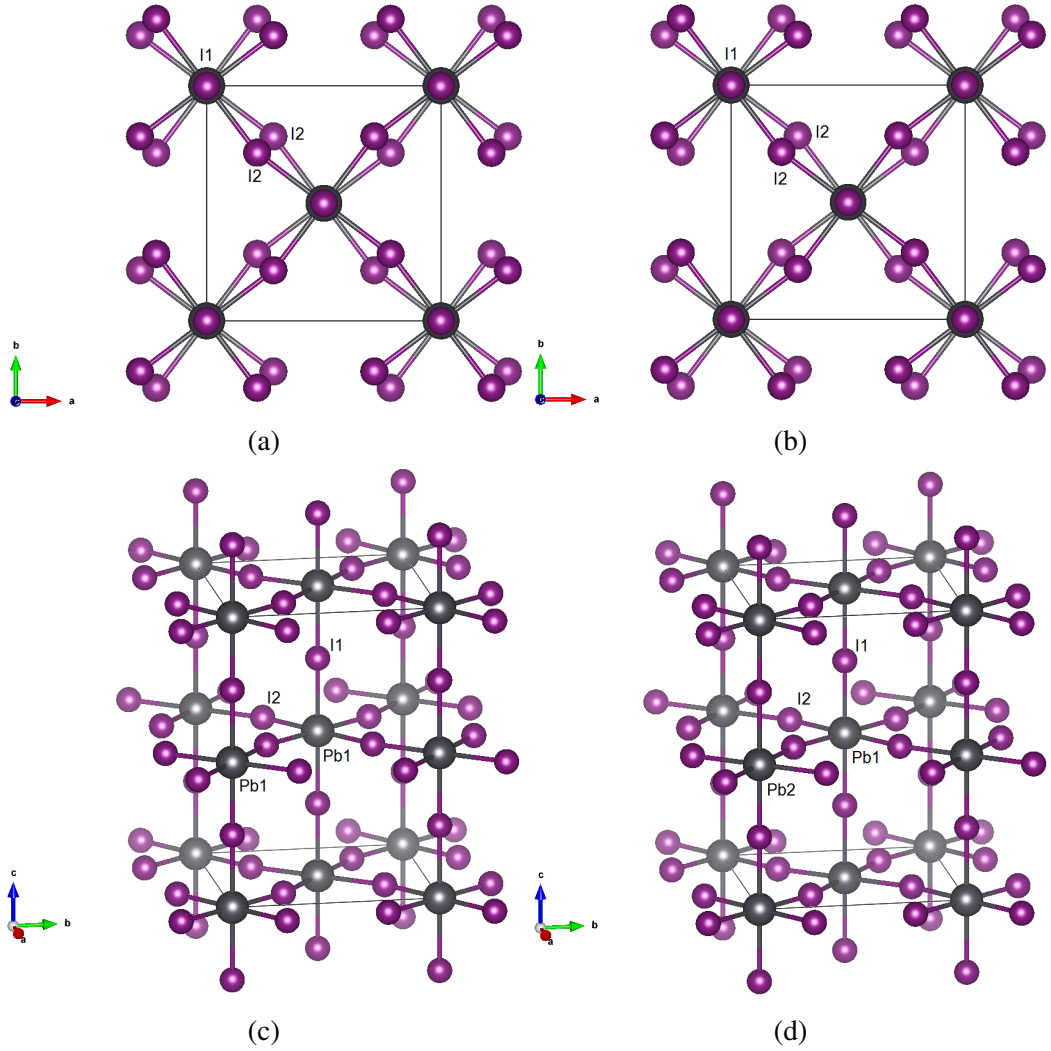

Fig. 3.10 Lead (grey spheres) and iodide positions (purple spheres) derived from initial structure determination (a) and (c) for the *I4/mcm* and (b) and (d) *I4/m* space groups.

Following the structure refinement process the multifaceted crystal with Gaussian integration absorption correction (Option 2) gave the best refinements for both space groups tested as outlined in Table 3.2. Based on initial structure factors and phases generated from the structure refinements outlined in Table 3.2, electron scattering density maps of the samples unit cell were generated through the application of the maximum entropy method (MEM).

Through examination of the Fourier difference residuals and electron scattering density maps generated through MEM analysis a number of interstitial iodide sites were identified for both *I4/m* and *I4/mcm* space groups that when included in the structural model improved the overall structural refinement (referred to under column heading "2 (I2A,I3)" in Table 3.2). The first additional site was found close to the I2 iodide site associated with a tilting of the PbI_6 framework as illustrated on Figure 3.11 and Figure 3.12. This localised scattering was identified approximately ~ 0.8 Å from the I2 site. This was assigned as an interstitial iodide site and is referred to as I2A in the crystallographic model.

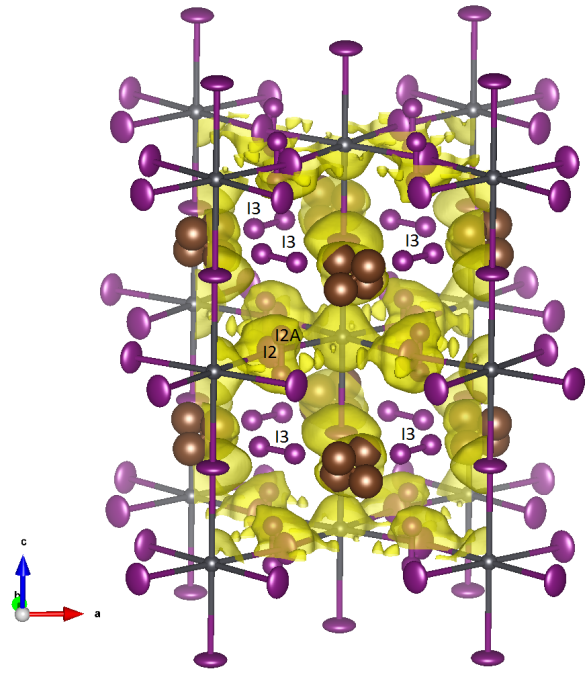

(a)

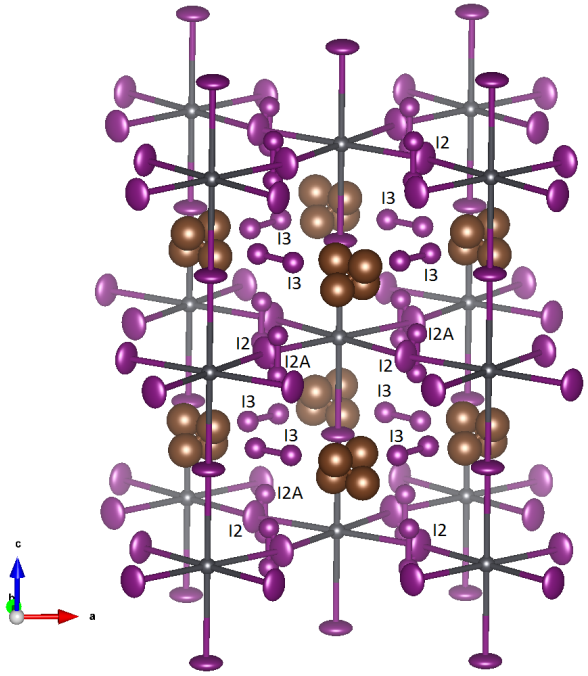

(b)

Fig. 3.11 Refined structural model (lead in grey, iodine in purple and carbon/nitrogen in brown) with interstitial iodide sites included, the electron scattering density map derived (isosurface level of 1.0 fmÅ^{-3}) from MEM analysis is shown (a) overlaid onto the structural model and (b) without the electron density map.

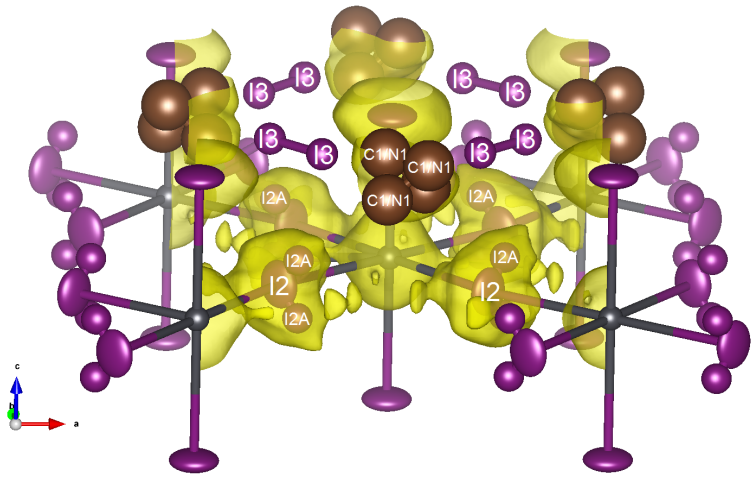

(a)

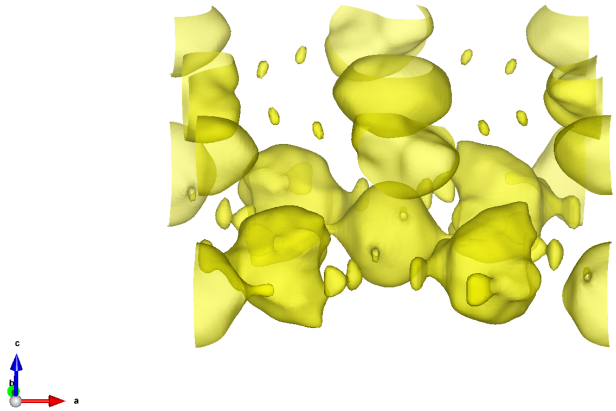

(b)

Fig. 3.12 A cross section of the refined structural model (lead in grey, iodine in purple and carbon/nitrogen in brown) with interstitial iodide sites (a) overlaid onto the electron scattering density map (isosurface level of 1.0 fmÅ^{-3}) derived from MEM analysis and (b) without electron density map.

An additional interstitial iodide site was located along the z ~ 0.25 plane and positioned in an interstitial site located within the voids of the perovskite framework for both space groups tested. This site is referred to as the I3 site and illustrated on Figure 3.11 and Figure 3.12.

As described above the methylammonium cation (MA^+) was found to be described by a 4 atom tetrahedron unit for both space groups and described in the structural model by a single shared carbon and nitrogen position (C1 and N1) as shown on Figure 3.13 and Figure 3.14. The primary difference between the refined models for the *I4/m* and *I4/mcm* space groups is the arrangement of the MA^+ cation. For the *I4/mcm* model, the tetrahedron unit is symmetric along the a and b-directions. For the *I4/m* model, the tetrahedron is rotated about the c-axis by ≈10° as illustrated on Figure 3.15. As illustrated on and Figure 3.14 the different space group orientations result in larger distances between the carbon and nitrogen sites of the MA^+ cation and the interstitial I3 sites at 1.84(8) Å and 1.91(13) Å for *I4/mcm* and *I4/m* respectively.

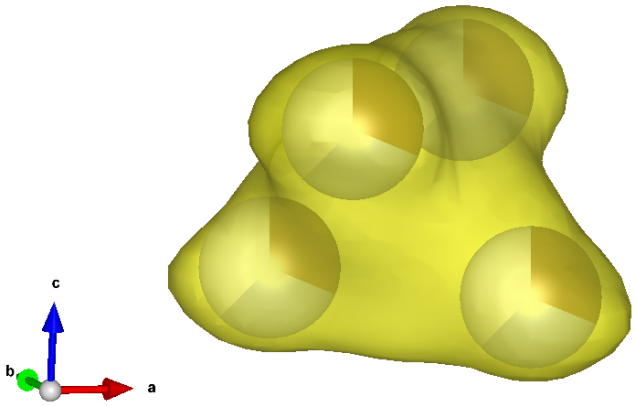

Fig. 3.13 X-ray scattering density map (isosurface level of 1.0 fmÅ^{-3}) and the refined atomic structural model for the methylammonium cation (brown/blue spheres) based on X-ray single crystal diffraction measurements.

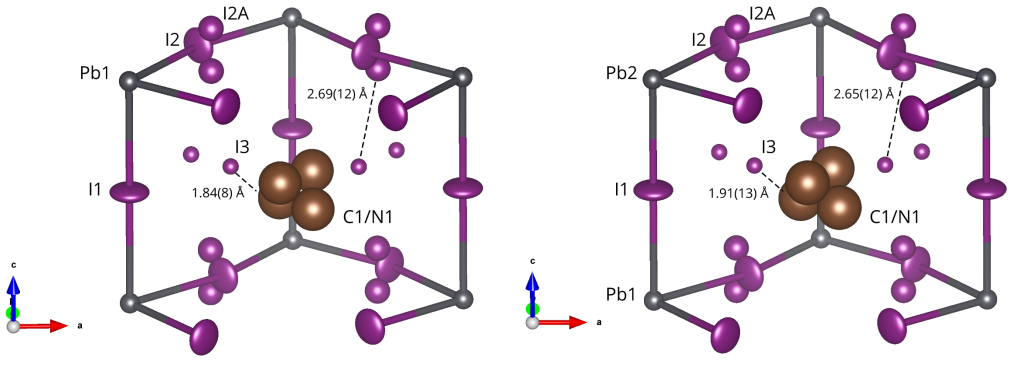

(a) (b)

Fig. 3.14 Lead (grey spheres), iodide (purple spheres) and carbon/nitrogen (brown and blue spheres respectively) derived from structure refinement of single crystal diffraction data for the (a) *I4/mcm* and (b) *I4/m* space groups.

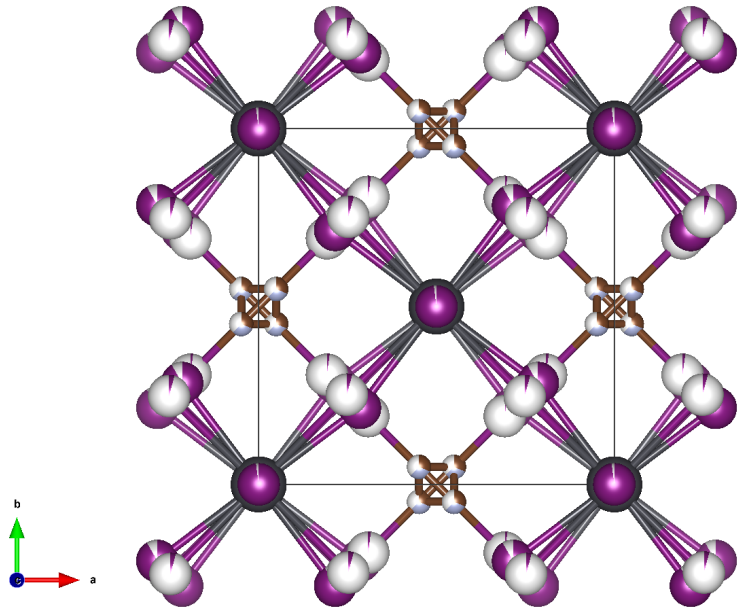

(a)

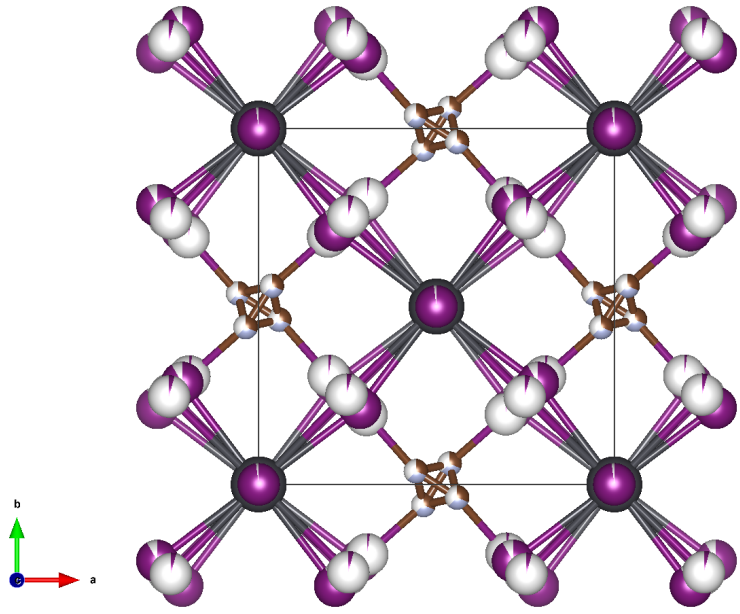

(b)

Fig. 3.15 Lead (grey spheres), iodide (purple spheres) and carbon/nitrogen (brown and blue spheres respectively) derived from structure refinement for the (a) *I4/mcm* and (b) *I4/m* space groups.

The refinement of the single crystal data results in chemically unrealistic MA^+ cation bond distances of 1.22 Å and 1.23 Å for *I4/m* and *I4/mcm* respectively.

As noted in the "Extra Sites" row of Table 3.2 multiple structural models were tested with increasing numbers of additional atomic sites. Specifically, the structure described above with interstitial iodide sites I2A and I3 (labelled 2 (I2A,I3) in Table 3.2) and a structure labelled "Multiple". For the "Multiple" structural model a number of additional iodide and lead atoms were included, identified from electron peaks in the residual electron density maps. The result of the additional sites was an improved fit as shown in Table 3.2. A direct comparison between the space groups for the "Multiple" model is difficult as the results were highly susceptible to the weighting scheme used in the refinement. Despite the improved fit, the addition of these extra atomic sites was disregarded in the final structural model as they served to better describe the non elliptical electron density of many of the atomic sites for this disordered system as opposed to distinct crystallographic sites.

Although the *I4/mcm* refinement generates better fit parameters, it relies on ignoring the significant number of observed -c- extinction violations and is determined from a much smaller number of unique reflections. For the *I4/mcm* solution, ROTAX was used to generate possible twin orientation matrices. Each was tested in the refinement, however none were shown to improve the fit. As such the final structure refinement was carried out with the *I4/m* space group with the inclusion of additional interstitial iodide sites (I2A and I3). The refinement details are given in the Appendix (Table A.1) with the respective refined atomic co-ordinates given in Table 3.3.

Single Crystal X-ray Diffraction Atomic Coordinated - *I4/m*

Atom	x	y	z	U(Å^3)	Occupancy
Pb1	0	0 0	0.0302(3)	1.0	1.0
Pb2	0	0 0.5	0.0302(3)	1.0	1.0
I1	0	0	0.24949(18)	0.0851(11)	0.971(9)
I2	-0.2148(3)	-0.2851(3)	0.5	0.0776(11)	0.925(13)
I2A	-0.252(3)	-0.248(3)	0.453(2)	0.045(7)	0.042(6)
I3	0.194(11)	0.305(11)	0.245(9)	0.04(3)	0.007(3)
C1/N1	-0.035(8)	0.438(6)	0.221(3)	0.17(3)	0.36(2)

Table 3.3 Crystallographic parameters obtained from refinement of single crystal X-ray diffraction measurements of the sample SE-MAPbI$_3$. Cell parameters were refined to be $a = b = 8.87560(10)$ Å and $c = 12.6517(3)$ Å with a volume of 996.65(9) Å^3.

3.3.3 Raman Spectroscopy

A series of Raman spectroscopy measurements have been carried out that aimed to further probe the local symmetry of the compound. Using near infrared excitation wavelength of 784.15 nm, Figure 3.16 shows the ambient temperature Raman spectra measured for $MAPbI_3$. It has been well reported that the 100 – 140 cm^{-1} and 210 – 280 cm^{-1} regions of the Raman spectra are associated with Pb–I motions and MA^+ vibrations respectively, both of which are apparent for our measurement [137]. Further scattering is observed at 420 cm^{-1}, this has been reported for I_2 molecules confined within nanopores of a zeolite where scattering is observed at around 210 and 420 cm^{-1}, corresponding to the first two vibrational quantum numbers [138]. The scattering at 210 cm^{-1} overlaps heavily with that of the MA^+ however significant scattering is observed at 420 cm^{-1}, consistent with confined I_2 molecules. Evidence of polyiodide species in $MAPbI_3$ through Raman spectroscopy has been reported [137, 139], here signals at higher frequencies are described compared with established polyiodide studies.

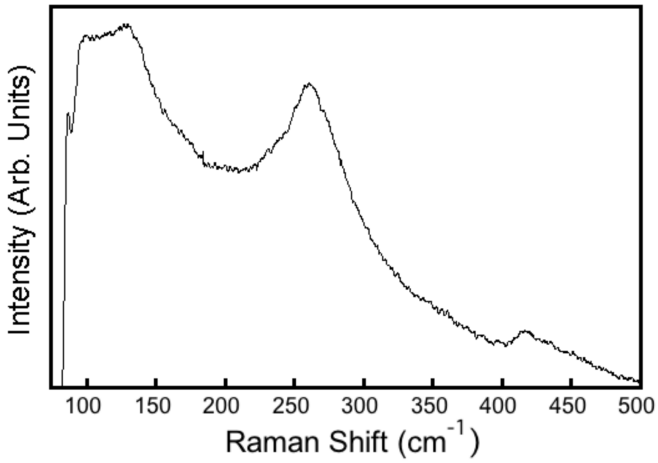

Fig. 3.16 Raman spectra of $MAPbI_3$ at ambient condition.

3.4 Variable Temperature Structural Dynamics

3.4.1 Variable Temperature Synchrotron Powder Diffraction

In order to understand how observation of these interstitial iodide sites relates to the migration of iodine described in the literature, variable temperature synchrotron X-ray powder diffraction experiments were carried out by Dr Wouter Van Beek and Dr Dmitry Chernyshov on the sample SE-$MAPbI_3$ at the Swiss-Norwegian beamline (SNBL) at the ESRF, France. The purpose of this was to measure how the occupancy

of the iodine sites varies as a function of temperature with an incident wavelength of λ = 0.6932 Å. Rietveld refinement was carried out using the software package FullProf for data measured between 200 K and 400 K. This temperature range covers two structural phases for SE-$MAPbI_3$, the ambient temperature tetragonal phase II (refined with space group *I4/m* and a structural model derived from section 3.3) and the high temperature cubic phase I, for which the data was refined with a simple cubic perovskite structure (refined with space group $Pm\bar{3}m$) comparable to structure published by Weber *et al* [47]. This structure consist of a single lead (Pb1) and iodide (I1) site, and a single carbon and nitrogen site (C1 and N1 respectively) placed on the same crystallographic site and restricted to be equivalent across all refined parameters as shown in Figure 3.17.

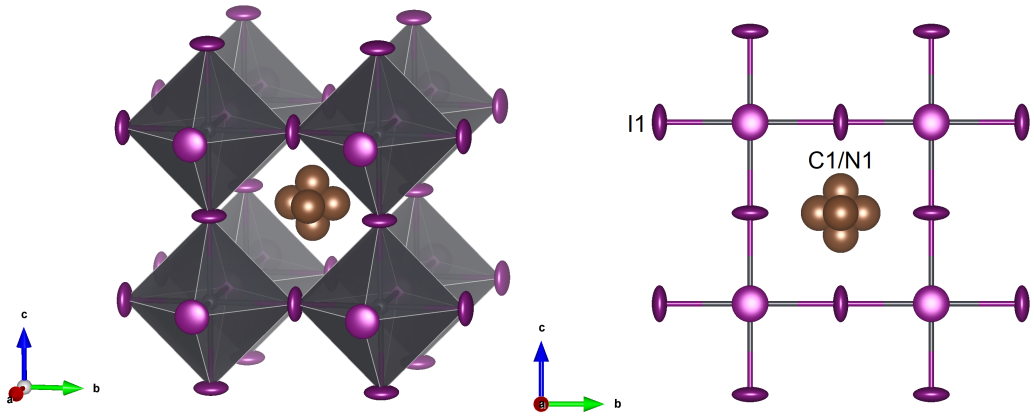

(a) (b)

Fig. 3.17 $Pm\bar{3}m$ structure of $MAPbI_3$ refined at 400 K from powder synchrotron diffraction measurements.

Considerable hysteresis is observed in the structural phase transition temperature, as shown in Figure 3.18a. Here, the pseudo-cubic lattice parameter are plotted as a function of temperature and show a tetragonal to cubic phase transition temperature at $\approx$ 335 K upon heating and $\approx$ 320 K on cooling. This hysteresis demonstrates the first order nature of the transition, where the continuous change in lattice parameters results from the coexistence of both tetragonal and cubic phases over a wide temperature range.

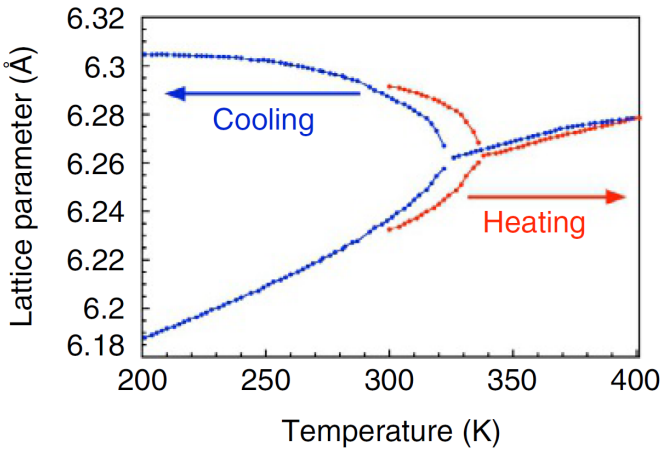

(a)

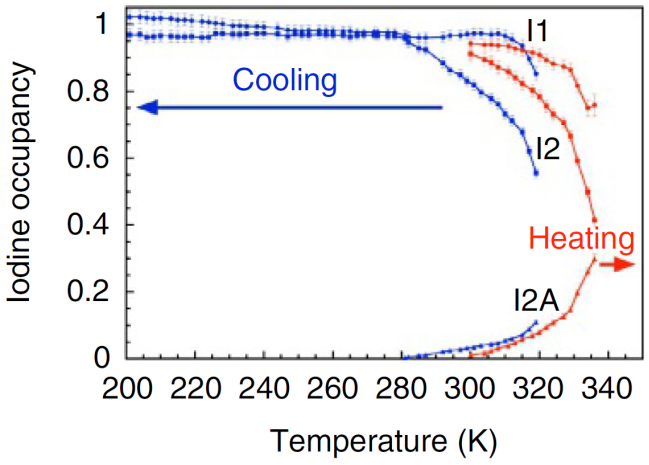

(b)

Fig. 3.18 (a) Change in pseudo-cubic lattice parameters as a function of temperature upon heating and cooling. (b) Temperature dependence of the I1, I2 and I2A iodide ion site occupancy as a function of temperature. Both structure parameters are determined from Rietveld refinement of variable temperature synchrotron powder diffraction measured on the sample SE-$MAPbI_3$.

The hysteresis described above is also expressed in the temperature dependence of the iodine composition as shown on Figure 3.18b. The occupancy of the I1 site is seen to drop close to the transition temperature upon both cooling and heating. However, it was observed that a substantial decrease in occupancy of the I2 site correlated with an increase in the occupancy of the I2A site at temperatures above 280 K. This is far below the tetragonal to cubic phase transition temperature. The occupancy of the I3 site was difficult to determine from such short runs of the synchrotron measurement as the occupancy is very low. There was however, an observed drop in the total iodine composition of the sample, this implies population of the I3 site

but it was sufficiently diffuse that it did not contribute significantly to the measured Bragg scattering.

3.5 Iodine Migration Mechanism

Through the observation of interstitial iodine sites and the analysis of the compositional variation of these sites as a function of temperature a mechanism for iodine migration via interstitial sites is proposed for $MAPbI_3$. As shown in Figure 3.18b, as the temperature increases above 280 K, the occupancy of the I2 site and the overall iodine composition is observed to decrease. This coincides with an increase in the occupancy of the I2A site, and implies that the I2 site is simultaneously populating both I2A and I3 interstitial iodide sites.

For an iodide atom to hop from site I2 to I3, results in a coordination such that the I3 site is approximately 3.2 Å away from surrounding I1 and I2 sites, as shown in Figure 3.19. Simultaneous population of both I3 and I2A sites results in a bond distance of 2.73 Å. Upon concurrent population of interstitial sites, the relevant bond distances, and analysis of reported I–I bond lengths reveals the nature of the interaction between these sites. Starting with solid I_2, for which the structure has been determined at ambient temperature by single crystal X-ray diffraction [140]. I_2 has been shown to form a layered 2D zigzag structure with intramolecular I–I bond lengths of 2.68 Å, and intermolecular I_2 distances of 3.56 Å, 4.04 Å and 4.40 Å [140]. For liquid iodine, a similar intramolecular bond length is reported as 2.70 Å, alongside short-range orientational order [141]. Similar bond lengths are found for I_2 confined within frameworks. The iodine in formate, $Zn_3(HCOO)_6$, has a bond length of 2.691 Å with a second weakly interacting molecule at 3.59 Å [142]. However, the $[I_2]^+$ ion in $I_2Sb_2F_{11}$ has a shorter I–I bond length of just 2.56 Å [143]. Other than the primary covalent bonds described above, a wide range of weakly bonded I–I lengths exist in polyiodides, forming iodine chains where the I_2 donates to the σ^* antibonding orbital in a charge transfer complex [144, 145]. A significant number of triiodides ions ($[I_3]^-$) have been studied with a range of I-I bond lengths between 2.7 Å and 3.2 Å (according to structures described in the Cambridge Structural Database [144]). For example, the triiodide ion in orthorhombic CsI_3 has I–I bond lengths of 2.84 Å and 3.04 Å [146]. This is larger than that of covalent I_2 with one longer bond possessing most of the additional charge. This range of bond distances has made it problematic in defining intramolecular and intermolecular bond boundaries, and clearly the I–I bond lengths for a number of low-valent iodide chains formed from

polyiodide ions are very sensitive to the iodine charges and nature of the bonding [144].

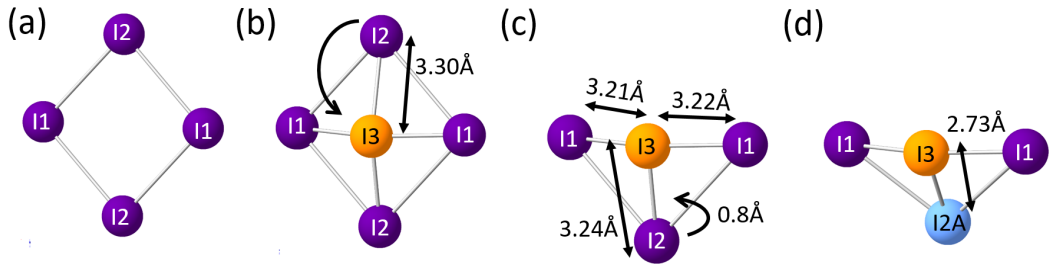

Fig. 3.19 (a) Section of the perovskite structure showing two I1 and two I2 position lying in the $(1\bar{1}0)$ plane, (b) Iodine I2 moves to the interstitial I3 position leaving (c) I3 surrounded by three roughly equidistant iodine ions, provoking I2 ions to jump to a I2A position creating (d) bond formation to produce I2 molecules.

With respect to the results presented here, the population of the I2A and I3 sites results in two I2A–I3 bond distances of 2.7(1) Å and 2.6(1) Å. Considering the discussion above it is proposed that, a covalent I_2 bond is formed through a static disorder and hop from I2 to I2A. This results in the formation of a neutral diatomic I_2 molecule within the perovskite framework. This mechanism has significant implications for the band structure of the material and suggests a redox reaction of $2I^- \rightarrow I_2 + 2e^-$. The structure upon the formation of a neutral I_2 molecule through the population of I2A and I3 sites is shown on Figure 3.20a. This shows the potential formation of chains of I_2 and I^- ions along the crystallographic z-axis. With respect to the coordination of the I3 site and the MA^+ cation, the bond distances between I3 and both orientations of the MA^+ ions are unphysical. This implies that the I3 site is only populated when the MA^+ molecule adopts a perpendicular orientation as shown in Figure 3.20b. Here, the collective motion of the MA^+ cations allows for the diffusion of iodine via the I3 site in a gate opening type mechanism.

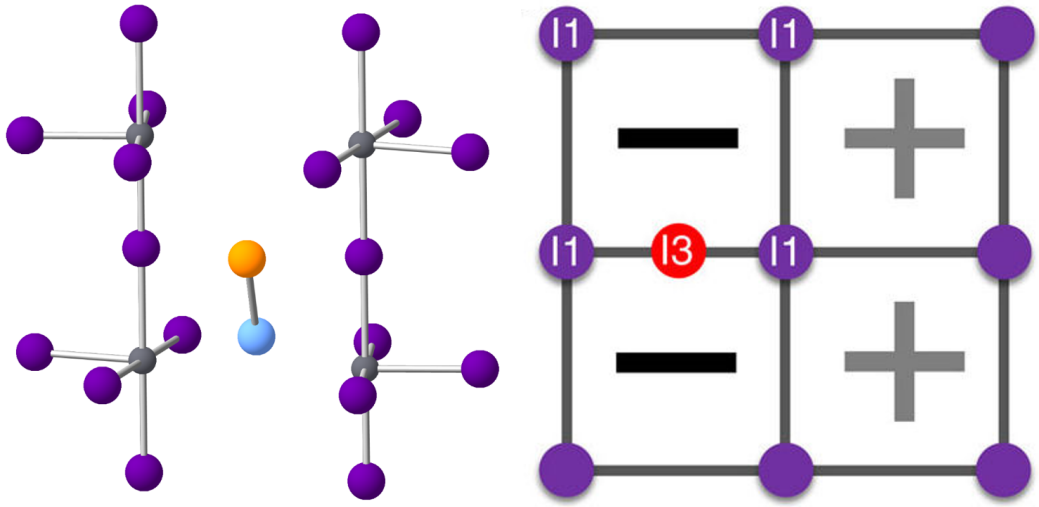

(a) (b)

Fig. 3.20 Representative local structure of $MAPbI_3$ after the proposed diatomic iodine formation. (a) Relative positions of I2 molecule (green and blue sphere) compared to the perovskite framework. Methylammonium ions are omitted for clarity, and (b) cooperative arrangements of the orientation of the methylammonium ions as a result of occupation of I3 sites. (-) and (+) represents single and shared orientations of MA molecule, respectively

3.6 Discussion

This work has derived an average structure model for the ambient temperature tetragonal phase II for $MAPbI_3$ described by the space group *I4/m* through a combination of complementary single crystal X-ray diffraction and neutron powder diffraction measurements performed on fully hydrogenous samples. The maximum entropy method was used to generate nuclear scattering density maps, from which a model for the MA^+ cation was determined to be comprised of a 4 atom tetrahedron unit with hydrogen positions located just over 1 Å from the carbon and nitrogen sites.

Following the generation of nuclear scattering density maps via MEM analysis, significant disorder associated with the iodide framework sites and additional areas of localised scattering were identified. These were assigned as interstitial iodine sites denoted I2A and I3 in the structural model. The temperature dependence of the occupancy of iodide sites was observed through variable temperature synchrotron powder diffraction measurements. A concurrent drop in the occupancy of framework iodide sites and increase in the occupancy of interstitial sites was observed, from which it has been inferred that framework iodide sites are populating the interstitial sites. Here, a mechanism for iodine migration has been proposed. Following bond

distance analysis it was concluded that the temporary formation of neutral I_2 occurs, implying the redox reaction $2I^- \rightarrow I_2 + 2e^-$. The population of interstitial iodine sites were found to result in nonphysical bond distances between sites I3 and the MA^+, meaning the migration of iodine to these sites occurs with the collective motion of surrounding MA^+ cations.

These results provide experimental evidence for significant disorder exhibited by both the PbI_6 framework and MA^+ cation for $MAPbI_3$ at ambient temperature, relevant to the operating temperature of hybrid perovskite solar cell devices. Here, experimental evidence for iodine migration via interstitial sites is also presented that supports a number of first-principle calculations for the activation energy of likely migrating species described in the literature [130, 131].

Following this work, there have been a number of experimental studies regarding ion conductivity in $MAPbI_3$ that are worth highlighting. These studies further emphasise iodine as the primary mobile species in $MAPbI_3$, and therefore support the work described in this chapter. Interestingly, ionic conductivity has been shown to massively increase upon illumination. Light induced ionic conductivity were first reported by Zhao *et al*. [147], where a reduction in activation energies were measured for I^-, MA^+ and H^+ ions upon illumination. Subsequent to this, a series of direct experimental observations were reported by Kim *et al*. definitively demonstrating increased ionic transport in $MAPbI_3$, and showed I^- to be the mobile ion [148]. Firstly, $MAPbI_3$ was used as the electrolyte phase in a battery cell. For this, the open-circuit voltage was shown to increase when illuminated, compared to dark conditions. Further to this, a $MAPbI_3$ film was grown on a Cu foil that was exposed to iodine gas at a constant partial pressure. Half the foil was then exposed to light and the other kept in dark conditions. The result was a steady-state flux of iodine that is only possible following iodine gas migration through the $MAPbI_3$ film, determined through the measurement of a CuI phase on the Cu/$MAPbI_3$ boundary. The illuminated side was found to have a much larger quantity of CuI formed at the boundary. Finally, a $MAPbI_3$ film was submerged in toluene (a strong solvent for I_2). Here, the ultraviolet-visible absorption of I_2 in toluene is recorded allowing for the quantity of iodine removed from the $MAPbI_3$ film to be calculated for both dark and illuminated conditions. From this it was found that approximately 10 times the amount of iodine was removed from the film under light conditions.

4

Average Structure Characterisation Following Thermal Treatment of $MAPbI_3$

Commercially viable hybrid perovskite materials require high power conversion efficiency and long-term thermal stability. To achieve this research has focused on compositional engineering of halides and cations within the perovskite framework that fit the criteria defined by the Goldschmidt tolerance factor. The work described in this chapter demonstrates subtle changes to the variable temperature structure of $MAPbI_3$ following different post synthesis thermal treatments. This lead to the development of a novel method for tuning the optically relevant structural features of the hybrid perovskite $MAPbI_3$. Here, single crystal and powder X-ray diffraction are combined with powder neutron diffraction techniques for the purpose of characterising precise vacuum annealing temperature dependent changes to the average structure that results from small composition changes.

4.1 Introduction

4.1.1 Conflicting Reports on Fundamental $MAPbI_3$ Properties

In recent years, interest in hybrid organic-inorganic perovskites (HOIHP) has stemmed from their promising applications in optoelectronics. Here, they combine high device efficiency and charge carrier mobility with low-cost deposition techniques [149–151]. However, for studies regarding more fundamental material properties of HOIHPs the consensus is diluted. Examining the most highly studied variant of HOIHP, $MAPbI_3$, there is currently considerable debate over the existence of ferroelectric [152, 153], pyroelectric [110] and ferroelastic [154] properties for the room temperature tetragonal phase (II) of $MAPbI_3$.

When reviewing the literature, specifically focusing on conflicting studies that report on the ferroelectric nature of $MAPbI_3$, a significant source of inconsistency becomes apparent. We found that the material synthesis process varies drastically across each study. Specifically, the thermal treatment the perovskite undergoes after the sample has crystallised, the environment in which the sample is annealed, the annealing temperature and the annealing time all vary across each study.

Ferroelectric Property	Annealing Environment	Annealing Temperature (°C)	Annealing Time
Ferroelectric	Not Annealed	Not Annealed	Not Annealed [110]
Ferroelectric	Nitrogen	100	20 Minutes [152]
Ferroelectric	Air	150	3 Minutes [153]
Not Ferroelectric	Air	180	3 Hours [155]
Not Ferroelectric	Nitrogen	100	20 Minutes[156]
Not Ferroelectric	Air	100	30 Minutes [157]

Table 4.1 Comparing the reported ferroelectric property and thermal treatment undertaken for a number of studies on $MAPbI_3$.

The purpose of presenting these inconsistencies is not to explain if $MAPbI_3$ is ferroelectric. Instead, the aim is to highlight the requirement for further clarification over changes to the average structure of $MAPbI_3$ that are dependent on the post synthesis thermal treatment. Here, many of the reported fundamental properties of this material such as ferroelectric, pyroelectric and ferroelastic properties are dependent on subtle structural dynamics and average crystal structure properties. Lab-to-lab reproducibility of solar cell performance characteristics has also been significant in preventing industrial fabrication of commercial perovskite based devices, this has

primarily been attributed to poor control of the morphology of perovskites, a property that is, at least in part, dependent on the post synthesis thermal treatment.

4.1.2 Thermal Engineering Studies

During the synthesis of hybrid perovskite films, thermal treatments are implemented in order to: synthesise the perovskite materials from precursors, remove residual solvents following solution processing and improve crystallinity, grain size and morphology of the perovskite film [158, 159]. Further thermal treatments are carried out during the fabrication process for the deposition of subsequent device layers including both hole transport layers and the metal contacts [160]. This means understanding the controllable factors of thermal annealing treatment, including annealing duration, temperature, environment and how this affects the quality of perovskite films is vital for improving the stability and efficiency of optoelectronic devices. Importantly, a controlled environment significantly increases the costs for industrial manufacturing of hybrid perovskite cells, making ambient condition processing advantageous.

In general, the preparation method for hybrid perovskite samples controls the micro- and nanostructure of the sample as well as the concentration, location and nature of defects. Primarily, studies have focused on determining the effects on grain size and morphology of perovskite films following thermal treatment [132, 161–163]. It has been shown that extended thermal annealing treatment can be detrimental to hybrid perovskite layer morphology at temperatures of >100 °C with the formation of significant voids, thus impacting the performance of solar cell devices [164]. The annealing temperature dependence of hybrid perovskite crystallinity has been investigated for $((FAI)_{0.85}(MABr)_{0.15}(PbI_2)_{0.85}(PbBr_2)_{0.15})$ between temperatures 80 °C and 100 °C when annealed for 120 minutes in air [165]. Specifically, XRD and SEM analysis has shown the formation of PbI_2 phases following the release of organic species. This was reported to increase for higher annealing temperatures, with the exception of films annealed at 80 °C. An increase in grain size was also observed resulting from increased annealing temperature along with reduced crystallinity. The presence of PbI_2 is reported to reduce non-radiative charge-carrier recombination hindering photovoltaic performance. For this study, perovskite devices annealed at 100 °C showed the highest J_{SC} (23.1 mA cm^{-2}) with a PCE of 19.5% following 90 minutes of annealing.

The effect of the environment during thermal annealing processes has also been studied with respect to perovskite morphology. Specifically the effect of humid-

ity, due to the moisture sensitivity of hybrid perovskites that are prone to rapidly degrade under high temperature [166, 167], light irradiation [168, 169], oxygen atmosphere [170, 171] and humidity [167], a result of the hygroscopic nature of organic cations [164]. The decomposition of hybrid perovskites such as $MAPbI_3$ will occur in the presence of water and light when exposed to air decomposing to the by-products CH_3NH_3I and PbI_2 [172]. Zhou *et al*. demonstrated that without humidity control the perovskite film process varies drastically. Whilst synthesised under 30% relative humidity in air, perovskite films of $CH_3NH_3PbI_{3-x}Cl_x$ exhibited improved optoelectronic properties compared with those grown under dry conditions. Under moist conditions it is proposed that reconstruction processes are improved during perovskite film formation by partial dissolving of the reactant species, thereby accelerating mass transport. Following this, the performance of $CH_3NH_3PbI_{3-x}Cl_x$ based solar cell devices was improved to 19.3% [173]. The use of water as an additive during the production of perovskite films has also been reported as beneficial to perovskite morphology [174]. Here, water additives were added to anhydrous DMF improving control of perovskite growth due to a lower boiling point. For the films grown with DMF-only the surface morphology showed significantly more pin holes and voids that results in reduced charge transport and light absorption for perovskite films. When water additives were included, the voids were seen to reduce and crystal grain size was reported to increase. It has also been reported that annealing in air opposed to a dry N_2 atmosphere increases the grain size and changes the composition when synthesising $MAPbI_{1-x}Cl_x$ films, where an air environment prevents spontaneous formation of $MAPbCl_3$, favouring $MAPbI_3$ phase [175].

With moisture and oxygen being plentiful during both synthesis and device operation, it is significant that both water and oxygen have been shown to accelerate the degradation of hybrid perovskites such as $MAPbI_3$ [171]. In considering the processing environment of hybrid perovskites, it has been reported that oxygen can improve the performance of optoelectronic devices and reduce nonradiative charge carrier recombination [176, 177]. Through time resolved luminescence microscopy, it has been reported that O_2 also increases the photoluminescence (PL) of $MAPbI_3$. This has been attributed to photochemical reactions involving oxygen, that passivates deep-lying trapping defects, interestingly these effects are reversible [176, 178, 179]. Furthering this, it has been reported that oxygen incorporation into the structure of $MAPbI_3$ is increased significantly under illumination [170]. This coincides with reports of O_2 and H_2O being absorbed onto the surface of $MAPbBr_3$ leading to an increase in PL [180]. The crystallinity and morphology of $MAPbI_3$ films has also been shown to improve following vacuum-assisted annealing at 70 °C [181],

with reports of enhanced temperature dependent optical characteristics. Interestingly, further improvements were observed by increasing the vacuum time prior to annealing.

It is apparent that the conditions under which thermal treatment of hybrid perovskites are carried out, not only impacts the crystallinity, grain size and morphology of the material, but also affects the optoelectronic properties. Reports of reversible oxygen absorption into the structure of hybrid perovskites following thermal treatment and the resulting effect on photoluminescence, suggests a need to clarify any changes to the average structure of hybrid perovskite materials following a wide range of thermal treatments. The majority of studies that look to observe changes induced through thermal annealing treatment have focused on the production and measurement of thin films, for obvious practical reasons, however, this hinders detailed experimental average structure studies.

4.1.3 Purpose of the Present Study

For perovskite films, the sublimation of the organic perovskite component during thermal annealing results in a significant defect concentration at the grain boundary and surface of the film [182, 183]. The high defect concentration at the grain boundary is confirmed through measurement of a significantly higher trap density for solution processed polycrystalline prototypical $MAPbI_3$ perovskite films (10^{16} cm^{-3} to 10^{17} cm^{-3}) compared with single crystal samples (10^{9} cm^{-3} to 10^{10} cm^{-3}) [184, 185]. Structure characterisation through measurement of the bulk is therefore favourable for determining changes to the average structure of the material, limiting the influence of surface defects. The purpose of this work is to measure changes to the average structure of bulk $MAPbI_3$, when subject to different thermal treatments. The thermal treatments chosen for this study vary in temperature and environment and are consistent with the variation in treatments described in the literature. Variable temperature powder synchrotron and single crystal X-ray diffraction techniques were combined with maximum entropy analysis of time-of-flight neutron powder diffraction for this purpose.

4.2 Low Temperature Thermal Treatment

4.2.1 Post Synthesis Thermal Treatment

The purpose of this experiment was to measure any changes to the average structure of solution processed $MAPbI_3$ when subjected to different post synthesis thermal

annealing treatments, including variation in annealing temperature and environment. The samples discussed in this chapter were synthesised by Rhianna Day, University of Kent. For this purpose, a single sample of $MAPbI_3$ was synthesised via a low temperature solution based method as outlined in Section 2.6.1 The sample was then divided into 4 subgroups of 0.5 g, where each subgroup was subsequently treated according to Table 4.2. Each subgroup has been assigned a sample ID and referenced to as such throughout this chapter.

Sample ID	Annealing Environment	Annealing Time (hours)	Annealing Temperature (°C)
SS-$MAPbI_3$	NA	24	NA
AA80-$MAPbI_3$	Air	24	80
AV80-$MAPbI_3$	Vacuum	24	80
AV200-$MAPbI_3$	Vacuum	24	200

Table 4.2 Post synthesis annealing conditions undertaken for a range of $MAPbI_3$ samples, each identified by a unique ID specifying the annealing condition and temperature.

A sample was also annealed at 200 °C in air for 24 hours, however data for this sample has not been included as the sample was found to completely degrade under these conditions, evidenced by a significant PbI_2 phase indexed in a subsequent powder X-ray diffraction measurement. Annealing in both air and under a vacuum is consistent with common thermal treatments found in the literature [110, 152, 153, 156, 157], as are the annealing times and temperatures described in Table 4.2. With the exception of 200 °C, this temperature was chosen for the purpose of maximising any changes induced in the sample. For the vacuum annealed samples (AV80-$MAPbI_3$ and AV200-$MAPbI_3$), $\approx$ 0.5 g of the sample was placed into a quartz tube with a diameter of 0.6 cm, the tube was then placed under 10^{-4} torr of pressure, sealed and placed in an oven to be heated at the respective temperature (80 °C for AV80-$MAPbI_3$ and 200 °C for AV200-$MAPbI_3$ for 24 hours). For the sample annealed in air (AA80-$MAPbI_3$), $\approx$ 0.5 g of the sample was placed in a ceramic boat where it was then transferred to an oven for annealing at 80 °C for 24 hour. The sample SS-$MAPbI_3$ was taken straight from the solution following synthesis for characterisation.

4.2.2 Variable Temperature Powder Diffraction

The average structure of each sample described in Table 4.2 was measured through variable temperature synchrotron X-ray powder diffraction measurements conducted using the PILATUS@SNBL diffractometer at the Swiss-Norwegian Beam Lines,

European Synchrotron Radiation Facility. Each sample was measured with a wavelength of $\lambda = 0.956910$ Å between the temperatures 300 K and 400 K. Sequential Rietveld refinements of each data set were carried out using the FullProf software suite [186].

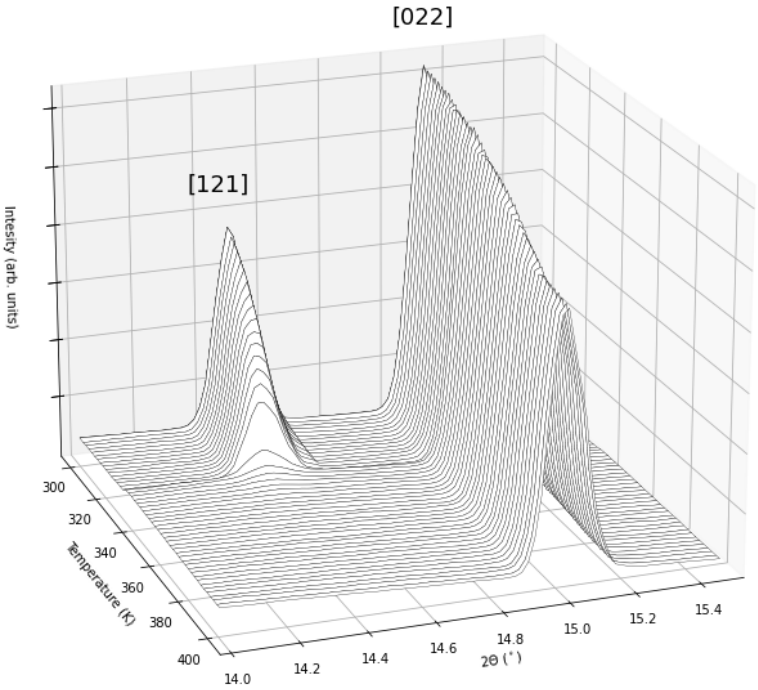

Fig. 4.1 Measured powder synchrotron diffraction data for the compound AV80-$MAPbI_3$. The pattern has been indexed with respect to the tetragonal phase II for $MAPbI_3$.

The measured temperature range was observed to cover the structural phases II (tetragonal) and I (cubic) for prototypical $MAPbI_3$, the specific transition temperature for each sample was determined through the suppression of the [121] reflection (as shown in Figure 4.1) and the gradual convergence of the lattice parameters, a and b, as illustrated in Figure 4.4. A tetragonal structural model (phase II) described by the space group *I4/m* was taken from Section 3.3.2 (Table 3.3) and used as a starting model to refine each of the samples at 300 K, as shown in Figure 4.2. Here, the PbI_6 perovskite framework is composed of two distinct lead (labelled Pb1 and Pb2) and two iodide (labelled I1 and I2 sites) atomic sites. The MA^+ cation is described by a single carbon and nitrogen site (C1 and N1 respectively) that were restricted to share the same atomic site, thermal parameters and occupancy. The refined structural model for each of the samples at 300 K is described in Table 4.3 for samples SS-$MAPbI_3$, AA80-$MAPbI_3$, AV80-$MAPbI_3$ and AV200-$MAPbI_3$ respectively.

SS-$MAPbI_3$ Refined Atomic Coordinates - 300 K					
Atom	x	y	z	Occupancy	U ($Å^3$)
Pb1	0.0	0.0	0.0	0.99(4)	0.0513(13)
Pb2	0.0	0.0	0.5	0.95(4)	0.0513(13)
I1	0.0	0.0	0.25	1.0	0.106(3)
I2	0.21197(17)	0.28804(17)	0.5	1.000(4)	0.112(4)
N1/C1	0.5587046(13)	-0.0628317(12)	0.2925779(9)	0.349(4)	0.245(15)
AA80-$MAPbI_3$ Refined Atomic Coordinates - 300 K					
Atom	x	y	z	Occupancy	U ($Å^3$)
Pb1	0.0	0.0	0.0	0.95(5)	0.062(2)
Pb2	0.0	0.0	0.5	0.99(5)	0.062(2)
I1	0.0	0.0	0.25	1.0	0.117(4)
I2	0.2164(3)	0.2836(3)	0.5	1.000(5)	0.120(4)
N1/C1	0.558699(3)	-0.062827(3)	0.292591(2)	0.349(5)	0.125(16)
AV80-$MAPbI_3$ Refined Atomic Coordinates - 300 K					
Label	x	y	z	Occupancy	U ($Å^3$)
Pb1	0.0	0.0	0.0	0.98(5)	0.0496(20)
Pb2	0.0	0.0	0.5	0.94(5)	0.0496(20)
I1	0.0	0.0	0.25	1.0	0.105(4)
I2	0.2119(3)	0.2881(3)	0.5	1.000(6)	0.104(4)
N1/C1	0.5581912(18)	-0.0633503(17)	0.2925799(12)	0.349(6)	0.22(2)
AV200-$MAPbI_3$ Refined Atomic Coordinates - 300 K					
Label	x	y	z	Occupancy	U ($Å^3$)
Pb1	0.0	0.0	0.0	0.94(3)	0.0433(17)
Pb2	0.0	0.0	0.5	0.96(3)	0.0433(17)
I1	0.0	0.0	0.25	1.0	0.094(4)
I2	0.2209(3)	0.2791(3)	0.5	1.000(4)	0.113(4)
N1/C1	0.5577418(13)	-0.0635307(12)	0.2926486(9)	0.349(2)	0.088(13)

Table 4.3 Crystallographic parameters for the samples SS-$MAPbI_3$ (a = 8.86742(4) Å, c = 12.66311(10) Å), AA80-$MAPbI_3$ (a = 8.86819(9) Å, c = 12.6592(2) Å), AV80-$MAPbI_3$ (a = 8.86429(6) Å, c = 12.66240(14) Å) and AV200-$MAPbI_3$ (a = 8.88185(6) Å, c = 12.64232(15) Å) obtained from Rietveld refinement of powder synchrotron diffraction data measured at 300 K.

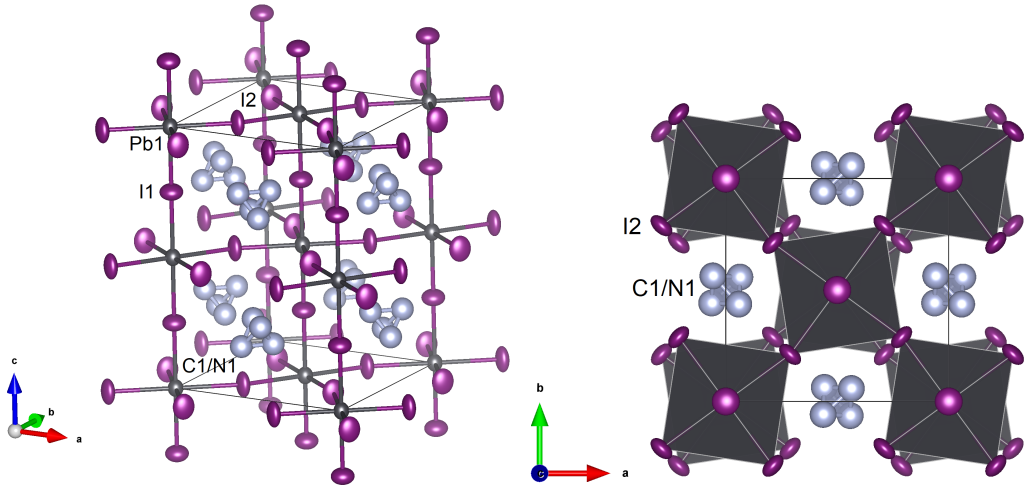

(a) (b)

Fig. 4.2 (a) and (b) the structural models refined for the samples SS-$MAPbI_3$, AA80-$MAPbI_3$, AV80-$MAPbI_3$ and AV200-$MAPbI_3$ at 300 K. For both (a) and (b) lead is shown in grey, iodine in purple and carbon/nitrogen in blue.

A starting structural model for the high temperature cubic phase I was obtained from a single crystal X-ray diffraction conducted on the sample AV80-$MAPbI_3$ at 370 K, for which details can be found in Appendix A.3. As shown in Figure 4.3, the model describes a simple cubic perovskite structure described by the space group $Pm\bar{3}m$ (Glazer notation $a^0a^0a^0$, zero-tilt system) for each of the samples described in Table 4.2. The structural model is comprised of a single lead, iodide, carbon and nitrogen atomic sites (labelled Pb1, I1, C1 and N1 respectively). Table 4.4 describes the structural model for the samples SS-$MAPbI_3$, AA80-$MAPbI_3$, AV80-$MAPbI_3$ and AV200-$MAPbI_3$ respectively, refined at 400 K.

Following the sequential Rietveld refinement of the diffraction data for the samples: SS-$MAPbI_3$, AA80-$MAPbI_3$, AV80-$MAPbI_3$ and AV200-$MAPbI_3$ subtle differences in the average structure were observed. In discussing the observations for each measured structural parameter, the sample that has undergone no thermal treatment and taken straight from the solution, SS-$MAPbI_3$, is taken as the standard upon which the other samples and there respective structural features are compared for clarity.

Figure 4.4 shows the refined pseudo-cubic lattice parameters a and c (where $a_{cubic} = b_{cubic} = a_{tetragonal}/\sqrt{2}$ and $c_{cubic} = c_{tetragonal}/2$ for the tetragonal II phase) as a function of temperature for each sample measured. Here, a shift in the structural phase transition temperature from phase II to I was observed for all samples. For both the sample taken straight from solution and the sample annealed under a vacuum at

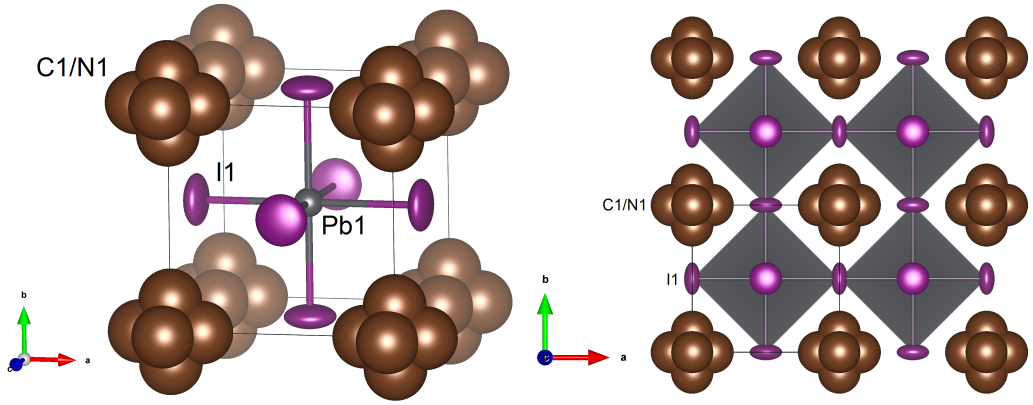

(a) (b)

Fig. 4.3 (a) and (b) the starting structural model refined for the samples SS-$MAPbI_3$, AA80-$MAPbI_3$, AV80-$MAPbI_3$ and AV200-$MAPbI_3$ at 400 K. For both (a) and (b) lead is shown in grey, iodine in purple and carbon/nitrogen in brown.

SS-$MAPbI_3$ Refined Atomic Coordinates - 400 K					
Label	x	y	z	Occupancy	U (Å^3)
Pb1	0.5	0.5	0.5	0.995(5)	0.0625(9)
I1	0.0	0.5	0.5	1.0	0.152(2)
N1/C1	0.0	-0.1377	0.0	0.233	0.336(20)
AA80-$MAPbI_3$ Refined Atomic Coordinates - 400 K					
Label	x	y	z	Occupancy	U (Å^3)
Pb1	0.5	0.5	0.5	0.967(6)	0.0677(12)
I1	0.0	0.5	0.5	1.0	0.157(3)
N1/C1	0.0	-0.1421	0.0	0.23287	0.161(16)
AV80-$MAPbI_3$ Refined Atomic Coordinates - 400 K					
Label	x	y	z	Occupancy	U (Å^3)
Pb1	0.5	0.5	0.5	0.998(8)	0.0558(12)
I1	0.0	0.0	0.25	1.0	0.147(3)
N1/C1	0.0	-0.1309	0.0	0.233	0.63(4)
AV200-$MAPbI_3$ Refined Atomic Coordinates - 400 K					
Label	x	y	z	Occupancy	U (Å^3)
Pb1	0.5	0.5	0.5	0.960(8)	0.0497(15)
I1	0.0	0.5	0.5	1.0	0.136(3)
N1/C1	0.0	-0.1547	0.0	0.233	0.33(4)

Table 4.4 Crystallographic parameters for the samples SS-$MAPbI_3$ (a = 6.31714(3) Å), AA80-$MAPbI_3$ (a = 6.30692(5) Å), AV80-$MAPbI_3$ (a = 6.31761(4) Å) and AV200-$MAPbI_3$ (a = 6.31799(4) Å) obtained from Rietveld refinement of powder synchrotron diffraction data conducted at 400 K.

80 °C, SS-$MAPbI_3$ and AV80-$MAPbI_3$ respectively, the transition occurs at 337 K. This was found to increase to 355 K for the sample annealed in air at 80 °C (AA80-$MAPbI_3$). For the sample annealed under a vacuum at 200 °C (AV200-$MAPbI_3$), the phase transition temperature is reduced down to 325 K.

The volumetric thermal expansion coefficient was determined to be 3.238×10^{-2} K^{-1}, 3.131×10^{-2} K^{-1}, 3.491×10^{-2} K^{-1} and 2.900×10^{-2} K^{-1} for the samples SS-$MAPbI_3$, AA80-$MAPbI_3$, AV80-$MAPbI_3$ and AV200-$MAPbI_3$ respectively. This was calculated from the unit cell volume shown as a function of temperature in Figure 4.5 using the equation:

$$\alpha_V = \frac{1}{V}\frac{\sigma V}{\sigma T} \tag{4.1}$$

Here, V has been taken as the primitive cell volume at 400 K for each sample. The rate of expansion for the unit cell volume was found to be consistent for the samples SS-$MAPbI_3$ and AV80-$MAPbI_3$. A reduction is observed for the samples AA80-$MAPbI_3$ and AV200-$MAPbI_3$. At 400 K the unit cell volumes of the samples SS-$MAPbI_3$, AV80-$MAPbI_3$ and AV200-$MAPbI_3$ are observed to be equivalent with a small drop in volume observed at 400 K for the sample AA80-$MAPbI_3$.

The structural phase transition from phase II (tetragonal) to I (cubic) corresponds to a complete suppression of the observed octahedral tilt about the crystallographic c-axis. Figure 4.7 describes the Pb1-I2-Pb1 bond angle (with respect to the atomic models outlined in Table 4.3) for phase II as a function of temperature, this illustrates the temperature dependence of the octahedral tilt for each sample. For each sample an increase in the Pb1-I2-Pb1 bond angle as a function of temperature is observed that approaches 180° as the sample transitions from tetragonal to cubic. The increase in bond angle is found to be consistent for the samples SS-$MAPbI_3$ and AV80-$MAPbI_3$, with the bond angle sharply approaching 180° at $\approx$ 337 K. For the sample AV200-$MAPbI_3$, the bond angle is found to be significantly larger compared to the other samples, meaning, the octahedral tilting is suppressed considerably over the same temperature range. A sharp increase in bond angle is observed as the temperature approaches the tetragonal to cubic transition at $\approx$ 325 K as shown in Figure 4.4. For the sample AA80-$MAPbI_3$, below 335 K a larger bond angle is observed compared with the samples SS-$MAPbI_3$ and AV80-$MAPbI_3$. At 335 K the bond angle of the samples SS-$MAPbI_3$, AV80-$MAPbI_3$ and AA80-$MAPbI_3$ are equivalent, above which a sharp increase in bond angle for the samples SS-$MAPbI_3$ and AV80-$MAPbI_3$ is observed. A smaller rate of change is observed for the increase in bond angle for AA80-$MAPbI_3$ above 335 K. The result is an increase in the structural phase

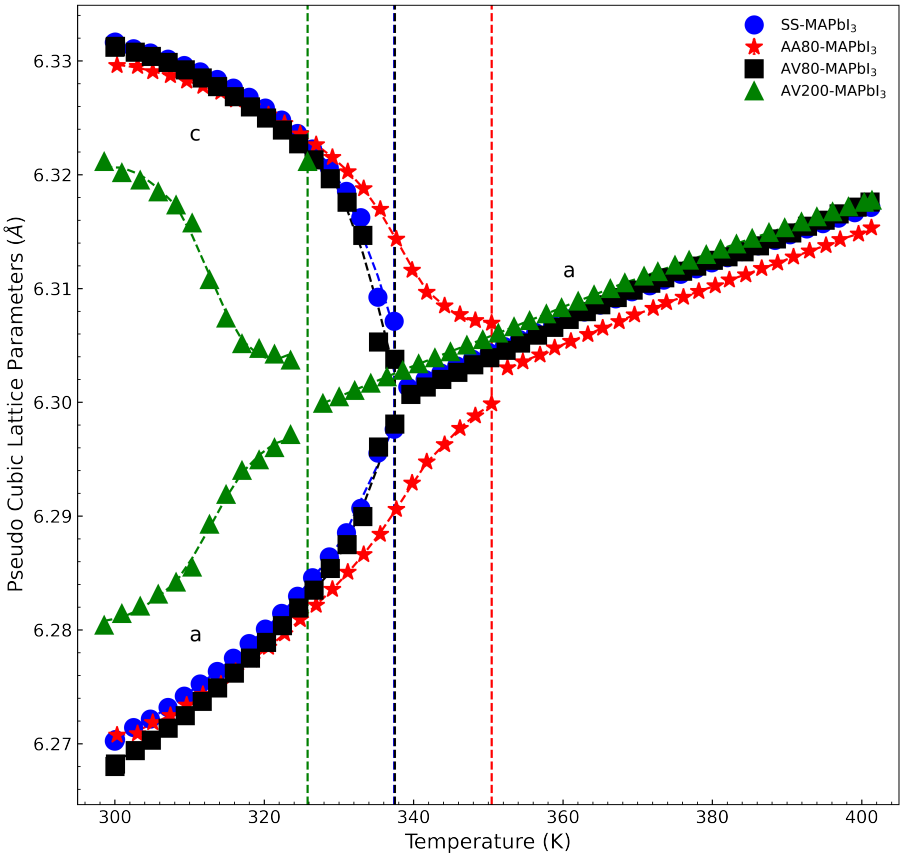

Fig. 4.4 Pseudo cubic lattice parameters for the samples SS-$MAPbI_3$ (blue circles), AA80-$MAPbI_3$ (red stars), AV80-$MAPbI_3$ (black squares) and AV200-$MAPbI_3$ (green triangles) derived from Rietveld refinement of powder X-ray diffraction measurements between 300 K and 400 K.

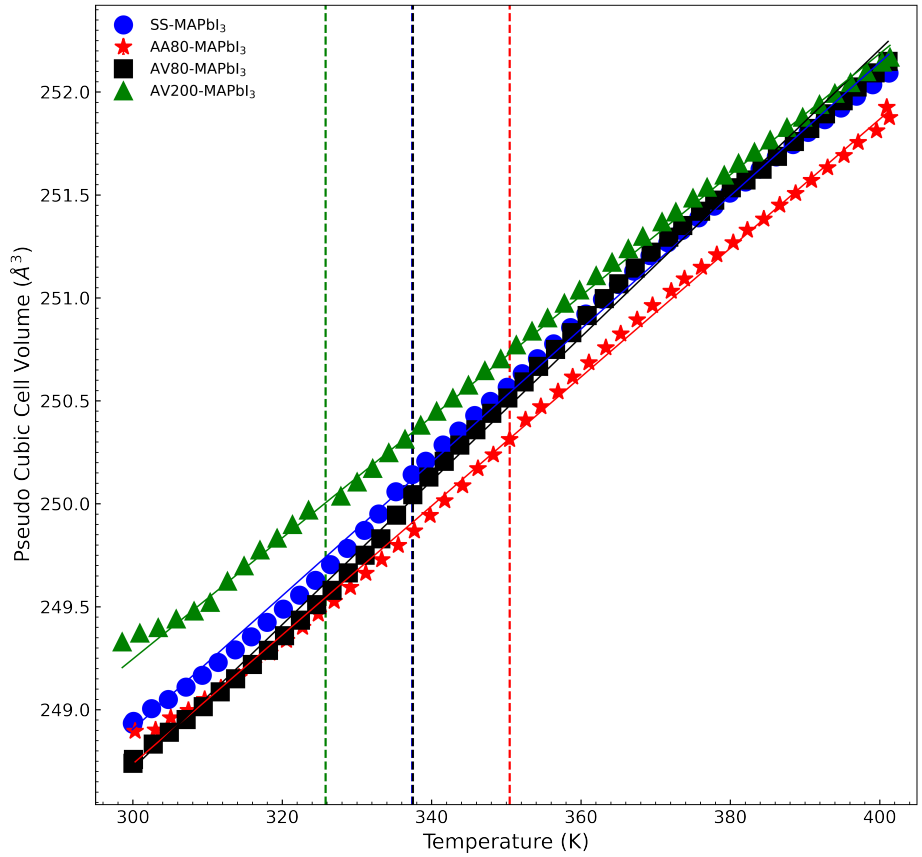

Fig. 4.5 Unit cell volume for the samples SS-$MAPbI_3$ (blue circles), AA80-$MAPbI_3$ (red stars), AV80-$MAPbI_3$ (black squares) and AV200-$MAPbI_3$ (green triangles) derived from Rietveld refinement of powder X-ray diffraction measurements between 300 K and 400 K.

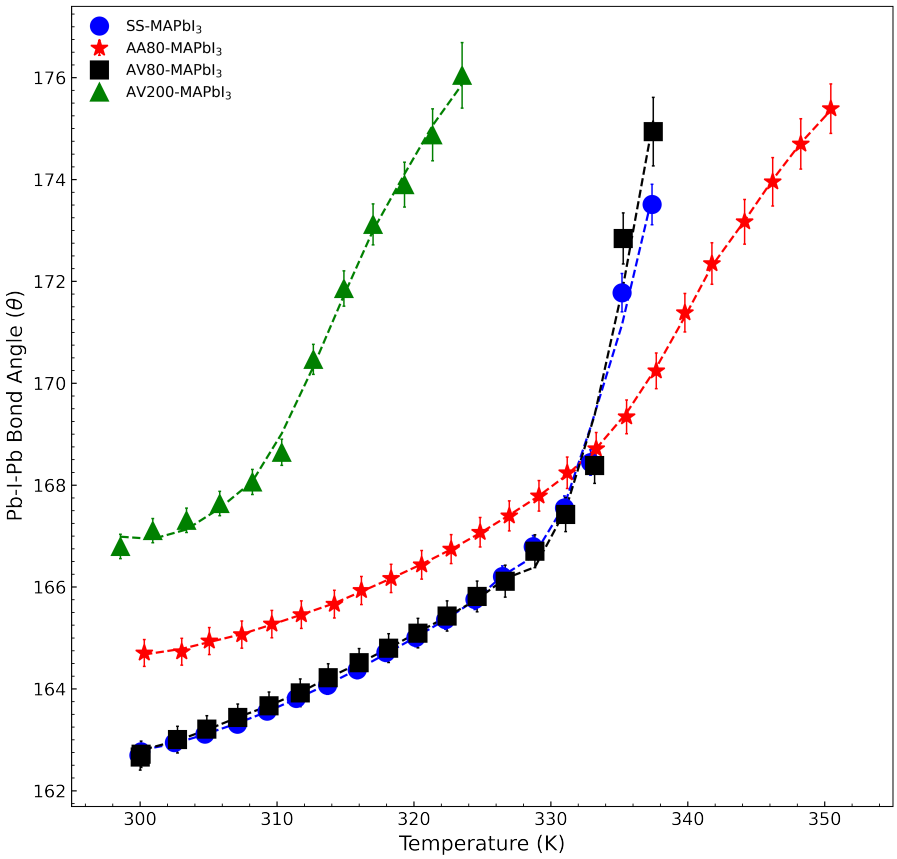

Fig. 4.6

Fig. 4.7 The bond angle Pb1-I2-Pb2 for the samples SS-$MAPbI_3$ (blue circles), AA80-$MAPbI_3$ (red stars), AV80-$MAPbI_3$ (black squares) and AV200-$MAPbI_3$ (green triangles) derived from Rietveld refinement of powder X-ray diffraction measurements between 300 K and 400 K.

transition and a significant change in the profile of this phase transition as a result of low temperature annealing in air that is also reflected in the change in Pb-I-Pb bond angle as a function of temperature. As shown by Figure 4.8 all samples exhibit a drop in Pb-I bond length as the temperature approaches the tetragonal to cubic phase transition temperature, this is a result of the increased thermal motion the iodide sites exhibit resulting in a drop in the observed average Pb-I length.

Compared to annealing under a vacuum, when $MAPbI_3$ is annealed in air at high temperature (200 °C) the compound rapidly degrades. Along with high temperature, the degradation of $MAPbI_3$ can be induced readily through exposure to water, high humidity and high-intensity light [166–171, 167, 164]. For a number of these degradation pathways, exposure to oxygen has been shown to be a considerable source of instability [170, 187]. For our experiments, oxygen is present during the solution synthesis of these compounds and throughout the post synthesis annealing process in air. There have been several studies on the solubility of oxygen in hybrid perovskites including reports of reversible increase in photoluminescence through exposure to oxygen [176, 179, 188]. It has also been shown that through prolonged exposure to a wet environment, considerable changes to the average structure of $MAPbI_3$ results from insertion of H_2O into the structure alongside considerable degradation of the material [107].

Further analysis of the refinements at 300 K (sample AV80-$MAPbI_3$) provided an insight into the observed changes from low temperature annealing in air. Specifically, examination of residual electron density maps generated by calculation of Fourier difference maps for the samples SS-$MAPbI_3$ (Figure 4.9a) and AA80-$MAPbI_3$ highlights additional localised maxima for the sample AA80-$MAPbI_3$ located along the axis (0, 0.5, z) as shown in Figure 4.9b. Following the discussion above, the additional electron density was proposed as an interstitial oxygen atom site. The refined structure of AA80-$MAPbI_3$ at 300 K with interstitial oxygen is shown in Table 4.5.

As shown in Table 4.5, at 300 K an occupancy of $8\pm2\%$ was refined for the interstitial oxygen site observed for AA80-$MAPbI_3$. As shown in Figure 4.10 the population of this interstitial oxygen site results in the I2 iodide sites being pushed apart, evidenced by a change in I2-I2 bond length of 5.317(3) Å for SS-$MAPbI_3$ to 5.433(6) Å for AA80-$MAPbI_3$. A small reduction in the Pb-I bond lengths Pb-I1 and Pb-I2 is observed for AA80-$MAPbI_3$, as shown in Figure 4.8 combined with a smaller unit cell volume as shown in Figure 4.5. This results in stronger interactions between the I^- framework sites and the MA^+ cation. This interaction is coupled with the

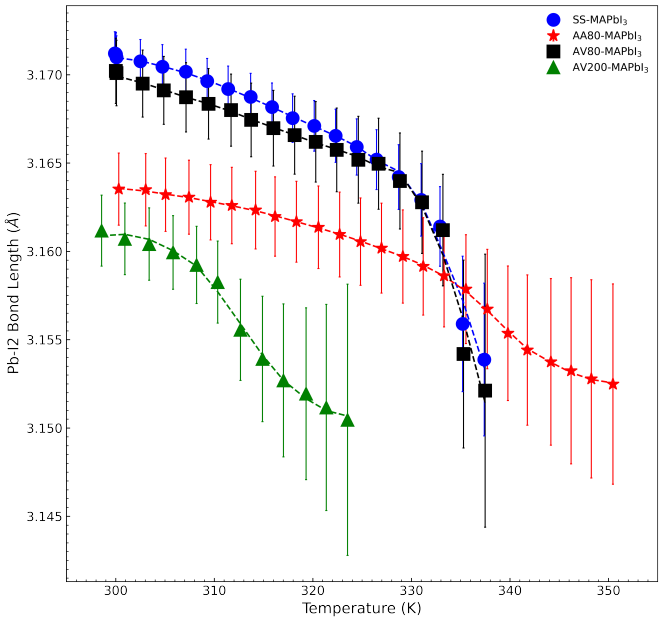

(a)

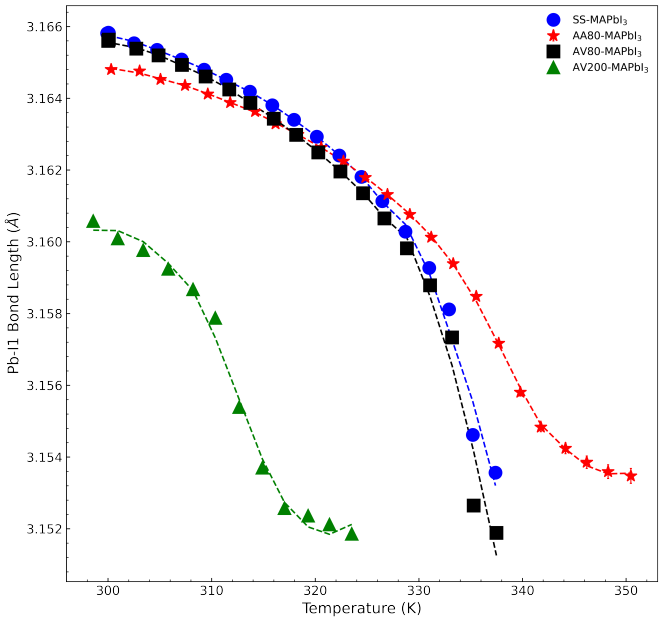

(b)

Fig. 4.8 Refined bond lengths (a) Pb-I1 and (b) Pb-I2 for the tetragonal phase II for the samples SS-$MAPbI_3$ (blue circles), AA80-$MAPbI_3$ (red stars), AV80-$MAPbI_3$ (black squares) and AV200-$MAPbI_3$ (green triangles) derived from Rietveld refinement of powder X-ray diffraction measurements between 300 K and 400 K.

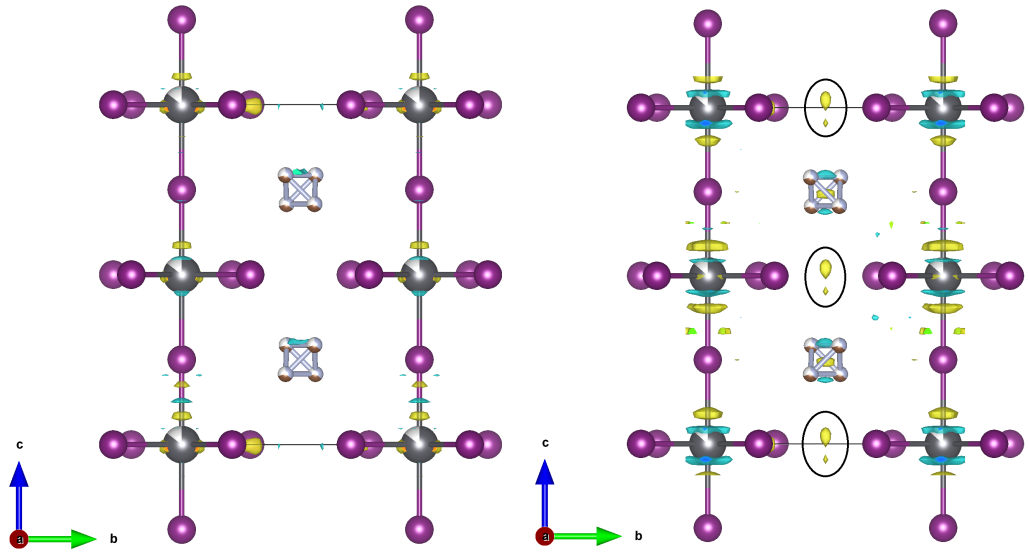

(a) (b)

Fig. 4.9 Calculated Fourier difference maps derived from Rietveld refinement of synchrotron powder diffraction data measured at 300 K for the samples (a) SS-$MAPbI_3$ and (b) AA80-$MAPbI_3$. Lead is shown in grey, iodine in purple and carbon/nitrogen in blue/brown.

AA80-$MAPbI_3$ Synchrotron Powder X-ray Diffraction Atomic Coordinated - 300K					
Label	x	y	z	Occupancy	U ($Å^3$)
Pb1	0.0	0.0	0.0	0.96(7)	0.063(2)
Pb2	0.0	0.0	0.5	0.98(7)	0.063(2)
I1	0.0	0.0	0.25	1.0	0.116(4)
I2	0.2166(3)	0.2834(3)	0.5	1.000(5)	0.120(4)
N1/C1	0.558699(4)	-0.062825(3)	0.292590(2)	0.349(5)	0.126(16)
O1	-0.5	1.0	0.97250	0.08(2)	0.01(8)

Table 4.5 Crystallographic parameters for the sample AA80-$MAPbI_3$ obtained from Rietveld refinement of powder synchrotron diffraction data using the space group *I4/m* at 300 K. Refined lattice parameters are a = 8.86817(9) Å, c = 12.6592(2) Å.

titling exhibited by the perovskite framework, as is the case for all hybrid perovskites. Here, the stronger interactions results in the observed increase in both the structural phase transition from tetragonal to cubic and the reduction in the rate of change of Pb1-I2-Pb2 bond angle observed above 335 K for AA80-$MAPbI_3$ compared with SS-$MAPbI_3$ as shown in Figure 4.7. Additionally, the structural distortions induced here are further illustrated by an increase in the atomic displacement parameters observed.

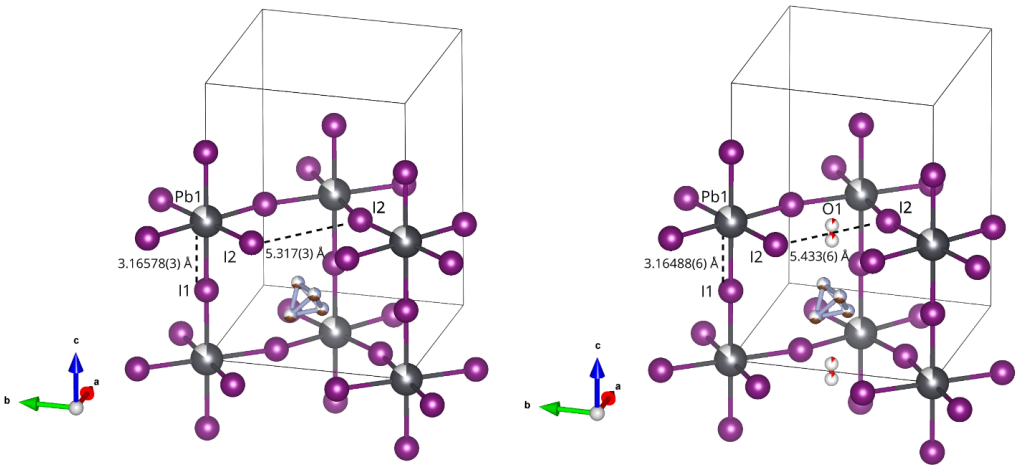

(a) (b)

Fig. 4.10 Structure of (a) SS-$MAPbI_3$ and (b) comparing Pb1-I1 and I2-I2 bond lengths derived from Rietveld refinement of synchrotron powder diffraction data at 300 K. Lead is shown in grey, iodine in purple and carbon/nitrogen in blue/brown.

When annealed in air it is proposed that, an oxygen partial pressure higher than under ambient conditions results in increased oxygen absorption. When annealed at 200 °C the level of oxygen absorption is higher than the oxygen solubility level of the material and the compound rapidly degrades. For AA80-$MAPbI_3$, the annealing temperatures and time involved results in a level of oxygen absorption via interstitial sites, such that the perovskite structure remains in intact as no impurity phases (specifically PbI_2) are detected in the diffraction data.

At processing temperatures higher than those typically found in the literature (>200 °C, significant changes to the average structure of solution processed $MAPbI_3$ were observed when annealed under a vacuum at high temperature (200 °C, sample AV200-$MAPbI_3$). A significant reduction in the tetragonal to cubic phase transition temperature was found to coincide with a reduction in the tilt angle of the PbI_6 perovskite framework. The explanation for the structural changes induced in AV200-

$MAPbI_3$ are less apparent from these measurements. This provided the motivation for the set of experiments outlined in the next section.

4.3 Variable Temperature Vacuum Annealing

The results of section 4.2 demonstrated subtle changes to the ambient temperature structure of prototypical $MAPbI_3$ induced through low temperature annealing when subject to both vacuum and air environments. In air, the observed changes are attributed to the insertion of oxygen into the perovskite structure through interstitial sites, without significant degradation of the compound. Under a vacuum, when annealing at higher temperatures (200 °C) the material remained intact with significant changes to the tilting of the PbI_6 octahedral framework observed alongside a large reduction in the transition temperature from tetragonal (phase II) to cubic (phase I) were observed as shown in Figure 4.5. However, an understanding of the cause for these changes was not established. This provided the motivation for the work described in the remainder of this chapter. For these experiments much higher vacuum annealing temperatures (from 280 °C to 320 °C) and shorter annealing durations were explored for $MAPbI_3$. For which, these samples were synthesised by Rhianna Day, University of Kent.

4.3.1 High Temperature Vacuum Annealing Synthesis

In order to investigate the changes observed in prototypical $MAPbI_3$ through high temperature vacuum annealing a sample of prototypical $MAPbI_3$ was synthesised according to the low temperature solution based method outlined in Section 2.6.1. The sample was then split into eight parts of equal weight and placed into quartz tubes, the tubes were evacuated to a pressure below 10^{-4} torr and sealed. Each tube was then placed at the centre of a tube furnace and annealed for 1 hour 30 minutes at temperatures between 280 °C and 320 °C, each sample is given a unique ID according to the temperature at which it was annealed, an outline for each sample synthesised is given in Table 4.6. The samples were then removed from the oven, the tubes were broken and the samples were removed and washed with acetone under a vacuum filter.

4.3.2 Powder X-ray Diffraction Study

Initial characterisation of the samples described in Table 4.6 was carried out through powder X-ray diffraction. Measurements were performed using the Panalytical

Sample ID	Annealing Condition	Annealing Temperature (C)	Annealing Time (Minutes)
AV280-$MAPbI_3$	Vacuum	280	90
AV285-$MAPbI_3$	Vacuum	285	90
AV290-$MAPbI_3$	Vacuum	290	90
AV295-$MAPbI_3$	Vacuum	295	90
AV300-$MAPbI_3$	Vacuum	300	90
AV305-$MAPbI_3$	Vacuum	305	90
AV310-$MAPbI_3$	Vacuum	310	90
AV315-$MAPbI_3$	Vacuum	315	90

Table 4.6 Post synthesis vacuum annealing conditions undertaken for a range of samples identified by a unique ID that specifies the annealing temperature and annealing time.

X'pert diffractometer at room temperature with an applied current and voltage of 40 mA and 45 kV respectively. Each sample was placed on a zero background silicon wafer and a 2θ range of 5° to 80° was scanned with a step size of 0.001^o. The measurement was carried with a dual source beam (Cu-$K_{\alpha 1}$ and Cu-$K_{\alpha 2}$) with an incident wavelength ratio of Cu-$K_{\alpha 1}$/Cu-$K_{\alpha 2}$ = 0.5. Structural characterisation of the data was then carried out through Rietveld refinement with the FullProf software suite.

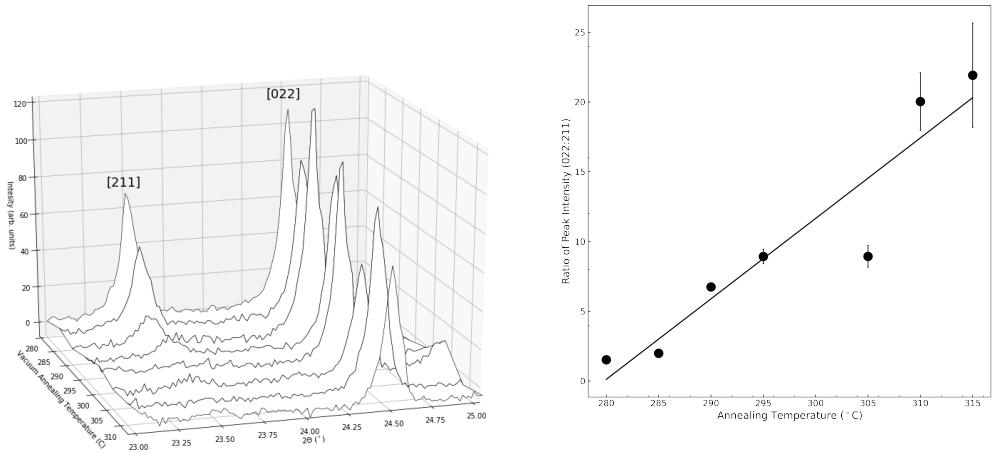

(a) (b)

Fig. 4.11 (a) Powder X-ray diffraction spectra measured for $MAPbI_3$ samples annealed under a vacuum at different temperatures for 1 hour 30 minutes. The tetragonal phase reflections (211)/(121) and (022) are labelled for reference, (b) the ratio of the intensity of these two peaks as a function of annealing temperature calculated through peak profile fitting.

Each pattern has been indexed with a tetragonal crystal system with unit cell dimensions approximately $a = b \approx 8.8$ Å and $c = 12.6$ Å, this is consistent with previous room temperature structural studies conducted on prototypical $MAPbI_3$ (structural phase II). Figure 4.11a shows a specific region of each diffraction pattern for the samples described in Table 4.6. Here, two peaks are observed that correspond to the Bragg reflections [211] and [022]. As the vacuum annealing temperature is increased, the ratio of peak intensity 022:211 is seen to increase (Figure 4.11b). For the sample annealed at the lowest temperature (280°C, AV280-$MAPbI_3$), the relatively high observed intensity of the [211] reflection is indicative of the tetragonal structural phase II for prototypical $MAPbI_3$, this was later confirmed through Rietveld refinement as shown in Figure 4.15b. At 315 °C the complete suppression of the [211] reflection correlates with a reduction in the peak splitting of high angle reflections. As a result the diffraction pattern can be indexed with a simple cubic crystal type consistent with the structural phase I for prototypical $MAPbI_3$. However, the resolution of the measurement does not allow for a distinction to be made between the coexistence of both tetragonal and cubic phases or the gradual suppression of a tetragonal phase reflection. Therefore all patterns were refined with a tetragonal structural model.

Structural characterisation of each diffraction pattern shown in Figure 4.13 and Figure 4.15 was carried out through sequential Rietveld refinement for each sample outlined in Table 4.6. The sequential refinement started with a refinement of the diffraction pattern corresponding to the sample AV280-$MAPbI_3$. Here, a starting structural model was obtained from previous single crystal X-ray diffraction studies carried out for prototypical $MAPbI_3$ (Section 4.2.2). The structure is described by a tetragonal crystal system and assigned the space group *I4/m*. The details of the refined structural model for the sample AV280-$MAPbI_3$ is described in Table 4.8. The diffraction pattern for each subsequent sample was refined sequentially in order of increasing annealing temperature, the starting model for each refinement is taken from the refined model of the previous refinement. For the sample annealed at higher temperatures a growing impurity phase was found, this was indexed as PbI_2. For each diffraction pattern an overall isothermal parameter was refined, with individual atomic positions, occupancy and thermal parameters fixed excluding the position of the I2 site that was refined for each pattern.

The ambient temperature tetragonal phase refined for each of the samples described in Table 4.6 is described by a perovskite structure comprised of a series of corner sharing PbI_6 octahedral that exhibit a single out of phase tilt about the crystallographic c-axis, Glazer notation $a^0a^0c^-$. In terms of the structural model, this tilt is represented by

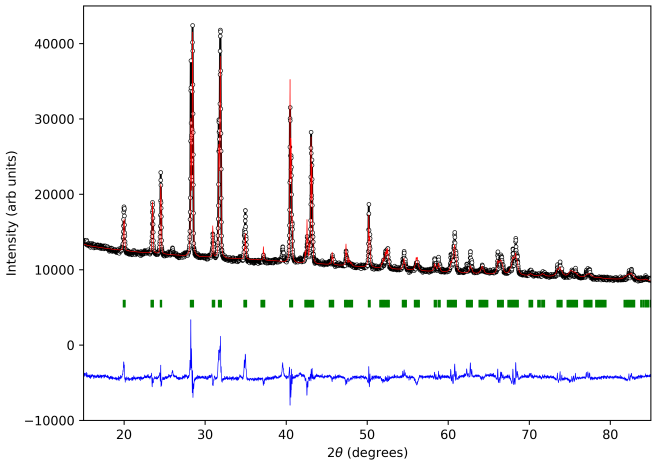

(a)

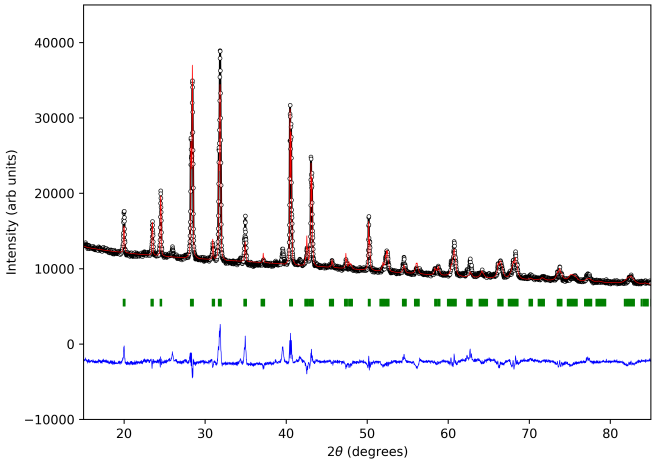

(b)

Fig. 4.12 Observed (circles) and calculated (solid lines) X-ray powder diffraction profile from Rietveld refinement for the samples (a) AV280-$MAPbI_3$ R_p = 2.31 % and R_{wp} = 3.62 % and (b) AV285-$MAPbI_3$ R_p = 2.32 % and R_{wp} = 3.48 % performed at room temperature. Vertical bars (green) represent the Bragg reflections and the bottom curve (blue) represents the difference between observed and calculated patterns.

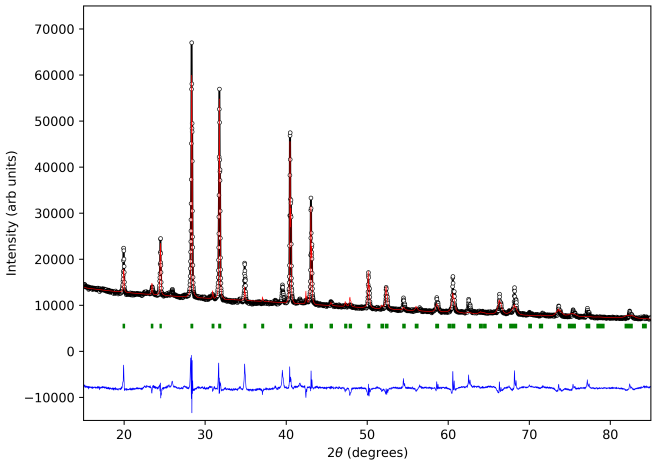

(a)

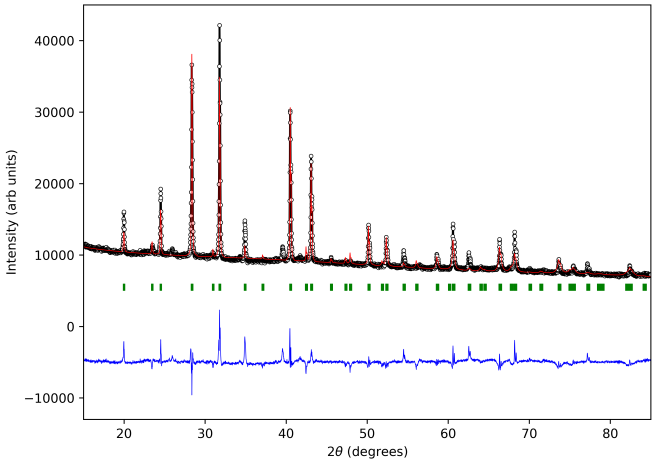

(b)

Fig. 4.13 Observed (circles) and calculated (solid lines) X-ray powder diffraction profile from Rietveld refinement for the samples (a) AV290-$MAPbI_3$ R_p = 3.09 % and R_{wp} = 4.95 % and (b) AV295-$MAPbI_3$ R_p = 2.59 % and R_{wp} = 4.12 % performed at room temperature. Vertical bars (green) represent the Bragg reflections and the bottom curve (blue) represents the difference between observed and calculated patterns.

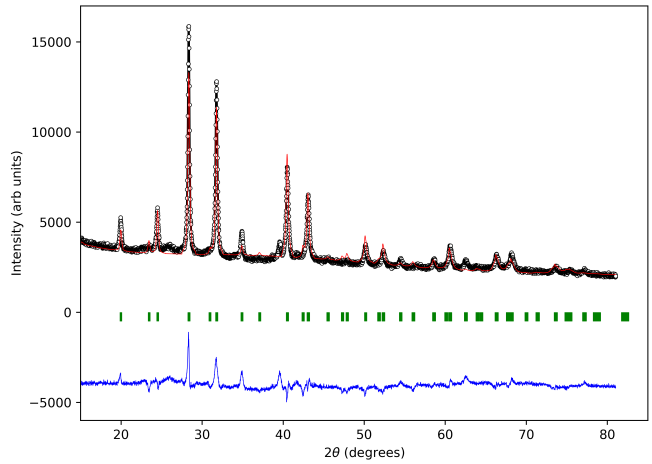

(a)

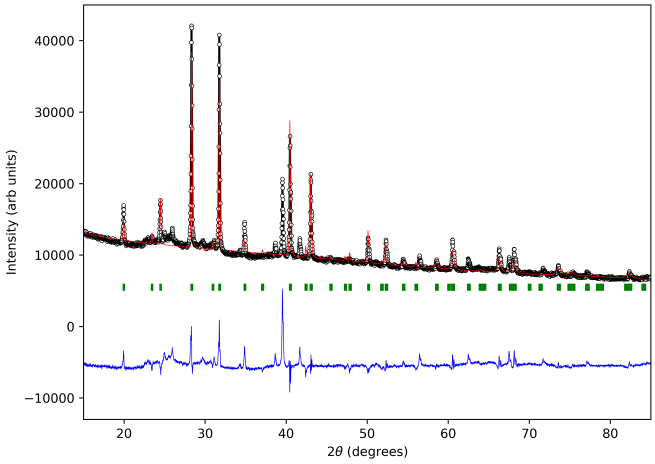

(b)

Fig. 4.14 Observed (circles) and calculated (solid lines) X-ray powder diffraction profile from Rietveld refinement for the samples (a) AV300-$MAPbI_3$ R_p = 5.26 % and R_{wp} = 6.76 % and (b) AV305-$MAPbI_3$ R_p = 3.60 % and R_{wp} = 5.75 % performed at room temperature. Vertical bars (green) represent the Bragg reflections and the bottom curve (blue) represents the difference between observed and calculated patterns.

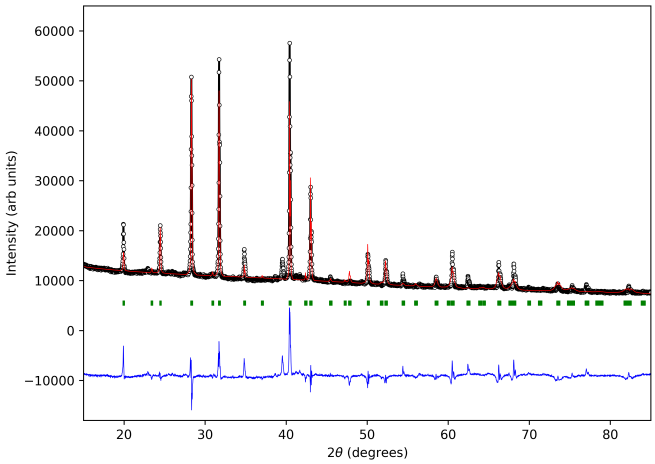

(a)

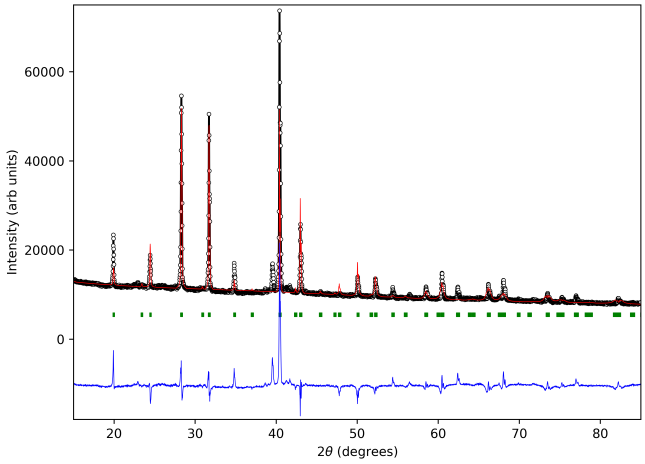

(b)

Fig. 4.15 Observed (circles) and calculated (solid lines) X-ray powder diffraction profile from Rietveld refinement for the samples (a) AV310-$MAPbI_3$ R_p = 3.40 % and R_{wp} = 5.80 % and (b) AV315-$MAPbI_3$ R_p = 3.94 % and R_{wp} = 7.58 % performed at room temperature. Vertical bars (green) represent the Bragg reflections and the bottom curve (blue) represents the difference between observed and calculated patterns.

AV280-$MAPbI_3$ - Powder X-ray Diffraction Atomic Coordinates				
Atom	x	y	z	Occupancy
Pb1	0.00	0.00	0.00	1.00
Pb2	0.00	0.00	0.50	1.00
I1	0.00	0.00	0.25	1.00
I2	0.2144(3)	0.2856(3)	0.50	1.00
N1/C1	0.55828	-0.0630	0.29260	0.25

Table 4.7 Crystallographic parameters obtained from Rietveld Refinement of powder X-ray diffraction measurements of AV280-$MAPbI_3$ measured at room temperature. Cell parameters were refined to be $a = b = 8.8848(4)$ Å and $c = 12.6577(5)$ Å with a volume of 999.21(7) $Å^3$.

AV315-$MAPbI_3$ - Powder X-ray Diffraction Atomic Coordinates				
Atom	x	y	z	Occupancy
Pb1	0.00	0.00	0.00	1.00
Pb2	0.00	0.00	0.50	1.00
I1	0.00	0.00	0.25	1.00
I2	0.2378(14)	0.2622(14)	0.500	1.00
N1/C1	0.55828	-0.0630	0.29260	0.25

Table 4.8 Crystallographic parameters obtained from Rietveld Refinement of powder X-ray diffraction measurements of AV315-$MAPbI_3$ measured at room temperature. Cell parameters were refined to be $a = b = 8.9310(6)$ Å and $c = 12.6498(9)$ Å with a volume of 1008.98(14) $Å^3$.

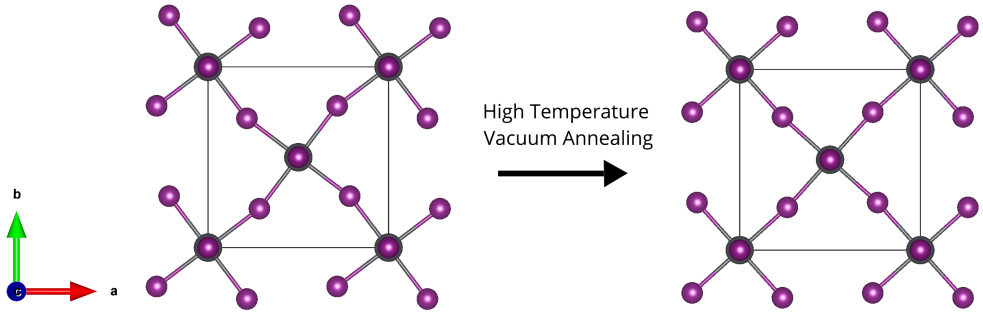

Fig. 4.16 The change in octahedral tilt of the PbI_6 perovskite framework for the samples AV280-$MAPbI_3$ (left image) and AV315-$MAPbI_3$ (right image) refined from powder X-ray diffraction data. Lead is shown in grey and iodine in purple.

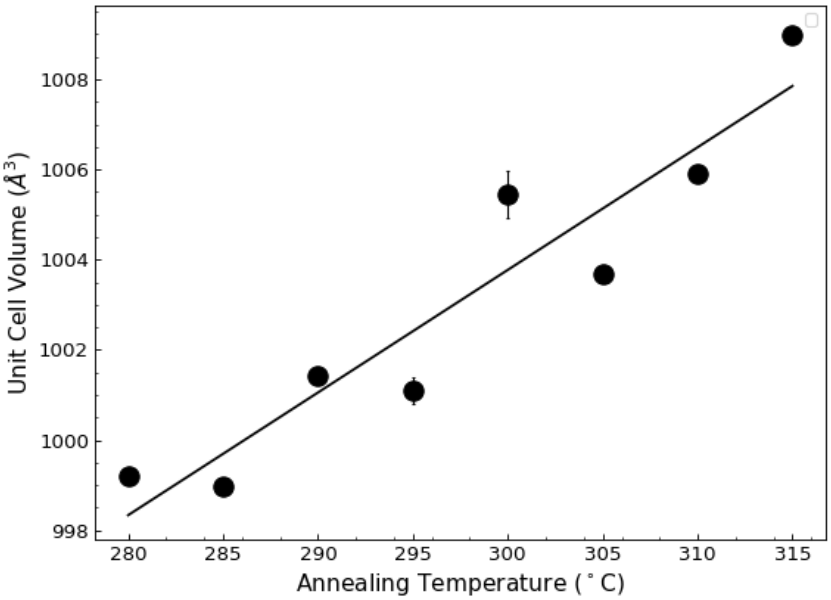

Fig. 4.17 Unit cell volume for the $MAPbI_3$ samples outlined in Table 4.6 derived from Rietveld refinement of powder X-ray diffraction measurements performed at room temperature.

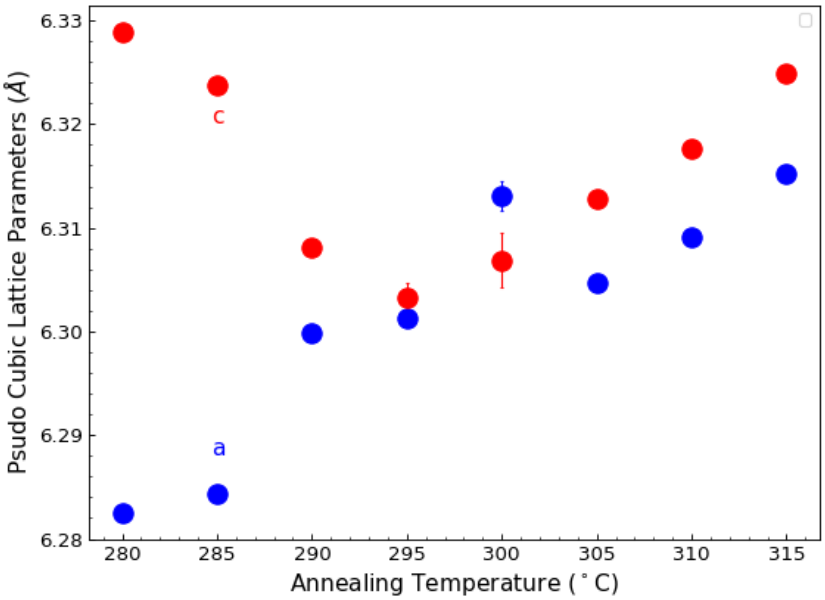

Fig. 4.18 Pseudo-cubic lattice parameters for the $MAPbI_3$ samples outlined in Table 4.6 derived from Rietveld refinement of powder X-ray diffraction measurements.

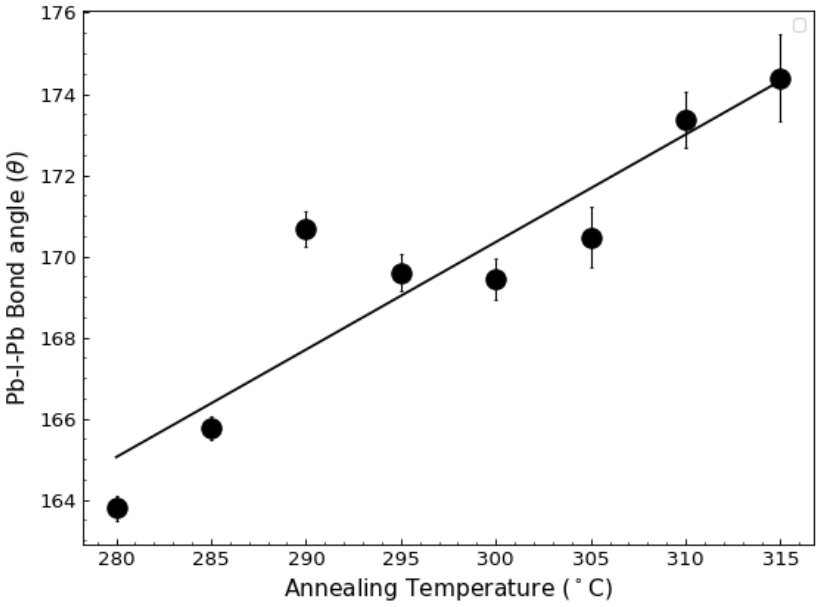

Fig. 4.19 Pb1-I2-Pb2 bond angle for the $MAPbI_3$ samples outlined in Table 4.6 derived from Rietveld refinement of powder X-ray diffraction measurements.

a single iodide atomic site (labelled I2) for which the bond angle Pb1-I2-Pb2 was calculated for each sample. As shown in Figure 4.19 the bond angle Pb1-I2-Pb2 was found to increase as a function of annealing temperature and corresponds to the gradual suppression of the PbI_6 octahedral tilting as illustrated in Figure 4.16. Figure 4.17 shows that this is correlated with an observed linear increase in the unit cell volume, and Figure 4.18 shows a convergence of lattice parameters *a* and *c* at 295 °C.

These results demonstrate consistent changes to the observed octahedral tilting and unit cell volume measured at ambient temperature for prototypical $MAPbI_3$ that are dependent on vacuum annealing temperature.

4.3.3 Single Crystal X-ray Diffraction Study

From the powder X-ray diffraction measurements described in Section 4.3.2, a detailed understanding of the changes induced in the average structure of prototypical $MAPbI_3$ were not possible due to inherent limitations of the powder diffraction technique and equipment used. For this purpose, single crystal X-ray diffraction measurements were carried out on samples annealed at temperatures between 280 °C and 310 °C under vacuum conditions (outlined in Table 4.9).

Measurements were carried out with a Rigaku Oxford Diffraction dual source Supernova diffractometer. Each crystal was mounted onto a cryoloop using perfluorinated oil. A nitrogen stream maintained an experimental temperature of 270 K. Both data collection and data reduction were carried out with CrysAlisPro. An absorption correction was applied using a multifaced crystal model with Gaussian integration and standard empirical spherical harmonics absorption.

Initial measurements were conducted on the sample AV300-$MAPbI_3$ with both Cu and Mo incident radiation at 290 K. This yielded two different solutions for the structure of AV300-$MAPbI_3$, a cubic and tetragonal crystal system respectively. The results of these measurements are discussed further in the Appendix A.5. It was determined that future measurements were to be carried out using Mo-K_α incident radiation (λ = 0.71069 Å).

The diffraction data for each sample was indexed with a tetragonal crystal system and lattice parameters as defined in Table 4.9. During data reduction, Friedel mates were merged and the peaks were indexed with a 4/m Laue class filter. Automatic peak indexing routines performed by the CrysAlisPro software package found no significant I centring systematic absence violations for all crystals measured and therefore I centring was chosen.

For each measurement the reflection [103] was observed, thereby violating the c-glide plane and ruling out the space group *I4/mcm*, the space group most often reported for prototypical $MAPbI_3$ [103, 104, 47]. Despite this, initial structural refinement was carried out with *I4/mcm*. Here, no reasonable carbon or nitrogen atomic sites could be refined even with the inclusion of additional twin components required to account for the observation of the [103] reflection as reflections [211] and [121] in the second twin component. Therefore structural refinement of each sample was carried out with the space group *I4/m*.

Initial structure determination was carried using the software program SHELXS. Structure refinement was carried for each data set with the software SHELXL.

The structure determination process began with the fitting of atomic sites that describe the PbI_6 framework as these contribute most to Bragg scattering. For each compound described in Table 4.9 the framework is described by two distinct lead atomic sites (Pb1 and Pb2) and two iodide sites (I1 and I2). The resulting framework exhibits out of phase tilting of the PbI_6 octahedral about the crystallographic c-axis (Glazer notation $a^0a^0c^-$).

Sample ID	a (Å)	b (Å)	c (Å)	Volume (Å^3)
SS-$MAPbI_3$	8.8432(3)	8.8432(3)	12.6735(7)	991.10(9)
AV280-$MAPbI_3$	8.8633(8)	8.8633(8)	12.620(2)	991.4(2)
AV285-$MAPbI_3$	8.8752(5)	8.8752(5)	12.6377(10)	995.45(14)
AV295-$MAPbI_3$	8.9043(9)	8.9043(9)	12.615(2)	1000.2(3)
AV300-$MAPbI_3$	8.8997(3)	8.8997(3)	12.5817(6)	996.53(8)
AV305-$MAPbI_3$	8.8944(6)	8.8944(6)	12.5818(15)	995.36(18)
AV310-$MAPbI_3$	8.8934(7)	8.8934(7)	12.584(4)	995.4(3)

Table 4.9 Refined lattice parameters and space group for a range of $MAPbI_3$ samples outlined in Table 4.9 derived from single crystal X-ray diffraction measurements performed at 270 K.

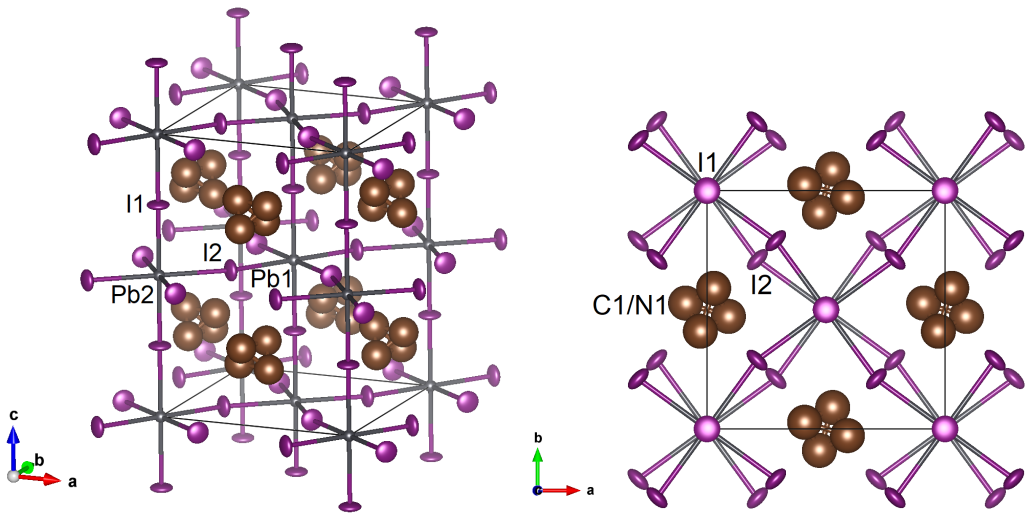

(a) (b)

Fig. 4.20 Structural model obtained for the sample AV290-$MAPbI_3$ from refinement of single crystal X-ray diffraction measurements conducted at 270 K. The label for each atomic site in the structural model is shown. Lead is shown in grey, iodine in purple and carbon/nitrogen in brown.

Initial fit factors for the structural refinement of each sample were slightly higher than expected. As such the program ROTAX was used to identify possible twin laws for each sample. The fit for each sample was found to be significantly improved with the inclusion of an additional twin component. This is likely a result of the vacuum thermal treatment, the temperature at which this was carried out is higher than the tetragonal-cubic structural phase transition temperature. As the temperature is reduced back to ambient following the treatment, the compounds undergo a cubic to tetragonal phase transition defined, in terms of the unit cell, by a relaxation of the constraints on the lattice parameters, where the c-axis is now independent of the a- and b-axis. Hence as the transition occurs there are three equivalent possibilities for which axis becomes the independent c-axis in the single crystals, resulting in a high probability of twinning domains.

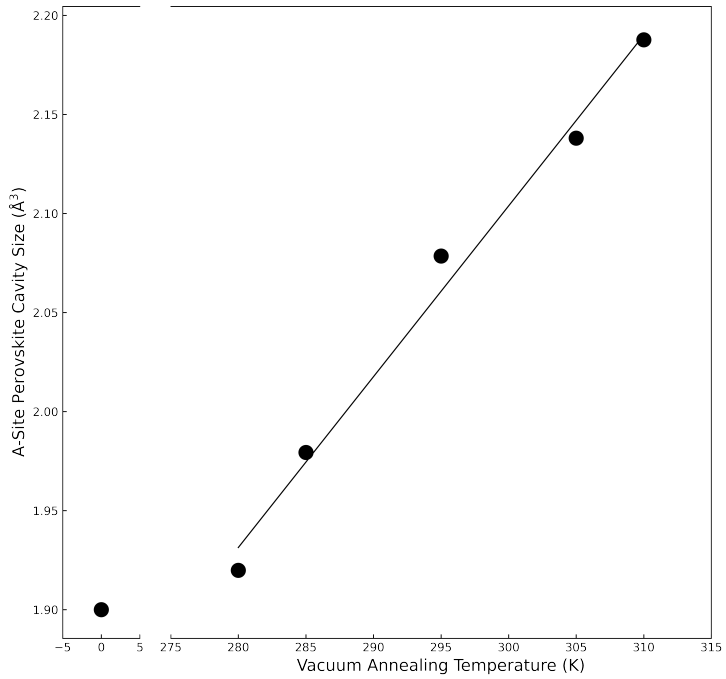

Fig. 4.21 A-site perovskite cavity size for a number of $MAPbI_3$ samples annealed under a vacuum at high temperature. The cavity is calculated using Shannon ionic radii of elements Pb and I of 1.19 Å and 2.2 Å respectively.

In determining an average structure model for the MA^+ cation, the samples annealed at higher temperature were found to exhibit considerably more disorder in the scattering density for those areas of the unit cell associated with the MA^+ cation

located at the centre cavity of the perovskite framework. This is highlighted in Figure 4.22 where the calculated Fourier difference maps are shown for the samples prototypical $MAPbI_3$, AV290-$MAPbI_3$ and AV305-$MAPbI_3$, these are calculated from a refinement of the PbI_6 framework alone. This shows a gradual reduction in areas of scattering associated with localised atomic sites for both the carbon and nitrogen of the MA^+ cation. For prototypical $MAPbI_3$ the density shows four distinct arms that point towards the iodide site I2 of the framework. For AV305-$MAPbI_3$ the density is found to be significantly more uniform in shape and indicates significantly more orientational disorder of the MA^+ cation. Initially, unrestrained refinement of the sites C1 and N1 were carried out. The resulting position and refined anisotropic thermal parameters were unstable, such that the observed scattering could not be sufficiently modelled by a single carbon and nitrogen site. This aligns with the scattering density shown in Figure 4.22. Therefore the position of sites C1 and N1 were refined for the sample AV280-$MAPbI_3$ and then fixed for the refinement of samples annealed at higher temperature where changes to the average structure of the PbI_6 framework were determined. For AV280-$MAPbI_3$, the resulting MA^+ cation was found to sit at the centre of the perovskite void and is described by a single atomic site shared by both carbon and nitrogen atoms (C1 and N1) as shown in Figure A.5. For the purpose of determining detailed changes to the average structure of the MA^+ cation when annealing prototypical $MAPbI_3$ at high temperatures under a vacuum, powder neutron diffraction measurements were implemented and are discussed in detail in Section 4.3.4.

The PbI_6 octahedra for each sample is tilted about the c-direction within the ab-plane. This is expressed through a deviation from 180° for the Pb1-I2-Pb2 bond angle. As shown in Figure 4.23a, a consistent linear increase in the Pb1-I2-Pb1 bond angle is observed as the vacuum annealing temperature is increased. This represents a suppression in the tilt of the octahedra along the ab-plane and is correlated with a shortening of both Pb-I bond lengths Pb-I1 and Pb-I2 as shown in Figure 4.23b over the same annealing temperature range. This implies stronger bonding between lead and iodide framework constituents and indicates a reduction in the hydrogen interactions between the MA^+ cation and PbI_6 framework. An increase in perovskite cavity size is observed as a function of increased vacuum annealing temperature as shown in Figure 4.21. An increase in the atomic displacement parameters is observed for both iodide atomic sites I1 and I2 as shown in Figure 4.24a and Figure 4.24b respectively. The increase in thermal motion is most significant perpendicular to the Pb-Pb direction corresponding to the parameters U_{22} and U_{11} for the sites I1 and I2

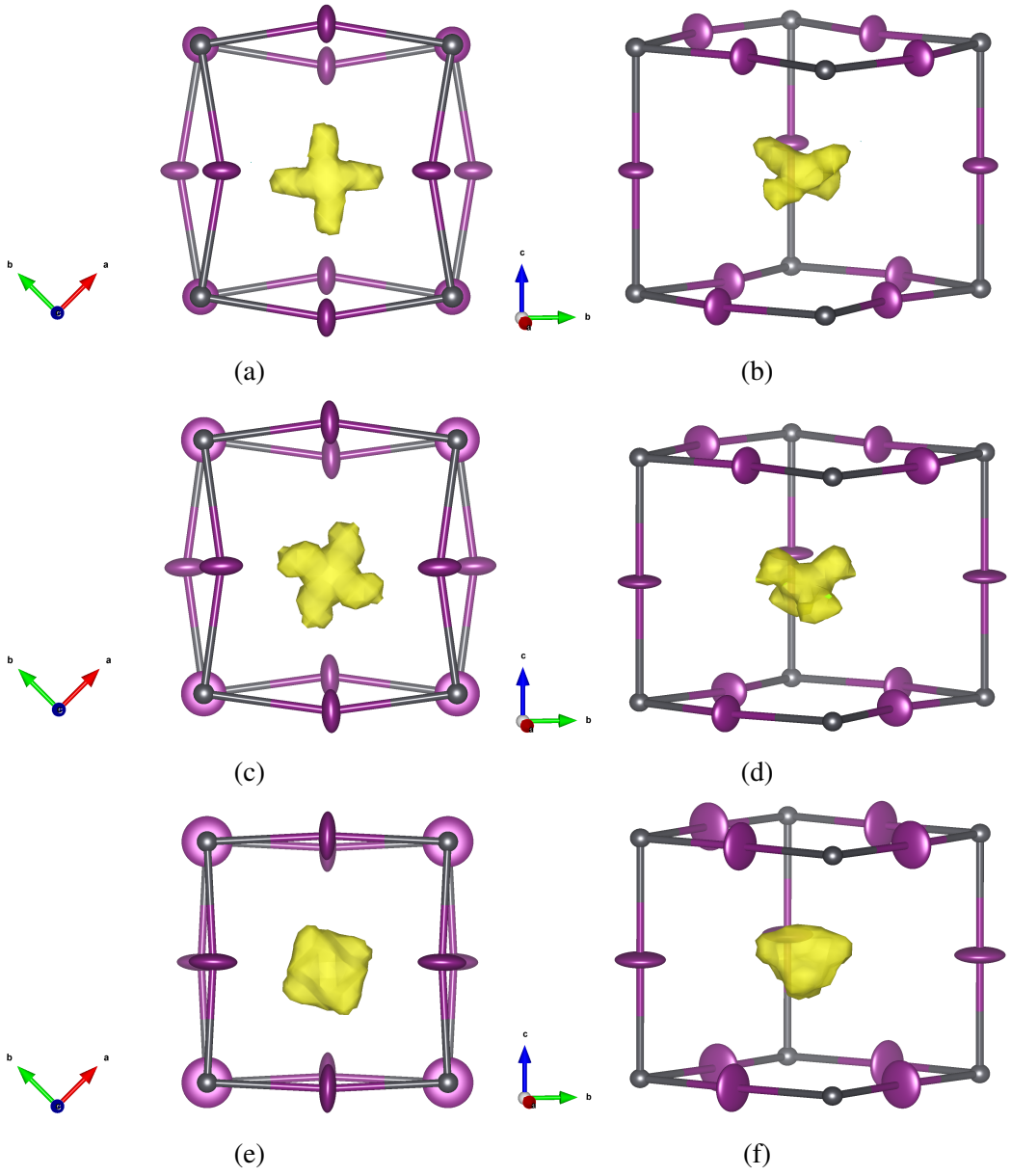

Fig. 4.22 Fourier difference maps for the samples (a) and (b) prototypical $MAPbI_3$, (c) and (d) AV290-$MAPbI_3$ and (e) and (f) AV305-$MAPbI_3$ highlighting the residual density associated with the MA^+ cation overlaid onto a model of the surrounding PbI_6 framework. Lead is shown in grey and iodine in purple.

respectively. This represents an increase in the disorder of the octahedra along the direction of the perovskite tilt as a function of vacuum annealing temperature.

The nature of the octahedral tilting exhibited by hybrid perovskites such as $MAPbI_3$, is driven by a mismatch in the cation/anion size and weak iodide hydrogen bonding. The observed reduction in both octahedral tilting, shorter Pb-I bond lengths and increased unit cell volume implies a change to the $NH_3 \cdots I$ interactions. Following this, it would be expected that the MA^+ cation exhibits increased statistical disorder over multiple orientations with a reduction in both the short and long range correlations observed in the orientation of this linear cation compared with prototypical $MAPbI_3$. In determining the average structure of these systems, scattering density obtained from Fourier difference calculations showed a reduction in areas of localised scattering associated with carbon and nitrogen compared with prototypical $MAPbI_3$, as shown in Figure 4.22. This indicates increased orientational disorder of the MA^+ cation that is coupled with the changes observed in the PbI_6 framework. For the samples where carbon and nitrogen positions were refined, prototypical $MAPbI_3$ and AV280-$MAPbI_3$, a reduction in the observed C-N bond length and an increase in the C1/N1 thermal parameters were observed for AV285-$MAPbI_3$ while the N-I bond length remains consistent within the error of the measurement as shown in Figure 4.25.

The consistency for which the observed structural changes observed here as a function of annealing temperature is significant. The results suggest that the degree of tilting for the perovskite octahedra and respective Pb-I bond length can be precisely dictated by the vacuum annealing temperature at which the sample is processed. Approaching complete suppression of the octahedra tilt and reduction of the Pb-I2 bond length as the annealing temperature is increased and coincides with a linear increase in unit cell volume derived from the results in Section 4.3.2 whilst the material remains intact.

The mechanism for many of the optical properties of hybrid perovskites is dependent on the nature of the interactions between the constituent components of the perovskite framework. The methods described here demonstrate a simple method for tuning the principal features of the perovskite structure, the bonding and tilting of the PbI_6 framework, through high temperature vacuum annealing.

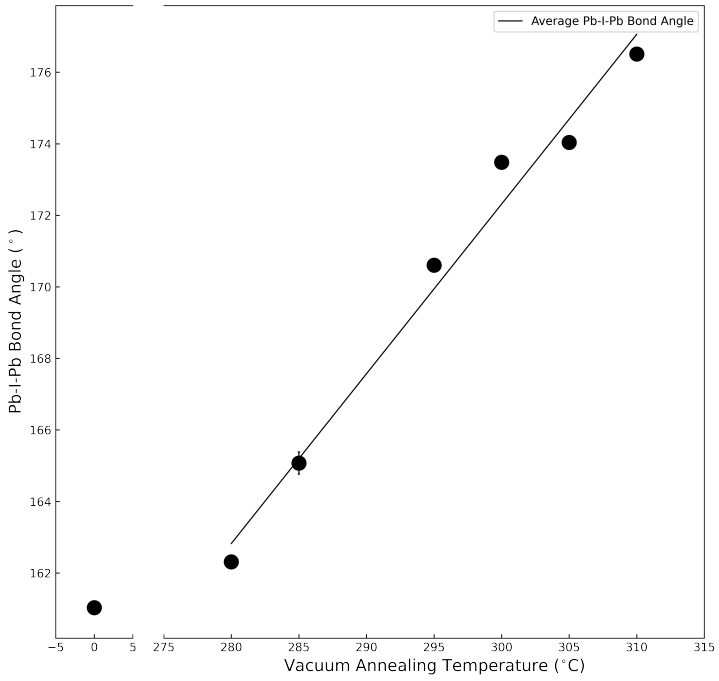

(a)

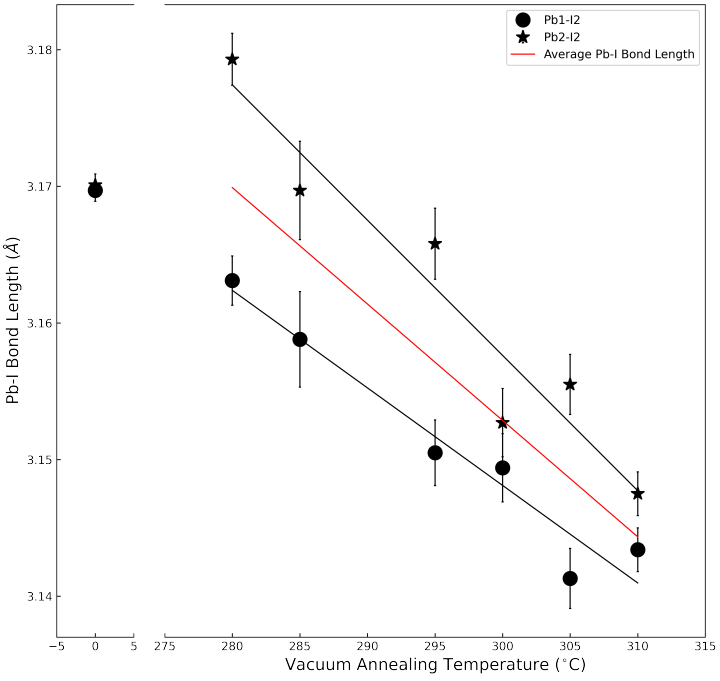

(b)

Fig. 4.23 (a) Pb-I-Pb bond angles and (b) Pb-I bond lengths for a range of $MAPbI_3$ samples annealed under a vacuum at different temperatures.

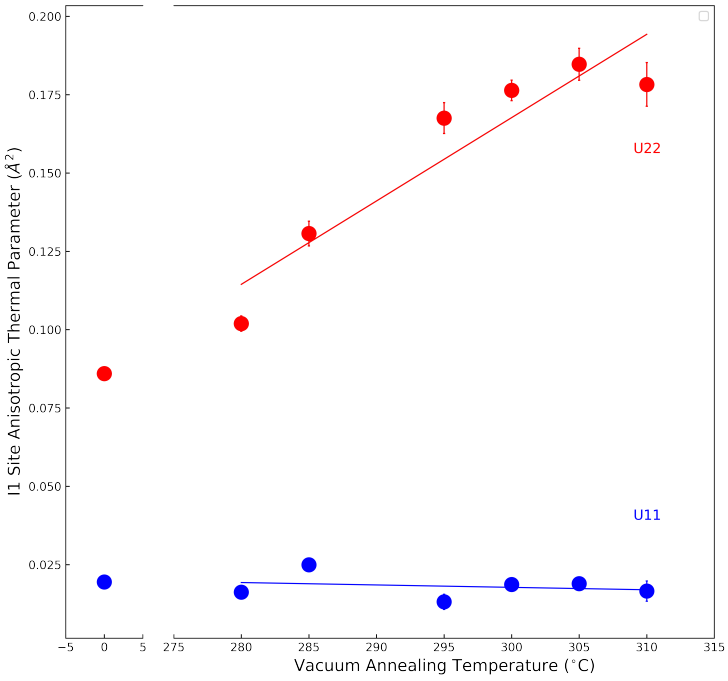

(a)

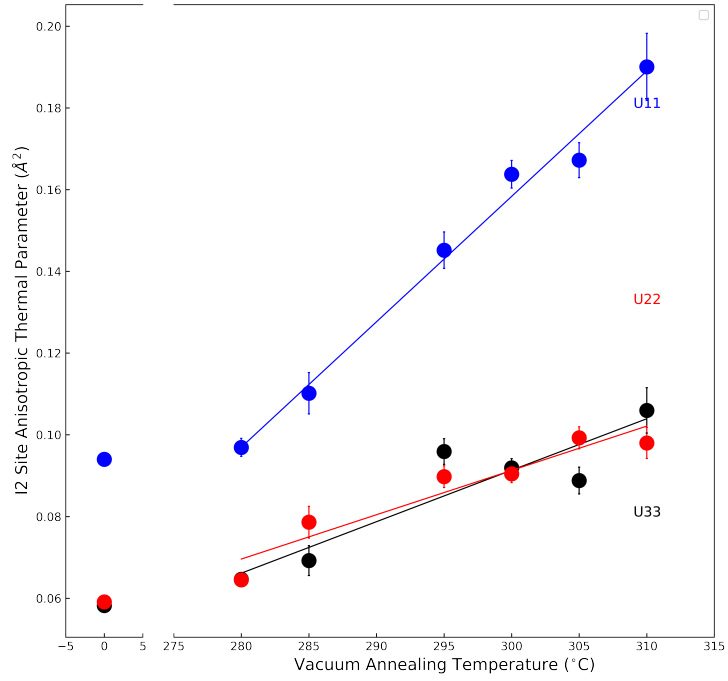

(b)

Fig. 4.24 Anisotropic displacement parameters for sites (a) I1 and (b) I2 for a range of $MAPbI_3$ samples annealed under a vacuum at different temperatures.

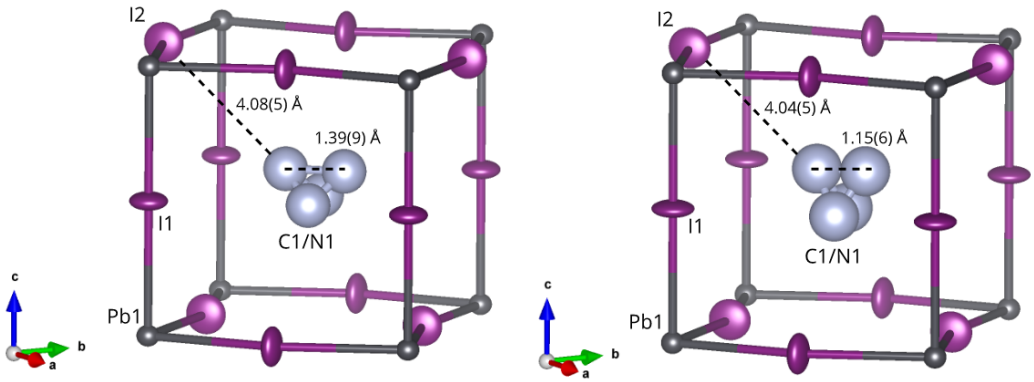

(a) (b)

Fig. 4.25 A comparison of (a) prototypical $MAPbI_3$ and (b) AV280-$MAPbI_3$ MA^+ coordination at 270 K. Lead is shown in grey, iodine in purple and carbon/nitrogen in blue.

4.3.4 Neutron Powder Diffraction Study

The results outlined in section 4.3 describe the synthesis and characterisation of a range of compounds derived from $MAPbI_3$ that have undergone a high temperature vacuum annealing process. Here, a characteristic range of structural features are found to be annealing temperature dependent, for solid state materials this is a particularly interesting result. However, the measurements described in section 4.3 were not sufficient to determine an average structure model for the MA^+ cation after undergoing this post synthesis vacuum annealing process. For the purposes of clarity reference to $MAPbI_3$ samples that have not undergone thermal vacuum treatment are refereed to as prototypical $MAPbI_3$. Characterisation of one of the high temperature vacuum annealing compounds, AV285-$MAPbI_3$, was carried out and compared against prototypical $MAPbI_3$ through variable temperature time of flight (TOF) neutron powder diffraction measurements, the synthesis for which is described in Section 4.3.1. The compound AV285-$MAPbI_3$ was chosen for these measurements as it minimised the presence of the impurity phase PbI_2 found for those samples annealed at higher temperature.

The measurements were performed on the POWGEN diffractometer located at the Spallation Neutron Source (SNS) of Oak Ridge National Laboratory (ORNL). Measurement were carried out at temperatures 160 K and 300 K. For $MAPbI_3$, this temperature range covers both low temperature orthorhombic (phase III) and ambient temperature tetragonal (phase II) structural phases. The transition temperature for this is approximately 160 K. Structure determination was carried out for the data recorded at 300 K through a maximum entropy method (MEM) based pattern fitting using the software packages Rietan-FP and Dysnomia. Rietveld refinement of the data measured at 160 K was carried out using the FullProf software package. The extensive incoherent hydrogen scattering contributions and resulting high signal to noise ratio limits the 2θ range of observed Bragg reflections for these measurements. Despite this, reasonable data quality allowed for structure determination to be carried out on the fully hydrogenous sample including refinement of hydrogen positions.

Orthorhombic Structure Determination - 160 K

For the data measured at 160 K, a starting model for the orthorhombic phase III described by the space group *Pnma* was adapted from structural characterisation work carried out by Weller *et al*. [47]. This was found to successfully index all peaks for both prototypical $MAPbI_3$ and AV285-$MAPbI_3$ samples. The starting model used to refine both data sets was identical, the PbI_6 framework is described by a

single lead atom (Pb1) for which the position and occupancy were fixed, and two distinct iodide sites (I1 and I2) where both the occupancy and positions were refined. The MA^+ cation is described by two distinct carbon (C1) and nitrogen (N1) atoms, the hydrogen positions are modelled by 4 distinct hydrogen sites (H1, H2, H3 and H4). The position and occupancy of the atoms that comprise the MA^+ were refined, where the individual occupancy of each atom were restricted to be equivalent giving an overall occupancy of the site. The refined atomic structure parameters for both prototypical $MAPbI_3$ and AV285-$MAPbI_3$ are given in Table 4.14 and Table 4.11 respectively.

prototypical $MAPbI_3$ - Powder Neutron Diffraction Atomic Coordinates at 160 K					
Atom	x	y	z	Occupancy	U_{iso} (Å^3)
Pb1	0.50	0.00	0.00	1.00	0.013(2)
I1	0.4956(18)	0.25	0.9479(12)	1.02(3)	0.031(5)
I2	0.1900(9)	0.0196(8)	0.1857(8)	1.004(19)	0.032(4)
C1	0.9216(19)	0.25	0.0578(20)	1.055(19)	0.04612
N1	0.9365(11)	0.75	0.0281(13)	1.054(19)	0.04540
H1	0.934(4)	0.25	0.182(4)	1.055(19)	0.117(4)
H2	0.879(2)	0.1762(18)	0.029(3)	1.055(10)	0.117(4)
H3	0.134(2)	0.2000(15)	0.006(3)	1.055(10)	0.117(4)
H4	0.944(4)	0.75	0.146(5)	1.054(19)	0.117(4)

Table 4.10 Refined structural parameters for prototypical $MAPbI_3$ derived from Rietveld refinement of neutron TOF powder diffraction data measured at 160 K. Lattice parameters a = 8.67(16) Å, b = 12.33(22) Å, c = 8.39(15) Å and a cell volume of 896.70(3) Å^3

Below 160 K the structure was found to retain the PbI_6 octahedral framework with tilts described by Glazer notation $a^-b^+a^-$, and the perovskite voids are populated by MA^+ cations. The refined position of the MA^+ cation for both samples were found to be fully ordered with C-N bonds that lie normal to the b-axis. The nature of the octahedral tilting for both samples was found to be equivalent with tilting about each crystallographic axis that is expressed by Pb-I-Pb bond angles. For prototypical $MAPbI_3$ and AV285-$MAPbI_3$ respectively, a tilt along the b-axis is described by the angle Pb1-I1-Pb1 = 163.8(4)° and 163.0(5)° respectively, the Pb1-I2-Pb1 bond angle of 150.8(3)° and 152.7(4)° results in a tilt about both a and c-axis for both samples respectively. The cell volume is found to be smaller for prototypical $MAPbI_3$ compared with AV285-$MAPbI_3$, this is consistent with the structure measured at high temperature and discussed in Section 4.3.3. As the positions of the lead sites were fixed, a large unit cell means larger Pb1-Pb1 bond lengths as shown in Table 4.12. The difference in Pb-I bond lengths Pb1-I1 and Pb1-I2 are also shown in Table

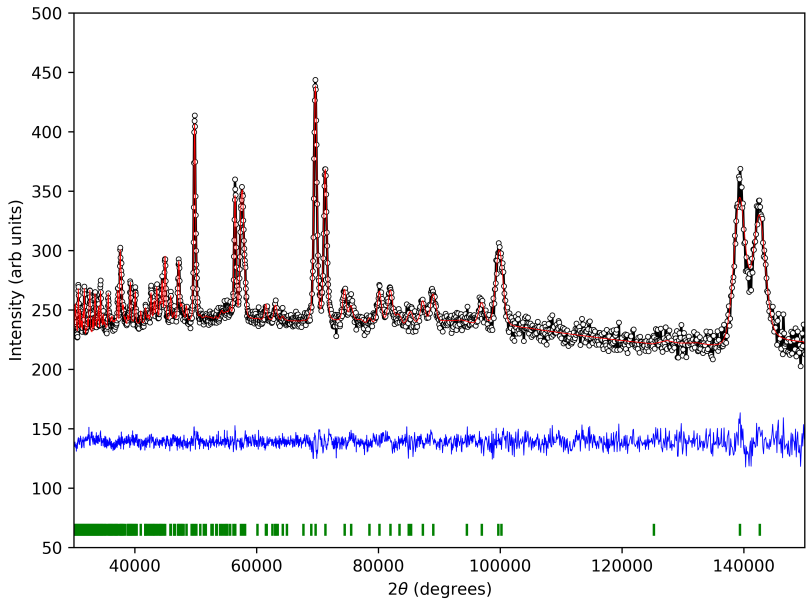

(a)

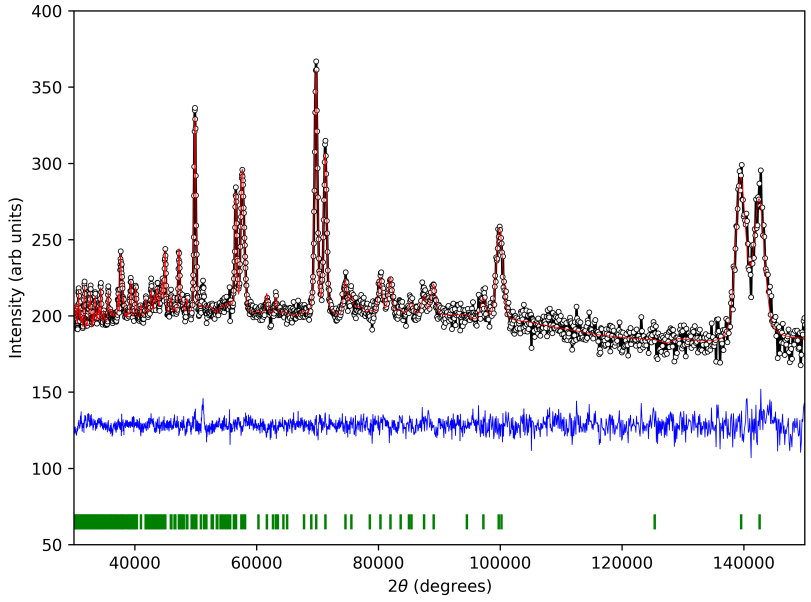

(b)

Fig. 4.26 Observed (circles) and calculated (solid lines) neutron powder diffraction profile from Rietveld refinement (structure outlined in Table 4.8) for the samples (a) prototypical $MAPbI_3$ R_p = 1.34 % and R_{wp} = 1.46 % and (b) AV280-$MAPbI_3$ R_p = 1.52 % and R_{wp} = 1.64 %, measured at 160 K. Vertical bars (green) represent the Bragg reflections and the bottom curve (blue) represents the difference between observed and calculated patterns.

AV285-$MAPbI_3$ - Powder Neutron Diffraction Atomic Coordinates at 160 K					
Atom	x	y	z	Occupancy	U_{iso} (Å^3)
Pb1	0.50	0.00	0.00	1.00	0.017(3)
I1	0.485(2)	0.25	0.9476(15)	0.99(3)	0.033(7)
I2	0.1933(11)	0.0170(13)	0.1902(10)	1.00(2)	0.042(5)
C1	0.919(2)	0.25	0.059(3)	0.90(4)	0.031(8)
N1	0.9404(17)	0.75	0.0233(16)	0.90(4)	0.033(7)
H1	0.894(4)	0.25	0.180(7)	0.90(4)	0.117(6)
H2	0.874(4)	0.174(3)	0.034(4)	0.901(18)	0.117(6)
H3	0.130(4)	0.199(2)	0.005(4)	0.901(18)	0.117(6)
H4	0.986(5)	0.75	0.178(5)	0.90(4)	0.117(6)

Table 4.11 Refined structural parameters for AV285-$MAPbI_3$ derived from Rietveld refinement of neutron TOF powder diffraction data measured at 160 K. Lattice parameters a = 8.683(20) Å, b = 12.36(3) Å, c = 8.426(18) Å and a cell volume of 904.005(4) Å^3

4.12, where the Pb1-I1 bond length for AV285-$MAPbI_3$ were found to be slightly larger.

Sample	Atom Label 1	Atom Label 2	Bond Length (Å)
prototypical $MAPbI_3$	Pb1	I1	3.1148(15)
prototypical $MAPbI_3$	Pb1	I2	3.115(8)
prototypical $MAPbI_3$	Pb1	Pb1	6.03060 & 6.16750 Å
AV280-$MAPbI_3$	Pb1	I1	3.123(2)
AV280-$MAPbI_3$	Pb1	I2	3.115(2)
AV280-$MAPbI_3$	Pb1	Pb1	6.04936 & 6.17855 Å

Table 4.12 Pb-I bond lengths for the samples prototypical $MAPbI_3$ and AV285-$MAPbI_3$ derived from Rietveld refinement at 160 K.

As well as a larger unit cell volume for AV285-$MAPbI_3$ a shift in the MA^+ position within the perovskite cavity was also observed, moving the -NH_3 end towards the centre face of the perovskite framework resulting in a shorter -NH_3-I bond length and a larger -CH_3-I bond length as shown in Figure 4.28. However, the primary difference observed between the two samples is a drop in the occupancy of the MA^+ cation, for which the occupancy is found to be 90±4% for AV285-$MAPbI_3$. This change in composition is significant in understanding the structural changes observed upon vacuum annealing. The octahedral tilting exhibited by $MAPbI_3$ is driven in part by weak hydrogen bonding, N-H$\cdots$I, between the iodide atoms that make up the PbI_6 framework and the MA^+ cation. Upon a small drop in the occupancy of the MA^+ site stronger bonding results between the components of PbI_6 framework,

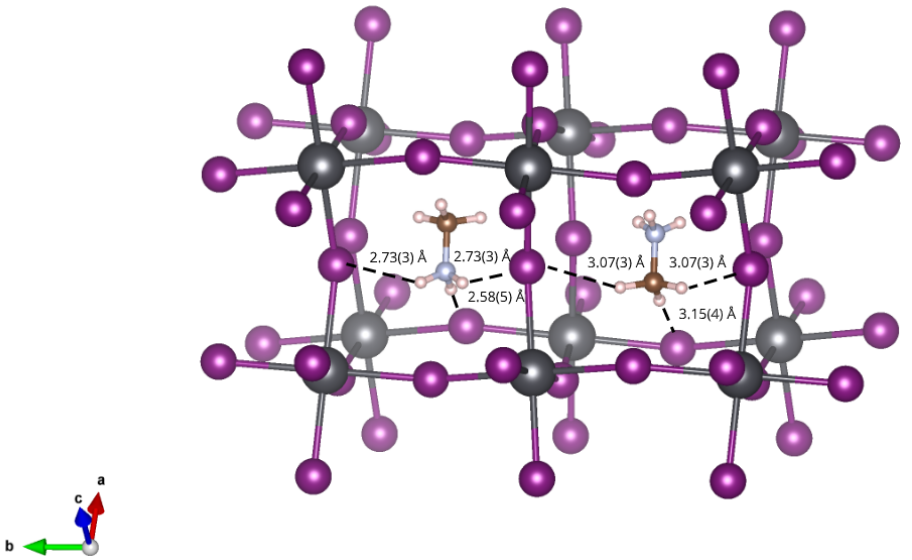

(a)

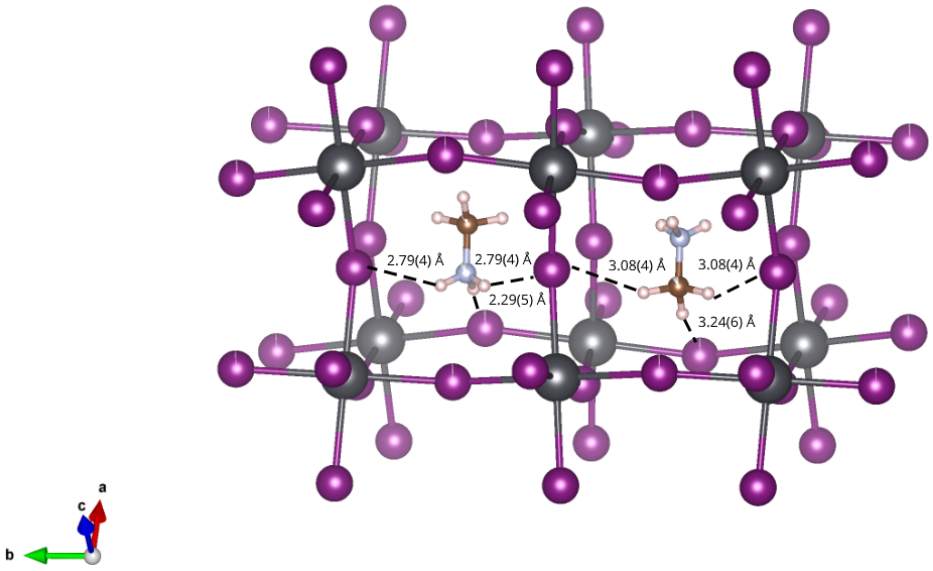

(b)

Fig. 4.27 Coordination of MA^+ cation for (a) prototypical $MAPbI_3$ and (b) AV285-$MAPbI_3$ at 160 K from Rietveld refinement of neutron powder diffraction. Lead spheres in grey, iodine spheres in purple, carbon and nitrogen in blue and hydrogen in pink.

this is observed at ambient temperature through a reduction in the Pb-I bond lengths, straighter Pb-I-Pb bond angles and an increase in the perovskite cavity size.

Tetragonal Structure Determination - 300 K

Section 4.3.3 demonstrates a consistent relationship between vacuum annealing temperature and changes to the tilting and disorder exhibited by the PbI_6 octahedral framework at ambient temperature. These changes are consistent with a change in orientational disorder of the MA^+ cation at 300 K. A small drop in the occupancy of the MA^+ cation site has been observed through Rietveld refinement of neutron powder diffraction data collected at 160 K.

The process of analysing the neutron diffraction data at 300 K started with a Rietveld refinement of the data for the prototypical $MAPbI_3$ sample using the structural model derived in Section 3.3.1 for the tetragonal ambient temperature structure. The structure for this phase is assigned the space group *I4/m*. A stable refinement and positive atomic displacement parameters for the refined structural model could not be achieved without applying constraints on almost all of the structural parameters. As such the symmetry of the model was increased and the data was refined in the space group *I4/mcm*, where the model was adapted accordingly. For this model a stable refinement was achieved with anisotropic displacement parameters for all model constituents with soft constraints applied to the C-N and C/N-H bond distances. Table 4.13 contains the final refined structure for this data. The successful convergence of the *I4/mcm* model is likely a result of the low number of peaks observed due to significant incoherent scattering contributions that results from the presence of hydrogen. Where the refinement of the lower symmetry *I4/m* model results in a high peak to refined parameters ratio.

The same starting model was used to refine the data measured at 300 K for the sample AV285-$MAPbI_3$. The model successfully converged, however the resulting anisotropic displacement parameters associated with carbon, nitrogen and hydrogen sites were non-physical. In order to observe subtle changes to the average structure of the MA^+ cation at 300 K, the maximum entropy method (MEM) was used to generate nuclear scattering density maps that are not biased towards any discrete atomic site modelling of the MA^+ cation or the symmetry of the space group used in Rietveld refinement. The MEM analysis was carried out for both prototypical $MAPbI_3$ and AV285-$MAPbI_3$ sample for comparison.

The process of performing MEM on both prototypical $MAPbI_3$ and AV285-$MAPbI_3$ is discussed concurrently. To begin, a Rietveld refinement of neutron powder diffrac-

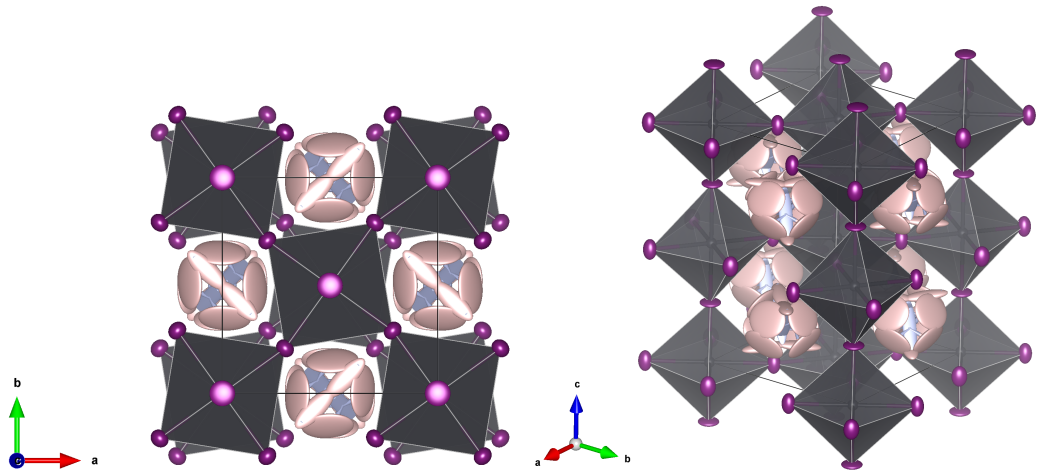

(a) (b)

Fig. 4.28 (a) and (b) the structure of prototypical $MAPbI_3$ at 300 K derived from Rietveld refinement of neutron powder diffraction. Lead spheres in grey, iodine spheres in purple, carbon in brown, nitrogen in blue and hydrogen in pink.

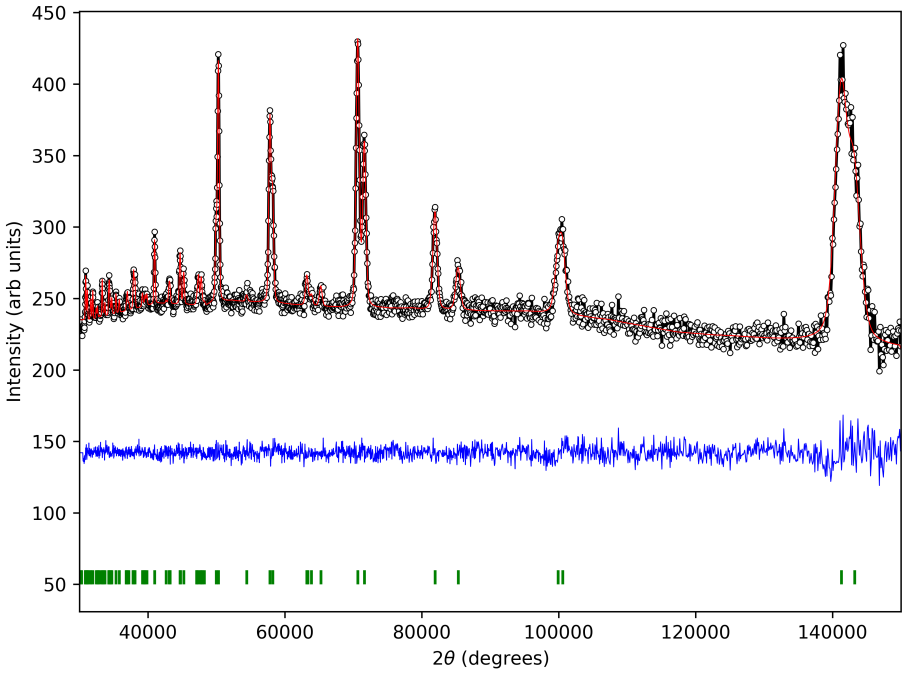

Fig. 4.29 Observed (circles) and calculated (solid lines) neutron powder diffraction profile from Rietveld refinement (structure outlined in Table 4.13) for the sample prototypical $MAPbI_3$ measured at 300 K. R_p = 1.28 % and R_{wp} = 1.36 %. Vertical bars (green) represent the Bragg reflections and the bottom curve (blue) represents the difference between observed and calculated patterns.

prototypical $MAPbI_3$ - Powder Neutron Diffraction Atomic Coordinates at 300 K					
Atom	x	y	z	Occupancy	U_{iso} (Å^3)
Pb1	0.50	0.50	0.50	1.00	0.032(3)
I2	0.2093(7)	0.2907(7)	0.50	1.00	0.078(6)
I1	0.50	0.50	0.75	1.00	0.085(8)
N1	0.05752(13)	0.44248(13)	0.230(3)	0.25000	0.32(5)
C1	0.05752(13)	0.44248(13)	0.230(3)	0.25000	0.32(5)
H1	0.150(2)	0.489(6)	0.195(4)	0.50000	0.28(4)
H2	0.078(6)	0.422(6)	0.1551(17)	0.50000	0.20(7)

Table 4.13 Refined structural parameters for prototypical $MAPbI_3$ derived from Rietveld refinement of neutron TOF powder diffraction data measured at 300 K. Lattice parameters $a = b = 8.8522(6)$ Å, $c = 12.6915(10)$ Å and a cell volume of 994.52(13) Å^3.

prototypical $MAPbI_3$ - Refined Powder Neutron Diffraction ADPs at 300 K						
Atom	U_{11}	U_{22}	U_{33}	U_{12}	U_{13}	U_{23}
Pb1	0.032(3)	0.032(3)	0.032(4)	0.00	0.00	0.00
I2	0.058(4)	0.058(4)	0.119(8)	-0.009(6)	0.00	0.00
I1	0.121(8)	0.121(9)	0.013(8)	0.00	0.00	0.00
N1	0.21(5)	0.21(5)	0.52(6)	-0.16(3)	-0.31(4)	0.31(4)
C1	0.21(5)	0.21(5)	0.52(6)	-0.16(3)	-0.31(4)	0.31(4)
H1	0.11(2)	0.4985)	0.26(4)	-0.01(5)	0.128(20)	-0.03(6)
H2	0.28(9)	0.28(9)	0.03(2)	-0.19(6)	-0.01(2)	0.01(2)

Table 4.14 Refined atomic displacement parameters for prototypical $MAPbI_3$ derived from Rietveld refinement of neutron TOF powder diffraction data measured at 300 K. Lattice parameters $a = b = 8.8522(6)$ Å, $c = 12.6915(10)$ Å and a cell volume of 994.52(13) Å^3.

tion data measured at 300 K was performed with a simplified structural model for both samples. This structural model is described by the space group *I4/mcm* and consists of a single lead site (Pb1) and two iodide sites (I1 and I2) that constitutes the PbI_6 framework. The MA^+ cation sits at the interstices of the surrounding PbI_6 framework and was modelled by a single site shared by a carbon and nitrogen atom (labelled C1/N1), as shown in Figure 4.37. The placement of this site was such that it posed complete orientation disorder and therefore unbiased towards any configuration of the MA^+ cation. No hydrogen positions were included in this structural model.

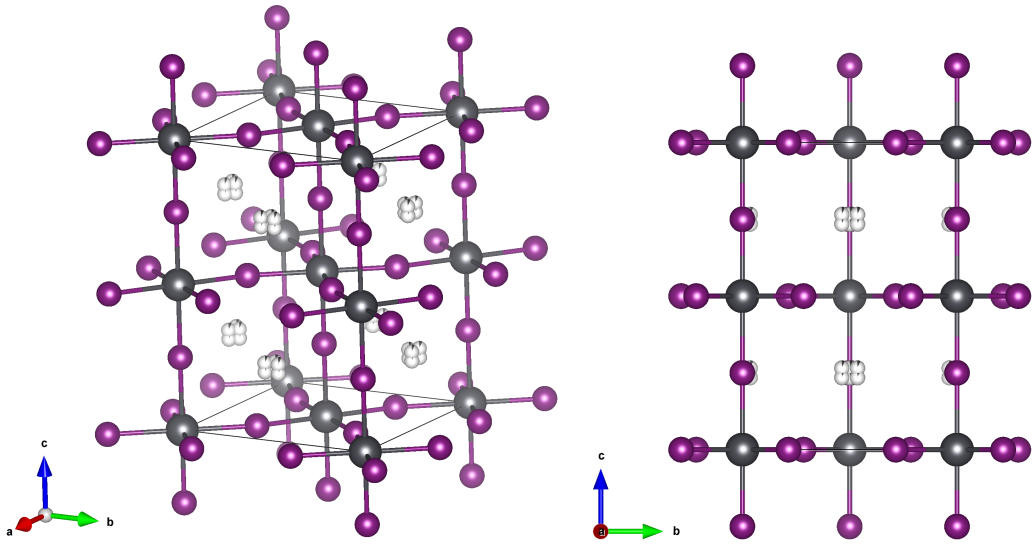

(a) (b)

Fig. 4.30 (a) and (b) a simplified structural model for $MAPbI_3$ used for initial refinement of TOF neutron powder diffraction measurements performed on the compound prototypical $MAPbI_3$ and AV285-$MAPbI_3$. Lead is shown in grey, iodine in purple and carbon/nitrogen in blue

Rietveld refinement was carried out for both samples according to the model shown in Figure 4.37 at 300 K, the resulting fit for prototypical $MAPbI_3$ and AV285-$MAPbI_3$ are shown in Figure 4.31a and Figure 4.31b respectively. The fits for these models is poor, which is to be expected with such a simplified modelling of the MA^+ cation.

Nuclear scattering density maps were generated based upon structure factors obtained from this initial refinement. Subsequent MEM remedy cycles were performed based on the density maps obtained previously upon which the observed diffraction pattern was fit, in a process known as MEM-based pattern fitting as shown in Figure 4.32a and Figure 4.32b for prototypical $MAPbI_3$ and AV285-$MAPbI_3$ respectively. The

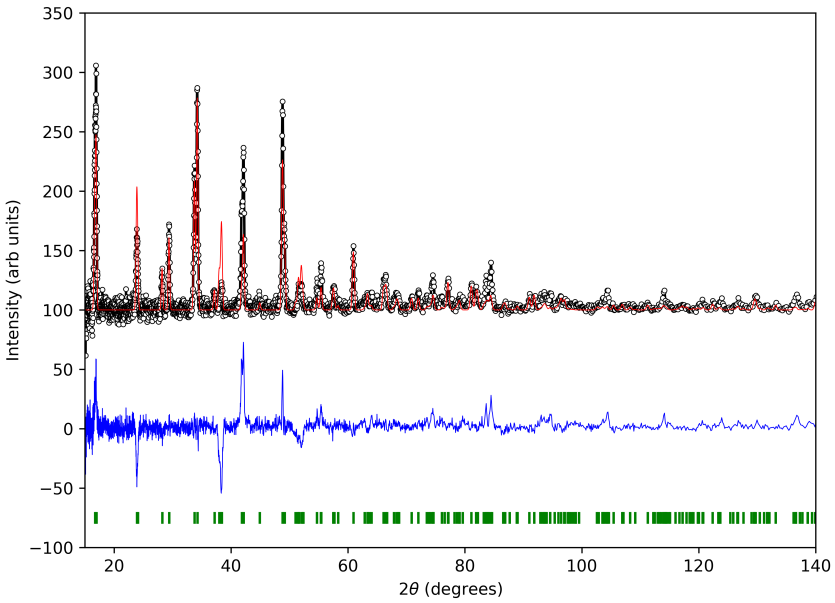

(a)

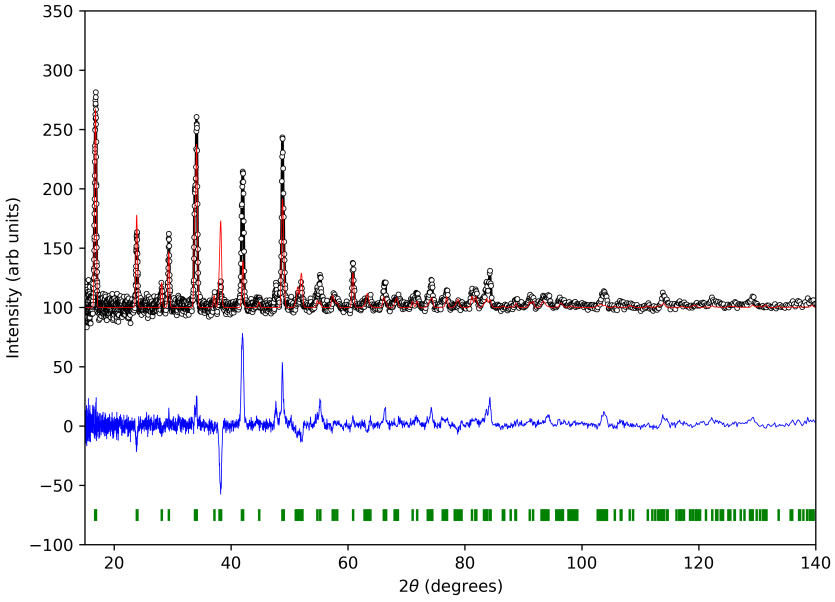

(b)

Fig. 4.31 Observed (circles), calculated (solid lines) and difference (blue line) neutron powder diffraction profile from Rietveld refinement (structure outlined in Table 4.8) for the samples (a) prototypical $MAPbI_3$ and (b) AV280-$MAPbI_3$ performed at 300 K. For the sample prototypical $MAPbI_3$ the fit factors are R_{wp} = 7.692 %, R_p = 4.684 % and S = 0.8064. Fit factors for the sample AV285-$MAPbI_3$ are R_{wp} = 6.563 %, R_p = 3.933 % and S = 0.6809.

resulting fits are significantly improved compared with those based on Rietveld refinement alone.

The nuclear density maps generated for both samples showed significant distribution of both positive (associated with scattering from both carbon and nitrogen) and negative (associated with scattering from hydrogen) scattering density located at the centre of the perovskite void corresponding to the MA^+ cation. These areas are highlighted in Figure 4.33a, Figure 4.33c and Figure 4.34a, Figure 4.34c for the samples prototypical $MAPbI_3$ and AV285-$MAPbI_3$ respectively. Significant differences in the calculated distribution were found between the two samples. For both positive and negative scattering the distribution was shown to be more disordered for the sample AV285-$MAPbI_3$ compared with prototypical $MAPbI_3$.

For the density maps of both samples, atomic positions were extracted for carbon/nitrogen and hydrogen sites from maxima in the scattering density as shown in Figure 4.33b, Figure 4.33d and Figure 4.34b, Figure 4.34d. The sample prototypical $MAPbI_3$ shows a density distribution and corresponding atomic sites consistent with previous measurements of prototypical $MAPbI_3$ as described in Section 3.3. The positive scattering density were fit with a model for the MA^+ cation described by a four atom tetrahedron unit. The MA^+ cation exhibits two orientations along the (220) and $(2\bar{2}0)$ planes. At the ends of the C-N unit three distinct maxima were located and assigned to hydrogen atoms in the crystallographic model describing both methyl and amine ends. The resulting C/N-H bond distances are approximately 1 Å.

For AV285-$MAPbI_3$ the distribution of both positive and negative scattering is found to be significantly more disordered as shown in Figure 4.33a and Figure 4.33c. Through extracting maxima in the regions of positive scattering density, shared atomic sites for both carbon and nitrogen sites were derived. These show two, four atom tetrahedron units inverted over each other, requiring two distinct sites shared by carbon and nitrogen sites. An increase in the disorder is observed for the areas of negative scattering compared with prototypical $MAPbI_3$, evidenced through a larger number of maxima close to the positive scattering associated with carbon and nitrogen. This meant that more hydrogen sites compared with prototypical $MAPbI_3$ were required in order to account for the distribution of negative scattering present. The resulting model shows an observable increase in the disorder of the MA^+ cation, this is consistent with previous results described in this work.

The discrete atomic sites shown in Figure 4.33b, Figure 4.33d, Figure 4.34b and Figure 4.34d extracted from nuclear scattering density were included in order for

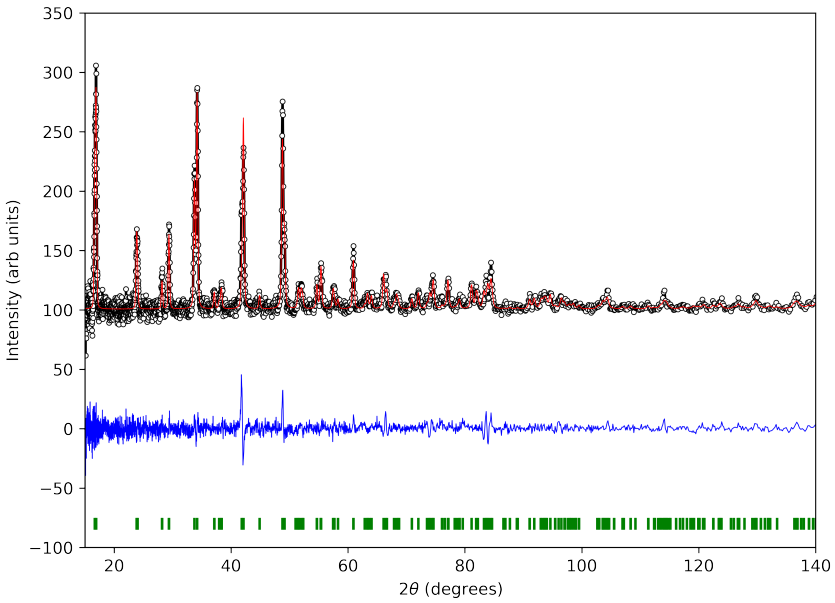

(a)

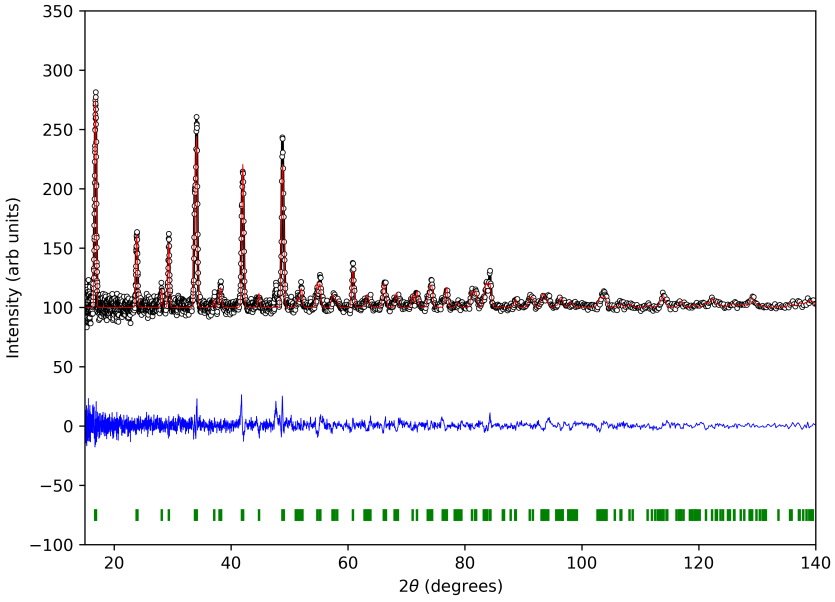

(b)

Fig. 4.32 Observed (circles), calculated (solid lines) and difference (blue line) neutron powder diffraction profile from MEM based pattern fitting for the samples (a) prototypical $MAPbI_3$ and (b) AV280-$MAPbI_3$ performed at 300 K. For the sample prototypical $MAPbI_3$ the fit factors are R_{wp} = 4.525 %, R_p = 3.141 % and S = 0.4744. Fit factors for the sample AV285-$MAPbI_3$ are R_{wp} = 4.525 %, R_p = 3.141 % and S = 0.4744.

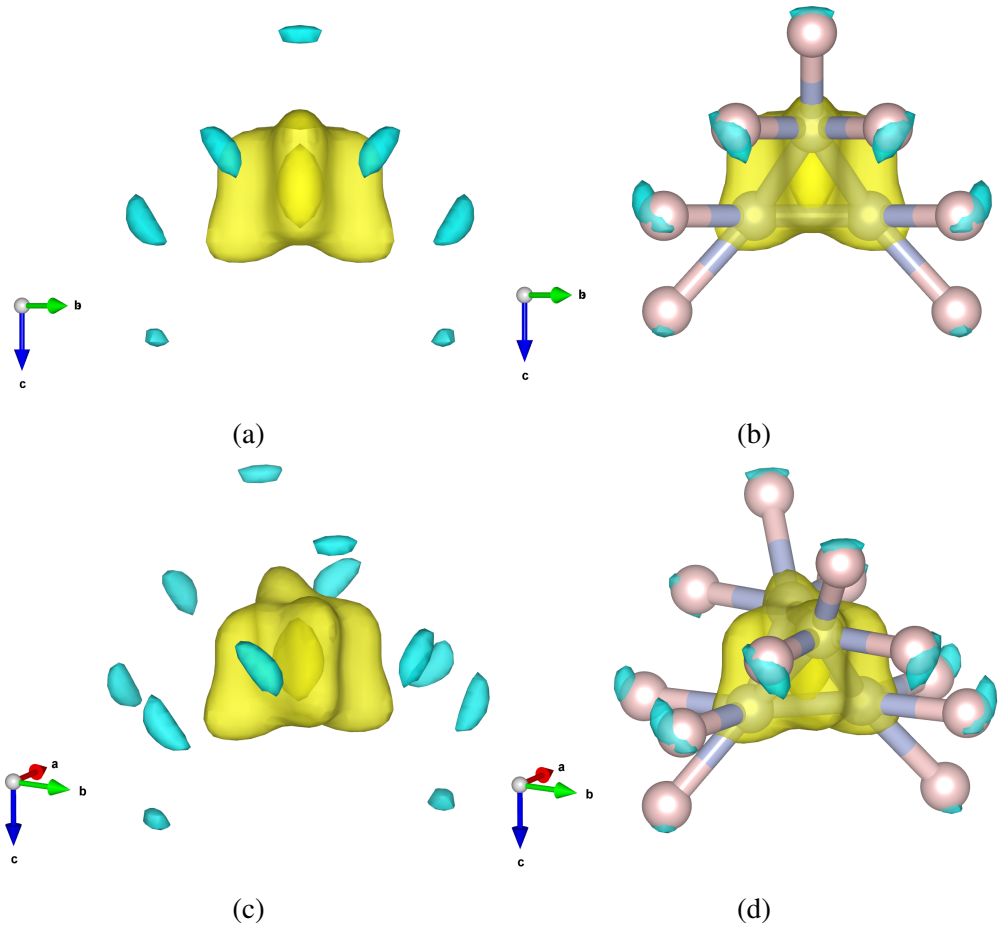

Fig. 4.33 (a), (b), (c) and (d) carbon/nitrogen (brown spheres) and hydrogen positions (pink spheres) derived from initial structure refinement for the *I4/mcm* space group. Here the nuclear scattering density maps are overlaid onto the structural model with both positive (yellow) and negative (blue) nuclear density shown (isosurface 1.93399 fmÅ^{-3}) derived from MEM analysis of time of flight (TOF) neutron powder diffraction measurements performed at 300 K.

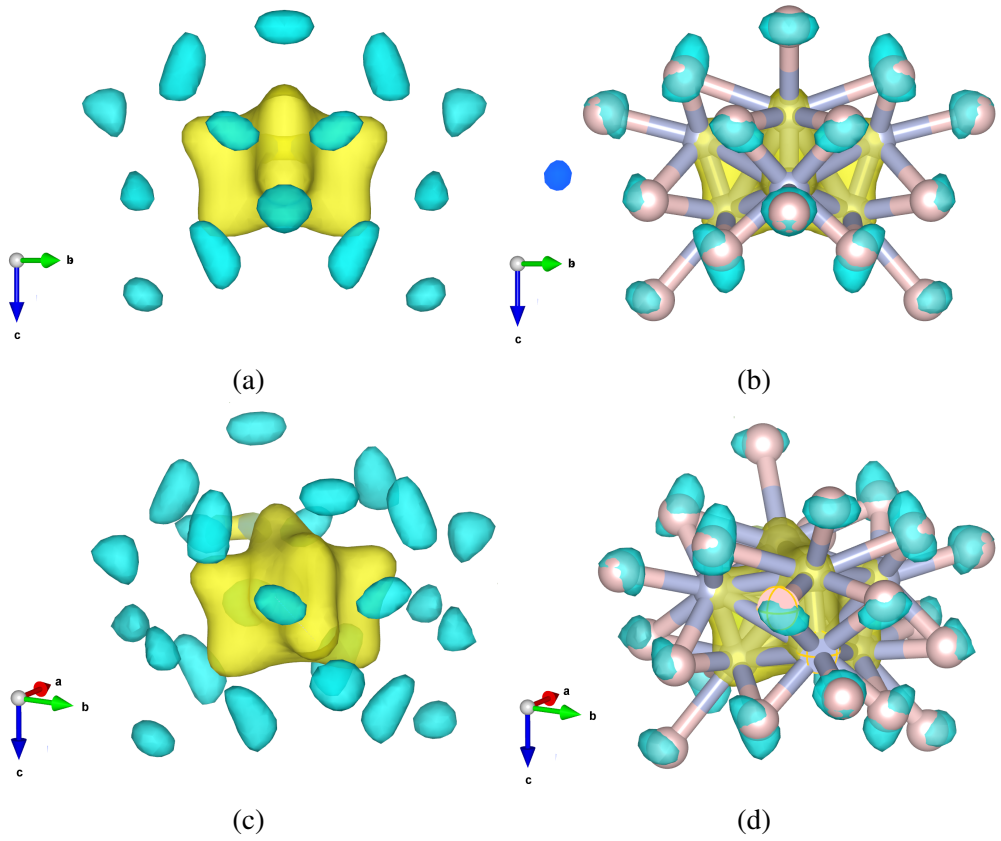

Fig. 4.34 (a), (b), (c) and (d) carbon/nitrogen (brown spheres) and hydrogen positions (pink spheres) derived from initial structure determination for the *I4/mcm* space group. Here the nuclear scattering density maps are overlaid onto the structural model with both positive (yellow) and negative (blue) nuclear density shown (isosurface 0.9 fmÅ^{-3}) derived from MEM analysis of time of flight (TOF) neutron powder diffraction measurements performed at 300 K.

traditional Rietveld refinement to be carried out. This is however a poor approximation for the average structure of the MA^+ for both prototypical $MAPbI_3$ and AV285-$MAPbI_3$ given the considerable disorder exhibited by the nuclear scattering density, which represents a better approximation of the average structure compared with discrete atomic modelling. The resulting refinements could only converge with fixed positions for all carbon, nitrogen and hydrogen constituents for the sample AV285-$MAPbI_3$ and isothermal displacement parameters. This may be due to the low observed peak to refined parameters for this refinement. From the scattering densities generated from MEM it is clear AV285-$MAPbI_3$ exhibits more orientational disorder. For organic perovskites, it is understood that a mismatch in the relative ionic sizes of the atomic components results in octahedral tilts that better accommodate the local environment. For hybrid organic inorganic perovskites, such as $MAPbI_3$, the insertion of an organic component into the perovskite structure introduces hydrogen bonding between the MA^+ cation and the anion framework. Here, hydrogen bonding is critical to the configuration observed for the PbI_6 framework and resulting octahedral tilts. At 160 K, Rietveld refinements show a drop in the occupancy of the MA^+ site for the sample AV285-$MAPbI_3$ compared with prototypical $MAPbI_3$. A change in composition that results in stronger bonding between the framework components, a straightening of Pb-I-Pb bonds and a larger cavity size at 300 K. This results in the increased orientation disorder for the MA^+ observed here. The larger effective size of the MA^+ cation for AV285-$MAPbI_3$ therefore drives the changes measured for the framework.

4.3.5 Thermal Gravimetric Analysis

In order to determine changes to the thermal stability of prototypical $MAPbI_3$ when annealed under a vacuum at high temperature, thermal gravimetric analysis were carried out on samples of prototypical $MAPbI_3$ and AV285-$MAPbI_3$ as shown in Figure 4.35. For both samples, two stages of mass loss are observed before 500°C, corresponding to the removal of MAI and PbI_2 species respectively [189, 190]. Both stages of mass loss occur at comparable temperatures for both samples demonstrating that no changes to the thermal stability of the compound results from high temperature vacuum annealing.

4.3.6 Residue Analysis - Joint XRD & SEM Study

Following a number of trials of the synthesis method outlined in Section 4.3.1, a black residue forms on the inside surface of the vacuum tube used for the high

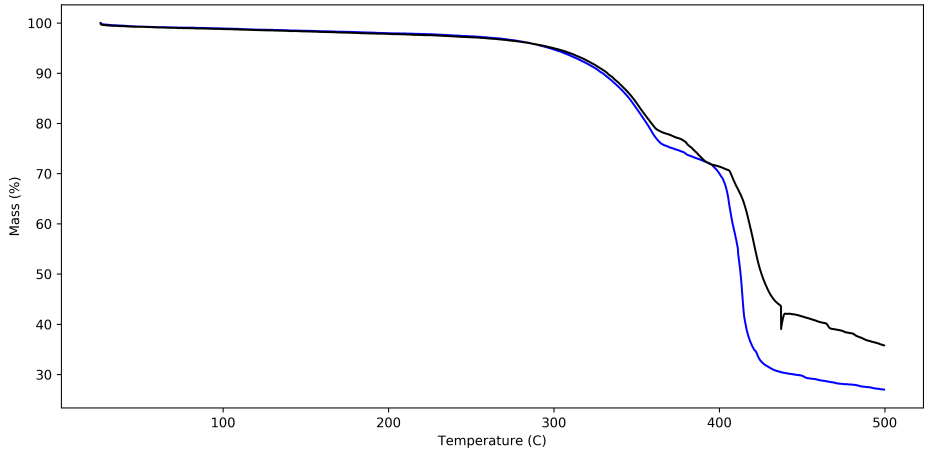

Fig. 4.35 TGA heating curves for prototypical $MAPbI_3$ (blue) and AV285-$MAPbI_3$ (black) in an atmosphere of air.

temperature annealing process. It was concluded that the residue originated from the annealed sample where the release of a chemical species during the vacuum annealing process described in Section 4.3.1 results from a composition change during the annealing process. Understanding the elemental contents of the residue was therefore vital in understanding the observed changes to the average structure. In order to characterise the residue a combination of powder X-ray diffraction and energy-dispersive X-Ray (EDX) spectroscopy techniques were used.

SEM-EDX measurements were conducted in order to determine the elemental composition of the vacuum tube residue. For this, the residue was secured to a sticky carbon pad and then secured to an aluminium stub for the subsequent SEM-EDX measurement. The EDX spectrum shows that the residue is mainly composed of carbon with only trace amounts of lead and iodine observed.

Site	Atomic Weight			
	Pb (%)	I (%)	C (%)	N (%)
1	0.02	0.02	99.39	0.57
2	0.02	-	71.16	28.83

Table 4.15 Composition of residue for two sites determined through SEM-EDX measurements.

A room temperature powder X-ray diffraction measurement was carried using a Panalytical X'pert diffractometer. The residue was placed onto a zero-background silicon wafer and the spectra was measured with incident wavelength Cu-$K_{\alpha 1}$ and Cu-$K_{\alpha 2}$ with a tube voltage of 40 mV and 40 mA current. As shown in Figure 4.36,

the primary characteristic of the diffraction pattern is two sharp peaks at 21.5° and 23.85° in 2θ, followed by several low intensity high angle peaks. The initial steps for characterisation were carried out using the search and match peak matching feature of the Panalytical High Score software package where the possible elemental composition was restricted to carbon alone following the EDX results. From this a match with paraffin, a polymer comprised of long-chain CH_2 groups was found. Here, the peak indexing of the XRD pattern agrees well with the literature [191]. Therefore, a Rietveld refinement was carried out with a starting structure obtained from the literature [191]. Here, the structure is assigned the space group *Pnma* with calculated lattice parameters of a = 7.45680(3) Å, b = 4.97140(16) Å and c = 2.53960(5) Å.

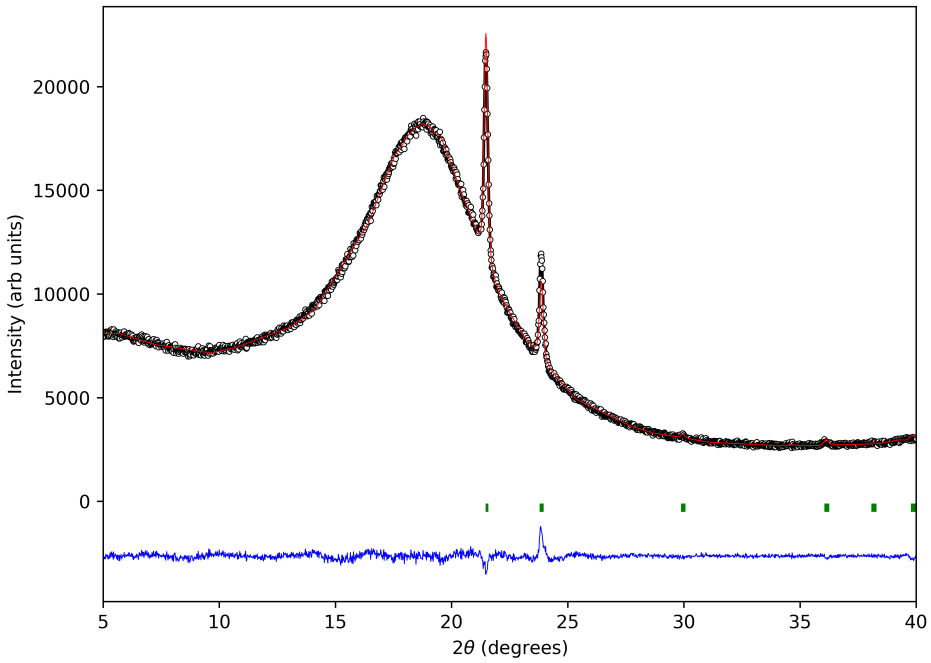

Fig. 4.36 X-ray diffraction spectra measured on the Panalytical X'pert diffractometer for the residue found on the inside of the vacuum annealing tube annealed at different temperatures for 1 hour 30 minutes. R_p = 1.84 % and R_{wp} = 2.58 %.

These results indicate the removal of carbon based atomic species from the sample when annealed under a vacuum at high temperature, and further indicates the break down and removal of MA^+ from the material. Therefore supporting the composition changes observed through neutron powder diffraction at 160 K (section 4.3.4).

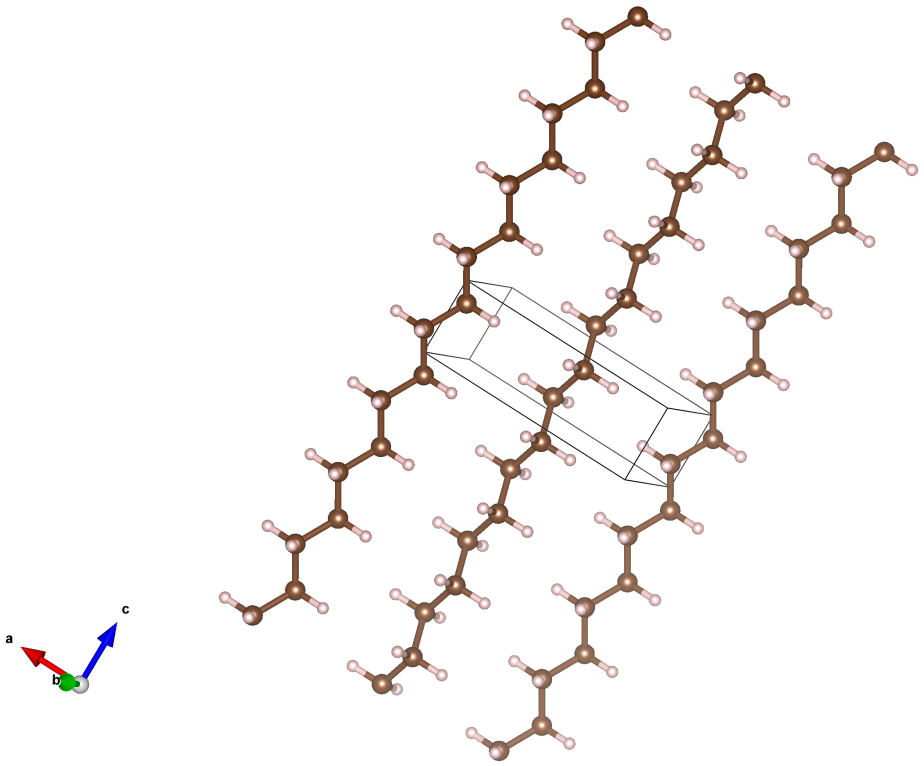

Fig. 4.37 A refined structural model of paraffin. Carbon is shown in brown and hydrogen in pink.

4.4 Discussion

The structure and phase transition dynamics have been characterised for a number of solution processed $MAPbI_3$ samples annealed under different conditions, including in air, under a vacuum and at different temperatures. When annealed in air, incorporation of interstitial oxygen was found to suppress the tilting of the PbI_6 framework at ambient temperature. Upon heating an increase in the structural phase transition temperature from tetragonal to cubic was observed resulting from a change in the interaction between the MA^+ cation and surrounding PbI_6 framework. No changes were observed when annealed under a vacuum at low temperature (<80 °C).

The conditions varied across the samples is consistent with the treatment hybrid perovskite thin-film layers undergo during the processing of perovskite based solar cells. This work demonstrates a dependence of low temperature thermal hybrid perovskite treatment on the structure of the perovskite material. Significant to these results is the variability in the structure of $MAPbI_3$ exhibited whilst the material remains intact. This is found to be highly dependent on the "history" of the sample, in this case variations in the thermal annealing treatment post synthesis. For a single compound these results are extraordinary and highlights the requirement for detailing the precise conditions for which a sample of $MAPbI_3$ has been synthesised and treated when reporting physical properties, structural characterisation and the performance of HOIHP based solar cells. It is clear that the compound $MAPbI_3$ encompasses a wide range of structures and compositions dependent on the specific defect chemistry of the material being studied.

When annealed at higher temperatures and under a vacuum (>200 °C) significant changes to the structural dynamics were observed including suppression of the octahedral tilting and a reduction in the tetragonal to cubic phase transition temperature upon heating. Further experiments were carried out to investigate the structural changes induced through high temperature vacuum annealing. A large sample of prototypical $MAPbI_3$ was synthesised and subsequently split into a number of parts and annealed under a vacuum at temperatures between 280 °C and 310 °C. For the first time powder and single crystal X-ray diffraction measurements established a consistent relationship between characteristic structural changes and vacuum annealing temperature. Precise control of both unit cell volume, tilting of the PbI_6 octahedral framework and Pb-I bond length were found to correlate with an apparent increase in the orientational disorder of the MA^+ cation.

The application of the maximum entropy method on neutron powder diffraction determined a significant increase in the orientational disorder of the MA^+ cation

upon vacuum annealing. Comparing the refinement of $MAPbI_3$ before and after high temperature vacuum annealing at 160 K revealed a small drop in the occupancy of the MA^+ site. This corresponds with the observation of a carbon based substance appearing on the inside surface of the quartz tubes used for the vacuum annealing process. This indicates a compositional change resulting from the removal of MA^+ inducing the observed structural changes. TGA measurements demonstrate that the vacuum thermal annealing process does not effect the thermal stability of the compound.

Intrinsic to the structure of $MAPbI_3$ is a relatively high defect concentration (between 10^{16} cm^3 and 10^{18} cm^3) [192], that stems from the high ionicity of the perovskite and its precursor materials during solution synthesis, as such the variability of these defects are to some degree random. For this work a new method for substantial tuning of the structure of hybrid perovskite materials such as prototypical $MAPbI_3$ has been devised that results from the removal of MA^+ species. The flexible bonding of the constituent components of the structure allow for considerable variation in the PbI_6 framework bond lengths and bond angles that originates from the interaction with the organic cation. This highlights the flexibility of these hybrid perovskite materials, that remain intact for a range of structural distortions that would typically be observed as a result of compositional substitution.

5

Stabilising New $MAPbI_{3+x}$ Phases through Iodine Thermal Treatment

Following the development of a post synthesis iodine thermal treatment, this chapter presents the synthesis and characterisation of a new structural phase of the hybrid perovskite $MAPbI_3$. This phase exhibits room temperature ordering of the MA^+ cation, reduced tilting of the PbI_6 framework and a reduction in framework disorder. Following the analysis of synchrotron powder and single crystal diffraction measurements, the stabilisation of this new phase is attributed to the population of an interstitial iodide site at the centre face of the perovskite framework, that is observed to order at low temperature. Therefore, intrinsic doping of additional iodine into the structure has resulted in a change to the composition, where the resulting new compound $MAPbI_{3+x}$ exhibits new structural phases.

5.1 Overview

5.1.1 $MAPbI_3$ response to I_2 exposure

Following on from the significant structural disorder we have reported for $MAPbI_3$ at ambient temperature including a mechanism for iodine mobility facilitated through the population of interstitial iodine sites, there have been a significant number of studies that report on the nature of defects in $MAPbI_3$. Both theoretical and experimental observation point towards a high concentration of iodine defects and significant iodine mobility. To this end, iodide vacancy and iodine interstitials are reported to have the lowest formation energies of ≈ 0.67 eV and ≈ 0.83 eV respectively compared with MA vacancies ($\approx$1.28 eV) [132, 131, 130]. With respect to photovoltaics, point defects that originate from the materials constituents will alter the intrinsic doping of the material. This is compared to extrinsic doping, whereby foreign atoms are introduced into the structure through the population of interstitial or lattice sites. Edri *et al*. have reported that $MAPbI_3$ based solar cells operate as p-i-n junctions for both planer thin-film and inert mesoporous scaffold architectures [58]. For both architectures the $MAPbI_3$ layer was reported as the intrinsic (i) component. Following this Wang *et al*. demonstrated that p and n self-doped $MAPbI_3$ films can be produced by varying the PbI_2/MAI precursor salt ratio resulting in MAI-rich and PbI_2-rich perovskite films respectively.

Efforts towards extrinsic doping of $MAPbI_3$ have mainly been limited to compositional substitution and are discussed in detail in Section 1.3.5. However, oxygen absorption into the structure has also been reported, where it was found to result in reversible changes in the photoluminescence of $MAPbI_3$ [180]. This was further demonstrated through our own work regarding significant changes to the temperature dependent structure of $MAPbI_3$ following absorption of oxygen into the structure (Section 4.2.2). With respect to intrinsic doping, initial experiments reported by Senocrate *et al*. aimed at determining the nature of mobile ions in $MAPbI_3$ through exposure of $MAPbI_3$ pellets to an I_2 vapour, demonstrating a reduction in iodine vacancies resulting from intrinsic doping of the material [193]. Following this, a set of experiments were reported that aimed to probe the defect chemistry of these materials through exposure of prototypical $MAPbI_3$ to I_2. These experiments involved mixing I_2 vapour with an inert gas such as nitrogen or argon just above room temperature. The resulting vapour is then introduced to the perovskite resulting in a high iodine partial pressure [194, 193]. Experiments conducted by Zohar *et al*. observe no significant structural changes except the measurement of a bulk lead impurity phase. However, there were significant changes to the electrical properties

of the material, here the films become irreversibly p-doped, with a measured increase in the work function by 150 mV whilst no change in the valence band maximum was observed [194]. Interestingly, the ionic conductivity is also shown to decrease, consistent with results reported by Senocrate *et al*. [193].

Theoretical calculations were later provided by Meggiolaro et. al in an attempt to explain the above experiments [195]. First-principle calculations of the defect formation energy (DFE) revealed a model for the defect chemistry involved in the interaction between prototypical $MAPbI_3$ and I_2 vapour. In this work two separate synthesis conditions were considered, both evaluate a 1:1 ratio of PbI_2 and MAI precursors. The first considers an iodine medium environment (a picture consistent with intrinsic prototypical $MAPbI_3$) and the second an iodine rich environment representative of experiments involving the exposure of the perovskite to I_2 vapours. Under iodine medium conditions both positive and negative iodine interstitials are shown to be the primary source of native defects. However, calculations for iodine rich conditions provided justification for experimental observations of p-doping following I_2 exposure due to stabilisation of positive interstitial iodine and lead vacancies. These results also reported a shift in the Fermi level consistent with the jump in work function measured by Zohar *et al* [194]. The calculated stability of lead vacancies is also consistent with the reported bulk lead impurity phase measured in experimental studies.

5.1.2 The purpose of present study

Intrinsic to the experiments outlined above is the incorporation of additional iodine into the structure through intrinsic doping of the perovskite material. From a material's synthesis point of view this presents an exciting opportunity as the flexibility of these defects opens the possibility of new phases. For all the reported experiments no significant structural changes have been observed. However, these experiments were limited in both the temperature ranges explored and the environment in which I_2 vapour was introduced. In chapter 4 we report significant structural changes to the crystal structure of $MAPbI_3$ following high temperature vacuum annealing, including changes to the octahedral tilting and an increase in the perovskite cavity size that can be dictated precisely by annealing temperature. We have also reported significant structural disorder in $MAPbI_3$ facilitated through the population of interstitial iodine sites. There have been reports of both oxygen and water absorption into the structure of $MAPbI_3$ [180], including our own work described in chapter 4, this indicates unexpected porous properties of hybrid perovskite materials. Consideration of the work described above and experiments reporting changes to the electronic structure

of $MAPbI_3$ following I_2 exposure, lead us to think about ways in which we can expand upon the flexibility and disorder exhibited by hybrid perovskite materials, specifically $MAPbI_3$, and towards the synthesis of new derivative structural phases. For this purpose we have developed a post synthesis thermal iodine treatment that aimed to incorporate additional iodine into the structure of $MAPbI_3$ to then be characterised through diffraction techniques. For clarity any reference to $MAPbI_3$ prior to undergoing this thermal iodine treatment is referred to as prototypical $MAPbI_3$ for the remainder of this chapter.

5.2 Iodine Thermal Treatment

The samples discussed in this chapter were synthesised by Rhianna Day, University of Kent. The post synthesis thermal iodine treatment we have developed begins with the synthesis of prototypical $MAPbI_3$, where microcrystals (<1 mm) are precipitated from solution according to the method outlined in Section 2.6.2. The treatment is then carried out in small batches, approximately 0.5 g of the prototypical $MAPbI_3$ sample is placed in a quartz tube and sealed alongside a small quantity of resublimed iodine crystals (0.1 g). The quartz tube is then evacuated to 10^{-4} torr and placed at the centre of a tube furnace and heated to 200 °C for 1 hour and 30 minutes. Samples that result from this treatment are referred to as AI200-$MAPbI_3$ for the remainder of this work.

For the purpose of determining the phase purity of the sample, Figure 5.1b shows a powder X-ray diffraction measurement performed on a sample of prototypical $MAPbI_3$ at ambient temperature following the post synthesis iodine thermal treatment outlined above. The diffraction pattern was found to be successfully indexed by a archetypal simple cubic perovskite structure consistent with the high temperature cubic phase I for $MAPbI_3$. Comparing this to prototypical $MAPbI_3$ (as reported in chapter 3 and Section 3.1.1), which exhibits a tetragonal ambient temperature phase II (shown in Figure 5.1a) this treatment has resulted in a significant change to the structure of the compound. For AI200-$MAPbI_3$ a number of additional peaks were also identified, and later characterised as two impurity phases NH_4PbI_3 and PbI_2 through single crystal X-ray diffraction measurements conducted at the University of Kent using a dual-source Rigaku Oxford Diffraction Supernova diffractometer. Details of these measurements can be found in Appendix A.5. The final refinement for the sample AI200-$MAPbI_3$ is shown in Figure 5.1b, the resulting fit is relatively poor and required a more rigorous structural determination process. For this purpose the

sample was characterised through synchrotron powder and single crystal diffraction measurements outlined later in this chapter.

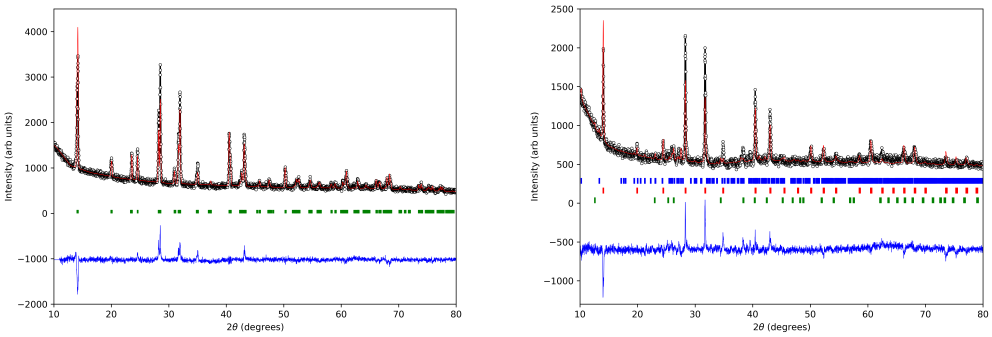

(a) (b)

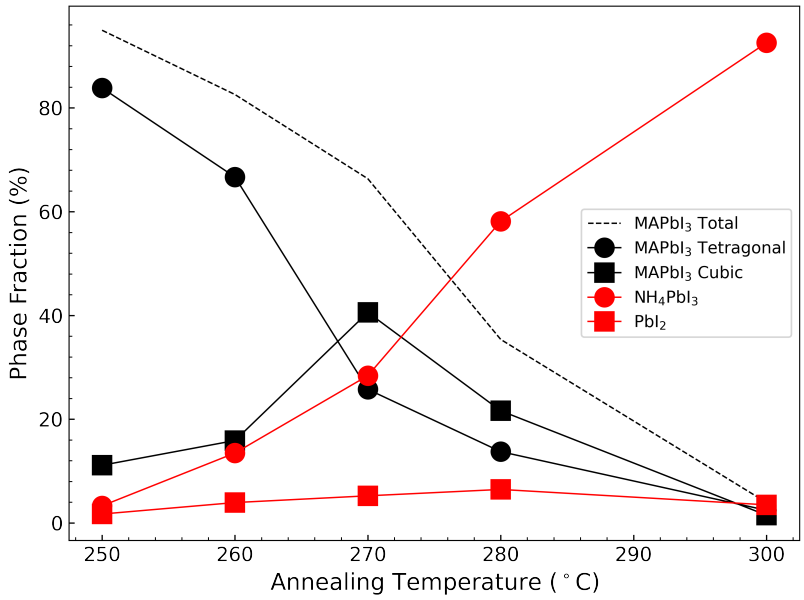

(c)

Fig. 5.1 Rietveld refinement of powder X-ray diffraction data measured for $MAPbI_3$ samples annealed with I_2 at (a) 250 °C R_p = 4.31 % and R_{wp} = 6.63 % and (b) 300 °C R_p = 4.32 % and R_{wp} = 6.95 % under ambient conditions. Bragg peak reflections corresponding to three phases, NH_4PbI_3 AI200-$MAPbI_3$ and PbI_2 are coloured blue, red and green respectively. (c) Phase fraction of samples following a post synthesis thermal iodine treatment annealed at different temperatures.

Following the initial synthesis experiment described above, subsequent synthesis trials were carried out in order to understand the temperature dependence of the phase change. It is important to note that these experiments were carried out in a different

type of furnace which resulted in a change in the temperature at which the phase transition occurred. The purity of the samples processed in this way varied drastically as the iodine thermal treatment requires refining. Therefore, other than the results outlined in this section the sample AI200-$MAPbI_3$ was used for all characterisation due to the high level of phase purity. For this experiment the annealing temperature was varied between 250 °C and 300 °C, other than this the experimental procedure was carried out as detailed above. Powder X-ray diffraction measurements were carried out on each sample for the purpose of determining phase purity, a plot of the phase fraction for each sample is shown in Figure 5.1c. For each sample two $MAPbI_3$ phases were refined that correspond to the tetragonal phase II and cubic phase I and represented by black circles and square markers on Figure 5.1b respectively. Two impurity phases, NH_4PbI_3 and PbI_2 were also refined consistent with the results shown in Figure 5.1b and represented by red circle and square markers on Figure 5.1b respectively. These results showed that as the annealing temperature increases the phase fraction of the cubic perovskite phase increases up to 270 °C before decreasing to approximately 0% at 300 °C. The tetragonal perovskite phase II, that $MAPbI_3$ exhibits under ambient conditions is observed to decrease from 250 °C to 300 °C where it makes up approximately 0% of the sample phase fraction. The total phase fraction represented by any perovskite phase is shown on Figure 5.1b as a black dashed line and seen to continually decrease from 250 °C to 300 °C. The phase fraction of the NH_4PbI_3 phase is found to continually increase from from 250 °C to 300 °C where it is found to make up close to 100% of the sample. A small quantity of PbI_2 was also measured for each sample, that is found to increase slightly as the annealing temperature increases.

Following the post synthesis thermal treatment the sample AI200-$MAPbI_3$ remained black in colour. SEM measurements of both prototypical $MAPbI_3$ and AI200-$MAPbI_3$ samples are shown in Figure 5.2a and Figure 5.2b respectively. Following the post synthesis treatment a significant change is observed in the microcrystals morphology, the crystals appear to be irregularly shaped and flakey compared to the distinct polyhedral microcrystals of prototypical $MAPbI_3$.

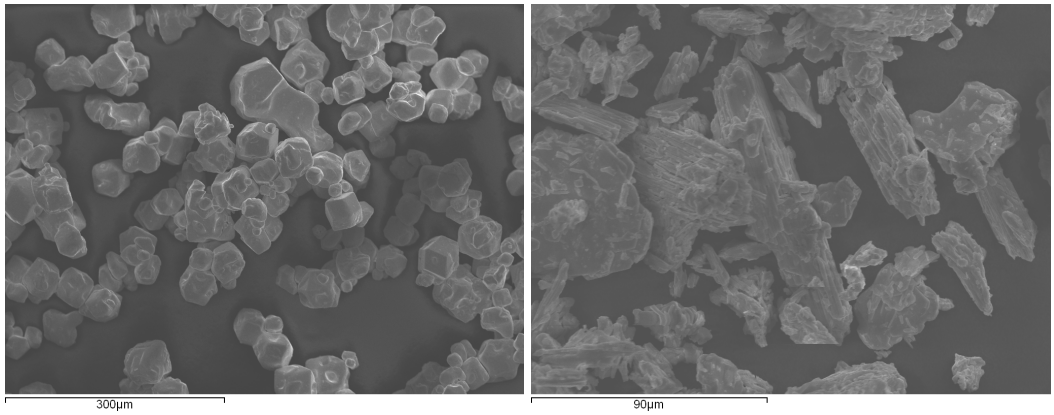

(a) (b)

Fig. 5.2 SEM images of prototypical $MAPbI_3$ (a) before and (b) after post synthesis iodine thermal treatment.

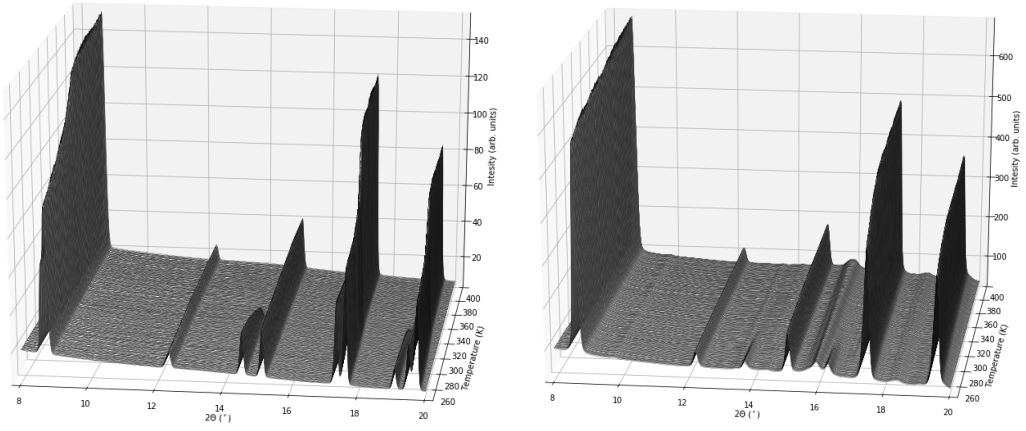

(a) (b)

Fig. 5.3 Measured powder synchrotron diffraction data conducted using the PILATUS@SNBL diffractometer for temperatures between 400 K and 270 K for two samples (a) prototypical $MAPbI_3$ and (b) AI200-$MAPbI_3$.

5.3 Structure Determination Between 100 K and 400 K

It is apparent that significant changes to the structure of prototypical $MAPbI_3$ have occurred following the post synthesis iodine thermal treatment described in Section 5.2. This section reports the structure of the sample AI200-$MAPbI_3$, characterised between 400 K and 100 K through variable temperature powder and single crystal X-ray diffraction measurements carried out using the PILATUS@SNBL diffractometer unless stated otherwise.

Below a brief overview of the temperature dependent structural phase transitions between 100 K and 400 K determined for the compound AI200-$MAPbI_3$ is provided, giving context to later discussions. The temperature dependent phase transitions between 400 K and 100 K for prototypical $MAPbI_3$ have been reported in detail [47, 48]. Upon cooling prototypical $MAPbI_3$ undergoes a series of successive cubic to tetragonal to orthorhombic phase transitions from the space groups $Pm\bar{3}m$, *I4/m* and *Pnma* respectively. As described in Table 5.1, the temperature dependent phase transitions observed for AI200-$MAPbI_3$ depart significantly from those exhibited by prototypical $MAPbI_3$. Here, it is reported that between 400 K and 100 K AI200-$MAPbI_3$ exhibits four structural phases: a simple cubic perovskite $Pm\bar{3}m$ phase (6.35980 Å) between 315 K and 400 K (phase I2-I), a larger cubic cell $Im\bar{3}$ (12.6294 Å) between 275 K and 315 K (phase I2-II), an orthorhombic *Immm* phase between 160 K and 275 K (phase I2-III), and a further orthorhombic *Pnma* phase between 160 K and 100 K (phase I2-IV). Temperatures below 100 K were not explored for these measurements. Figure 5.4 shows the group-subgroup relationship between the highest symmetry (I2-I, $Pm\bar{3}m$) and lowest symmetry (I2-IV, *Pnma*) phases. This plot confirms that the transitions between the space groups determined for AI200-$MAPbI_3$ can be related through the inner-relations defined by the connecting vertices shown in Figure 5.4. Here, each relation (vertices) describes a single symmetry element change that results in a set of order parameters that in accordance with Landau theory of phase transitions allows the transitions $Pm\bar{3}m \rightarrow Im\bar{3} \rightarrow Immm \rightarrow Pnma$.

Structural Phases for the compound AI200-$MAPbI_3$ between 100 K and 400 K			
Phase Label	Crystal System	Space Group	Temperature Range
I2-I	Cubic	$Pm\bar{3}m$	>315 K
I2-II	Cubic	$Im\bar{3}$	270 K > T < 315 K
I2-III	Orthorhombic	*Immm*	160 K > T < 270 K
I2-IV	Orthorhombic	*Pnma*	<160 K

Table 5.1 The phase transitions for the compound AI200-$MAPbI_3$ along with the respective label given to denote each structural phase.

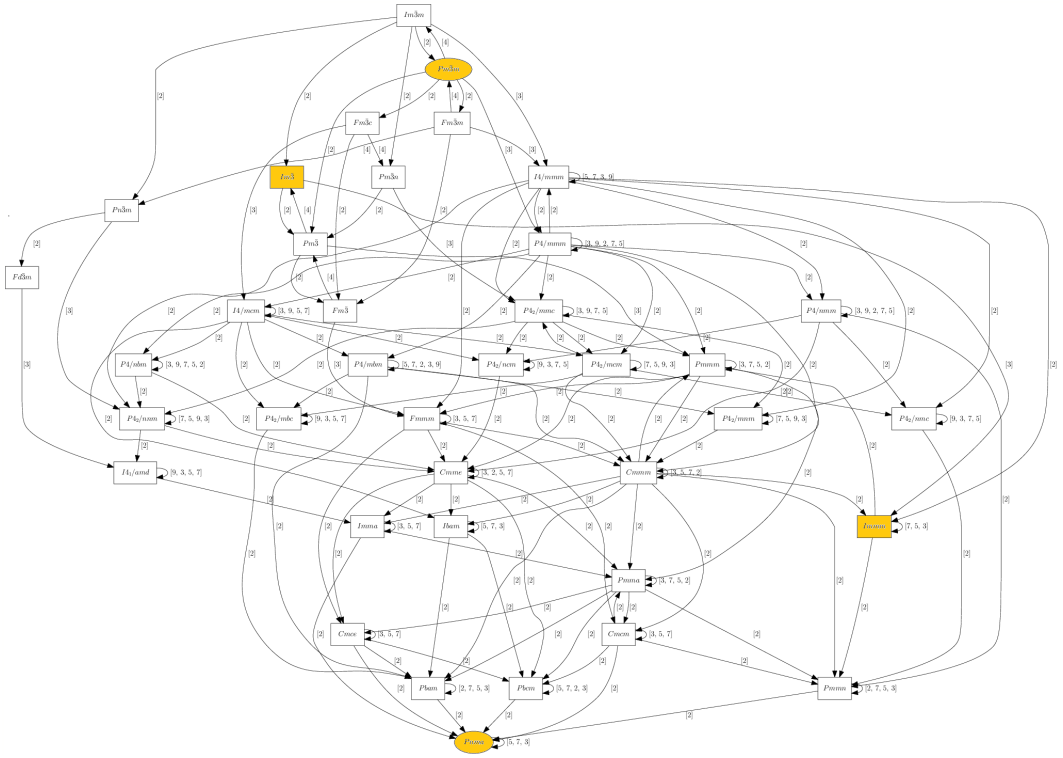

Fig. 5.4 The group-subgroup graph relating the space groups $Pm\bar{3}m$ and *Pnma* and the respective intermediate subgroups outlining the allowed transitions via a series of connected vertices. This plot was generated using the SUBGROUPGRAPH program as provided by the Bilbao Crystallographic Server [196].

5.3.1 Phase I2-I - 315 K to 400 K

As described in Table 5.1, this work has determined the high temperature (>315 K) structure of the compound AI200-$MAPbI_3$ to be described by the simple cubic perovskite space group $Pm\bar{3}m$. This section outlines the structure determination process undertaken for the high temperature cubic phase (>315 K) exhibited by

AI200-$MAPbI_3$ through synchrotron X-ray single crystal diffraction measurements using the PILATUS@SNBL based single-crystal diffractometer conducted at 400 K.

The observed reflections were indexed with a cubic crystal system with lattice parameters a = 6.35980(10) Å respectively. Upon data reduction Friedel mates were not merged and no Laue class filter was applied. A Standard empirical spherical harmonics (SADABS) absorption correction was used.

Automatic space group determination was carried out using the GRAL software routine as part of the CrysAlisPro software package. All centring systematic absences conditions were violated and therefore P type centring was chosen. The space groups *P23*, $Pm\bar{3}$, *P432*, $P\bar{4}3m$ and $Pm\bar{3}m$ were given as possible options, with identical reflection conditions structure determination was carried out for all space group options.

Assignment of PbI_6 Octahedra

For each space group, initial structure determination was carried out using direct methods with the software package SHELXS. Here, lead (labelled Pb1 in the final structural model) and iodide (labelled I1 in the structural model) atomic sites were located. These sit on each of the crystallographic axis and constitute a perovskite framework of PbI_6 octahedra sharing vertices with a zero tilt system (Glazer notation $a^0a^0a^0$) as shown in Figure 5.5 and Figure 5.6a.

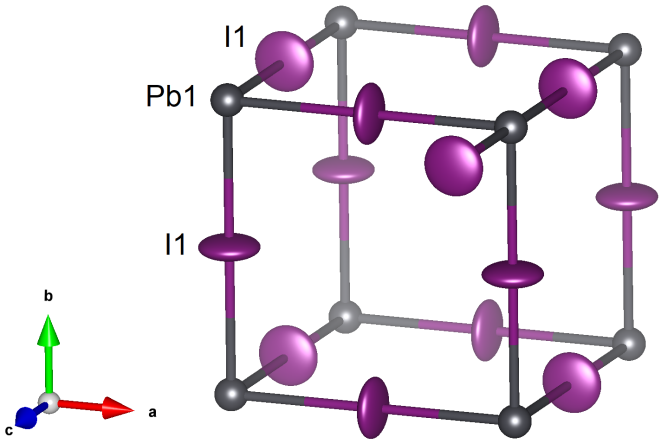

Fig. 5.5 The structure of the PbI_6 framework for the compound AI200-$MAPbI_3$ at 400 K derived from a single crystal X-ray diffraction measurement. Here the atoms are labelled according to the final structural model outlined in Table 5.3.

Assignment of MA^+ Cation

Structure refinement was carried out using the software package SHELXL for each space group option. Through which the location of the MA^+ cation was identified through maxima in the calculated electron difference map. For each space group this was found to sit at the centre of the unit cell on the Wyckoff site 1(b) $(\frac{1}{2},\frac{1}{2},\frac{1}{2})$ and assigned to a single carbon and nitrogen atom referred to as C1 and N1 in the final structural model as shown in Figure 5.6a and Figure 5.6b.

This initial solution for the structure was refined for each space group, for which the relevant refinement fit factors are shown in Table 5.2. Here, the space group $Pm\bar{3}m$ was found to result in the best R1, wR fit factors and therefore, the final structure solution was solved for the space group $Pm\bar{3}m$, representing an ideal cubic perovskite structure.

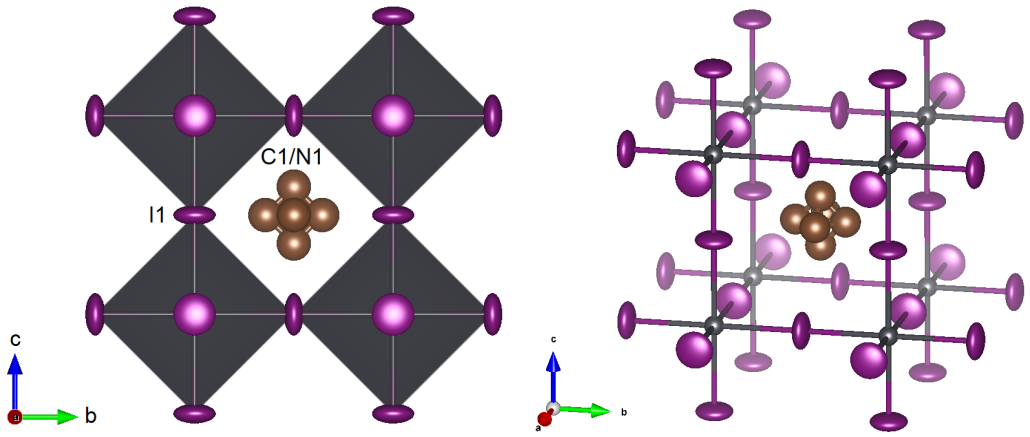

(a) (b)

Fig. 5.6 (a) and (b) the initial solution for the structure of AI200-$MAPbI_3$ derived from single crystal X-ray diffraction measurements conducted at 400 K with respect to the space group $Pm\bar{3}m$. The atoms are labelled according to the final structural model for the phase I2-I.

Space Group	R_{int} (%)	R_{sigma} (%)	R1 (%)	R_{all} (%)	wR(F^2) (%)	S	Parameters
P23	3.82	1.59	6.28	6.29	11.82	1.394	8
Pm-3	3.87	1.46	7.37	13.67	7.37	1.471	9
P432	3.07	1.36	6.49	6.49	11.39	1.427	7
P-43m	3.03	1.4	5.88	10.61	5.88	1.368	8
$Pm\bar{3}m$	3.09	1.30	5.07	10.49	5.07	1.449	10

Table 5.2 The refinement R factors for each of the possible space groups options for the structure of AI200-MAPbI$_3$ derived from a single crystal X-ray diffraction measurement conducted at 400 K.

Further MA^+ Disorder

Following the assignment of the $Pm\bar{3}m$ space group, a final structure solution was determined through further refinement of the data. Here, significant electron peaks present in the difference Fourier map located close to the Wyckoff site 1(b) $(\frac{1}{2},\frac{1}{2},\frac{1}{2})$ was assigned to further carbon and nitrogen atoms referred to as C2 and N2 in the final structural model. The result was a MA^+ cation located at the centre of the perovskite void that shows complete orientational disorder consistent with structural phase I of prototypical $MAPbI_3$. Coupled with Pb-I-Pb bond angles of 180° are weak N-I interactions at 3.60(13) Å and 3.96(8) Å as shown in Figure 5.7.

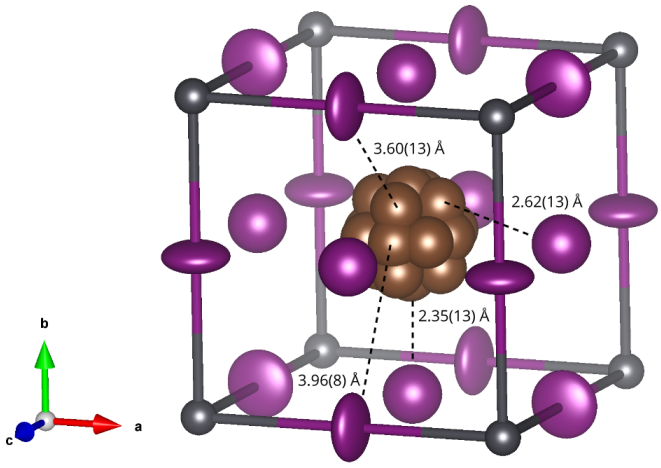

Fig. 5.7 The orientational disorder modelled for the cubic phase I2-I at 400 K for the compound AI200-$MAPbI_3$ highlighting the bond lengths C/N-I.

Further Disorder of the PbI_6 Framework and Interstitial Iodine

The structural model described so far is consistent with the high temperature cubic phase of prototypical $MAPbI_3$ that is described by the space group $Pm\bar{3}m$ (Z=1). Calculation of Fourier difference electron density maps highlighted significant additional maxima located close to the I1 site as shown in Figure 5.8a. A significant reduction of the R-factors resulted from the refinement of anisotropic thermal parameters for the iodide site (I1) and the addition of a partially occupied iodine site close to the iodine site (I1) labelled I1A. The addition of the iodide site I1A results from the inability of an elliptical model to adequately model the thermal motion and disorder of the PbI_6 framework, derived form additional maxima located in the difference Fourier maps as shown in Figure 5.8a.

An additional peak in the difference Fourier maps was also identified and sits at the centre of the perovskite framework as shown in Figure 5.8a. This peak was assigned

to an interstitial iodide atom (labelled IA in the structural model) with a refined occupancy of 0.028(14). The observed bond distances of 2.35(13) Å and 2.62(13) Å N1-IA and N2-IA suggest strong interactions between the respective sites as shown in Figure 5.7. The Pb:I composition of the PbI_6 framework is 1:3.18±0.18, including the interstitial site the overall Pb:I composition is 1:3.264±0.186, the interstitial component of this being 1:0.084±0.042.

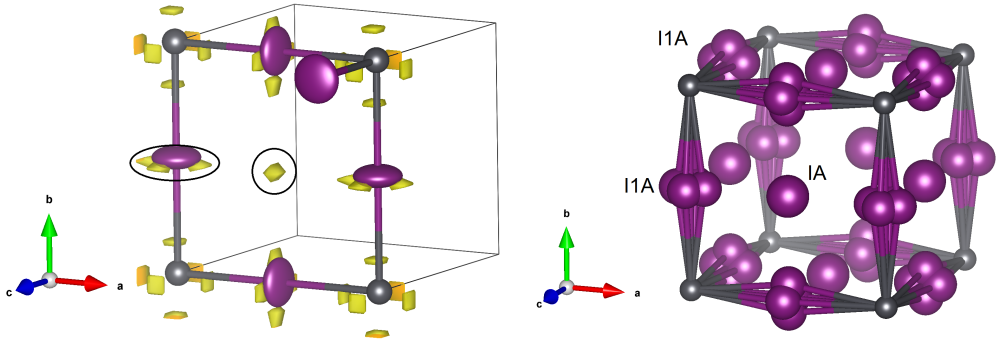

(a) (b)

Fig. 5.8 (a) A slice of both the calculated Fourier difference map and structure of AI200-$MAPbI_3$ derived from single crystal X-ray diffraction measured at 400 K. An area of significant density has been highlighted. Areas of density coloured yellow correspond to positive electron density. (b) The structure of the PbI_6 framework for the compound AI200-$MAPbI_3$ at 400 K derived from a single crystal X-ray diffraction measurement. Here the atoms are labelled according to the final structural model outlined in Table 5.3.

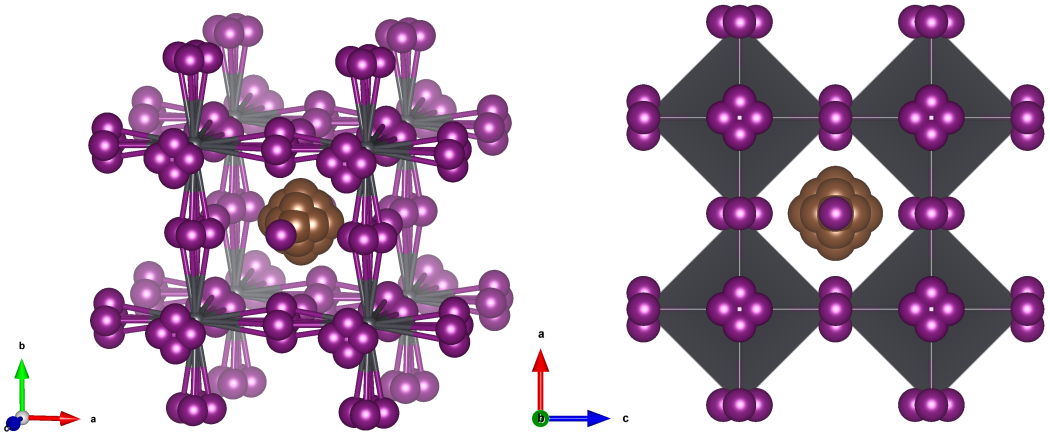

(a) (b)

Fig. 5.9 (a) and (b) the structure of the compound AI200-$MAPbI_3$ at 400 K derived from a single crystal X-ray diffraction measurement.

Single Crystal X-ray Diffraction Atomic Coordinated - $Pm\bar{3}m$					
Atom	x	y	z	Occupancy	U ($Å^3$)
Pb01	0.0	0.00	0.0	1.000	0.0520(14)
I1	0.5	0.00	0.0	0.82(6)	0.129(4)
I1A	0.5	0.5	0.084(9)	0.060(18)	0.134(16)
C1	0.5	0.36(3)	0.5	0.15(2)	0.20(7)
C2	0.58(3)	0.58(3)	0.5	0.073(11)	0.20(7)
N1	0.5	0.36(3)	0.5	0.15(2)	0.20(7)
N2	0.58(3)	0.58(3)	0.5	0.073(11)	0.20(7)
IA	0.5	0.00	0.5	0.028(14)	0.134(16)

Table 5.3 Crystallographic parameters obtained from structural refinement of single crystal X-ray diffraction measurements carried out at 400 K on the sample AI200-$MAPbI_3$. $a = b = c = 6.35980(10)$ Å.

Crystal X-ray Diffraction ADPs - $Pm\bar{3}m$						
Atom	U_{11}	U_{22}	U_{33}	U_{12}	U_{13}	U_{23}
Pb01	0.0520(14)	0.0520(14)	0.0520(14)	0.000	0.000	0.000
I1	0.034(4)	0.177(5)	0.177(5)	0.000	0.000	0.000

Table 5.4 Refined atomic displacement parameters obtained from structural refinement of single crystal X-ray diffraction measurements carried out at 400 K on the sample AI200-$MAPbI_3$. $a = b = c = 6.35980(10)$ Å.

5.3.2 Phase I2-II - 290 K to 315 K

Upon cooling the sample AI200-$MAPbI_3$ from 400 K, a structural phase transition was observed below 315 K through synchrotron X-ray powder diffraction measurements. This transition was identified through the appearance of subtle super-lattice reflections as shown in Figure 5.10.

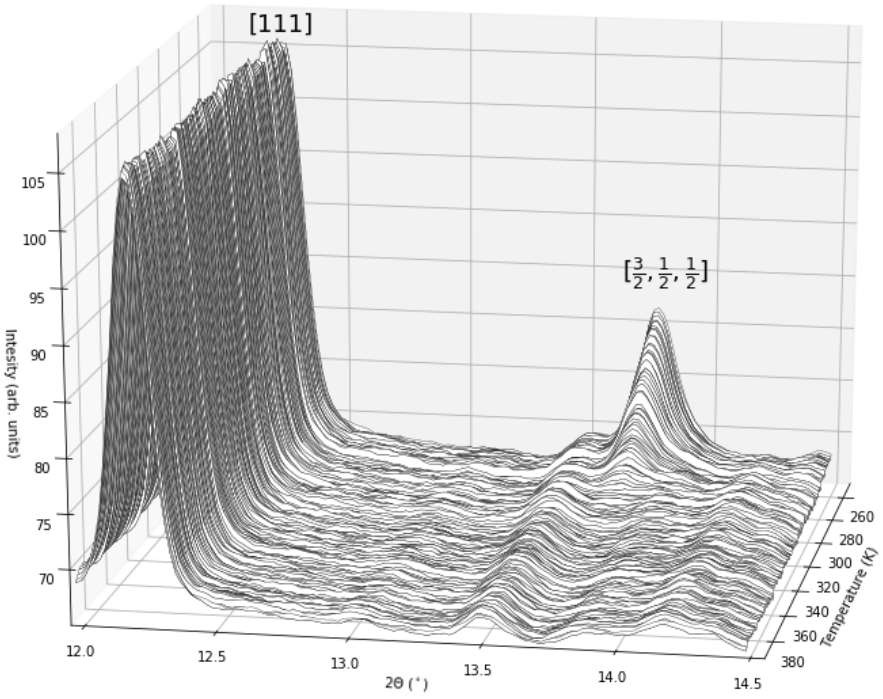

Fig. 5.10 Measured powder synchrotron diffraction data as a function of temperature for the compound AI200-$MAPbI_3$. The pattern has been indexed with respect to the simple cubic perovskite phase I2-I (described in Section 5.3.1) with respective super lattice reflections labelled.

The observation of super-lattice reflections $[\frac{3}{2}, \frac{1}{2}, 0]$ and $[\frac{3}{2}, 1, \frac{1}{2}]$ at 13.75° 2θ and 16.3° 2θ respectively, does not coincide with further splitting of peaks down to 270 K, this indicates a doubling of unit cell parameters from the simple cubic perovskite structure (Phase I2-I, a = 6.35980(10) Å, $Pm\bar{3}m$, described in Section 5.3.1) observed at temperatures above the 315 K transition. This was confirmed through Le Bail fits of synchrotron X-ray powder diffraction data measured at 290 K as shown in Figure 5.11. Here, a cubic cell with lattice parameters a = 12.6054(6) Å and space group P23 successfully index all observed perovskite peaks. This structural phase is observed to exist between 315 K and 270 K and is denoted I2-II.

This section describes the structure determination process carried out for the ambient temperature phase I2-II (270K-315K) for the compound AI200-$MAPbI_3$ through

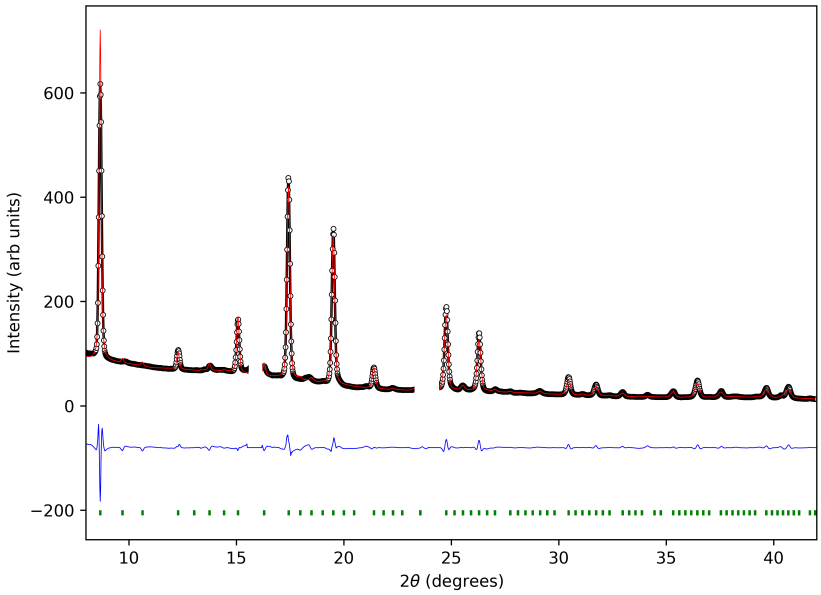

Fig. 5.11 Le Bail refinement of powder synchrotron diffraction data conducted at the Swiss Norwegian Beamline (BM01) measured at 275 K for the compound AI200-$MAPbI_3$. Impurity Phase peaks have been removed. R_p = 3.39 % and R_{wp} = 5.04 %. Here the structure has lattice parameters a = 12.6054(6) Å with space group P23.

synchrotron single crystal diffraction measurements carried out at 290 K. This temperature range is critical to the operating temperature of photovoltaic devices.

All data reduction of the single crystal diffraction data was carried out using the CrysAlisPro software package. Initial structure determination was carried out using SHELXS and further structure refinements were performed using the program SHELXL.

The data reduction process started by indexing the observed reflections with a cubic crystal system type unit cell. Lower symmetry options were ruled out through analysis of synchrotron powder diffraction data measured at the same temperature. Here, no peak splitting was observed associated with slight tetragonal/orthorhombic distortions or non 90° cell angles at high 2θ angles (as observed for lower temperature measurements of the same sample). The data was indexed with a cell dimensions for a = 12.6265(2) Å.

The experimental data contains 46 of 3421 (1.34 %) possible reflections that violate I-centring, the intensity of which is less than 0.5 Mean I/σ. As such I-centring was was chosen for the unit cell.

Through automatic space group determination routines carried out by GRAL CrysAlisPro the following possible space groups were determined for the cubic crystal system: *I23*, *I213*, *Im*$\bar{3}$, *I432*, *I*$\bar{4}$*3m* and *Im*$\bar{3}$m.

These space group options are described by identical reflection conditions. Direct methods were used to devise an initial structural model for each space group. This routine was performed using the software program SHELXS which generated a pseudo-solution containing the most likely positions of heavy elements within the structure, Pb and I in this case. This model was refined for each possible space group where an initial location of the MA^+ cation within the perovskite framework was found through maxima in the calculated difference electron density maps.

Assignment of PbI_6 Octahedra

The resulting pseudo-solution describes a perovskite structure composed of a corner-shared PbI_6 octahedra. As shown in Figure 5.32b, the octahedra are located at the Wyckoff position c at $\frac{1}{4},\frac{1}{4},\frac{1}{4}$ etc and exhibit perovskite tilting with the Glazer notation $a^+a^+a^+$, each space group showed slight tilting of the octahedra represented by a deviation from 180° for the bond angle Pb-I-Pb.

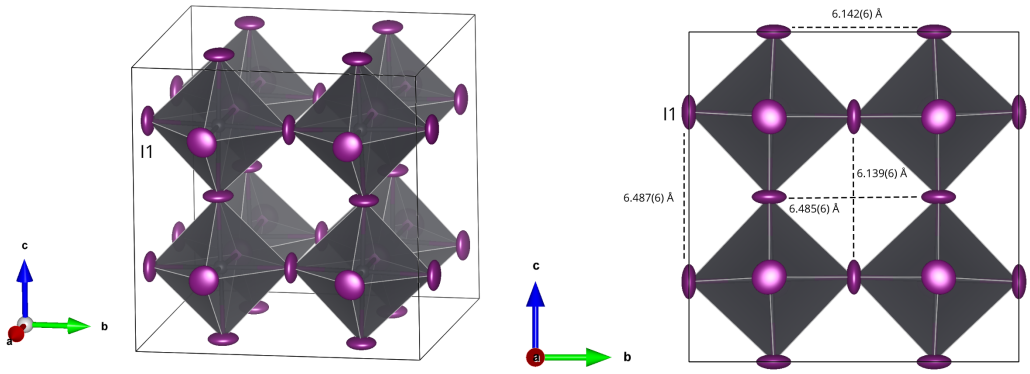

(a) (b)

Fig. 5.12 (a) and (b) the general structure for which the space groups were tested in order to determine the proper space group for the compound AI200-$MAPbI_3$ at 290 K, this model is derived from the space group $Im\bar{3}$.

Assignment of MA^+ Cation

The perovskite voids are populated by $CH_3NH_3^+$ cations. The model contains two distinct MA^+ sites, the first located at the 000 and $\frac{1}{2},\frac{1}{2},\frac{1}{2}$ sites (Wyckoff a positions), this site exhibits complete orientational disorder across the space groups with no distinct orientation of the MA^+ cation. The second $CH_3NH_3^+$ site at $0,\frac{1}{4},\frac{1}{4}$ (Wycoff b positions) exhibits ordering along a single crystal axis or disordered across all three for the space groups tested.

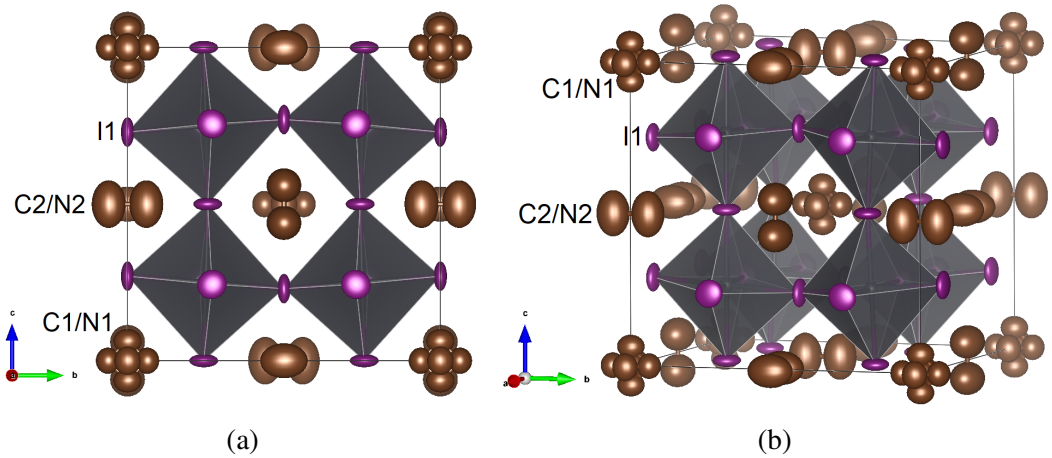

(a) (b)

Fig. 5.13 (a) and (b) the structure for which the space groups were tested with in order to determine the proper space group for the compound AI200-$MAPbI_3$ at 290 K.

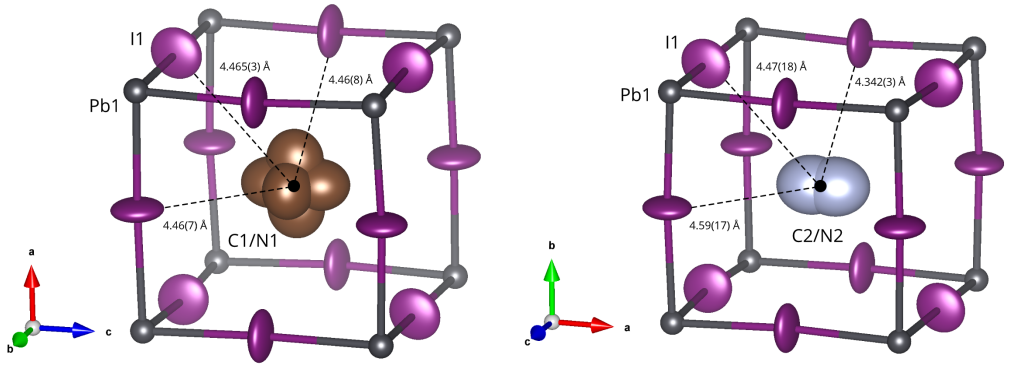

(a) (b)

Fig. 5.14 Surrounding coordination from the centre of mass for two distinct MA^+ sites labelled (a) C1/N1 and (b) C2/N2 in the structural model derived from single crystal X-ray diffraction measurements at 290 K for the space group $Im\bar{3}$.

Space Group	R_{int} (%)	R_{sigma} (%)	R1 (%)	R_{all} (%)	wR(F^2) (%)	S	Parameters
I23	2.08	1.61	3.07	4.3	5.99	1.126	41
I213	2.08	1.61	6.54	8.2	18.87	1.084	32
$Im\bar{3}$	2.09	1.19	3.66	4.32	6.52	1.291	32
I432	2.54	1.27	13.24	12.83	53.01	2.2501	32
I-43	2.44	1.69	20.39	20.86	51.62	2.419	30
$Im\bar{3}m$	2.54	1.02	8.49	10.44	17.10	1.303	21

Table 5.5 The refinement R factors for each of the possible space groups options for the structure of AI200-$MAPbI_3$ derived from a single crystal X-ray diffraction measurement conducted at 290 K.

Table 5.5 describes the refined R factors for each space group tested. Of the possible space group options, the space groups $Im\bar{3}$ and *I23* showed the lowest refined R factors. For $Im\bar{3}$ a lower number of structural parameters were used in the refinement and no distinct differences between the two structures were found. Therefore, the space group $Im\bar{3}$ was chosen for the ambient temperature structural phase I2-II for the compound AI200-$MAPbI_3$. Following this, a more rigorous structure refinement process was carried out. The result was a significantly more disordered structure than the pseudo-solution obtained during the space group testing described above.

Ordering of the MA^+

The nature of the octahedral tilt for AI200-$MAPbI_3$ at 290 K results in two distinct perovskite cavity sizes, calculated to accommodate a sphere size of radius 2.27 Å and 2.14 Å respectively, based on Shannon ionic radii for the framework components using the software program Platon. This results in two distinct MA^+ cation sites, each distinguishable by the orientational disorder the two sites exhibit. The first site is modelled by a single carbon and nitrogen site, denoted C1 and N1 in the final structural model, exhibits complete orientational disorder along all crystallographic axis, this site is highlighted on Figure 5.15a (see Table 5.6). For the structural refinement the occupancy of the sites C1 and N1 were fixed such that the total composition of carbon and nitrogen on the site were individually 1.462, opposed to fully occupied value of 1.0. This accounts for additional scattering from hydrogen that originates from the MA^+ site and not accounted for in the structural model. A C1-N1 bond length of 1.3(3) Å was observed. The respective bond lengths between the sites C1/N1 and I1 are 4.04(6) Å and 4.07(6) Å.

The second MA^+ site is described by the atomic sites C2 and N2 in the final structural model (see Table 5.6). This MA^+ site exhibits ordering along a single crystallographic axis. The tilting of the PbI_6 octahedral conforms to the ordering where each Pb-I-Pb bridge points towards the centre of the perovskite void. For the refinement, the occupancy of sites C2/N2 were restricted to be equivalent and a refined to a value of 0.71(5). Considering the mirror symmetry of the site the total carbon and nitrogen occupancy of the site is 1.42(10), the value higher than unity follows the same justification as sites C1 and N1. This coincides with a significant reduction in the bond length C2-N2 of 0.7(5) Å. The bond length C2/N2-I1 is observed as 4.23(16) Å. Further to this, the shape of the refined anisotropic displacement ellipsoid is found to be elongated along the respective crystallographic axis that the MA^+ is ordered along, indicating significant disorder in the observed bond length C2-N2 as shown in Figure 5.15. The results presented in Section 5.2

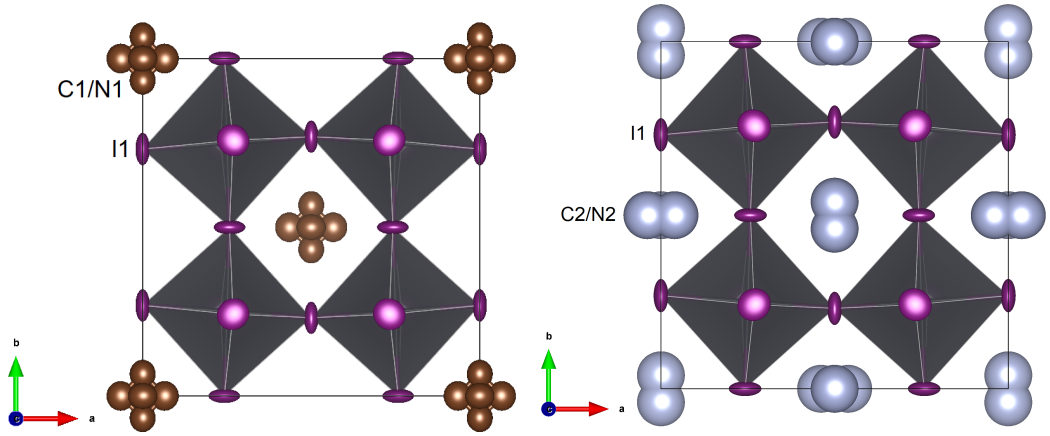

(a) (b)

Fig. 5.15 Two distinct MA^+ sites derived from single crystal X-ray diffraction measurements at 290 K. (a) Corresponds to atomic sites C1 and N1 in the structural model describing complete orientational disorder of the MA^+ site. (b) Highlights atomic sites C2 and N2 in the structural model, this MA^+ site is orientated along a single crystallographic axis.

report the formation of the impurity phases NH_4PbI_3 and PbI_2 during the synthesis of AI200-$MAPbI_3$. The observed reduction in the bond length C2-N2 and C2/N2-I1 compared with C1-N1 and C1/N1-I1 may result from the partial population of NH_4 onto the MA^+ site. However, separating these two molecules in the structural model was not possible and therefore not included in the final structural model.

Further Disorder of PbI_6 Framework

Calculation of Fourier difference electron density maps highlighted significant additional maxima located close to the I1 site as shown in Figure 5.17a. Here, the R-factors were significantly reduced from the refinement of anisotropic thermal parameters for the iodide site (I1) and the addition of multiple partially occupied iodine sites that are located close to the iodine site (I1) and labelled I1A and I1B as shown in Figure 5.17b. The bond distances I1-I1A and I1-I1B are 0.51(3) Å and 0.52(3) Å respectively and the combined occupancy of the sites I1, I1A and I1B is $102.1 \pm 1.65\%$, the requirement for additional iodide sites I1A and I1B is therefore attributed to the inadequacy of an elliptical model in modelling the thermal motion of a single iodide site and significant disorder of the PbI_6 framework.

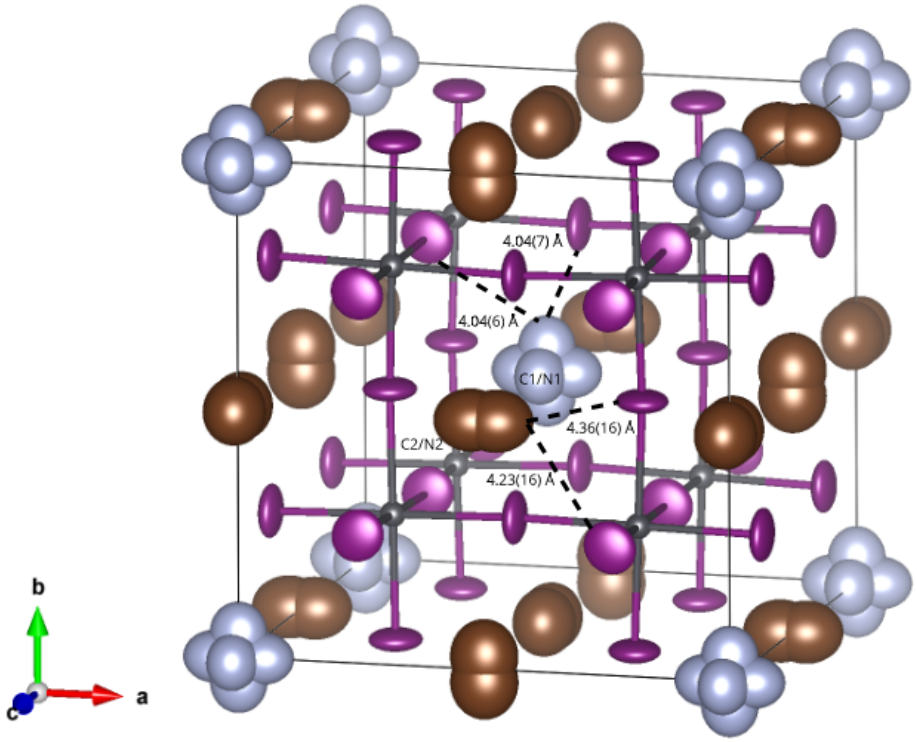

(a)

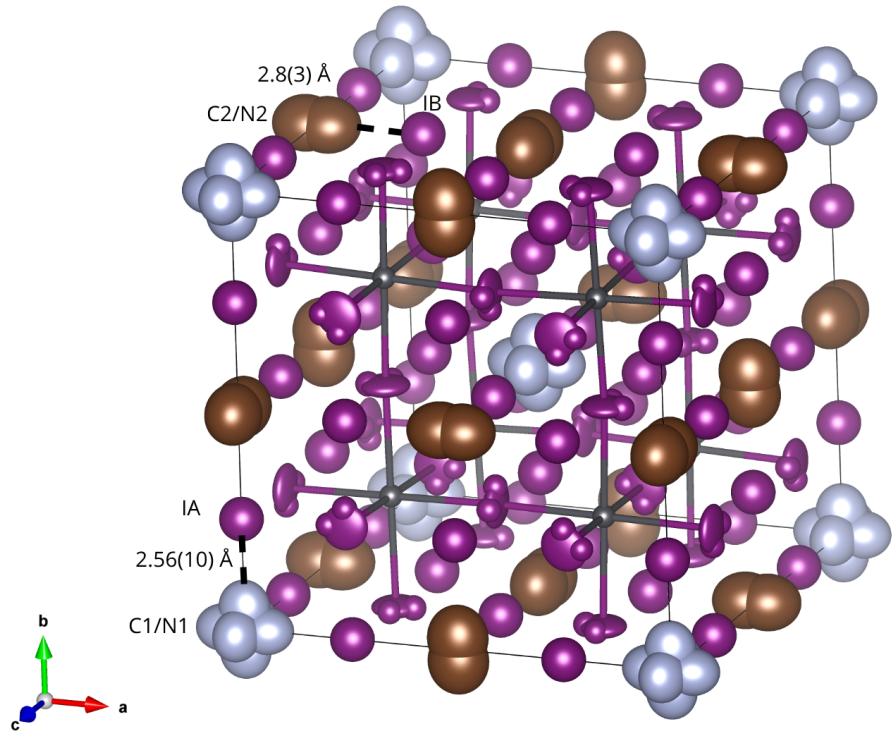

(b)

Fig. 5.16 (a) The coordination of the two MA^+ cation sites described by the atomic sites C1/N1 and C1/N2 in the structural model (as shown in Table 5.6) for the the compound AI200-$MAPbI_3$ measured at 290 K. (b) A diagram showing the bond lengths between different MA^+ sites and the interstitial iodide sites C1/N1-IA and C2/N2-IB.

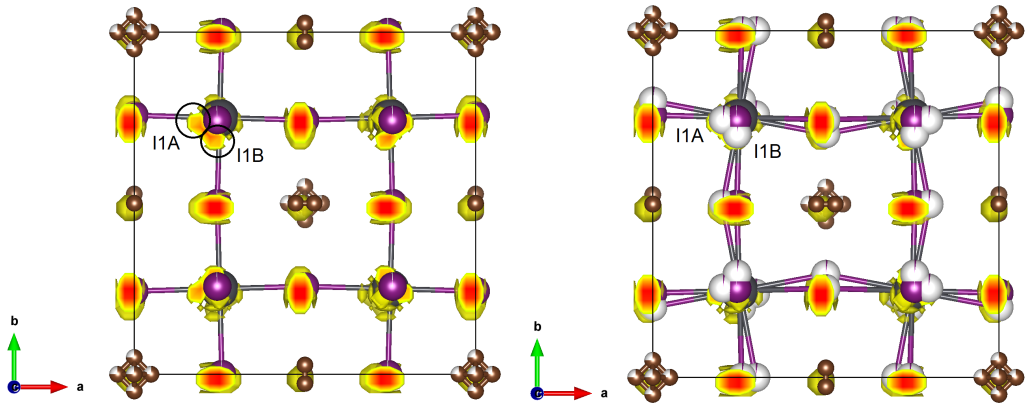

(a) (b)

Fig. 5.17 Calculated Fourier difference map and structure of AI200-$MAPbI_3$ derived from single crystal X-ray diffraction measured at 290K, here yellow areas of density represent positive peaks in the difference Fourier map. (a) An area of significant density has been highlighted that sits ≈ 0.52 Å away from the I1 site. (b) Additional partially occupied iodide sites I1A and I1B have been included in the structural model and have been highlighted accordingly.

Interstitial Iodine

Further maxima located in the calculated electron difference map were found at the centre face of the perovskite framework as shown in Figure 5.19a. This is described in the structural model through the addition of further iodine atomic sites labelled as IA and IB. As shown in Figure 5.18a and Figure 5.19. In order to verify the identity of the atomic species of the interstitial sites, structure refinements were carried out with interstitial carbon sites. However, the refined occupancy of this site was found to be greater than unity and therefore ruled out.

The nature of the framework tilting for AI200-$MAPbI_3$ results in two distinct cavities for the perovskite framework for the phase I2-II, one larger than then other. The centre of the larger cavity is populated by a MA^+ cation that exhibits complete orientational disorder (labelled C1/N1). As shown in Figure 5.18a the interstitial iodide site IA is shifted away from the centre of the perovskite face and away from the MA^+ site labelled C1/N1 and towards the second smaller cavity site. The centre of the smaller second cavity site is occupied by a second MA^+ site (labelled C2/N2). This site exhibits orientational ordering along the crystallographic axis. The population of the interstitial site IA restricts the possible orientations of the second MA^+ site whereby any other orientation would result in nonphysical bond distances between the MA^+ ends and interstitial iodide site IA. The ends of the second ordered MA^+ points towards a second interstitial iodide site labelled IB that sits further away

from the MA^+ cation (labelled C2/N2). The orientational disorder observed for the site C1/N1 and ordering along each crystallographic axis exhibited by the site C2/N2 both conform to the tilting of the octahedral framework.

When refined individually the occupancy of each interstitial site were found to be close to equivalent, the final refined occupancy was found to be 0.044(14) and 0.045(13) for sites IA and IB respectively. The location and occupancy of these sites are consistent with additional interstitial sites found for the high temperature I2-I phase for described in Section 5.3.1. The Pb:I composition of the PbI_6 framework is found to be 1:3.06±0.050, including the interstitial site the overall Pb:I composition is 1:3.194±0.110, the interstitial component of this being 1:0.134±0.099. This is compared with 1:3 for prototypical $MAPbI_3$. The final atomic co-ordinates derived from the above experiment for AI200-$MAPbI_3$ at 290 K are described in Table 5.6.

Single Crystal X-ray Diffraction Atomic Coordinated - $Im\bar{3}$					
Atom	x	y	z	Occupancy	U ($Å^3$)
Pb1	0.25	0.25	0.25	1.0	0.0435(10)
I1	0.2431(2)	0.2568(2)	0.00	0.974(15)	0.1376(18)
I1A	0.203(2)	0.258(2)	0.0	0.022(5)	0.050(11)
I1B	0.2436(18)	0.298(2)	0.0	0.024(5)	0.053(10)
C1	0.0	0.050(8)	0.0	0.37(4)	0.2432
N1	0.0	0.050(8)	0.0	0.37(4)	0.2432
C2	0.474(19)	0.5	0.0	0.71(5)	0.32(5)
N2	0.474(19)	0.5	0.0	0.71(5)	0.32(5)
IA	0.0	-0.2520(18)	0.0	0.044(14)	0.143(15)
IB	0.2500(18)	0.5	0.0	0.045(13)	0.143(4)

Table 5.6 Crystallographic parameters obtained from single crystal X-ray diffraction measurements carried out at 290 K on the sample AI200-$MAPbI_3$. $a = b = c =$ 12.6265(2) Å.

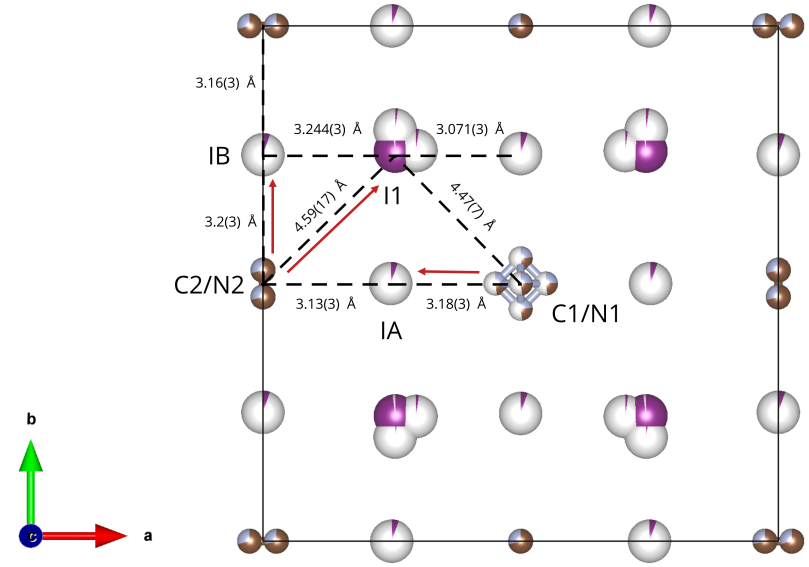

(a)

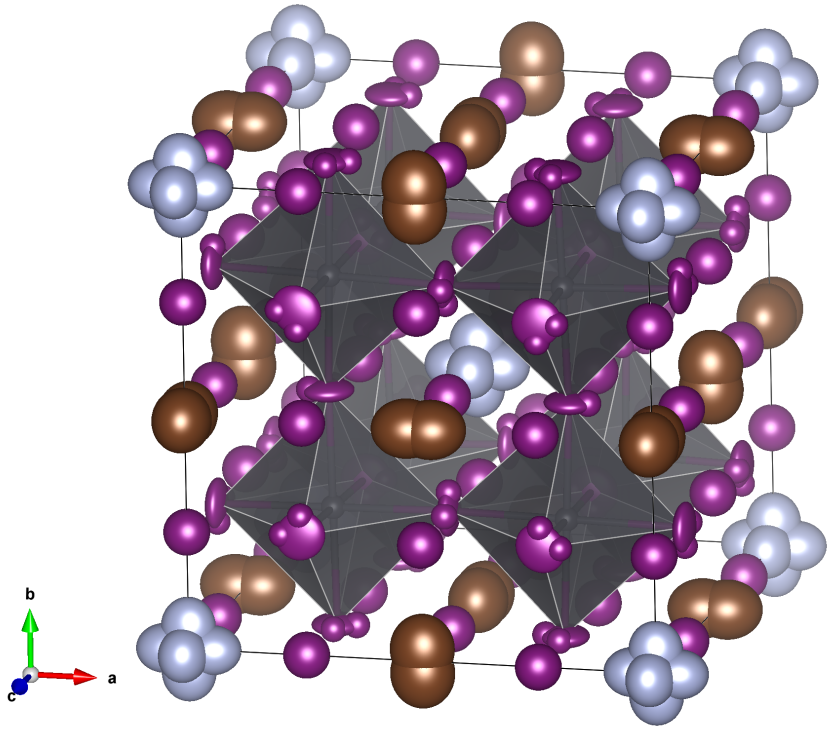

(b)

Fig. 5.18 (a) The bond lengths between the centre of mass for the two MA^+ sites and the interstitial iodide sites C1/N1-IA and C2/N2-IB. (b) A diagram showing the final structural model solved from single crystal X-ray diffraction measurements conducted at 290 K for the compound AI200-$MAPbI_3$.

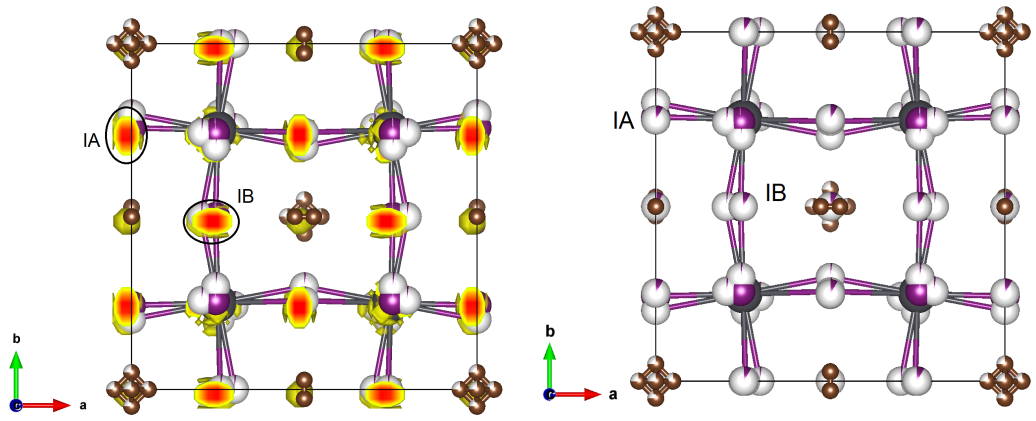

(a) (b)

Fig. 5.19 The calculated Fourier difference map and structure of AI200-$MAPbI_3$ derived from single crystal X-ray diffraction measured at 290 K, here yellow areas of density represent positive peaks in the difference Fourier map. (a) An area of significant density has been highlighted that sits at the centre face of the perovskite framework. (b) Additional partially occupied interstitial iodide sites IA and IB have been included in the structural model and have been highlighted accordingly.

Single Crystal X-ray Diffraction ADPs - $Im\bar{3}$						
Atom	U_{11}	U_{22}	U_{33}	U_{12}	U_{13}	U_{23}
Pb1	0.0435(10)	0.0435(10)	0.0435(10)	0.00002(7)	0.00002(7)	0.00002(7)
I1	0.189(3)	0.189(3)	0.0351(16)	0.000	0.000	0.0132(11)
C2	0.37(16)	0.26(3)	0.31(4)	0.000	0.000	0.000
N2	0.37(16)	0.26(3)	0.31(4)	0.000	0.000	0.000
N1	0.23(16)	0.26(9)	0.18(10)	0.000	0.000	0.000
C1	0.23(16)	0.26(9)	0.18(10)	0.000	0.000	0.000

Table 5.7 Refined atomic displacement parameters obtained from single crystal X-ray diffraction measurements carried out at 290 K on the sample AI200-$MAPbI_3$. $a = b = c = 12.6265(2)$ Å.

5.3.3 Phase I2-III - 160 K to 290 K

Through variable temperature synchrotron X-ray powder diffraction measurement a structural phase transition was identified at ≈ 270 K for the compound AI200-$MAPbI_3$. Subtle high 2θ angle peak splitting below 270 K (e.g. the [800] and [280] peak at ≈ 35.26 2θ and ≈ 36.5 2θ as shown in Figure 5.20) indicate the transition to a lower symmetry phase from the ambient temperature cubic phase I2-II. The phase was observed to exist down to 160 K where further peak splitting was observed.

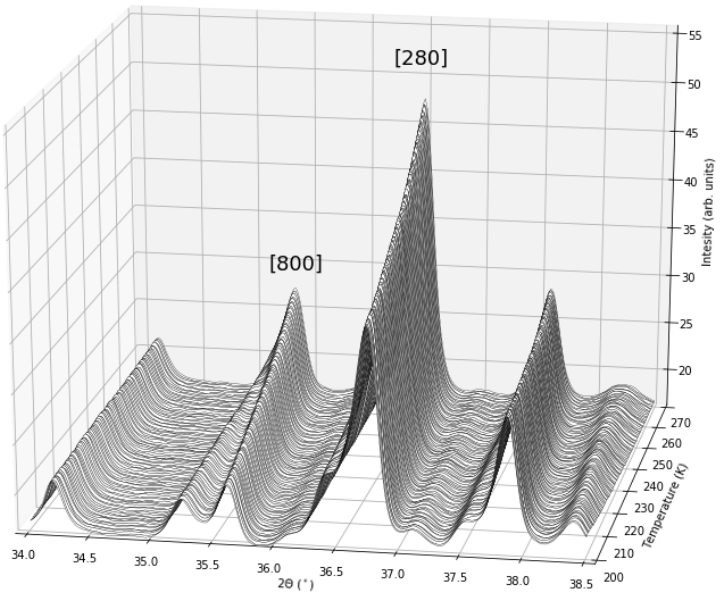

Fig. 5.20 Measured powder synchrotron diffraction data for temperatures between 270 K and 200 K for the compound AI200-$MAPbI_3$. The pattern has been indexed with respect to the cubic perovskite phase I2-II (described in Section 5.3.2) with respect to the lattice reflections labelled.

In order to characterise the structural phase I2-III single crystal X-ray diffraction measurements were conducted on the in-house dual-source Rigaku Oxford Diffraction Supernova diffractometer located at the University of Kent. The measurement was conducted at 220 K.

The reflections observed in the single crystal measurement were indexed with both tetragonal and orthorhombic crystal systems, the resulting unit cells showed lattice parameters close to cubic and from the single crystal pattern alone would likely have been indexed as such. The clear peak splitting identified in the powder data ruled out a cubic crystal type. A number of tetragonal space groups were trialled however all the resulting fits were poor with significantly high R-factors at the start of the structure determination process. Therefore, the structure was assigned an orthorhombic crystal system.

From the single crystal data 65 of 14513 reflections violated I-centring conditions, the intensity of which is less than 0.4 mean I/σ. Hence, I centring was chosen for the unit cell orthorhombic type system. This narrowed the choice of space group to *Immm*, Imm2 and I222, a list generated by automatic space group determination routines carried out by GRAL.

The measured datum has been refined with a structure solution for all three space group options: *I222*, *Imm2* and *Immm*. Twinning complicated the structure determination process, an issue that has caused significant confusion in the literature over proper space group assignment for all structural phases of prototypical $MAPbI_3$ [197]. Here, a single twin component was refined for the final structure solution for each space group.

A starting structural model was generated through direct methods where initial positions of heavy elements including Pb and I were located for each space group option. The results were consistent across each space group tested, describing a perovskite framework constructed from a series of connected PbI_6 octahedra.

Space Group	R_{int} (%)	R_{sigma} (%)	R1 (%)	R_{all} (%)	wR(F^2) (%)	S	Parameters
I222	4.83	2.11	3.92	12.16	4.99	1.025	92
Imm2	4.7	2.32	4.13	13.2	5.18	1.052	97
Immm	4.91	1.64	3.76	11.78	4.38	1.099	72

Table 5.8 The refinement R factors for each of the possible space groups options for the structure of AI200-$MAPbI_3$ derived from a single crystal X-ray diffraction measurement conducted at 220 K.

The structure refinement process was carried out for each of the possible space group options, for which the the final refinement fit factors are shown in Table 5.8. The space group *Immm* was chosen for the final structure solution where lower values for the the fit factors R1, R_{all}, wR(F^2) and S were obtained for a lower number of refinement parameters. The final structure refinement process was carried out using SHELXL for the space group *Immm* and is described in detailed below.

Assignment of PbI_6 Octahedra

The PbI_6 octahedra is modelled by a single lead site (labelled Pb1 in the structural model) and three iodide sites (labelled I1, I2 and I3 in the structural model) allowing for a three-tilt system, the octahedra is located at Wyckoff position *k* (a special reflection position for the space group *Immm*) and exhibits tilting about all three crystallographic axis denoted by Glazer notation $a^+b^+c^+$. The specific tilt angle about each crystallographic axis are described by the bond angles Pb1-I1-Pb1, Pb1-I2-Pb1 and Pb1-I3-Pb1 with values 159.14(14)°, 159.9(3)° and 170.40(19)° respectively.

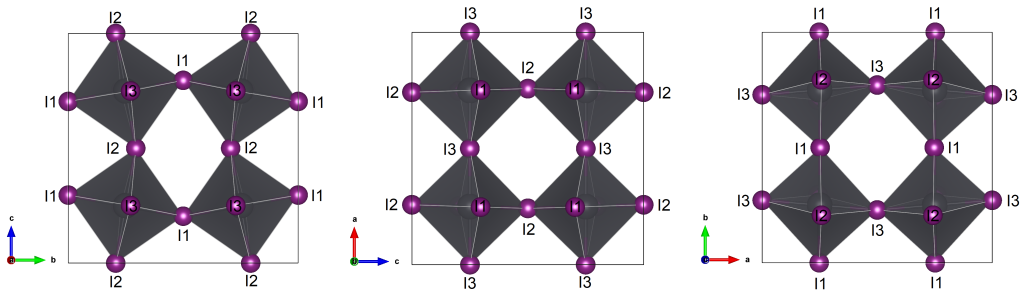

(a) (b) (c)

Fig. 5.21 The refined PbI_6 framework for the compound AI200-$MAPbI_3$ at 220 K derived from single crystal X-ray diffraction measurements. The atom labels correspond to the final structural model as described in Table 5.11. (a) The model is orientated along the *a*-axis. (b) The model is orientated along the *b*-axis. (c) The model is orientated along the *c*-axis.

Further Disorder of PbI_6 Framework

Significant maxima in the calculated difference electron density maps (as shown in Figure 5.23) located close to the iodide sites I1 and I2 highlight significant disorder in the tilting of the octahedral framework. This was modelled in the final structure solution through additional partially occupied iodide sites labelled I1B, I2AA and I2AB.

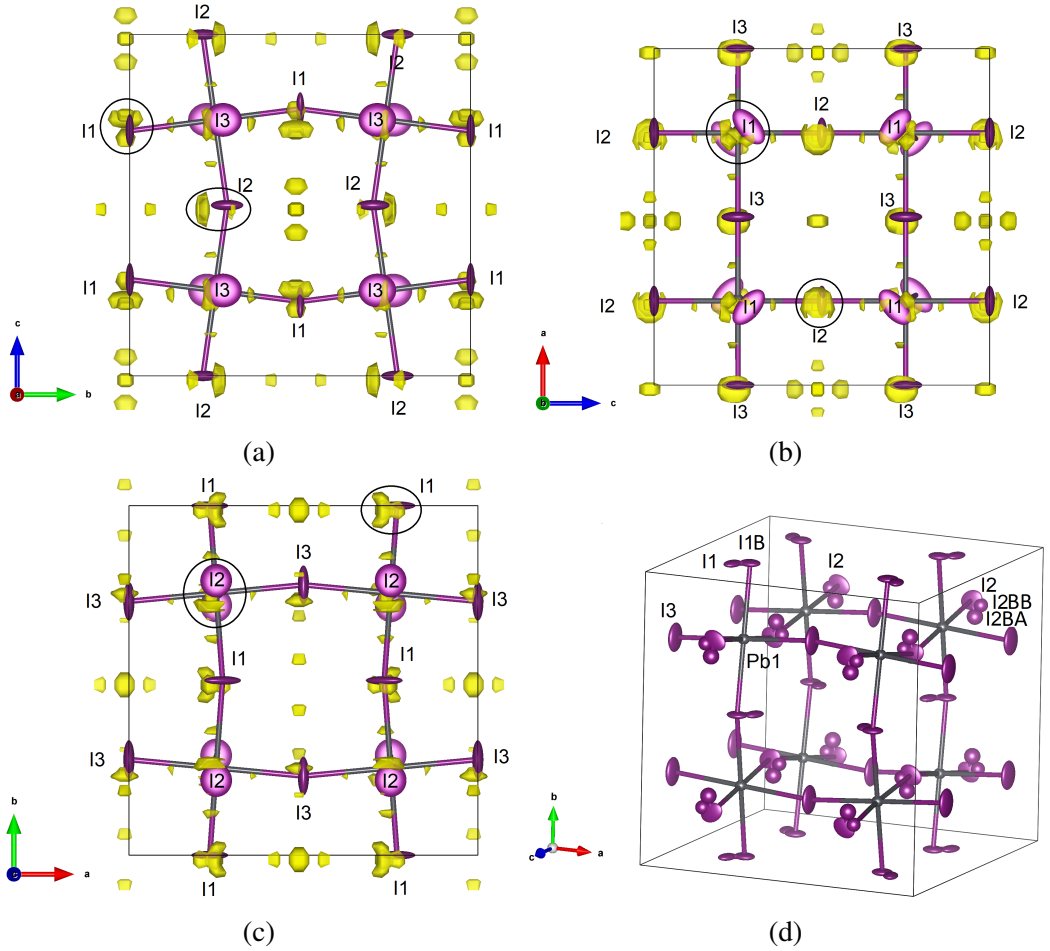

Fig. 5.22 Both the calculated Fourier difference map and structure of AI200-$MAPbI_3$ derived from single crystal X-ray diffraction measured at 220 K. Yellow areas of density represent positive peaks in the difference Fourier map, areas corresponding to density assigned to partially occupied iodide sites I1B, I2BA, I2BB are circled. The atom labels correspond to the final structural model as described in Table 5.11. (a) The model is orientated along the *a*-axis. (b) The model is orientated along the *b*-axis. (c) The model is orientated along the *c*-axis. (d) A diagram showing the atomic positions corresponding to the PbI_6 framework.

Assignment of MA^+ Cation

The position of the perovskite A-site MA^+ cation sites were located through additional maxima in the calculated difference electron density shown in Figure 5.23. The structural model consists of four distinct MA^+ cation sites, that due to the symmetry of the system, results in eight distinct MA^+ cation sites for the unit cell, each located at the centre of a respective perovskite void. Three of the four MA^+ cation sites are ordered along a single crystallographic axis. Due to the mirror symmetry of the space group *Immm* both ends of the MA^+ unit are modelled by a single carbon (C) and nitrogen (N) atom, where each pair of carbon and nitrogen atoms are restricted to share the same position, occupancy and thermal parameters in the refinement. These are labelled C1/N1, C2/N2 and C3/N3 in the structural model and orientated along the crystallographic axis *a*, *b* and *c* respectively. A fourth MA^+ cation is found to be orientationally disordered and split across two sites. It is modelled by two carbon and nitrogen pairs, where each respective pair of carbon and nitrogen atoms are restricted to share the same position, occupancy and thermal parameters. These are labelled C4A/N4A and C4B/N4B in the structural model, the result of this split site is a MA^+ cation that shows orientational disorder along the crystallographic *a* and *c*-axis respectively.

A change in the C-N bond length was also observed across the four MA^+ sites. C-N bond lengths of 0.80(16) Å, 1.18(11) Å, 1.2(4) Å, 1.65(13) Å and 2.25(13) Å for the cations C1-N1, C2-N2, C3-N3, C4A-N4A and C4B-N4B respectively. This discrepancy was also observed for the ambient temperature phase I2-II. For prototypical $MAPbI_3$, X-ray diffraction data has repeatedly resulted in a shorter C-N bond length for our own single crystal studies at ambient temperature (chapter 3). However, following the results reported in Section 5.2, the formation of the compound AI200-$MAPbI_3$ results from annealing at high temperature under a high iodine partial pressure. It was also shown that as the annealing temperature increases two impurity phases NH_4PbI_3 and PbI_2 are formed. It is proposed here that the reduced C-N bond distance observed, may result from the partial population of NH_4 onto the MA^+ site. However, the separation of these two molecules can't be refined by the diffraction measurements here due to the disorder of the site.

Interstitial Iodine

Following the assignment of the MA^+ cations, further calculated difference electron maps showed significant electron density peaks within the centre faces of the perovskite framework as shown in Figure 5.24a, these were assigned as interstitial

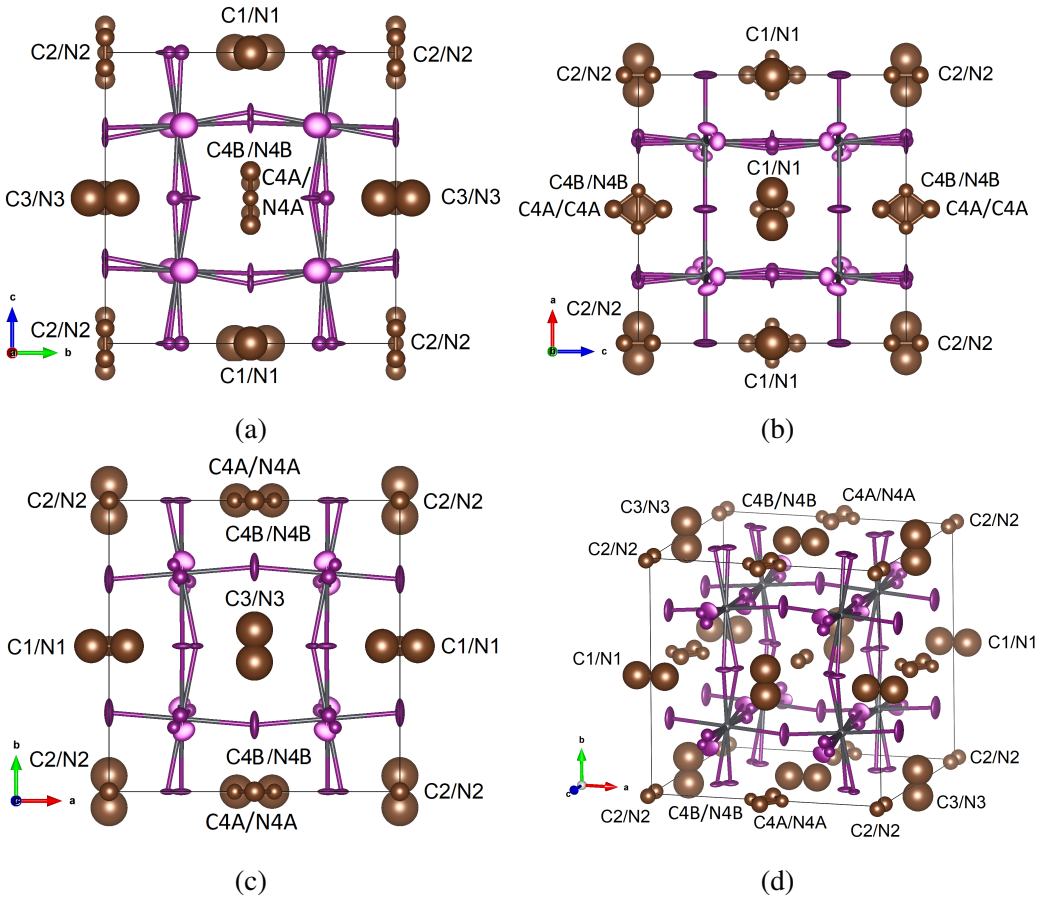

Fig. 5.23 Four distinct MA^+ sites for the compound AI200-$MAPbI_3$ derived from single crystal X-ray diffraction measurements conducted at 220 K. The diagrams highlight the positions of the atomic sites C1/N1, C2/N2, C3/N3, C4A/N4A and C4B/N4B. (a) The model is orientated along the *a*-axis. (b) The model is orientated along the *b*-axis. (c) The model is orientated along the *c*-axis. (d) A diagram showing the atomic positions corresponding to four distinct MA^+ sites.

iodide sites in the structure refinement. However, unlike the high temperature phases I2-I and I2-II, a interstitial site was not observed for all perovskite faces. In order to populate the observed interstitial sites in the refined structural model, four additional iodide atoms were added to the structural model labelled IAA, IAB, IBA and IBB. From the structural refinement, two distinct groups of interstitial iodide sites were identified amongst the total four interstitial atoms added to the model, these groups reflect the common occupancy the pairs share (IAX and IBX where X = A or B, coloured red and green in Figure 5.24 respectively).

The Pb:I composition of the PbI_6 framework is 1:2.889±0.037, including the interstitial site the overall Pb:I composition is 1:3.089±0.049, the interstitial component of this being 0.20±0.032.

Low Temperature Ordering of Interstitial Iodine

Following analysis of the occupancy of each site for the phase I2-III, specifically those partially occupied sites, it became apparent that the phase I2-III is made up of two distinct configurations of both the framework, MA^+ orientation and ordering of the interstitial iodide sites at low temperature. The occupancy of two of the iodide sites that make up the framework arms I1 and I2 are split across the sites I1B and I2BA/I2BB, with a split of the occupancy of 60.82 % and 39.12 % for sites I1 and I1B and 63.21 % and 36.79 % for sites I2 and I2BA/I2BB respectively. The split MA^+ cation site C4A/N4A and C4B/N4B are split 66.66 % and 33.33 % respectively. Finally, the occupancy of the interstitial sites IAA/IAB and IBA/IBB are split 70.00 % and 30.00 % respectively. Given the occupancy splits of these sites, two distinct configurations of the structure have been derived that are grouped by the sites I1, I2, C4A/N4A, IAA and IAB for configuration 1 (as presented in Table 5.9) and I1B, I2BA, I2BB, C4B/N4B, IBA and IBB for configuration 2 (as presented in Table 5.10) where the sites Pb1, I3, C1/N1, C2/N2, C3/N3 are common across both configurations. A plot of the structure for each configuration is shown in Figure 5.25a and Figure 5.25b for configuration 1 and 2 respectively.

For each of the configurations 1 and 2 shown on Figure 5.25a and Figure 5.25b respectively, the nature of the tilting of the perovskite framework, the orientation of the MA^+ and the location of the interstitial iodine sites are found to correlate. For configuration 1 it is found that the positions of the iodide sites I1, I2 result in an octahedral tilt away from the direction of the C-N bond of the MA^+ described by the site C4A/N4A as shown in Figure 5.26c. The same is found for configuration 2, where the iodide sites I1B, I2BA and I2BB tilt away from the direction of the MA^+ C-N bond described by the site C4B/N4B as shown in Figure 5.26d. It was found

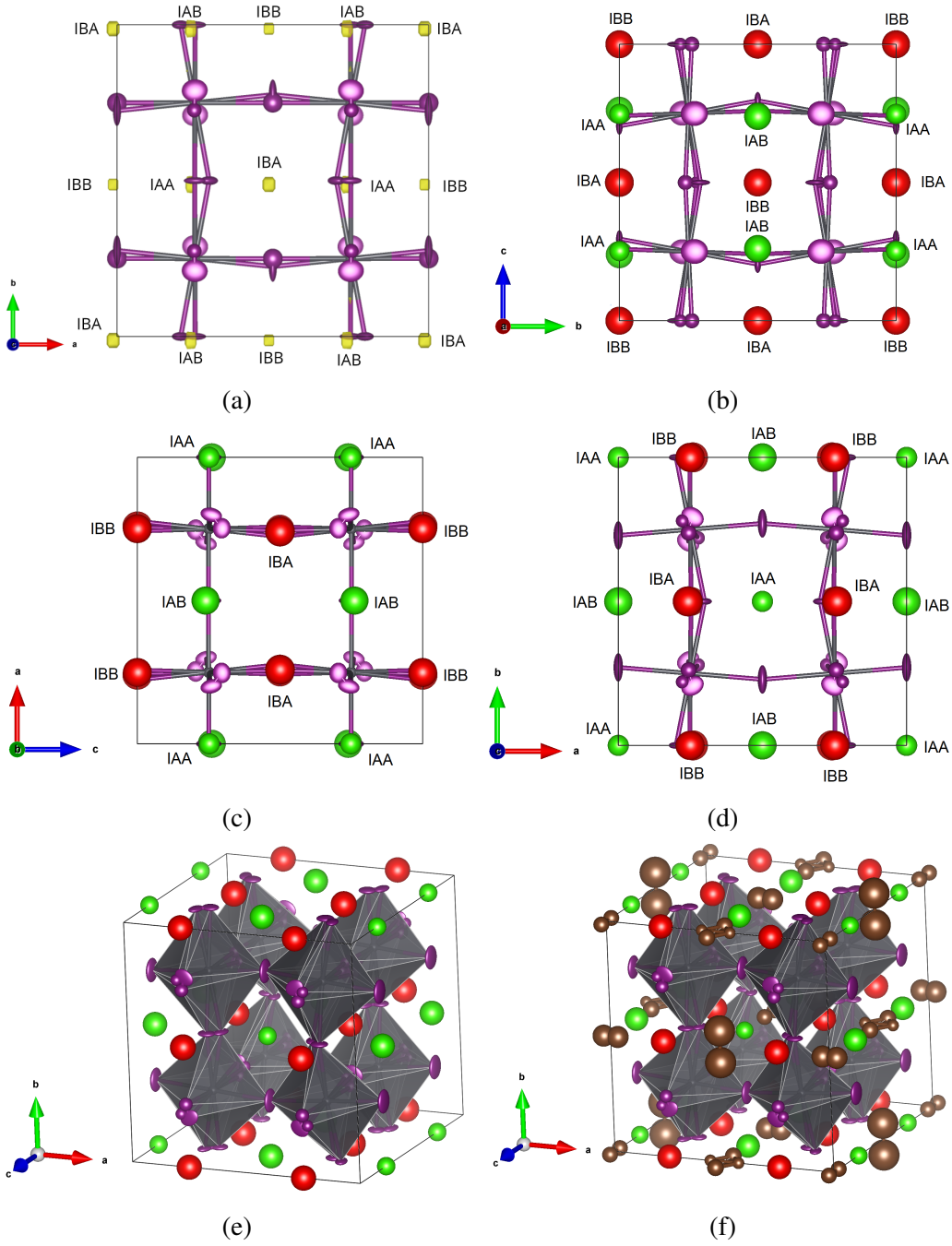

Fig. 5.24 The position of additional interstitial iodide sites have been added to figures (b), (c), (d) and (e) and coloured according to the grouping for which they apply with sites IAA and IAB coloured red and sites IBA and IBB coloured green. Atoms associated with MA^{+} cations have been removed for clarity from (a), (b), (c) and (d). (a) The model is orientated along the c-axis with calculated difference electron maps showing significant electron density peaks within the centre faces of the perovskite framework. Yellow areas of density represent positive peaks in the difference Fourier map.

Phase I2-III Configuration 1 - *Immm*					
Atom	x	y	z	Occupancy	U (Å^3)
Pb1	0.75	0.25	0.25	1	0.0248(3)
I1	0.7476(9)	0.50	0.2400(11)	0.354(18)	0.048(3)
I2	0.7579(9)	0.2936(5)	0.50	0.198(18)	0.0617(14)
I3	0.50	0.2291(4)	0.2494(5)	1.01(2)	0.1041(16)
C1	0.468(7)	0.00	0.50	0.38(7)	0.14(4)
N1	0.468(7)	0.00	0.50	0.38(7)	0.14(4)
C2	0.50	0.50	0.551(4)	0.43(6)	0.072(13)
N2	0.50	0.50	0.551(4)	0.43(6)	0.072(13)
C3	0.50	0.431(9)	0.00	0.57(10)	0.28(8)
N3	0.50	0.431(9)	0.00	0.57(10)	0.28(8)
C4A	0.50	0.00	0.090(5)	0.34(7)	0.08(2)
N4A	0.50	0.00	0.090(5)	0.34(7)	0.08(2)
IAA	0.741(5)	0.00	0.50	0.14(4)	0.18(4)
IAB	0.749(5)	0.50	0.50	0.14(4)	0.17(4)

Table 5.9 Configuration 1 crystallographic parameters obtained from single crystal X-ray diffraction measurements carried out at 220 K on the sample AI200-$MAPbI_3$ a = 12.5316(9) Å, b = 12.5213(10) Å, c = 12.5113(9) Å.

Phase I2-III Configuration 2 - *Immm*					
Atom	x	y	z	Occupancy	U (Å^3)
Pb1	0.75	0.25	0.25	1	0.0248(3)
I1B	0.7006(8)	0.50	0.2408(11)	0.354(18)	0.048(3)
I2BA	0.7440(14)	0.2384(18)	0.50	0.195(18)	0.050(4B
I2BB	0.7574(9)	0.2936(5)	0.50	0.16(2)	0.37(5)
I3	0.50	0.2291(4)	0.2494(5)	1.01(2)	0.1041(16)B
C1	0.468(7)	0.00	0.50	0.38(7)	0.14(4)
N1	0.468(7)	0.00	0.50	0.38(7)	0.14(4)
C2	0.50	0.50	0.551(4)	0.43(6)	0.072(13)
N2	0.50	0.50	0.551(4)	0.43(6)	0.072(13)
C3	0.50	0.431(9)	0.00	0.57(10)	0.28(8)
N3	0.50	0.431(9)	0.00	0.57(10)	0.28(8)
C4B	0.436(5)	0.00	0.00	0.17(5)	0.04(2)
N4B	0.436(5)	0.00	0.00	0.17(5)	0.04(2)
IBA	0.50	0.50	0.752(5)	0.06(2)	0.09(3)
IBB	0.50	0.00	0.239(13)	0.06(2)	0.16(6)

Table 5.10 Configuration 2 crystallographic parameters obtained from single crystal X-ray diffraction measurements carried out at 220 K on the sample AI200-$MAPbI_3$ a = 12.5316(9) Å, b = 12.5213(10) Å, c = 12.5113(9) Å.

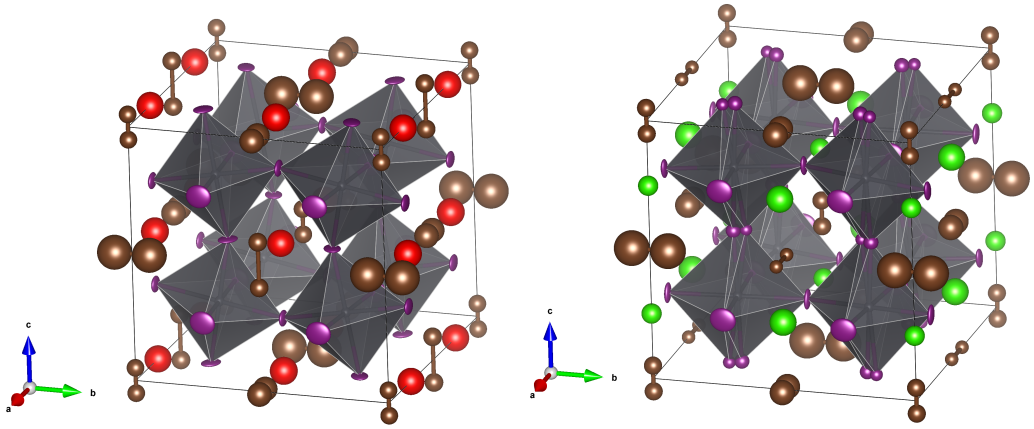

(a) (b)

Fig. 5.25 (a) Configuration 1 and (b) configuration 2 for the compound AI200-$MAPbI_3$ at 220 K.

that the MA^+ sites C1/N1, C2/N2 and C3/N3 conform to the nature of the perovskite tilting for both configurations.

The locations of interstitial iodine sites IAA/IAB and IBA and IBB are found to sit perpendicular to the direction of the C-N bond of the MA^+ sites C4A/N4A and C4B/N4B respectively. This can be seen in Figure 5.27a and Figure 5.27b for configurations 1 and 2 respectively, where the coordination of the MA^+ cation for both configurations is shown. The refined positions of interstitial iodine sites IAA/IAB and IBA/IBB for configuration 1 and 2 respectively demonstrate low temperature ordering of interstitial iodine. The positions for which ensure maximum separation of interstitial sites. Figure 5.28b and Figure 5.28a show the coordination of the interstitial sites with the surrounding framework for configuration 1 and 2 respectively. From this we see that for configuration 2, which contains the more populated interstitial sites of the two configurations, exhibits a shorter Pb1-Pb1 bond length where the framework has contracted around this site, such that the surrounding Pb-I arms exhibit more tilting. This results in the relaxing of lattice parameter constraints and therefore a drop in symmetry from cubic to orthorhombic.

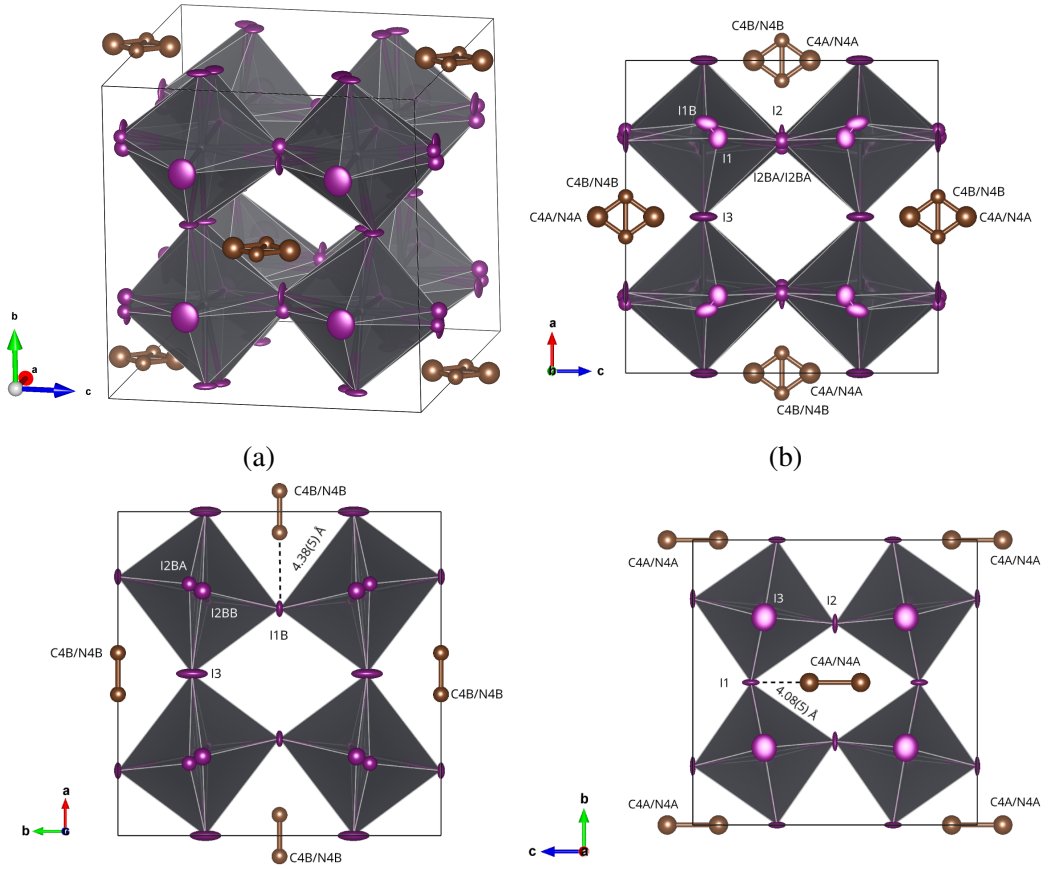

Fig. 5.26 (a) and (b) the coordination of the MA^+ for both configurations and (c) and (d) for configuration 1 and configuration 2 respectively, as described by Table 5.11 for the compound AI200-$MAPbI_3$ at 220 K.

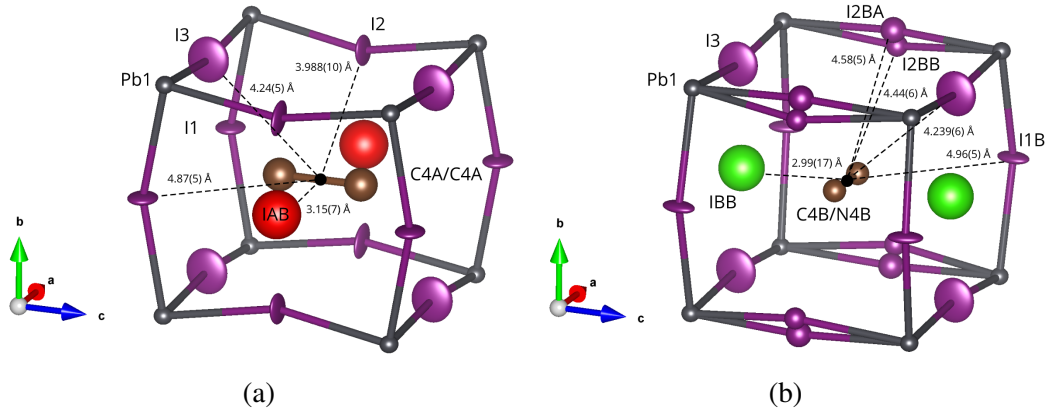

Fig. 5.27 The coordination for (a) configuration 1 and (b) configuration 2 of the MA^+ site described by the atomic sites C4/N4 and C4A/N4A and the iodide sites I1 and I1A as described by Table 5.11 compound AI200-$MAPbI_3$. This model was solved from single crystal X-ray diffraction measurement performed at 220 K on the compound AI200-$MAPbI_3$.

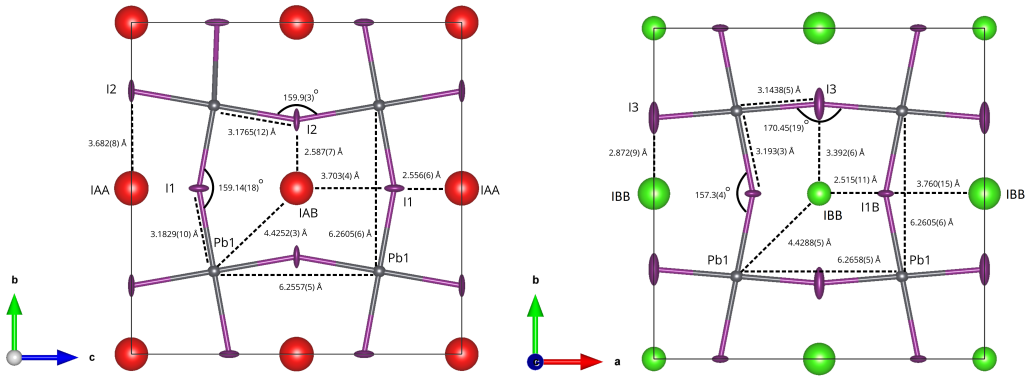

(a) (b)

Fig. 5.28 The coordination of interstitial iodine sites for (a) configuration 1 and (b) configuration 2 as described by Table 5.11 compound AI200-$MAPbI_3$ at 220 K.

Single Crystal X-ray Diffraction Atomic Coordinated - *Immm*					
Atom	x	y	z	Occupancy	U (Å^3)
Pb1	0.75	0.25	0.25	1	0.0248(3)
I1	0.7476(9)	0.50	0.2400(11)	0.354(18)	0.048(3)
I1B	0.7006(8)	0.50	0.2408(11)	0.354(18)	0.048(3)
I2	0.7579(9)	0.2936(5)	0.50	0.198(18)	0.0617(14)
I2BA	0.7440(14)	0.2384(18)	0.50	0.195(18)	0.050(4B
I2BB	0.7574(9)	0.2936(5)	0.50	0.16(2)	0.37(5)
I3	0.50	0.2291(4)	0.2494(5)	1.01(2)	0.1041(16)
C1	0.468(7)	0.00	0.50	0.38(7)	0.14(4)
N1	0.468(7)	0.00	0.50	0.38(7)	0.14(4)
C2	0.50	0.50	0.551(4)	0.43(6)	0.072(13)
N2	0.50	0.50	0.551(4)	0.43(6)	0.072(13)
C3	0.50	0.431(9)	0.00	0.57(10)	0.28(8)
N3	0.50	0.431(9)	0.00	0.57(10)	0.28(8)
C4A	0.50	0.00	0.090(5)	0.34(7)	0.08(2)
N4A	0.50	0.00	0.090(5)	0.34(7)	0.08(2)
C4B	0.436(5)	0.00	0.00	0.17(5)	0.04(2)
N4B	0.436(5)	0.00	0.00	0.17(5)	0.04(2)
IAA	0.741(5)	0.00	0.50	0.14(4)	0.18(4)
IAB	0.749(5)	0.50	0.50	0.14(4)	0.17(4)
IBA	0.50	0.50	0.752(5)	0.06(2)	0.09(3)
IBB	0.50	0.00	0.239(13)	0.06(2)	0.16(6)

Table 5.11 Crystallographic parameters obtained from single crystal X-ray diffraction measurements carried out at 220 K on the sample AI200-$MAPbI_3$ a = 12.5316(9) Å, b = 12.5213(10) Å, c = 12.5113(9) Å.

Single Crystal X-ray Diffraction ADPs - *Immm*						
Atom	U_{11}	U_{22}	U_{33}	U_{12}	U_{13}	U_{23}
Pb1	0.0269(10)	0.0224(8)	0.0253(5)	0.00000(9)	-0.0002(3)	-0.0004(3)
I1	0.085(4)	0.0096(7)	0.0642(17)	0.000	0.002(2)	0.000
I1B	0.043(3)	0.0091(15)	0.093(6)	0.000	-0.013(3)	0.000
I2	0.099(3)	0.079(2)	0.0068(11)	0.000	0.000	-0.020(2)
I3	0.0177(13)	0.161(2)	0.134(3)	-0.0024(17)	0.000	0.000

Table 5.12 Refined atomic displacement parameters obtained from single crystal X-ray diffraction measurements carried out at 220 K on the sample AI200-$MAPbI_3$ a = 12.5316(9) Å, b = 12.5213(10) Å, c = 12.5113(9) Å.

5.3.4 Phase I2-IV - 100 K to 160 K

Through variable temperature synchrotron powder X-ray diffraction measurements a low temperature structural phase transition was identified for the compound AI200-$MAPbI_3$ at 160 K. The transition temperature was determined through the splitting of the reflection [400] at 160 K.

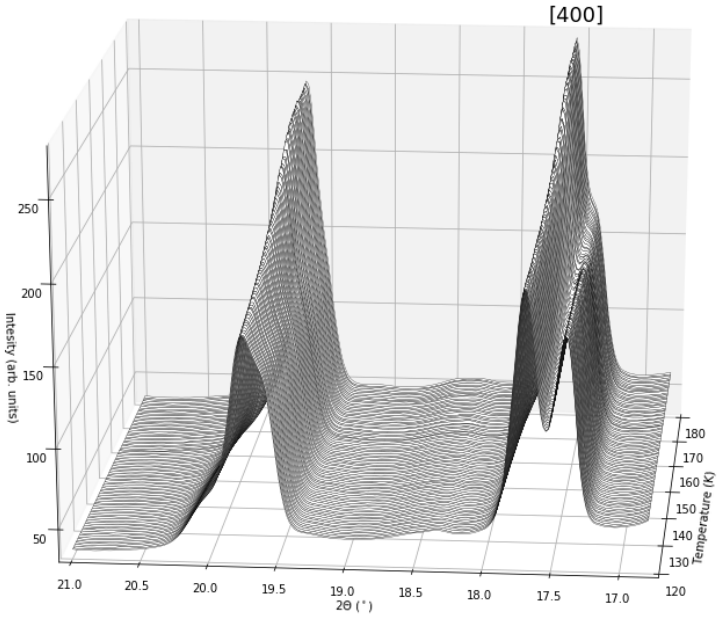

Fig. 5.29 Measured powder synchrotron diffraction data for temperatures between 180 K and 100 K for the compound AI200-$MAPbI_3$ indexed with respect to phase I2-III [92].

This transition temperature corresponds to the low temperature structural phase transition of prototypical $MAPbI_3$ from tetragonal phase II (I4/m) to the orthorhom-

bic space group *Pnma* phase III. For AI200-$MAPbI_3$, the low temperature phase was found to be successfully index with the orthorhombic structural phase III for prototypical $MAPbI_3$. The structure for which was adapted from those published by Weller *et al*. [47] upon which Rietveld refinement of the synchrotron powder X-ray diffraction data was performed. This phase has been given the denotation I2-IV.

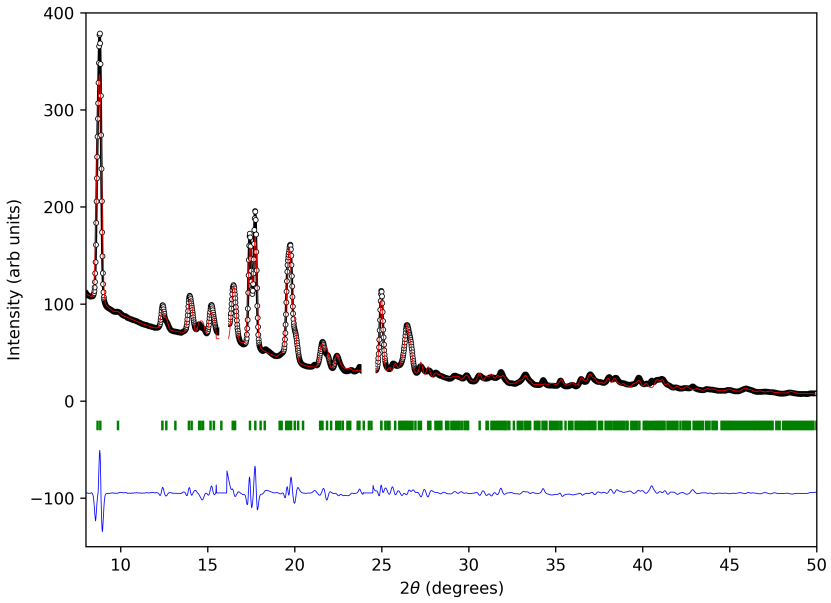

Fig. 5.30 Rietveld refinement of powder synchrotron diffraction data conducted at 100 K for the compound AI200-$MAPbI_3$ R_p = 3.79 % and R_{wp} = 5.18 %. Impurity peaks have been excluded from the refinement.

The refined model exhibits tilting of the PbI_6 octahedral framework described by Glazer notation $a^-b^+a^-$. The perovskite voids are populated by MA^+ cations that are fully ordered with a C-N bond that lies normal to the b-axis. The crystallographic structural model is assigned a single lead atom (Pb1) and two distinct iodide sites (I1 and I2) as shown in Figure 5.31a and Figure 5.31b. The positions of the two iodide sites make two Pb-I-Pb bond angles of 154.4(2)° and 165.9(4)° for the angles Pb1-I2-Pb1 and Pb1-I1-Pb1 respectively. The MA^+ cation is described by two distinct carbon (C1) and nitrogen (N1) with a bond distance of 1.87(13) Å at 100 K.

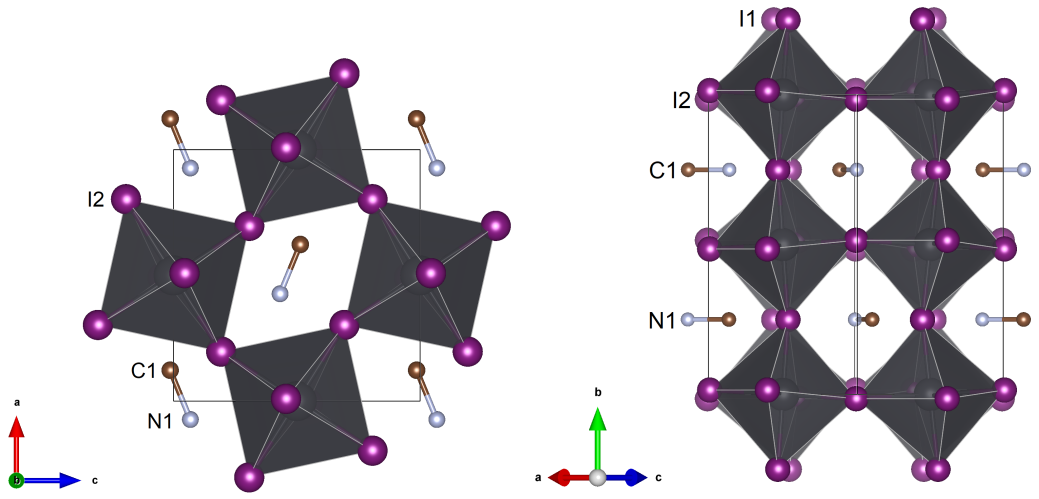

(a) (b)

Fig. 5.31 The structural phase I2-IV for the compound AI200-$MAPbI_3$ as refined from Rietveld refinement of powder diffraction data at 100 K.

Powder X-ray Diffraction Atomic Coordinated - *Pnma*					
Atom	x	y	z	Occupancy	U (Å^3)
Pb1	0.50000	0.00000	0.00000	1.013(15)	0.068(4)
I1	0.5236(17)	0.25000	1.0346(19)	1.00	0.140(12)
I2	0.1997(7)	-0.0116(7)	0.1912(8)	1.00	0.098(6)
N1	0.93380	0.75000	0.03140	1.00000	0.23(4)
C1	0.92700	0.25000	0.05400	1.00000	0.23(4)

Table 5.13 Crystallographic parameters obtained from powder crystal X-ray diffraction measurements carried out at 100 K on the sample AI200-$MAPbI_3$. a = 8.8364(3) Å, b = 12.6033(4) Å and c = 8.6874(4) Å.

Single Crystal X-ray Diffraction ADPs - *Pnma*						
Atom	U_{11}	U_{22}	U_{33}	U_{12}	U_{13}	U_{23}
Pb1	0.045(3)	0.060(4)	0.099(5)	0.006(6)	-0.015(6)	-0.057(6)
I1	0.121(13)	0.057(6)	0.241(17)	0.00000	-0.154(12)	0.00000
I2	0.088(5)	0.080(5)	0.127(6)	-0.025(7)	0.043(5)	0.031(7)

Table 5.14 Refined atomic displacement parameters obtained from powder crystal X-ray diffraction measurements carried out at 100 K on the sample AI200-$MAPbI_3$. a = 8.8364(3) Å, b = 12.6033(4) Å and c = 8.6874(4) Å.

5.3.5 Structure Determination Summary

For this section we report that between 400 K and 100 K, AI200-$MAPbI_3$ exhibits four structural phases as shown on Figure 5.32. Between 400 K and 315 K a simple cubic perovskite phase has been assigned the space group $Pm\bar{3}m$ and denoted I2-I (a = 6.35980(10) Å). This phase exhibits a zero tilt PbI_6 octahedral framework, at the centre of the perovskite framework the MA^+ cation is found to be completely orientational disordered. An interstitial iodide site is found to occupy the centre of each of the perovskite faces.

As the temperature is reduced, at 315 K the compound undergoes a structural phase transition that results in a doubling of the unit cell (a = 12.6265(2) Å) and is described by the space group $Im\bar{3}$. This phase transition is driven by in-phase tilting of the octahedral framework about each of the crystallographic axis. The framework tilting results in two distinct perovskite cavity sizes, the larger of the two is found to be occupied by a MA^+ cation that is orientationally disordered. The second cavity is occupied by a MA^+ cation where the C-N bond orders along a crystallographic axis such that the tilting of the perovskite framework conforms to the ordering of MA^+ cation. Consistent with the high temperature phase I2-I an interstitial iodide site is found to occupy the centre face of the perovskite framework.

As the temperature is reduced further, at 270 K the structure transitions to an orthorhombic phase described by the space group *Immm* (a = 12.5316(9) Å, b = 12.5213(10) Å and c = 12.5113(9) Å). The PbI_6 octahedral framework exhibits independent in-phase tilts about each of the crystal axis. Two of the framework iodine sites were found to be comprised of multiple partially occupied iodide sites demonstrating considerable structural disorder. The ordering of the MA^+ was increased compared with the phase I2-II with all but a single MA^+ site found to order along a specific crystallographic axis. The disordered MA^+ site was found to be orientationally disordered about the *a*-*b* unit cell plane. Interstitial iodide sites were also identified for this phase, however, not all of the perovskite framework faces are occupied. The occupancy of the split framework iodide sites, disordered MA^+ sites and interstitial iodine sites were found to have an approximate 30:70 split. These two configurations of the structure represent different ordering of the MA^+ cation and interstitial iodine sites at low temperature.

At 160 K a further structural phase transition was observed, the structure at this temperature is described by the orthorhombic space group *Pnma* (phase I2-IV). The structure exhibits tilting of the PbI_6 octahedral framework described by Glazer

notation $a^-b^+a^-$. At the centre of the perovskite voids the MA^+ cations are fully ordered with a C-N bond that lie normal to the b-axis.

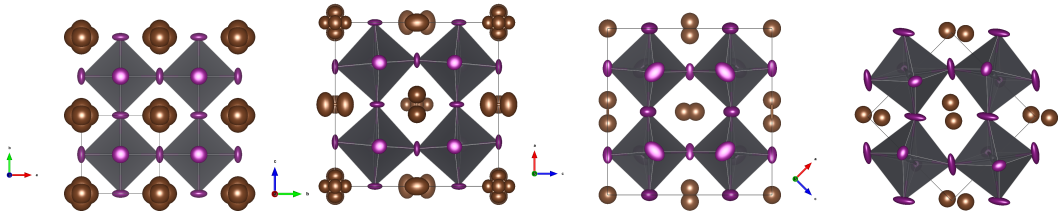

(a) (b) (c) (d)

Fig. 5.32 (a), (b), (c) and (d) show the structure of AI200-$MAPbI_3$ for the structural phases I2-I, I2-II, I2-III and I2-IV respectively highlighting the corner sharing PbI_6 framework and configuration of the MA^+ cation.

5.4 Comparison Against Prototypical $MAPbI_3$

The results presented in the section above outlines four structural phases observed between 400 K and 160 K (labelled I2-I, I2-II, I2-III and I2-IV) for the compound AI200-$MAPbI_3$. Here, significant changes to the structure of prototypical $MAPbI_3$ have been observed following a post synthesis thermal annealing iodine treatment. Specifically, this demonstrates for the first time the synthesis of a new derivative compound of $MAPbI_3$, AI200-$MAPbI_3$ that has very contrasting structural properties. In this section the temperature dependent structure of the compound AI200-$MAPbI_3$ is compared against prototypical $MAPbI_3$ through variable temperature synchrotron X-ray powder diffraction measurements performed using the PILATUS@SNBL diffractometer between 400 K and 100 K [92]. Following analysis of the data, significant differences in the temperature dependent structure of prototypical $MAPbI_3$ and AI200-$MAPbI_3$ are observed. The change in observed diffraction and lattice parameters between 400 K and 160 K, across the respective phase transitions are highlighted in Figure 5.33a, Figure 5.33b, Figure 5.33a and Figure 5.33b for prototypical $MAPbI_3$ and AI200-$MAPbI_3$ respectively. The incremental change in lattice parameters observed for AI200-$MAPbI_3$ across each phase transition indicates second order transitions, this contrasts the first order transition observed for prototypical $MAPbI_3$ at 160 K.

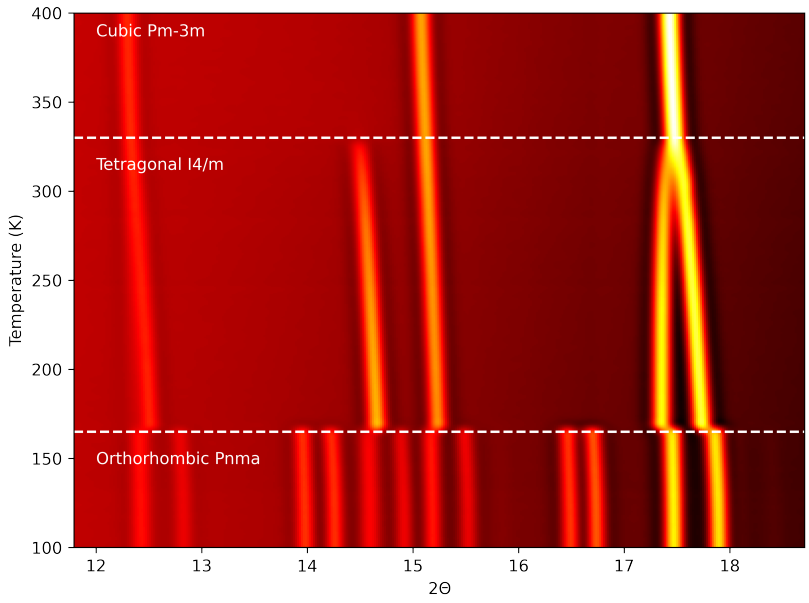

(a)

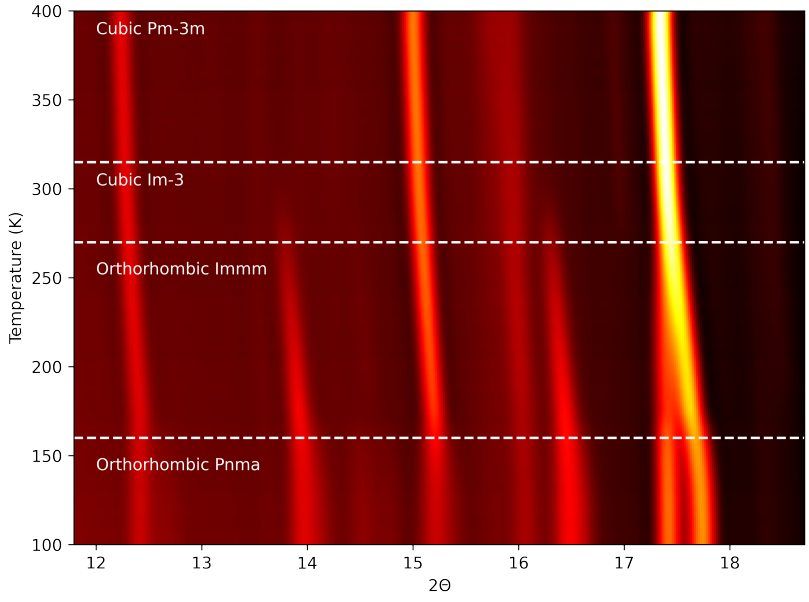

(b)

Fig. 5.33 Measured diffraction intensity between 400 K and 100 K for both (a) prototypical $MAPbI_3$ and (b) AI200-$MAPbI_3$.

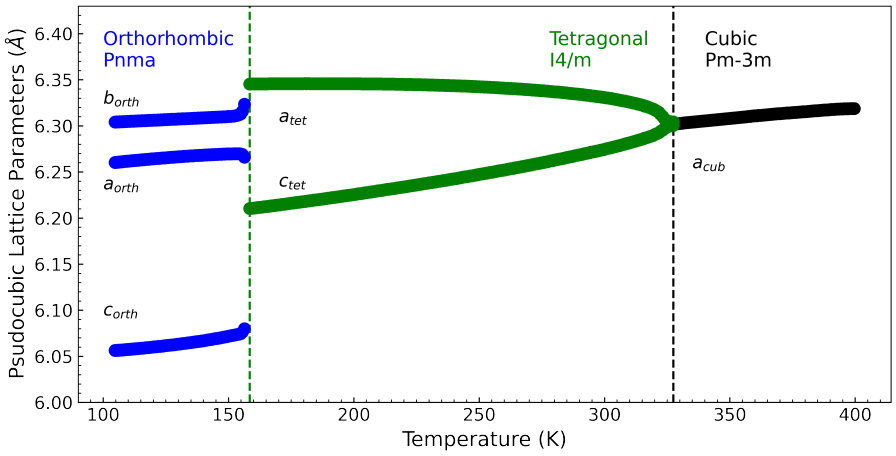

(a)

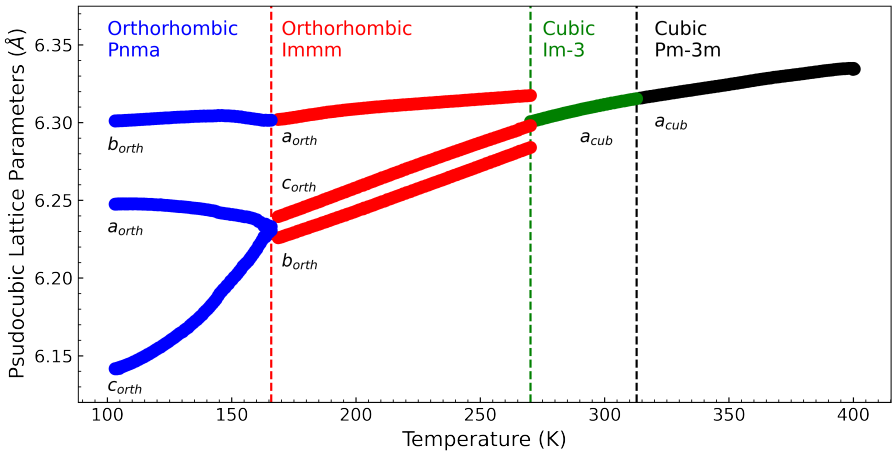

(b)

Fig. 5.34 Reduced lattice parameters as a function of temperature for both (a) prototypical $MAPbI_3$ and (b) AI200-$MAPbI_3$ derived from Rietveld refinement of powder diffraction data measured between 400 K and 100 K.

5.4.1 Comparison of $Pm\bar{3}m$ Phases

At high temperature (>340 K) both prototypical $MAPbI_3$ and AI200-$MAPbI_3$ exhibit a simple cubic perovskite structure described by the space group $Pm\bar{3}m$. For both samples the structure solution was derived from previous single crystal diffraction studies conducted on both samples and presented in Section 5.3.1 for AI200-$MAPbI_3$ and in Appendix A.3 for prototypical $MAPbI_3$.

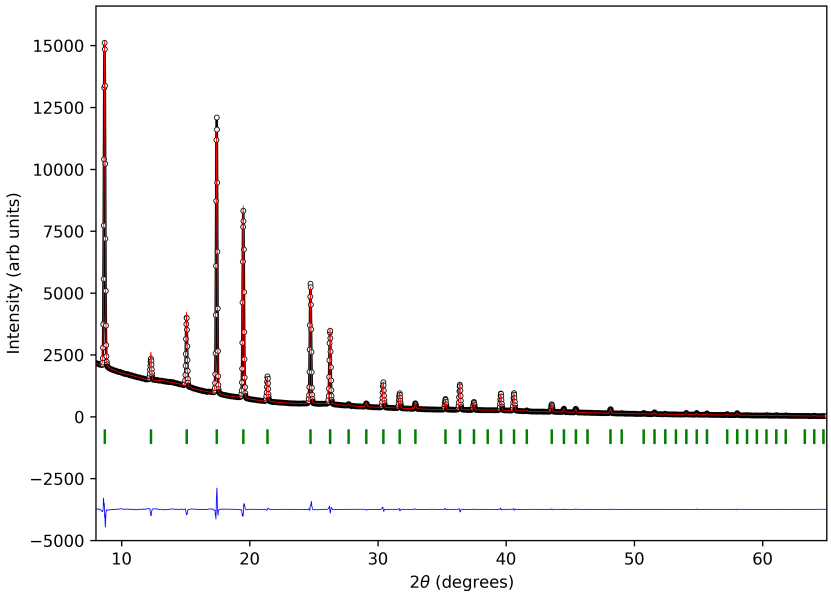

(a)

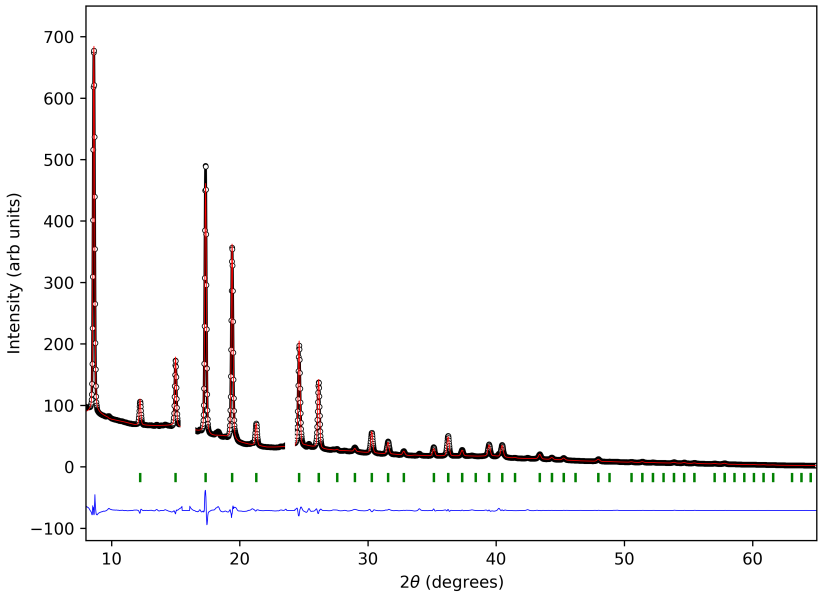

(b)

Fig. 5.35 Rietveld refinement of powder synchrotron diffraction data conducted at 400 K for the compound (a) AI200-$MAPbI_3$ R_p = 2.36 % and R_{wp} = 3.10 % and (b) prototypical $MAPbI_3$ R_p = 1.59 % and R_{wp} = 2.73 %. Impurity peaks have been excluded from the refinement.

Across the measured temperature range for all structural phases the unit cell volume is found to be significantly larger for AI200-$MAPbI_3$, as shown in Figure 5.36. The zero tilt system for this phase ($a^0a^0a^0$) means the larger cell volume corresponds to an increase in the Pb-I bond length for the AI200-$MAPbI_3$ sample as shown in Figure 5.39b. For AI200-$MAPbI_3$, the population of a small interstitial site (labelled IA on Figure 5.48) is observed at the centre face of the perovskite. This correlates with a larger perovskite cavity size, evidenced by an increase in unit cell volume, resulting in a reduction in the interaction between the MA^+ and iodine component of the PbI_6 framework. This is further evidenced by an increase from approximately 12.5 $Å^3$ to 25 $Å^3$ in the measured thermal displacement parameters associated with the MA^+ cation for the AI200-$MAPbI_3$ compound as shown in Figure 5.38. The anisotropic thermal displacement parameters of both the Pb and I sites as shown in Figure 5.40a and Figure 5.40b respectively, show comparable disorder of the PbI_6 framework across the entire measured temperature range for the $Pm\bar{3}m$ phase, despite the increase in Pb-I bond length. Therefore, it is proposed that the interstitial iodine site is stabilising the larger PbI_6 framework.

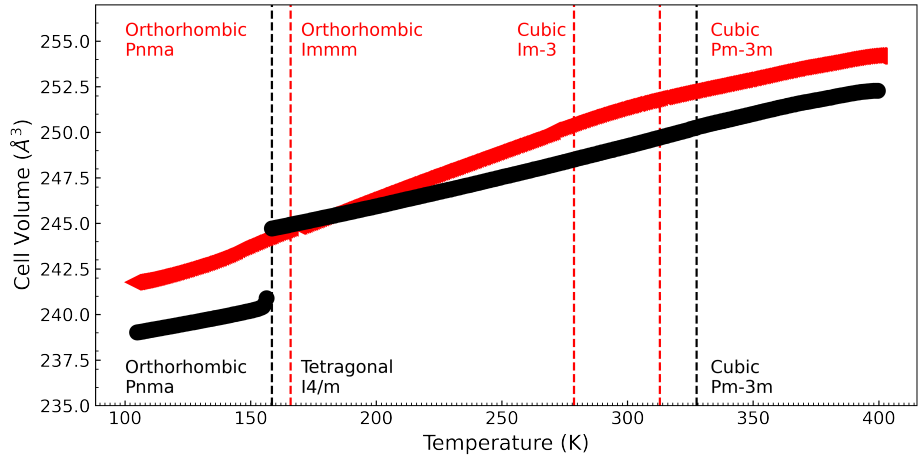

Fig. 5.36 Unit cell volume as a function of temperature for both prototypical $MAPbI_3$ (black) and AI200-$MAPbI_3$ (red) derived from Rietveld refinement of powder diffraction measured between 400 K and 100 K.

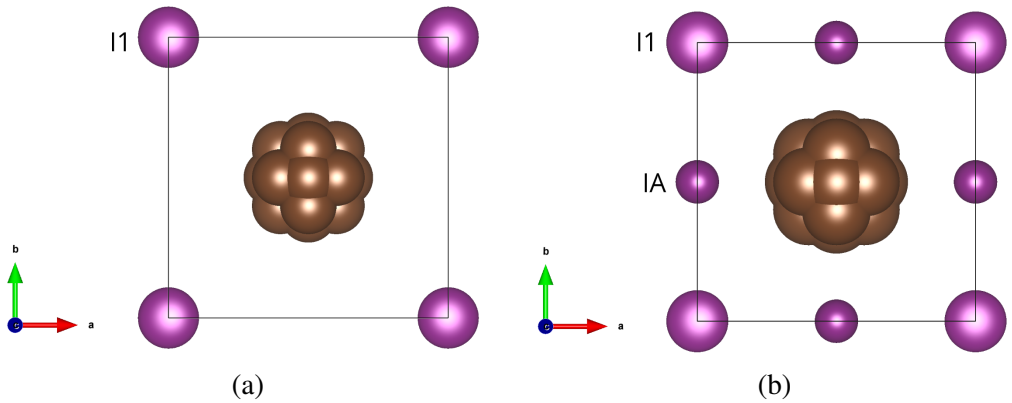

Fig. 5.37 A structural model of the samples (a) AI200-$MAPbI_3$ and (b) prototypical $MAPbI_3$ derived from Rietveld refinement of powder diffraction data at 400 K.

5.4.2 Comparison of *I4/m* and *Im*$\bar{3}$*/Immm* Phases

Both prototypical $MAPbI_3$ and AI200-$MAPbI_3$ undergo structural phase transitions as the temperature is reduced from 400 K. Upon cooling the compound prototypical $MAPbI_3$ undergoes a phase transition from a cubic $Pm\bar{3}m$ to tetragonal *I4/m* space group at 345 K. This transition is confirmed through the observation of the superlattice reflection $[\frac{3}{2},\frac{1}{2},0]$ (at $\approx$14.4735° 2θ), the intensity of this reflection increases over a wide temperature range as shown in Figure 5.3a. Over this region the structure has been modelled with a single tetragonal phase. This transition is driven by tilting

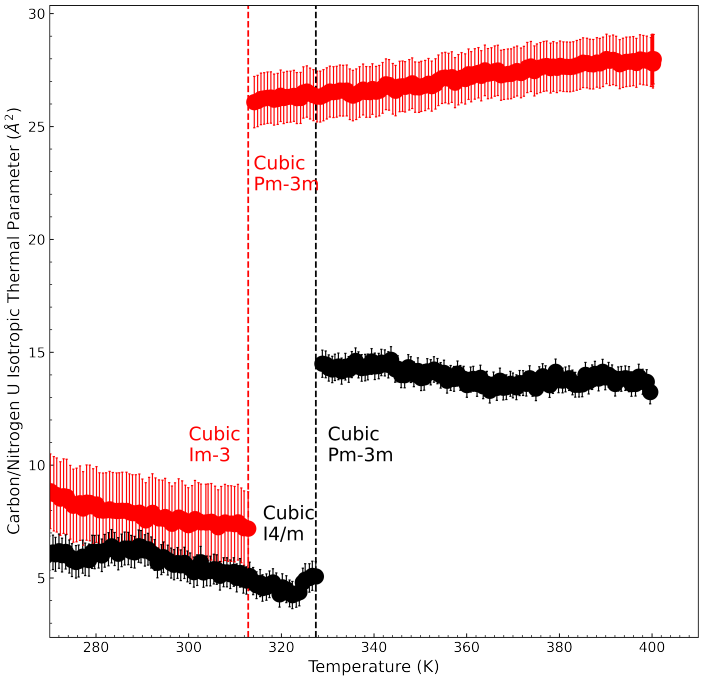

Fig. 5.38 Carbon and nitrogen (restrained to be equivalent) isotropic thermal parameters as a function of temperature for both prototypical $MAPbI_3$ (black) and AI200-$MAPbI_3$ (red) derived from Rietveld refinement of powder diffraction data.

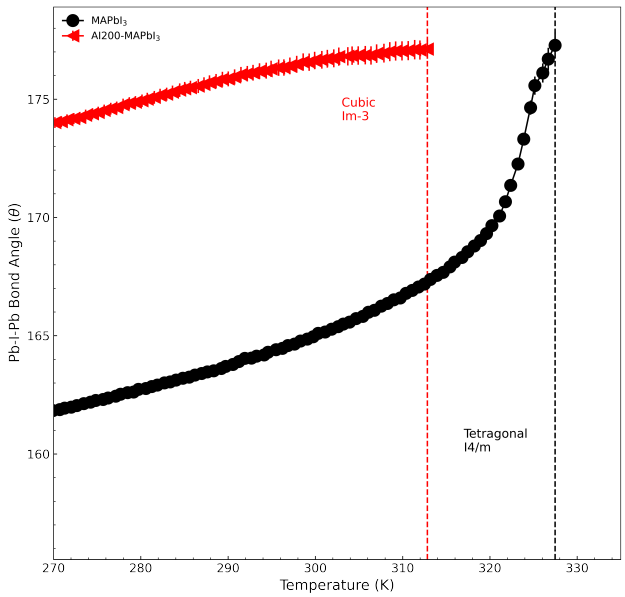

(a)

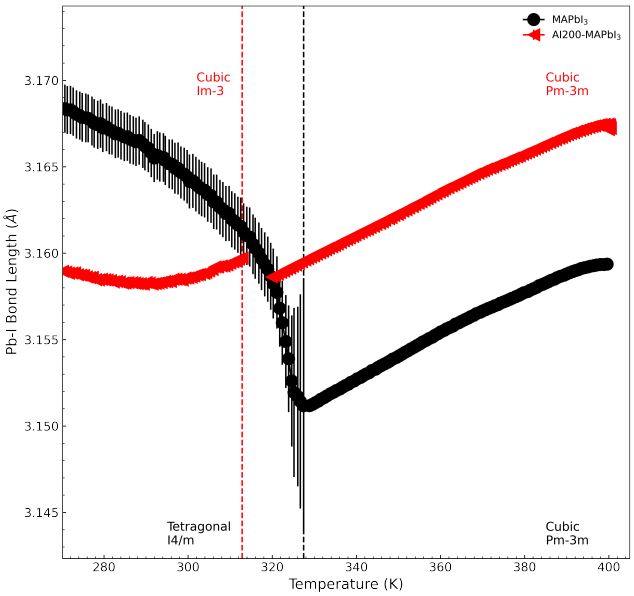

(b)

Fig. 5.39 (a) Pb-I-Pb bond angle and (b) Pb-I bond length as a function of temperature for both prototypical $MAPbI_3$ (black) and AI200-$MAPbI_3$ (red) derived from Rietveld refinement of powder diffraction data. For AI200-$MAPbI_3$ this corresponds to the bond length Pb1-I1 and bond angle Pb1-I1-Pb1 where atom labels correspond with Table 5.6. For prototypical $MAPbI_3$ this corresponds to the bond length Pb1-I2 and bond angle Pb1-I2-Pb1.

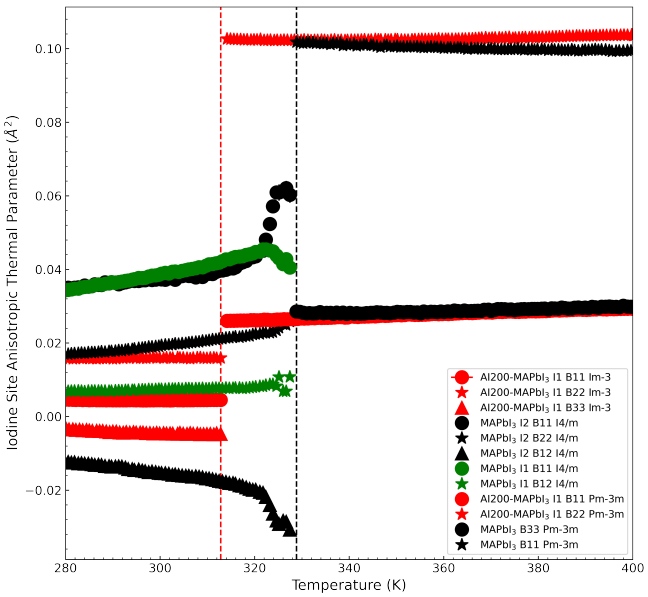

(a)

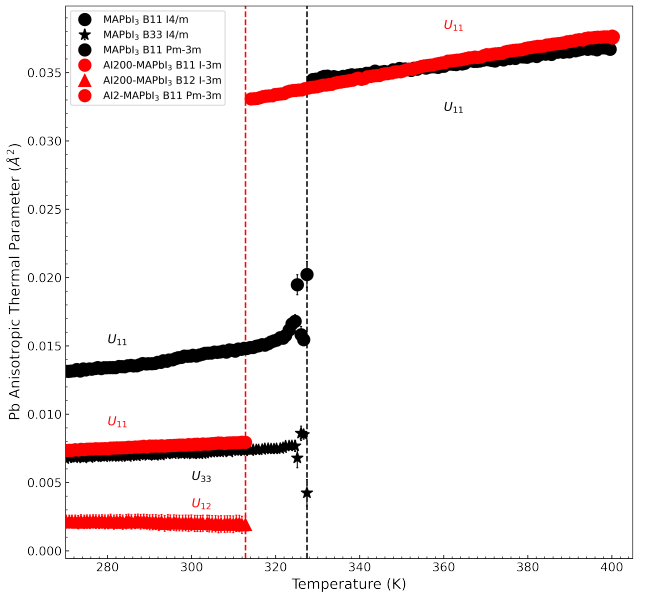

(b)

Fig. 5.40 (a) iodide and (b) lead anisotropic thermal parameters as a function of temperature for both prototypical $MAPbI_3$ (black) and AI200-$MAPbI_3$ (red) derived from Rietveld refinement of powder diffraction data. For AI200-$MAPbI_3$ the anisotropic thermal parameters correspond to the iodide and lead sites I1 and Pb1 where atom labels correspond with Table 5.6. For prototypical $MAPbI_3$ the anisotropic thermal parameters correspond to the iodide and lead sites I1, I2 and Pb1.

of the octahedra described by Glazer notation $a^0a^0c^-$ and freezing of the rotational modes of the MA^+ cation. Upon cooling, the sample AI200-$MAPbI_3$ undergoes a phase transition from the simple cubic phase ($Pm\bar{3}m$) to a larger cubic phase ($Im\bar{3}$) at 300 K. This transition results in a doubling of the unit cell volume and is confirmed through the emergence of superlattice reflections $[\frac{3}{2}, \frac{1}{2}, 0]$ and $[\frac{3}{2}, 1, \frac{1}{2}]$ at $2\theta = 13.75°$ and 16.3° respectively (in reference to the $Pm\bar{3}m$ phase I2-I) as shown in Figure 5.10. The structure determination process for this phase is outlined in Section 5.3.2, for which the subsequent structural model was used as a starting model for Rietveld refinement carried out for data measured between 270 K and 310 K.

Prototypical $MAPbI_3$ - *I4/m*

As shown in Figure 5.42a and Figure 5.42b the primary structural differences between prototypical $MAPbI_3$ and AI200-$MAPbI_3$ at ambient temperature is the configuration of the Pb-I framework. For prototypical $MAPbI_3$ a cubic ($Pm\bar{3}m$) to tetragonal (*I4/m*) structural phase transition occurs at $\approx$ 340 K. Here, prototypical $MAPbI_3$ exhibits out of phase tilting about the *c*-axis described by Glazer notation $a^0a^0c^-$, where the octahedral tilt angle is suppressed across the tetragonal to cubic phase transition as described by the bond angle Pb-I-Pb in Figure 5.39a. This corresponds with a drop in both the Pb-I bond length as shown in Figure 5.39b, a result of increased disorder in the tilting of the framework across the transition as observed by a large increase in the disorder of the lead and iodide sites prior to the tetragonal-cubic transition (the temperature range of 330 K and 345 K), this is evidenced by an increase in the anisotropic thermal parameters shown in Figure 5.40b and Figure 5.40a respectively. The MA^+ cation for prototypical $MAPbI_3$ is described by a 4 atom tetrahedron unit, where the MA^+ cation can adopt 4 orientations, each of which is shifted off-centre from the centre of the perovskite cavity. The orientation of the MA^+ cation for the tetragonal phase of prototypical $MAPbI_3$ are coupled with the out of phase tilting in the PbI_6 octahedra, crossing the tetragonal-cubic transition the MA^+ cation exhibits complete orientational disorder correlating with the suppression of octahedra tilting.

AI200-$MAPbI_3$ - $Im\bar{3}$

In contrast the temperature dependent phase transition for AI200-$MAPbI_3$ is vastly different over the same temperature range. AI200-$MAPbI_3$ undergoes a structural phase transition from a simple cubic structure (*a a a*) described by the space group $Pm\bar{3}m$ (phase I2-I) to a larger cubic structure (2*a* 2*a* 2*a*) described by the space group $Im\bar{3}$ (phase I2-II) at $\approx$ 315 K. Consistent with the high temperature phase

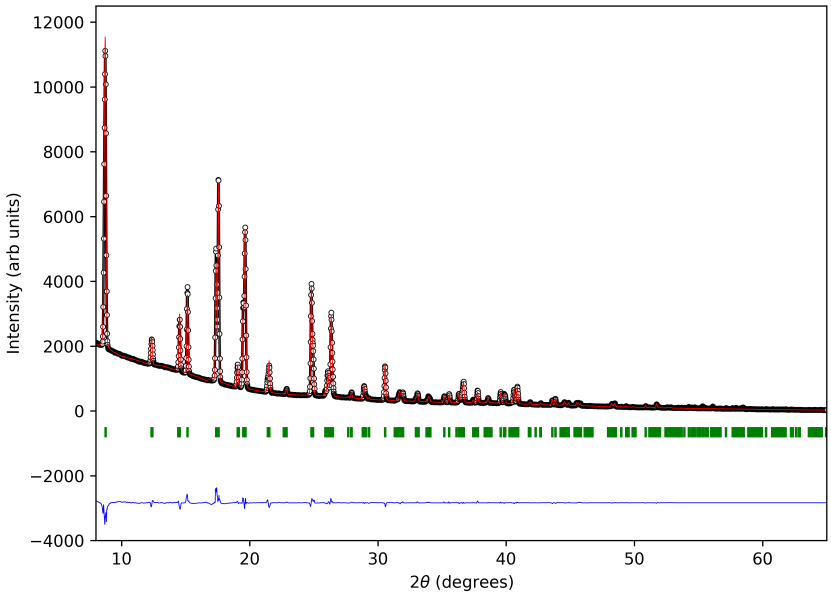

(a)

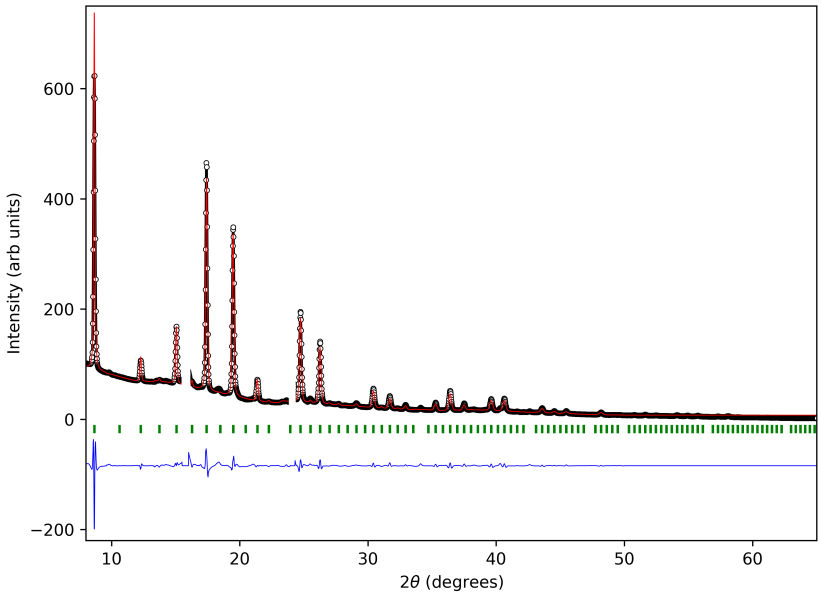

(b)

Fig. 5.41 Rietveld refinement of powder synchrotron diffraction data conducted at 300 K for the compounds (a) prototypical $MAPbI_3$ R_p = 2.15 % and R_{wp} = 3.05 % and AI200-$MAPbI_3$ R_p = 3.60 % and R_{wp} = 5.11 %. Impurity peaks have been excluded from the refinement.

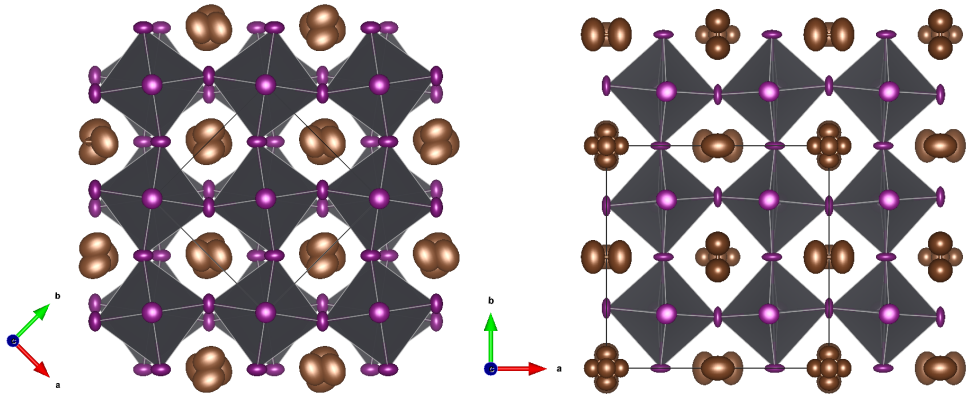

(a) (b)

Fig. 5.42 (a) The room temperature structure of the compound prototypical $MAPbI_3$ orientated along *c* the axis and derived from single crystal X-ray diffraction measurements. (b) A diagram showing the room temperature structure of AI200-$MAPbI_3$ along *c* the axis. Both diagrams were derived from single crystal X-ray diffraction measurements performed at 290 K. Interstitial iodide sites have been removed for clarity

I2-II, a low occupied interstitial iodine site is observed that sits close to the centre face of the perovskite framework, this supports the larger perovskite framework observed for AI200-$MAPbI_3$ evidenced by a larger unit cell volume measured over the entire temperature region for AI200-$MAPbI_3$ as shown in Figure 5.39b. The larger perovskite cavity size means reduced bonding between the MA^+ cation and PbI_6 framework, that for prototypical $MAPbI_3$ drives the tilting exhibited by the perovskite framework. Interestingly, unlike prototypical $MAPbI_3$ the MA^+ cation adopts orientations such that the centre of mass of the cation sits at the centre of the perovskite cavity. As the temperature is reduced and the lattice contracts, the tilt angle of the PbI_6 octahedra is significantly less compared with prototypical $MAPbI_3$ as shown in Figure 5.39a. Here, the PbI_6 octahedra exhibits in-phase tilting about all crystallographic axis with Glazer notation $a^+a^+a^+$. This accommodates smaller Pb-I bond lengths as shown in Figure 5.39b whilst retaining a larger cavity size compared with prototypical $MAPbI_3$. As shown in Figure 5.40a, across the transition from phase I2-I to I2-II, unlike prototypical $MAPbI_3$, there is no observed drop in the anisotropic displacement parameters of either the lead (Pb1) and iodine (I1). The thermal parameters associated with the lead and iodide sites for AI200-$MAPbI_3$ are significantly less disordered compared to prototypical $MAPbI_3$. This is despite the larger unit cell volume and indicates a more rigid perovskite framework supported by the population of interstitial iodide sites, compared with prototypical $MAPbI_3$.

AI200-$MAPbI_3$ Structural Dynamics - *Immm*

As described in Section 5.3.3 a structural phase transition was observed at 270 K for AI200-$MAPbI_3$ from a cubic phase I2-II ($Im\bar{3}$) to an orthorhombic I2-III phase (*Immm*) upon cooling to 160 K. The transition is evident by subtle high angle peak splitting observed below this temperature. For prototypical $MAPbI_3$ no phase transition is observed over this temperature range. The data was refined with a structural model as described in Section 5.3.3 where the structure determination is described in detail. However, the interstitial iodide sites were not included in the refinement as they did not contribute sufficiently to the diffraction such that they could be refined without significant divergence, this is likely a result of the low number of observed peaks.

In Section 5.3.3, the average structure of the phase I2-III was characterised at 220 K and found to be comprised of two distinct configurations that were determined from analysis of the occupancy of a number of partially occupied iodine framework sites labelled I1, I1B, I2, I2BA, I2BB and I3 in the structural model. Refinement of variable temperature powder diffraction measurements between 270 K and 160 K allowed for the temperature dependence of these configurations to be observed. For this purpose, the occupancy of the split PbI_6 framework sites I1 and I1B were refined as shown in Figure 5.44. The sites I2, I2BA and I2BA were refined as a single site labelled I2 due to the low number of observed peaks. This describes two separate tilt configurations of the octahedra that conform to both orientations of the partially ordered MA^+ cation site as described in Section 5.3.3. As with other organic-inorganic hybrid perovskites, the orientational dynamics of the organic cation are correlated with the nature of inorganic octahedral framework tilting. Therefore the orientational disorder of MA^+ cation is correlated with the occupancy of the split iodide site I1 and I1B, the refinement of the occupancy of these sites as a function of temperature allows for the degree of ordering of the MA^+ cation to be observed indirectly. The two configurations represented by the refinement of sites I1 and I1B also correspond to two different orderings of the interstitial iodide. Therefore the refinement of the sites I1 and I1B allows for the degree of mixing of these two configurations to be determined. As shown in Figure 5.45 the occupancy of sites I1 and I1B is approximately 50% each at 270 K, representing an equal mix of both configurations. As the temperature is reduced and the occupancy of the site I1 increases, the occupancy of the I1B site decreases. This represents increased ordering of the MA^+ cation and interstitial iodide at low temperature as temperature is reduced from 270 K to 160 K.

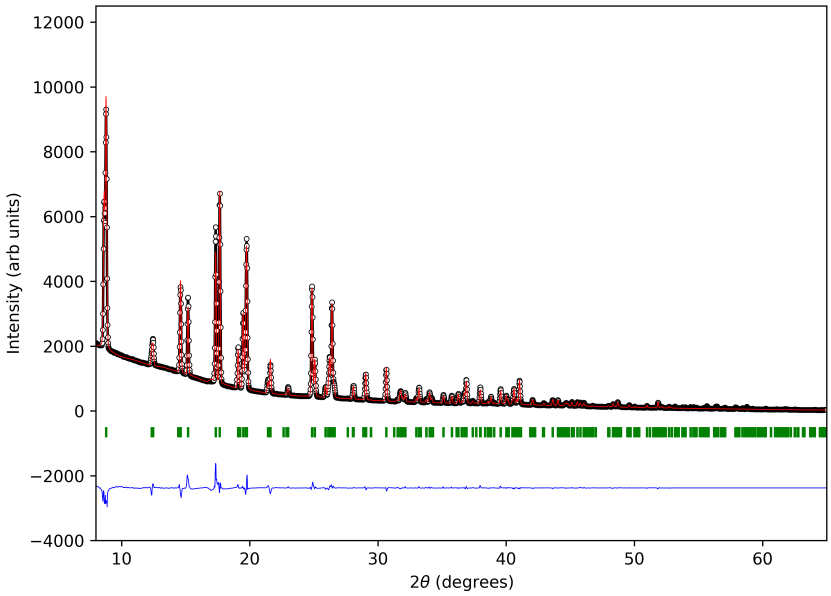

(a)

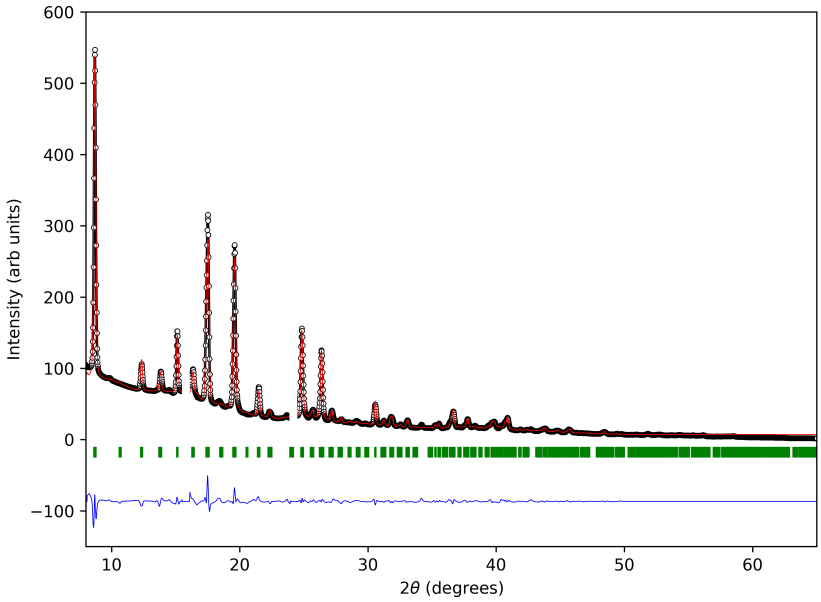

(b)

Fig. 5.43 Rietveld refinement of powder synchrotron diffraction data at 220 K for the compounds (a) prototypical $MAPbI_3$ R_p = 2.50 % and R_{wp} = 3.54 % and (b) AI200-$MAPbI_3$ R_p = 3.38 % and R_{wp} = 4.65 %. Impurity phase peaks have been excluded from the refinement.

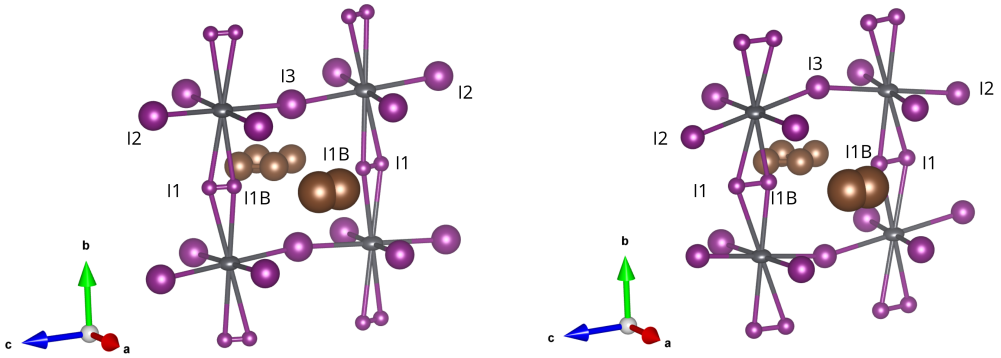

(a) (b)

Fig. 5.44 The structure of (a) AI200-$MAPbI_3$ at 270 K and (b) 160 K determined from refinement of powder X-ray diffraction.

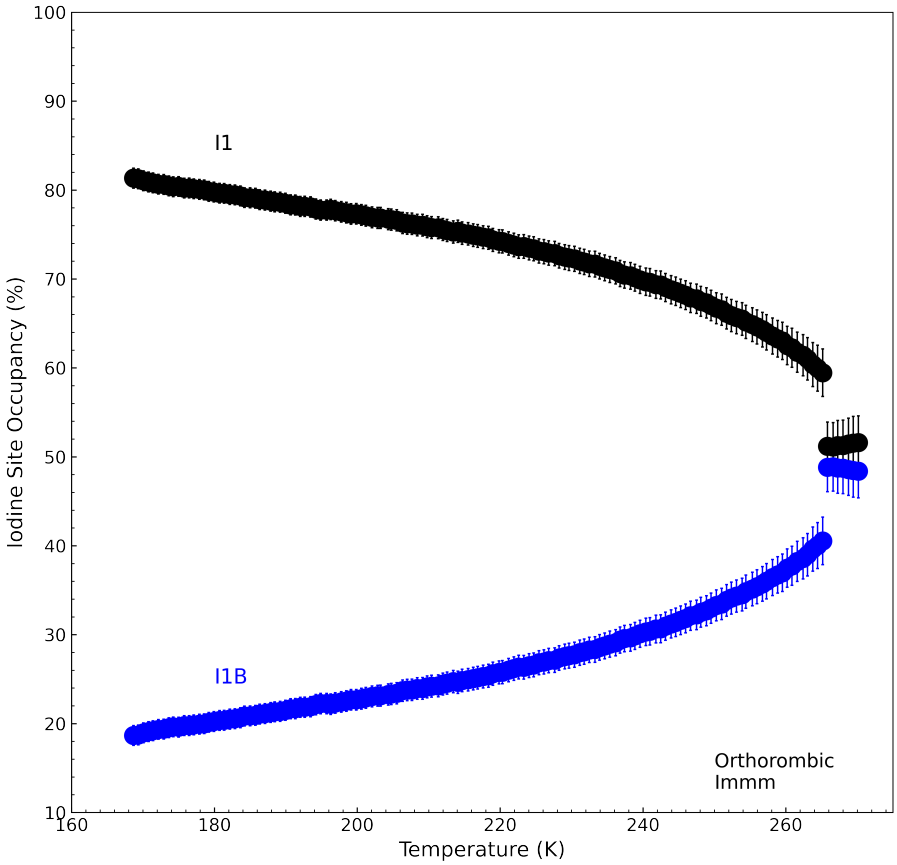

Fig. 5.45 The occupancy of iodide sites I1 and I1B for the phase I2-III (*Immm* as described in Table 5.11) as a function of temperature derived from Rietveld refinement of powder diffraction data. For this refinement the occupancy of the site I3 was restrained to 1.0.

5.5 Discussion

5.5.1 Hybrid Perovskites Under Pressure

A number of papers have been published on the high pressure phase transitions for prototypical $MAPbI_3$ and eventual amorphisation of the compound, the most detailed of which derive the structure of these transitions from synchrotron single crystal diffraction measurements [197–199]. As described elsewhere in this work, whilst maintained at ambient temperature the structure of prototypical $MAPbI_3$ is tetragonal where the octahedral tilts are described by Glazer notation $a^0a^0c^-$. For clarity this phase is often denoted II in the literature. Above 0.3 GPa prototypical $MAPbI_3$ undergoes a structural phase transition denoted IV that has been assigned the space group $Im\bar{3}$. The nature of these tilts differ drastically from the phase II and are described by the Glazer notation as $a^+a^+a^+$, this corresponds to a shortening of the Pb-I bond distances and large distortions of the PbI_6 octahedra that continues up to 2.5 GPa. Here a further phase transition occurs that is also described by the $Im\bar{3}$ space group, the Pb-I-Pb angles undergo a sudden straightening whilst continued shortening of the Pb-I bond distances. Beyond this point a gradual amorphisation occurs resulting from strong pressure induced interionic and $NH^+\cdots I^-$ interactions that become fixed at random orientation, meaning a loss of long-range crystallographic order and an increase in atomic displacement parameters. [197]. The structures determined in these high pressure studies are directly analogous to the structures we have stabilised through post synthesis iodine thermal treatment, other than sharing the same space group and the same type of tilting of the PbI_6 octahedral denoted by the Glazer notation $a^+a^+a^+$ they also both exhibit ordering of the MA^+ cation along each crystallographic axis. The comparison between those structures determined for prototypical $MAPbI_3$ at high pressure and the compound AI200-$MAPbI_3$ is most compelling when comparing both the Pb-I-Pb bond angles (Figure 5.46a) and Pb-I bond distances (Figure 5.46b) against the unit cell volume of the respective phases II, IV and I_2-II (derived in this work in Section 5.3.2). Here, cell volume has been used as a pressure independent dimension. The relationship established for Pb-I-Pb bond angle and Pb-I bond distance as a function of unit cell volume, extracted from pressure induced phase transition studies of $MAPbI_3$ correlates well with the structural parameters observed for the I_2-II phase reported in this work. This points towards a shared structural phase transition mechanism between the high pressure phases and the transition resulting from thermal annealing iodine treatment. The atomic displacement parameters of the iodine and lead sites for the AI200-$MAPbI_3$ compound also correlate well with those for the high pressure

phases when compared against cell volume as shown in Figure 5.47a and Figure 5.47b.

More recent high pressure studies report the absorption of the pressure transmitting medium onto interstitial sites in the perovskite framework during high pressure single crystal diffraction studies [199]. This provides a useful insight into the structures obtained in this work. These studies show that the pressure transmitting medium (in this case Ne and Ar) are not inert. They are incorporated into the structure at high pressure, resulting in the compounds $NeMAPbI_3$ and $ArMAPbI_3$. Here Ne interacts with the I atoms, and prevents amorphization up to 20.27 GPa. Interestingly from the work presented here upon depressurisation the high pressure phase remains stable. In the case of Ar, interactions with both I and MA^+ cations results in an irreversible amorphization of the compound. These differences are attributed to the difference in atomic radii and the resulting interatomic interactions between Ne (0.38) and Ar (0.71). This serves as a useful analogy for the results reported in this work. We have already shown that the structural features of both high pressure phase transitions, and those resulting from the thermal iodine treatment developed for this work are consistent. We have also shown the population of an interstitial iodine site located at the centre face of the perovskite framework, consistent with those found for Ne and Ar during high pressure studies of $MAPbI_3$. This discussion provides further support to the mechanism for incorporating additional iodine into the structure of $MAPbI_3$ proposed in this work, where the structure of $MAPbI_3$ exhibits significant porous properties. These studies serve as useful comparative results for understanding the incorporation of iodine into the structure of $MAPbI_3$.

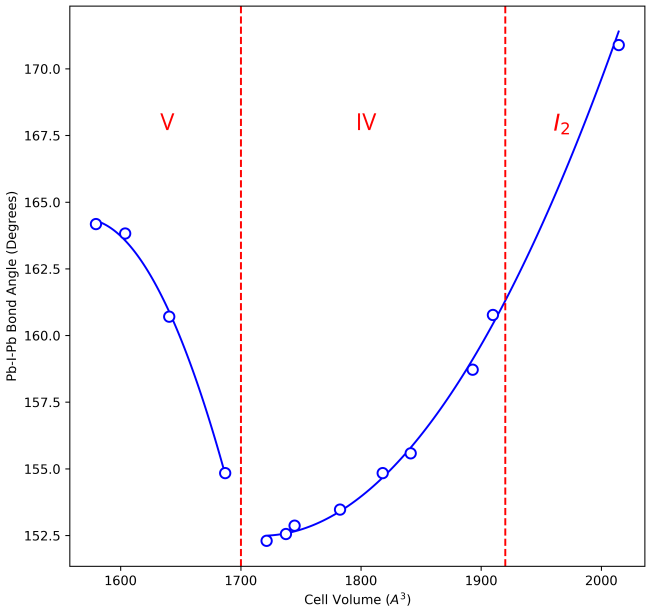

(a)

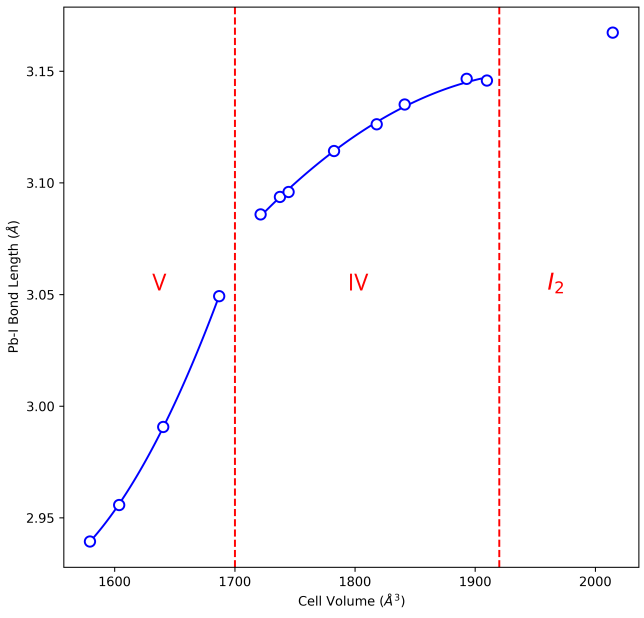

(b)

Fig. 5.46 (a) and (b) compare the Pb-I-Pb bond angle and Pb-I bond distances for the high pressure phases IV and V through single crystal diffraction by Szafranski *et al*. [197] against the structure found for the compound AI200-$MAPbI_3$ at 290 K.

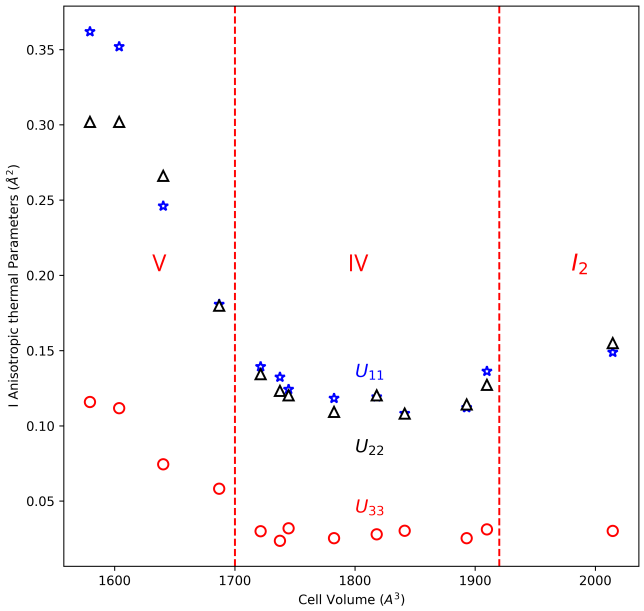

(a)

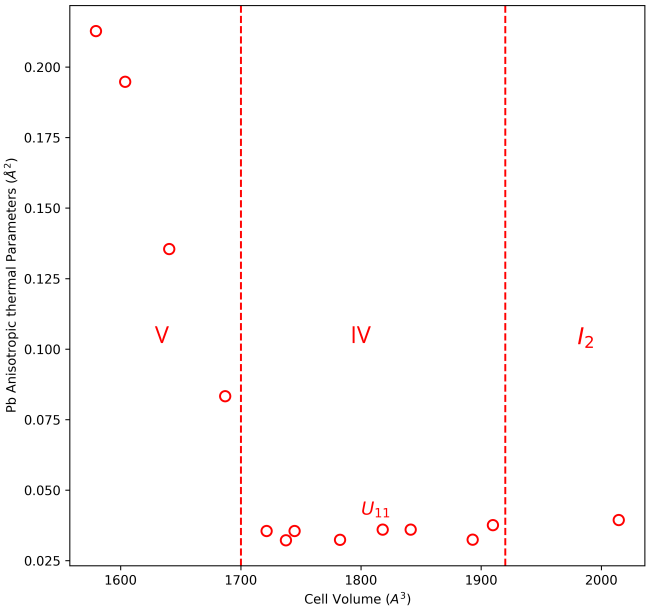

(b)

Fig. 5.47 (a) and (b) compare the iodine and lead atomic displacement parameters for the high pressure phases IV and V through single crystal diffraction by Szafranski *et al*. [197] against the structure found for the compound AI200-MAPbI$_3$ at 290 K.

5.5.2 Incorporation of Additional Iodine and Stabilising of New Structural Phases

For this work, a post synthesis thermal iodine treatment has been devised, whereby pre-synthesised samples of prototypical $MAPbI_3$ were placed inside a quartz tube along with a small amount of iodine crystals, the tube was evacuated, sealed and annealed in a furnace at 200 °C. The crystal structure of the resulting compound has been characterised, and the stabilisation of a new derivative compound of $MAPbI_3$ is reported that is denoted AI200-$MAPbI_3$.

Prior to the iodine thermal treatment, prototypical $MAPbI_3$ exhibits out of phase octahedral tilting about the crystallographic *c*-axis at ambient temperature, this accommodates for the rotational dynamics and disorder of the MA^+ cation. Post iodine thermal treatment, significant changes to the average crystal structure were observed. At ambient temperature the compound AI200-$MAPbI_3$ exhibits in-phase tilting of the PbI_6 octahedra that accommodates a semi-ordered state of the MA^+ cation along each crystallographic axis. The tilt angle is found to be suppressed significantly, supporting shorter Pb-I bond lengths than prototypical $MAPbI_3$. Through variable temperature powder synchrotron X-ray diffraction measurements a significant reduction in the disorder of the PbI_6 octahedral framework (as shown in Figure 5.40a) and shorter Pb-I bond lengths were observed for the ambient temperature phase I2-II, post iodine treatment. A significantly larger unit cell volume (as shown in Figure 5.36) for all measured temperatures (100 K to 400 K) was also observed. Upon cooling from 400 K, the compound AI200-$MAPbI_3$ was found to exhibit a number of temperature dependent structural phase transitions that results in a drop in symmetry defined by the transition $Pm\bar{3}m \rightarrow Im\bar{3} \rightarrow Immm \rightarrow Pnma$.

As well as the changes observed for the PbI_6 framework, single crystal diffraction experiments conducted on AI200-$MAPbI_3$, demonstrate a partially occupied interstitial iodine site that sits at the centre face of the perovskite framework that is sufficiently localised such that it contributes to Bragg scattering and therefore observed through the diffraction methods implemented in this work. This site was observed for each of the phases I2-I, I2-II and I2-III. An observed reduction in the anisotropic thermal parameters of the lead and iodide sites associated with the PbI_6 framework suggests reduced iodine disorder compared with prototypical $MAPbI_3$ and a more rigid perovskite framework upon population of the interstitial site. Compared with the interstitial iodide site found for prototypical $MAPbI_3$ and discussed in chapter 3, the occupancy of this site is much higher, 0.044(14) for AI200-$MAPbI_3$ compared to 0.007(3) for prototypical $MAPbI_3$ at ambient temperature (both values derived from

single crystal X-ray diffraction). The surrounding coordination of the interstitial sites I3 and IA/IB is found to be considerably different as shown on Figure 5.48a and Figure 5.48b respectively. The observed I-I bond distances are much larger for the IA/IB sites of AI200-$MAPbI_3$, a result of the larger unit cell, and the location of this interstitial site is much closer to the centre face of the perovskite framework differentiating itself from the I3 site observed for prototypical $MAPbI_3$. Therefore, it was concluded that the interstitial sites observed for AI200-$MAPbI_3$ are not a result of increased iodine disorder or mobility (as is the case for prototypical $MAPbI_3$) but intrinsic to the structure and composition of the compound AI200-$MAPbI_3$. The transition from $Im\bar{3}$ to *Immm* is found to correlate with low temperature ordering of the interstitial iodine sites and further ordering of the PbI_6 framework and MA^+ cation.

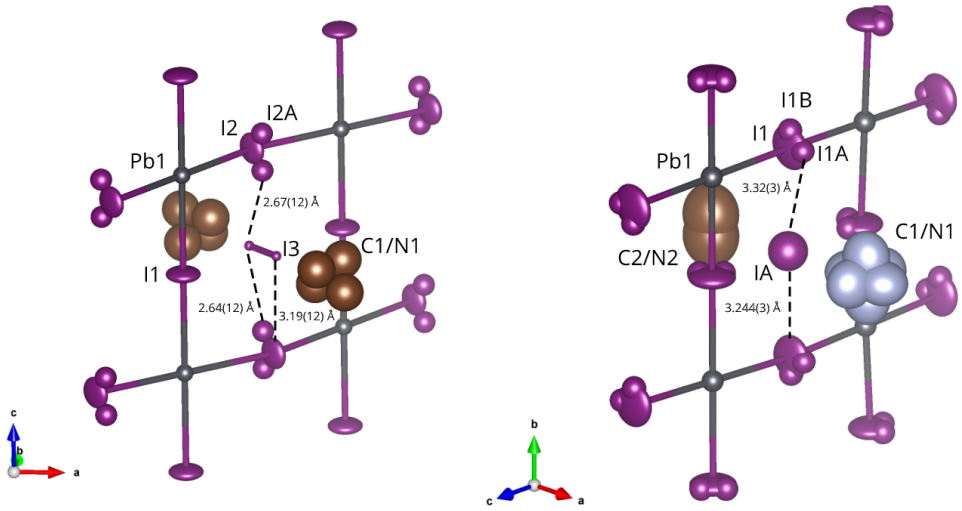

(a) (b)

Fig. 5.48 A comparison of the coordination for the interstitial iodine sites I3 and IA/IB for (a) prototypical $MAPbI_3$ and (b) AI200-$MAPbI_3$ at ambient temperature respectively. For prototypical $MAPbI_3$ the shortest C1/N1-I3 bond distance observed is 1.93(12) Å, compared with AI200-$MAPbI_3$ where the shortest C1/N1-IA bond distance observed is 2.55(11) Å.

Further evidence for the incorporation of additional iodine into the structure and a change in the composition of the material, is the refined composition of AI200-$MAPbI_3$ for each of the structural phases I2-I, I2-II and I2-III. Specifically, from single crystal X-ray diffraction measurements the total Pb:I composition for each of the phases were found to be 1:3.264±0.186, 1:3.194±0.110 and 1:3.089±0.049 respectively demonstrating a small increase in the total iodine composition compared to the ideal 1:3 stoichiometry of prototypical $MAPbI_3$.

So far the charged nature of the interstitial iodine has not been discussed as it cannot be directly measured through the diffraction techniques described in this chapter. However, there are some important notes to made on the subject. Firstly, the contraction of the atomic radii of I^- (2.2 Å) compared with the oxidized I^{+4} atoms for the ion periodate $[IO_4]^-$] (0.53 Å), makes positive interstitial iodine (I^+) more likely to populate the interstitial sites observed at the centre face of the perovskite framework for the sample AI200-$MAPbI_3$. The radius even being comparable to Ne and Ar found to populate interstitial sites for high pressure phases for $MAPbI_3$ discussed above, despite the smaller unit cell of those structures [199]. Positive interstitial iodine would also be in good agreement with first-principle calculations reported by Meggiolaro *et al*. [195] (described in Section 5.1.1), where the defect chemistry of $MAPbI_3$ is discussed under iodine medium and iodine rich conditions. For the later, which is consistent with our own experiments reported in this chapter, the filling of iodine vacancies in the lattice is found to be favourable and result in the production of I^+ following the reaction:

$$V_i^+ + I_2 \rightarrow perf + I_i^+ \tag{5.1}$$

Where perf indicates the formation of a perfect crystal and V_i^+ represents positive iodide vacancies. In the case of Meggiolaro *et al*. these calculation were carried out in order to understand experimental observations of a reduction in iodine mobility upon exposure to I_2 by Senocrate *et al*., whereby the population of interstitial sites was given as an explanation for an increase in the migration barrier following I_2 exposure. For all experimental reports of I_2 exposure no structural changes have been reported. For our own results these calculations would also suggest positive interstitial iodine as the source of the interstitial sites observed in this work. Given the high defect density of $MAPbI_3$ following solution synthesis of $MAPbI_3$ prior to iodine thermal treatment, iodide vacancies are likely. These iodine vacancies are then saturated following the iodine thermal treatment through exposure to I_2 at high temperature resulting in I^+ defects and the resulting structural changes observed.

Following the above, it is evident that small quantities of additional iodine have been incorporated into the structure of prototypical $MAPbI_3$ through a post synthesis iodine thermal treatment resulting in the synthesis of a new range of compounds $MAPbI_{3+x}$. The structure of the compound AI200-$MAPbI_3$ is supported by interstitial iodine that results in changes to the interactions between the X-site iodide and A-site MA^+ cation. These results highlight the soft nature of the hybrid perovskite material, that remains stable given considerable changes to the the octahedral tilting and Pb-I

bond lengths at ambient temperature, the operating temperature of solar cell devices, and shows a significant reduction in the disorder of the perovskite framework at these temperatures.

6

Conclusion

This research has focused on the structural characterisation of hybrid organic-inorganic perovskites (HOIHPs), in particular $MAPbI_3$. The photovoltaic performance of HOIHP based solar cells has increased rapidly since first being incorporated as the sensitised layer in a dye sensitised solar cell in 2009 [200]. In part, this can be attributed to the extraordinary academic interest the material has received, with 4,100 research paper published on the topic of "perovskite solar cell" in 2019 [201]. However, the fundamental mechanism by which the impressive photovoltaic performance has been realised remains largely unknown. This in part results from a lack of clarity on their structures, thereby providing the initial motivation for the work described in this thesis. The work that followed revealed $MAPbI_3$ to be a highly dynamic solid, where the structure is shown to be highly dependent on the 'history' of the sample being studied. This originates from the combining of molecular and valence solids, in this way HOIHPs separate themselves from traditional perovskite materials, with flexible bonding compared with inorganic oxide perovskites [202, 203]. Molecular disorder means that compared to traditional perovskites the A-site cation does not exhibit highly periodic long range order at high temperature [49]. These materials possess significant structural distortions and disorder that is not limited to their molecular component. The framework itself exhibits significant disorder, for which there is evidence of coupled molecular and framework dynamics [50]. Not only do these complex structures exhibit photovoltaic properties, but both ferroelectric [153, 152, 110] and ion conductivity [130, 119, 193] properties have been reported. This picture of HOIHP materials was the starting point upon which the work described in this thesis has further contributed to.

Initial research started with the characterisation of the ambient temperature tetragonal phase (denoted phase II) for the hybrid perovskite $MAPbI_3$. Maximum entropy

method (MEM) analysis of X-ray single crystal and neutron powder diffraction measurements were used to derive an average structure model for the orientationally disordered MA^+ cation. These results revealed significant structural disorder of the Pb_6^{4-} framework. Specifically, interstitial iodide sites were identified, from which a mechanism for iodine migration was proposed through the population of interstitial sites resulting in the formation of a neutral I_2 molecule. This is facilitated through the collective motion of MA^+ cations, demonstrating complex coupled dynamics. The population of interstitial sites implies the redox reaction $2I^- \rightarrow I_2 + 2e^-$ which has significant implications for the band structure of the material. Iodine migration has since been confirmed by a number of ion mobility experiments reported in the literature [147, 148, 193].

On understanding the considerable structural disorder exhibited by $MAPbI_3$, variable temperature synchrotron powder diffraction measurements were carried out to determine changes to the structural dynamics of $MAPbI_3$ following a range of thermal treatments. These treatments are consistent with the processing of hybrid perovskite based solar cell devices described in the literature [110, 152, 153, 156, 157]. Low temperature (80 °C) thermal annealing in air was observed to induce subtle changes to the temperature dependant structural dynamics of the material, these were attributed to the incorporation of interstitial oxygen into the perovskite framework. Low temperature (80 °C) vacuum annealing was found to have little effect on the structure of $MAPbI_3$. However, upon annealing under a vacuum at 200 °C a significant reduction in the octahedral tilting of the perovskite framework was observed and a reduction in the structural phase transition temperature from tetragonal (phase II) to cubic (phase I). These results demonstrate observable changes to the average structure of $MAPbI_3$ following a range of thermal treatments. This not only highlights the flexibility of the hybrid perovskite structure, but also the structural dynamics of the material are highly dependant on the "history" of the sample. This allows the structure of the material to be manipulated, in this case via the specific post processing thermal treatment undertaken.

In aiming to understand the significant structural changes induced following high temperature vacuum annealing (200 °C) a series of X-ray powder and single crystal diffraction measurements were performed, together with the application of MEM analysis on neutron powder diffraction data. Interestingly, for the first time structural changes were observed to be dependent on the temperature of the vacuum annealing process, allowing for precise control of principle perovskite structural features such as unit cell volume, framework octahedral tilting and Pb-I bond length. In this case, the changes to the average structure of $MAPbI_3$ following high temperature

vacuum annealing were attributed to the loss of MA^+. This further demonstrates and was attributed to the soft chemical bonding of the PbI_6^- framework, where the loss of MA^+ changes the interaction between the A-site MA^+ cation and the X-site halide component of the framework. This highlights the coupling of these dynamic components, and demonstrates a new route for tuning the structure of hybrid perovskite materials. Following processing, TGA measurements showed the thermal stability of the material to be unaffected. These results demonstrate that despite the reported poor thermal stability of $MAPbI_3$, attributed to the hygroscopic nature of the MA^+ component [164], the material stability is highly tolerant to compositional change, owing to an intrinsic flexibility that allows the material to stabilise for a range of structures.

This research has demonstrated considerable structural disorder for the hybrid perovskite $MAPbI_3$, iodine migration facilitated by the population of interstitial sites and shown that tuning of principle structural features is possible following high temperature vacuum thermal annealing. The combination of these results provided the motivation for the final experiments reported. A post synthesis thermal iodine treatment was devised and a new structural phase $MAPbI_{3+x}$ has been stabilised. This results from the incorporation of additional iodine into the structure and therefore demonstrates iodine composition engineering. The new phases were characterised between the temperatures 100 K and 400 K through a combination of variable temperature powder and single crystal X-ray diffraction measurements. Ambient temperature ordering of the MA^+ cation was observed, alongside a partially occupied interstitial iodine site that sits at the centre face of the perovskite framework. The population of this interstitial site was found to correlate with an increase the rigidity of the perovskite framework observed through a reduction in the anisotropic displacement parameters of the lead and iodine sites. The compound was found to exhibit a number of temperature dependant structural phase transitions that deviate from those exhibited by $MAPbI_3$ prior to the iodine thermal treatment. At high temperatures the compound exhibits a simple cubic phase I2-I ($Pm\bar{3}m$), upon cooling the structure undergoes a series of successive phase transitions starting with a doubling of the unit cell and the formation of a cubic I2-II phase ($Im\bar{3}$). Following this the compound transitions to an orthorhombic phase I2-III (*Immm*) and at low temperatures an orthorhombic phase I2-IV (*Pnma*). This was found to be driven by low temperature ordering of the interstitial iodine upon transitioning from $Im\bar{3}$ to *Immm*. The incorporation of additional iodine into the structure through the population of interstitial sites provides experimental evidence of intrinsic doping and demonstrates the porous nature of these materials.

The results of this research provide experimental evidence for the flexible and highly disordered nature of the structure of hybrid perovskites, specifically, $MAPbI_3$ the defacto compound for this family of materials. This in part explains why efforts towards structure determination has resulted in so many partially contradicting studies on the topic [103, 104, 47, 105–109]. However, what has now become the overriding theme of this research and an unexpected result of this work, is the range for which the average structure of hybrid perovskite materials stabilise. This has been shown to be highly dependant on the synthesis method and post synthesis treatment of the compound. Focusing on $MAPbI_3$, this is most apparent when comparing the Pb-I bond length, Pb-I-Pb bond angle and unit cell volume as a function of temperature for the different $MAPbI_3$ samples synthesised and then processed under different conditions during this work. This is illustrated by Figure 6.1b, Figure 6.1a and Figure 6.2 respectively. Here, the different synthesis methods and following thermal treatments distinctly separate themselves on each plot, the variability in structure of a single compound, in this case $MAPbI_3$, has been staggering allowing us to classify these materials as highly dynamic solids. Specifically, the range of Pb-I bond lengths, Pb-I-Pb bond angles and unit cell volumes clearly demonstrates the tunability and dynamic nature of the materials framework that has resulted in the formation of new phases. This work enables the design of materials tailored to specific functional requirements, for the case of hybrid perovskites this means more stable, highly efficient photovoltaic devices.

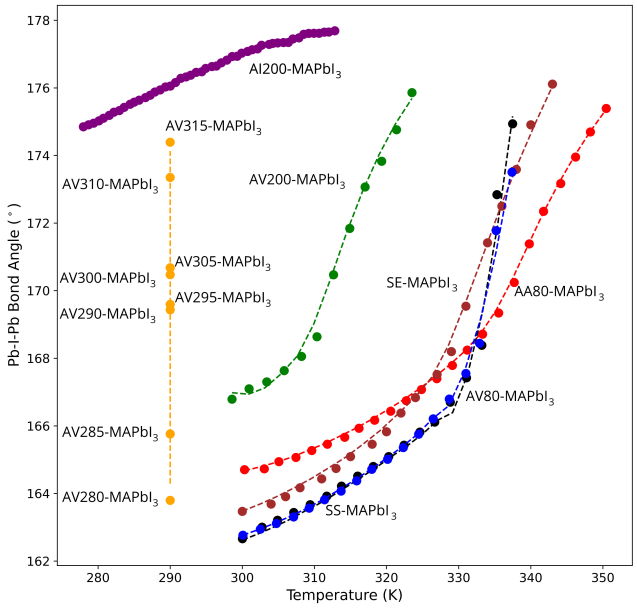

(a)

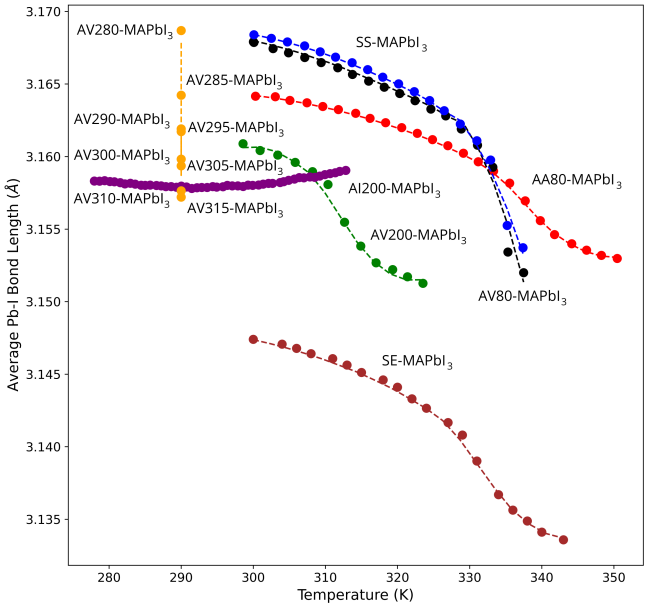

(b)

Fig. 6.1 (a) Pb-I-Pb bond angle and (b) Pb-I bond length as a function of temperature for a range of $MAPbI_3$ samples determined through Rietveld refinement of powder X-ray diffraction data.

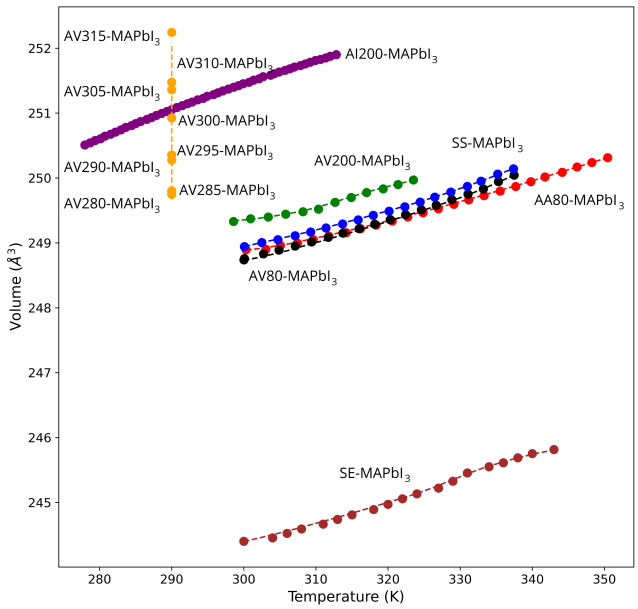

Fig. 6.2 Unit cell volume as a function of temperature for a range of $MAPbI_3$ samples determined through Rietveld refinement of powder X-ray diffraction data.

References

[1] N. S. Lewis and D. G. Nocera, "Powering the planet: Chemical challenges in solar energy utilization," *Journal for Quality Participation*, vol. 104, no. 42, pp. 20142–20142, 2007.

[2] BP, "Statistical Review of World Energy, 2020 | 69th Edition," 2020.

[3] J. Nelson, *The Physics of Solar Cells*, ch. 3. Imperial College Press, 2004.

[4] J.-P. Correa-Baena, M. Saliba, T. Buonassisi, M. Grätzel, A. Abate, W. Tress, and A. Hagfeldt, "Promises and challenges of perovskite solar cells," *Science*, vol. 358, no. 6364, pp. 739–744, 2017.

[5] W. S. Yang, B.-W. Park, E. H. Jung, N. J. Jeon, Y. C. Kim, D. U. Lee, S. S. Shin, J. Seo, E. K. Kim, J. H. Noh, and S. I. Seok, "Iodide management in formamidinium-lead-halide–based perovskite layers for efficient solar cells," *Science*, vol. 356, no. 6345, pp. 1376–1379, 2017.

[6] Q. Jiang, Y. Zhao, X. Zhang, X. Yang, Y. Chen, Z. Chu, Q. Ye, X. Li, Z. Yin, and J. You, "Surface passivation of perovskite film for efficient solar cells," *Nature Photonics*, vol. 13, no. 7, pp. 460–466, 2019.

[7] Z. K. Tan, R. S. Moghaddam, M. L. Lai, P. Docampo, R. Higler, F. Deschler, M. Price, A. Sadhanala, L. M. Pazos, D. Credgington, F. Hanusch, T. Bein, H. J. Snaith, and R. H. Friend, "Bright light-emitting diodes based on organometal halide perovskite," *Nature Nanotechnology*, vol. 9, no. 9, pp. 687–692, 2014.

[8] L. Protesescu, S. Yakunin, M. I. Bodnarchuk, F. Krieg, R. Caputo, C. H. Hendon, R. X. Yang, A. Walsh, and M. V. Kovalenko, "Nanocrystals of cesium lead halide perovskites ($CsPbX_3$, X = Cl, Br, and I): Novel optoelectronic materials showing bright emission with wide color gamut," *Nano Letters*, vol. 15, no. 6, pp. 3692–3696, 2015. PMID: 25633588.

[9] C. R. Kagan, D. B. Mitzi, and C. D. Dimitrakopoulos, "Organic-inorganic hybrid materials as semiconducting channels in thin-film field-effect transistors," vol. 286, no. 5441, pp. 945–947, 1999.

[10] X. Y. Chin, D. Cortecchia, J. Yin, A. Bruno, and C. Soci, "Lead iodide perovskite light-emitting field-effect transistor," *Nature Communications*, vol. 6, no. May, pp. 1–9, 2015.

[11] S. Yakunin, M. Sytnyk, D. Kriegner, S. Shrestha, G. J. Matt, H. Azimi, C. J. Brabec, J. Stangl, V. Kovalenko, and W. Heiss, "Europe PMC Funders Group Detection of X-ray photons by solution-processed organic- inorganic perovskites," *Nature Photonics*, vol. 9, no. 7, pp. 444–449, 2015.

[12] T. Saga, "Advances in crystalline silicon solar cell technology for industrial mass production," *NPG Asia Materials*, vol. 2, no. 3, pp. 96–102, 2010.

[13] A. Shah, "Photovoltaic technology: The case for thin-film solar cells," *Science*, vol. 285, no. 5428, pp. 692–698, 1999.

[14] M. A. Green, *Crystalline Silicon Solar Cells*, ch. 3, pp. 87–137.

[15] J. Nelson, *The Physics of Solar Cells*, ch. 7. Imperial College Press, 2004.

[16] S. Ruhle, "Tabulated values of the Shockley–Queisser limit for single junction solar cells," *Solar Energy*, vol. 130, pp. 139–147, 2016.

[17] D. E. Carlson and C. R. Wronski, "Amorphous silicon solar cell," *Applied Physics Letters*, vol. 28, no. 671, 1976.

[18] P. D. P. K. L. Chopra and V. Dutta, "Thin-film solar cells: An overview," *Progress in Photovoltaics: Research and Application*, vol. 12, pp. 69–92, 2004.

[19] J. Nelson, *The Physics of Solar Cells*, ch. 8. Imperial College Press, 2004.

[20] H. S. et. al, "Triple-junction thin-film silicon solar cell fabricated on periodically textured substrate with a stabilized efficiency of 13.6%," *Applied Physics Letters*, vol. 106, no. 213902, 2015.

[21] Y. Tawada, "Hydrogenated amorphous silicon carbide as a window material for high efficiency -Si solar cells," *Solar Energy Materials Solar Cells*, vol. 6, no. 3, pp. 299–315, 1982.

[22] D. E. Carlson, "Multijunction amorphous silicon solar cells," *Philosophical Magazine Part B*, vol. 63, no. 1, pp. 305–313, 1991.

[23] F. W. L.L. Kazmerski and G. Morgan, "Thin-film $CuInSe_2$/CdS heterojunction solar cells," *Applied Physics Letters*, vol. 29, no. 4, pp. 268–270, 1976.

[24] F. Solar, "First solar sets world record for CdTe solar pv efficiency."

[25] T. Silverman, U. Jahn, G. Friesen, M. Pravettoni, M. Apolloni, A. Louwen, W. van Sark, M. Schweiger, G. Belluardo, A. Tetzlaff, P. Ingenhoven, and D. Moser, "Characterisation of performance of thin-film photovoltaic technologies," 05 2014.

[26] T. D. Lee and A. U. Ebong, "A review of thin film solar cell technologies and challenges," *Renewable and Sustainable Energy Reviews*, vol. 70, pp. 1286 – 1297, 2017.

[27] Joel Jean, "Pathways for solar photovoltaics," *Energy Environmental Science*, vol. 8, no. 4, pp. 1200–1219, 2015.

[28] D. L. Morgan, "Comparative pulmonary absorption, distribution, and toxicity of copper gallium diselenide, copper indium diselenide, and cadmium telluride in sprague–dawley rats," *Toxicology and Applied Pharmacology*, vol. 147, no. 2, pp. 399–410, 1997.

[29] F. A, "Leaching tests with thin film solar cells based on copper indium diselenide (cis)," *Chemosphere*, vol. 32, no. 8, pp. 1633–1641, 1996.

[30] P. F.-X. C. Yannick-Serge Zimmermann, Andreas Schaffer and M. Lenz, "Thin-film photovoltaic cells: Long-term metal(loid) leaching at their end-of-life," *Environmental Science Technology*, vol. 47, no. 22, pp. 13151–13159, 2013.

[31] NREL, "Champion Photovoltaic Module Efficiency Chart." https://www.nrel.gov/pv/module-efficiency.html, 2020. Online; accessed 05 February 2021.

[32] F. Solar, "First solar hits record 22.1% conversion efficiency for CdTe solar cell."

[33] M. G. Brian O'Regan, "A low-cost, high-efficiency solar cell based on dye-sensitized colloidal TiO_2 films," *Nature*, vol. 353, pp. 737–740, 1991.

[34] A. H. . M. Grätzel, "Molecular photovoltaics," *Accounts of Chemical Research*, vol. 353, pp. 269–277, 2000.

[35] A. Kojima, K. Teshima, Y. Shirai, and T. Miyasaka, "Organometal halide perovskites as visible-light sensitizers for photovoltaic cells," *Journal of the American Chemical Society*, vol. 131, no. 17, pp. 6050–6051, 2009. PMID: 19366264.

[36] J.-H. Im, C.-R. Lee, J.-W. Lee, S.-W. Park, and N.-G. Park, "6.5 % efficient perovskite quantum-dot-sensitized solar cell," *Nanoscale*, vol. 3, pp. 4088–4093, 2011.

[37] H.-S. Kim, C.-R. Lee, J.-H. Im, K.-B. Lee, T. Moehl, A. Marchioro, S.-J. Moon, R. Humphry-Baker, J.-H. Yum, J. E. Moser, M. Grätzel, and N.-G. Park, "Lead iodide perovskite sensitized all-solid-state submicron thin film mesoscopic solar cell with efficiency exceeding 9%.," *Scientific reports*, vol. 2, no. 7436, p. 591, 2012.

[38] NREL, "Best Research-Cell Efficiency Chart." https://www.nrel.gov/pv/cell-efficiency.html, 2020. Online; accessed 06 December 2020.

[39] H. J. Snaith, "Perovskites: The emergence of a new era for low-cost, high-efficiency solar cells," *The Journal of Physical Chemistry Letters*, vol. 4, no. 21, pp. 3623–3630, 2013.

[40] V. M. Goldschmidt, "Die Gesetze der Krystallochemie," *Naturwissenschaften*, vol. 14, no. 21, pp. 477–485, 1926.

[41] A. M. Glazer, "The classification of tilted octahedra in perovskites," *Acta Crystallographica Section B*, vol. 28, pp. 3384–3392, Nov 1972.

[42] P. M. Woodward, "Octahedral tilting in perovskites. i. geometrical considerations," *Acta Crystallographica Section B*, vol. 53, no. 1, pp. 32–43, 1997.

[43] H. T. Stokes, E. H. Kisi, D. M. Hatch, and C. J. Howard, "Group-theoretical analysis of octahedral tilting in ferroelectric perovskites," *Acta Crystallographica Section B*, vol. 58, pp. 934–938, Dec 2002.

[44] C. J. Bartel, C. Sutton, B. R. Goldsmith, R. Ouyang, C. B. Musgrave, L. M. Ghiringhelli, and M. Scheffler, "New tolerance factor to predict the stability of perovskite oxides and halides," *Science Advances*, vol. 5, no. 2, 2019.

[45] M. K. Corpinot and D.-K. Bučar, "A practical guide to the design of molecular crystals," *Crystal Growth & Design*, vol. 19, no. 2, pp. 1426–1453, 2019.

[46] A. Poglitsch and D. Weber, "Dynamic disorder in methylammoniumtrihalogenoplumbates (II) observed by millimeter-wave spectroscopy," *The Journal of Chemical Physics*, vol. 87, no. 11, pp. 6373–6378, 1987.

[47] M. T. Weller, O. J. Weber, P. F. Henry, A. M. Di Pumpo, and T. C. Hansen, "Complete structure and cation orientation in the perovskite photovoltaic methylammonium lead iodide between 100 and 352 K," *Chemical Communications*, vol. 51, no. 20, pp. 4180–4183, 2015.

[48] P. S. Whitfield, N. Herron, W. E. Guise, K. Page, Y. Q. Cheng, I. Milas, and M. K. Crawford, "Structures, Phase Transitions and Tricritical Behavior of the Hybrid Perovskite Methyl Ammonium Lead Iodide," *Scientific Reports*, vol. 6, oct 2016.

[49] A. M. Leguy, J. M. Frost, A. P. McMahon, V. G. Sakai, W. Kochelmann, C. Law, X. Li, F. Foglia, A. Walsh, B. C. O'Regan, J. Nelson, J. T. Cabral, and P. R. Barnes, "The dynamics of methylammonium ions in hybrid organic-inorganic perovskite solar cells," *Nature Communications*, vol. 6, no. May, 2015.

[50] J.-H. Lee, N. C. Bristowe, P. D. Bristowe, and A. K. Cheetham, "Role of hydrogen-bonding and its interplay with octahedral tilting in $CH_3NH_3PbI_3$," *Chemical Communications*, vol. 51, pp. 6434–6437, 2015.

[51] A. Kojima, K. Teshima, Y. Shirai, and T. Miyasaka, "Novel Photoelectrochemical Cell with Mesoscopic Electrodes Sensitized by Lead-halide Compounds (11)," *Meeting Abstracts*, vol. MA2008-02, no. 1, p. 27, 2008.

[52] K. T. Akihiro Kojima and T. M. Yasuo Shirai, "Organometal halide perovskites as visible- light sensitizers for photovoltaic cells," *Journal of the American Chemical Society*, vol. 131, no. October, pp. 6050–6051, 2009.

[53] J.-H. Im, C.-R. Lee, J.-W. Lee, S.-W. Park, and N.-G. Park, "6.5 % Efficient Perovskite Quantum-Dot-Sensitized Solar Cell.," *Nanoscale*, vol. 3, no. 10, pp. 4088–93, 2011.

[54] M. A. Green, A. Ho-Baillie, and H. J. Snaith, "The emergence of perovskite solar cells," *Nature Photonics*, vol. 8, no. 7, pp. 506–514, 2014.

[55] S. D. Stranks, G. E. Eperon, G. Grancini, C. Menelaou, M. J. P. Alcocer, T. Leijtens, L. M. Herz, A. Petrozza, and H. J. Snaith, "Electron-hole diffusion lengths exceeding 1 micrometer in an organometal trihalide perovskite absorber," *Science*, vol. 342, no. 6156, pp. 341–344, 2013.

[56] M. M. Lee, J. Teuscher, T. Miyasaka, T. N. Murakami, and H. J. Snaith, "Efficient hybrid solar cells based on meso-superstructured organometal halide perovskites," *Science*, vol. 338, no. 6107, pp. 643–647, 2012.

[57] M. J. P. Alcocer, T. Leijtens, L. M. Herz, A. Petrozza, and H. J. Snaith, "Electron-Hole Diffusion Lengths Exceeding 1 Micrometer in an Organometal Trihalide Perovskite Absorber," *Science*, vol. 342, no. 2013, pp. 341–344, 2014.

[58] E. Edri, S. Kirmayer, S. Mukhopadhyay, K. Gartsman, G. Hodes, and D. Cahen, "Elucidating the charge carrier separation and working mechanism of $CH_3NH_3PbI_{3-x}Cl_x$ perovskite solar cells.," *Nature communications*, vol. 5, p. 3461, 2014.

[59] M. M. Lee, J. Teuscher, T. Miyasaka, T. N. Murakami, and H. J. Snaith, "Efficient hybrid solar cells based on meso-superstructured organometal halide perovskites," *Science (New York, N.Y.)*, vol. 338, no. 6107, pp. 643–647, 2012.

[60] A. H. James M. Ball, Michael M. Lee and H. J. Snaith, "Low-temperature processed meso-superstructured to thin-film perovskite solar cells," *Energy Environmental Science*, vol. 6, pp. 1739–1743, 2013.

[61] J. Burschka, N. Pellet, S.-J. Moon, R. Humphry-Baker, P. Gao, M. K. Nazeeruddin, and M. Grätzel, "Sequential deposition as a route to high-performance perovskite-sensitized solar cells.," *Nature*, vol. 499, no. 7458, pp. 316–320, 2013.

[62] J. T.-W. Wang, J. M. Ball, E. M. Barea, A. Abate, J. A. Alexander-Webber, J. Huang, M. Saliba, I. Mora-Sero, J. Bisquert, H. J. Snaith, and R. J. Nicholas, "Low-temperature processed electron collection layers of graphene/TiO_2 nanocomposites in thin film perovskite solar cells," *Nano Letters*, vol. 14, no. 2, pp. 724–730, 2014. PMID: 24341922.

[63] D. Liu and T. L. Kelly, "Perovskite solar cells with a planar heterojunction structure prepared using room-temperature solution processing techniques," *Nature Photonics*, vol. 8, no. 2, pp. 133–138, 2014.

[64] H. P. Zhou, Q. Chen, G. Li, S. Luo, T.-b. B. Song, H.-S. S. Duan, Z. R. Hong, J. B. You, Y. S. Liu, and Y. Yang, "Interface engineering of highly efficient perovskite solar cells," *Science*, vol. 345, no. 6196, pp. 542–546, 2014.

[65] J. H. N. Woon Seok Yang, Y. C. K. Nam Joong Jeon, J. S. Seungchan Ryu, and S. I. Seok, "High-performance photovoltaic perovskite layers fabricated through intramolecular exchange," *Science*, vol. 348, no. 6240, pp. 1234–1237, 2015.

[66] M. Saliba, T. Matsui, J.-Y. Seo, K. Domanski, J.-P. Correa-Baena, M. K. Nazeeruddin, S. M. Zakeeruddin, W. Tress, A. Abate, A. Hagfeldt, and M. Grätzel, "Cesium-containing triple cation perovskite solar cells: improved stability, reproducibility and high efficiency," *Energy Environmental Science*, vol. 9, no. 6, pp. 1989–1997, 2016.

[67] M. R. Filip, G. E. Eperon, H. J. Snaith, and F. Giustino, "Steric Engineering of Metal-halide Perovskites with Tunable Optical Band Gaps," *Nature Communications*, vol. 5, p. 5757, 2014.

[68] S. Yang, W. Fu, Z. Zhang, H. Chen, and C.-Z. Li, "Recent advances in perovskite solar cells: efficiency, stability and lead-free perovskite," *Journal of Materials Chemistry A*, vol. 00, pp. 1–21, 2017.

[69] G. E. Eperon, S. D. Stranks, C. Menelaou, M. B. Johnston, L. M. Herz, and H. J. Snaith, "Formamidinium lead trihalide: a broadly tunable perovskite for efficient planar heterojunction solar cells," *Energy Environmental Science*, vol. 7, pp. 982–988, 2014.

[70] T. Salim, S. Sun, Y. Abe, A. Krishna, A. C. Grimsdale, and Y. M. Lam, "Perovskite-based solar cells: impact of morphology and device architecture on device performance," *Journal of Materials Chemistry A*, vol. 3, pp. 8943–8969, 2015.

[71] N.-G. P. Hui-Seon Kim, Michael Grätzel, "Lead iodide perovskite sensitized all-solid-state submicron thin film mesoscopic solar cell with efficiency exceeding 9 %," *Scientific Reports*, vol. 2, no. 591, 2012.

[72] T. Leijtens, S. D. Stranks, G. E. Eperon, R. Lindblad, E. M. J. Johansson, J. M. Ball, M. M. Lee, H. J. Snaith, and I. J. Mcpherson, "Electronic Properties of Meso-Superstructured and Planar Organometal Halide Perovskite Films : Charge Trapping, Photodoing, and Carrier Mobility," *ACS nano*, no. 7, pp. 7147–7155, 2014.

[73] A. Dualeh, N. Tétreault, T. Moehl, P. Gao, M. K. Nazeeruddin, and M. Grätzel, "Effect of annealing temperature on film morphology of organic-inorganic hybrid pervoskite solid-state solar cells," *Advanced Functional Materials*, vol. 24, no. 21, pp. 3250–3258, 2014.

[74] H. Wang, Y. Liu, M. Li, H. Huang, H. M. Xu, R. J. Hong, and H. Shen, "Study on stability of $CH_3NH_3PbI_3$ films and effect of post modification by Aluminum oxide in all-solid-state hybrid solar cells," *Optoelectronics and Advanced Materials, Rapid Communications*, vol. 2, pp. 705–710, 2014.

[75] Official Journal of the European Union , "Directive 2011/65/EU of the European Parliament and of the Council of 8 June 2011 on the restriction of the use of certain hazardous substances in electrical and electronic equipment (recast)." https://eur-lex.europa.eu/LexUriServ/LexUriServ.do?uri=OJ:L:2011:174:0088:0110:en:PDF, 2011. Online; accessed 30 January 2021.

[76] A. Amat, E. Mosconi, E. Ronca, C. Quarti, P. Umari, M. K. Nazeeruddin, M. Grätzel, and F. De Angelis, "Cation-induced band-gap tuning in organohalide perovskites: Interplay of spin–orbit coupling and octahedra tilting," *Nano Letters*, vol. 14, no. 6, pp. 3608–3616, 2014. PMID: 24797342.

[77] A. Binek, F. C. Hanusch, P. Docampo, and T. Bein, "Stabilization of the trigonal high-temperature phase of formamidinium lead iodide," *The Journal of Physical Chemistry Letters*, vol. 6, no. 7, pp. 1249–1253, 2015. PMID: 26262982.

[78] B. Slimi, M. Mollar, I. B. Assaker, I. Kriaa, R. Chtourou, and B. MarĂ, "Perovskite fa1-xmaxpbi3 for solar cells: Films formation and properties," *Energy Procedia*, vol. 102, pp. 87 – 95, 2016. The Proceedings of the 2016 E-MRS Spring Meeting Symposium T - Advanced materials and characterization techniques for solar cells III.

[79] P. Gao, M. Grätzel, and M. K. Nazeeruddin, "Organohalide lead perovskites for photovoltaic applications," *Energy Environmental Science*, vol. 7, pp. 2448–2463, 2014.

[80] S. Kazim, M. K. Nazeeruddin, M. Grätzel, and S. Ahmad, "Perovskite as light harvester: A game changer in photovoltaics," *Angewandte Chemie International Edition*, vol. 53, no. 11, pp. 2812–2824, 2014.

[81] L. M. Pazos-Outón, T. P. Xiao, and E. Yablonovitch, "Fundamental efficiency limit of lead iodide perovskite solar cells," *The Journal of Physical Chemistry Letters*, vol. 9, no. 7, pp. 1703–1711, 2018. PMID: 29537271.

[82] G. Xing, N. Mathews, S. Sun, S. S. Lim, Y. M. Lam, M. Grätzel, S. Mhaisalkar, and T. C. Sum, "Long-range balanced electron- and hole-transport lengths in organic-inorganic $CH_3NH_3PbI_3$," *Science*, vol. 342, no. 6156, pp. 344–347, 2013.

[83] J. A. Christians, P. A. Miranda Herrera, and P. V. Kamat, "Transformation of the excited state and photovoltaic efficiency of $CH_3NH_3PbI_3$ perovskite upon controlled exposure to humidified air," *Journal of the American Chemical Society*, vol. 137, no. 4, pp. 1530–1538, 2015. PMID: 25590693.

[84] S. Aharon, B. E. Cohen, and L. Etgar, "Hybrid lead halide iodide and lead halide bromide in efficient hole conductor free perovskite solar cell," *The Journal of Physical Chemistry C*, vol. 118, no. 30, pp. 17160–17165, 2014.

[85] S. A. Kulkarni, T. Baikie, P. P. Boix, N. Yantara, N. Mathews, and S. Mhaisalkar, "Band-gap tuning of lead halide perovskites using a sequential deposition process," *Journal of Materials Chemistry A*, vol. 2, pp. 9221–9225, 2014.

[86] R. Sheng, A. Ho-Baillie, S. Huang, S. Chen, X. Wen, X. Hao, and M. A. Green, "Methylammonium lead bromide perovskite-based solar cells by vapor-assisted deposition," *The Journal of Physical Chemistry C*, vol. 119, no. 7, pp. 3545–3549, 2015.

[87] T. Baikie, N. S. Barrow, Y. Fang, P. J. Keenan, P. R. Slater, R. O. Piltz, M. Gutmann, S. G. Mhaisalkar, and T. J. White, "A combined single crystal neutron/x-ray diffraction and solid-state nuclear magnetic resonance study of the hybrid perovskites $CH_3NH_3PbX_3$ (X = I, Br and Cl)," *Journal of Materials Chemistry A*, vol. 3, pp. 9298–9307, 2015.

[88] R. Comin, G. Walters, E. S. Thibau, O. Voznyy, Z.-H. Lu, and E. H. Sargent, "Structural, optical, and electronic studies of wide-bandgap lead halide perovskites," *Journal of Materials Chemistry C*, vol. 3, pp. 8839–8843, 2015.

[89] G. E. Eperon, S. D. Stranks, C. Menelaou, M. B. Johnston, L. M. Herz, and H. J. Snaith, "Formamidinium lead trihalide: a broadly tunable perovskite for efficient planar heterojunction solar cells," *Energy Environmental Science*, vol. 7, pp. 982–988, 2014.

[90] E. Prince, *International Tables for Crystallography. Volume C, Mathematical, Physical and Chemical Tables.* Springer, Dordrecht, 2004.

[91] I. L. Karle, K. S. Dragonette, and S. A. Brenner, "The crystal and molecular structure of the serotonin–creatinine sulphate complex," *Acta Crystallographica*, vol. 19, pp. 713–716, Nov 1965.

[92] V. Dyadkin, P. Pattison, V. Dmitriev, and D. Chernyshov, "A new multipurpose diffractometer PILATUS@SNBL," *Journal of Synchrotron Radiation*, vol. 23, no. 3, pp. 825–829, 2016.

[93] G. Caglioti, A. Paoletti, and F. Ricci, "Choice of collimators for a crystal spectrometer for neutron diffraction," *Nuclear Instruments*, vol. 3, no. 4, pp. 223–228, 1958.

[94] G. Caglioti, A. Paoletti, and F. P. Ricci, "Choice of collimators for a crystal spectrometer for neutron diffraction," *Nuclear Instruments*, vol. 3, pp. 223–228, Jan. 1958.

[95] M. Sakata, R. Mori, S. Kumazawza, M. Takata, and H. Toraya, "Electron-density distribution from X-ray powder data by use of profile fits and the maximum-entropy method," *Journal of Applied Crystallography*, vol. 23, pp. 526–534, Dec 1990.

[96] M. Sakata, T. Uno, M. Takata, and C. J. Howard, "Maximum-entropy-method analysis of neutron diffraction data," *Journal of Applied Crystallography*, vol. 26, pp. 159–165, Apr 1993.

[97] E. T. Jaynes, "Information theory and statistical mechanics," *Physical Review*, vol. 106, pp. 620–630, May 1957.

[98] E. T. Jaynes, "Information theory and statistical mechanics. ii," *Physical Review*, vol. 108, pp. 171–190, Oct 1957.

[99] A. Miyata, A. Mitioglu, P. Plochocka, O. Portugall, J. Tse-wei, S. D. Stranks, H. J. Snaith, and R. J. Nicholas, "Direct measurement of the exciton binding energy and effective," pp. 1–22, 2015.

[100] Q. Lin, A. Armin, R. C. R. Nagiri, P. L. Burn, and P. Meredith, "Electro-optics of perovskite solar cells," *Nature Photonics*, vol. 9, no. 2, pp. 106–112, 2015.

[101] A. R. Srimath Kandada and A. Petrozza, "Photophysics of Hybrid Lead Halide Perovskites: The Role of Microstructure," *Accounts of Chemical Research*, vol. 49, no. 3, pp. 536–544, 2016.

[102] C. Wehrenfennig, G. E. Eperon, M. B. Johnston, H. J. Snaith, and L. M. Herz, "High charge carrier mobilities and lifetimes in organolead trihalide perovskites," *Advanced Materials*, vol. 26, no. 10, pp. 1584–1589, 2014.

[103] Y. Kawamura, H. Mashiyama, and K. Hasebe, "Structural Study on Cubic-Tetragonal Transition of $CH_3NH_3PbI_3$," *Journal of the Physical Society of Japan*, vol. 71, no. 7, pp. 1694–1697, 2002.

[104] Y. Yamada, T. Yamada, L. Q. Phuong, N. Maruyama, H. Nishimura, A. Wakamiya, Y. Murata, and Y. Kanemitsu, "Dynamic Optical Properties of $CH_3NH_3PbI_3$ Single Crystals As Revealed by One- and Two-Photon Excited Photoluminescence Measurements," *Journal of the American Chemical Society*, vol. 137, no. 33, pp. 10456–10459, 2015.

[105] C. C. Stoumpos, C. D. Malliakas, and M. G. Kanatzidis, "Semiconducting tin and lead iodide perovskites with organic cations: Phase transitions, high mobilities, and near-infrared photoluminescent properties," *Inorganic Chemistry*, vol. 52, no. 15, pp. 9019–9038, 2013.

[106] J. Xie, Y. Liu, J. Liu, L. Lei, Q. Gao, J. Li, and S. Yang, "Study on the correlations between the structure and photoelectric properties of $CH_3NH_3PbI_3$ perovskite light-harvesting material," *Journal of Power Sources*, vol. 285, pp. 349–353, 2015.

[107] A. Arakcheeva, D. Chernyshov, M. Spina, L. Forró, and E. Horváth, "$CH_3NH_3PbI_3$: precise structural consequences of water absorption at ambient conditions," *Acta Crystallographica Section B*, vol. 72, pp. 716–722, Oct 2016.

[108] T. Baikie, Y. Fang, J. M. Kadro, M. Schreyer, F. Wei, S. G. Mhaisalkar, M. Graetzel, and T. J. White, "Synthesis and crystal chemistry of the hybrid perovskite $CH_3NH_3PbI_3$ for solid-state sensitised solar cell applications," *Journal of Materials Chemistry A*, vol. 1, no. 18, pp. 5628–5641, 2013.

[109] A. Jaffe, Y. Lin, C. M. Beavers, J. Voss, W. L. Mao, and H. I. Karunadasa, "High-pressure single-crystal structures of 3d lead-halide hybrid perovskites and pressure effects on their electronic and optical properties," *ACS Central Science*, vol. 2, no. 4, pp. 201–209, 2016. PMID: 27163050.

[110] Y. Rakita, O. Bar-Elli, E. Meirzadeh, H. Kaslasi, Y. Peleg, G. Hodes, I. Lubomirsky, D. Oron, D. Ehre, and D. Cahen, "Tetragonal $CH_3NH_3PbI_3$ is ferroelectric," *Proceedings of the National Academy of Sciences*, vol. 114, no. 28, pp. E5504–E5512, 2017.

[111] A. Leguy, P. Azarhoosh, M. I. Alonso, M. Campoy-Quiles, O. J. Weber, J. Yao, D. Bryant, M. T. Weller, J. Nelson, A. Walsh, M. van Schilfgaarde, and P. R. F. Barnes, "Experimental and theoretical optical properties of methylammonium lead halide perovskites," *Nanoscale*, pp. 6317–6327, 2015.

[112] T. Chen, B. J. Foley, B. Ipek, M. Tyagi, J. R. D. Copley, C. M. Brown, J. J. Choi, and S.-H. Lee, "Rotational dynamics of organic cations in the $CH_3NH_3PbI_3$ perovskite," *Physical Chemistry Chemical Physics*, vol. 17, pp. 31278–31286, 2015.

[113] Y. Kawamura, H. Mashiyama, and K. Hasebe, "Structural Study on Cubic-Tetragonal Transition of $CH_3NH_3PbI_3$," *Journal of the Physical Society of Japan*, vol. 71, no. 7, pp. 1694–1697, 2002.

[114] R. Wasylishen, O. Knop, and J. Macdonald, "Cation rotation in methylammonium lead halides," *Solid State Communications*, vol. 56, no. 7, pp. 581 – 582, 1985.

[115] O. Knop, R. E. Wasylishen, M. A. White, T. S. Cameron, and M. J. M. V. Oort, " Alkylammonium lead halides. Part 2. $CH_3NH_3PbX_3$ (X = Cl, Br, I) perovskites: cuboctahedral halide cages with isotropic cation reorientation ," *Canadian Journal of Chemistry*, vol. 68, no. 3, pp. 412–422, 1990.

[116] N. Onoda-Yamamuro, "Calorimetric and IR spectroscopic studies of phase transitions in methylammonium trihalogenoplumbates (II)†," *Journal of Physics and Chemistry of Solids*, vol. 51, pp. 1383–1395, Jan. 1990.

[117] K. Yamada, K. Isobe, E. Tsuyama, T. Okuda, and Y. Furukawa, "Chloride ion conductor $CH_3NH_3GeCl_3$ studied by Rietveld analysis of X-ray diffraction and 35Cl NMR," *Solid State Ionics*, vol. 79, no. C, pp. 152–157, 1995.

[118] Z. Xiao, Y. Yuan, Y. Shao, Q. Wang, Q. Dong, C. Bi, P. Sharma, A. Gruverman, and J. Huang, "Giant switchable photovoltaic effect in organometal trihalide perovskite devices," *Nature Materials*, vol. 14, no. 2, pp. 193–197, 2015.

[119] T. Y. Yang, G. Gregori, N. Pellet, M. Grätzel, and J. Maier, "The Significance of Ion Conduction in a Hybrid Organic-Inorganic Lead-Iodide-Based Perovskite Photosensitizer," *Angewandte Chemie - International Edition*, vol. 54, no. 27, pp. 7905–7910, 2015.

[120] C. Wagner, "Galvanische Zellen mit festen Elektrolyten mit gemischter Stromleitung," *Zeitschrift für Elektrochemie, Berichte der Bunsengesellschaft für physikalische Chemie*, vol. 60, no. 1, pp. 4–7, 1956.

[121] H. J. Snaith, A. Abate, J. M. Ball, G. E. Eperon, T. Leijtens, N. K. Noel, S. D. Stranks, J. T.-W. Wang, K. Wojciechowski, and W. Zhang, "Anomalous hysteresis in perovskite solar cells," *The Journal of Physical Chemistry Letters*, vol. 5, no. 9, pp. 1511–1515, 2014. PMID: 26270088.

[122] E. L. Unger, E. T. Hoke, C. D. Bailie, W. H. Nguyen, A. R. Bowring, T. Heumüller, M. G. Christoforo, and M. D. McGehee, "Hysteresis and transient behavior in current–voltage measurements of hybrid-perovskite absorber solar cells," *Energy Environmental Science*, vol. 7, pp. 3690–3698, 2014.

[123] J. S. Han, Q. V. Le, J. Choi, H. Kim, S. G. Kim, K. Hong, C. W. Moon, T. L. Kim, S. Y. Kim, and H. W. Jang, "Lead-free all-inorganic cesium tin iodide perovskite for filamentary and interface-type resistive switching toward environment-friendly and temperature-tolerant nonvolatile memories," *ACS Applied Materials & Interfaces*, vol. 11, no. 8, pp. 8155–8163, 2019.

[124] A. Shaban, M. Joodaki, S. Mehregan, and I. W. Rangelow, "Probe-induced resistive switching memory based on organic-inorganic lead halide perovskite materials," *Organic Electronics*, vol. 69, pp. 106 – 113, 2019.

[125] H. Wang, M. Zhou, and H. Luo, "Electric-field-induced dynamic electronic junctions in hybrid organic inorganic perovskites for optoelectronic applications," *ACS Omega*, vol. 3, no. 2, pp. 1445–1450, 2018.

[126] X. Wang, Y. Ling, Y.-C. Chiu, Y. Du, J. L. Barreda, F. Perez-Orive, B. Ma, P. Xiong, and H. Gao, "Dynamic electronic junctions in organic inorganic hybrid perovskites," *Nano Letters*, vol. 17, no. 8, pp. 4831–4839, 2017. PMID: 28661680.

[127] H.-S. Duan, H. Zhou, Q. Chen, P. Sun, S. Luo, T.-B. Song, B. Bob, and Y. Yang, "The identification and characterization of defect states in hybrid organic–inorganic perovskite photovoltaics," *Physical Chemistry Chemical Physics*, vol. 17, pp. 112–116, 2015.

[128] J. R. Ayres, "Characterization of trapping states in polycrystallineâsilicon thin film transistors by deep level transient spectroscopy," *Journal of Applied Physics*, vol. 74, no. 3, pp. 1787–1792, 1993.

[129] A. Balcioglu, R. K. Ahrenkiel, and F. Hasoon, "Deep-level impurities in CdTe/CdS thin-film solar cells," *Journal of Applied Physics*, vol. 88, no. 12, pp. 7175–7178, 2000.

[130] C. Eames, J. M. Frost, P. R. Barnes, B. C. O'Regan, A. Walsh, and M. S. Islam, "Ionic transport in hybrid lead iodide perovskite solar cells," *Nature Communications*, vol. 6, no. May, pp. 2–9, 2015.

[131] J. M. Azpiroz, E. Mosconi, J. Bisquert, and F. De Angelis, "Defect migration in methylammonium lead iodide and its role in perovskite solar cell operation," *Energy Environmental Science*, vol. 8, pp. 2118–2127, 2015.

[132] W.-J. Yin, T. Shi, and Y. Yan, "Unusual defect physics in $CH_3NH_3PbI_3$ perovskite solar cell absorber," *Applied Physics Letters*, vol. 104, no. 6, p. 063903, 2014.

[133] Y. Yuan, J. Chae, Y. Shao, Q. Wang, Z. Xiao, A. Centrone, and J. Huang, "Photovoltaic switching mechanism in lateral structure hybrid perovskite solar cells," *Advanced Energy Materials*, vol. 5, no. 15, p. 1500615, 2015.

[134] M. De Bastiani, G. Dell'Erba, M. Gandini, V. D'Innocenzo, S. Neutzner, A. R. S. Kandada, G. Grancini, M. Binda, M. Prato, J. M. Ball, M. Caironi, and A. Petrozza, "Ion migration and the role of preconditioning cycles in the stabilization of the j–v characteristics of inverted hybrid perovskite solar cells," *Advanced Energy Materials*, vol. 6, no. 2, p. 1501453, 2016.

[135] K. Miyata, D. Meggiolaro, M. Tuan Trinh, P. P. Joshi, E. Mosconi, S. C. Jones, F. De Angelis, and X. Y. Zhu, "Large polarons in lead halide perovskites," *Science Advances*, vol. 3, no. 8, 2017.

[136] C. C. Stoumpos, C. D. Malliakas, and M. G. Kanatzidis, "Semiconducting tin and lead iodide perovskites with organic cations: Phase transitions, high mobilities, and near-infrared photoluminescent properties," *Inorganic Chemistry*, vol. 52, no. 15, pp. 9019–9038, 2013.

[137] P. Pistor, A. Ruiz, A. Cabot, and V. Izquierdo-Roca, "Advanced Raman Spectroscopy of Methylammonium Lead Iodide: Development of a Non-destructive Characterisation Methodology," *Scientific Reports*, vol. 6, no. September, pp. 1–8, 2016.

[138] W. Guo, D. Wang, J. Hu, Z. K. Tang, and S. Du, "Raman spectroscopy of iodine molecules trapped in zeolite crystals," *Applied Physics Letters*, vol. 98, no. 4, p. 043105, 2011.

[139] H. Mittag, H. Stegemann, H. Füllbier, and G. Irmer, "Raman spectroscopic investigation of n-alkylurotropinium polyiodides," *Journal of Raman Spectroscopy*, vol. 20, no. 4, pp. 251–255, 1989.

[140] P. M. Harris, E. Mack, and F. C. Blake, "The atomic arrangement in the crystal of orthorhombic iodine," *Journal of the American Chemical Society*, vol. 50, no. 6, pp. 1583–1600, 1928.

[141] C. V. D. Marel, W. Bras, and W. V. D. Lugt, "X-ray diffraction measurements on liquid iodine and some dilute mixtures of KI in I_2," *Molecular Physics*, vol. 64, no. 3, pp. 445–456, 1988.

[142] Z. Wang, Y. Zhang, M. Kurmoo, T. Liu, S. Vilminot, B. Zhao, and S. Gao, "$[Zn_3(HCOO)_6]$: A porous diamond framework conformable to guest inclusion," *Australian Journal of Chemistry*, vol. 59, no. 9, pp. 617–628, 2006.

[143] T. Gibiński, E. Cisowska, W. Żdanowicz, Z. Henkie, and A. Wojakowski, "The Preparation and Crystal Structure of MgP_4," *Kristall und Technik*, vol. 9, no. 2, pp. 161–163, 1974.

[144] P. H. Svensson and L. Kloo, "Synthesis, structure, and bonding in polyiodide and metal iodide-iodine systems," *Chemical Reviews*, vol. 103, no. 5, pp. 1649–1684, 2003.

[145] W. L. Jolly, "Advances in inorganic chemistry and radiochemistry," *Inorganic Chemistry*, vol. 3, no. 8, pp. 1204–1204, 1964.

[146] H. A. Tasman and K. H. Boswijk, " Re-investigation of the crystal structure of CsI_3 ," *Acta Crystallographica*, vol. 8, no. 12, pp. 857–857, 1955.

[147] Y. C. Zhao, W. K. Zhou, X. Zhou, K. H. Liu, D. P. Yu, and Q. Zhao, "Quantification of light-enhanced ionic transport in lead iodide perovskite thin films and its solar cell applications," *Light: Science and Applications*, vol. 6, no. 5, pp. e16243–8, 2017.

[148] G. Y. Kim, A. Senocrate, T. Y. Yang, G. Gregori, M. Grätzel, and J. Maier, "Large tunable photoeffect on ion conduction in halide perovskites and implications for photodecomposition," *Nature Materials*, vol. 17, no. 5, pp. 445–449, 2018.

[149] J. S. Manser, J. A. Christians, and P. V. Kamat, "Intriguing optoelectronic properties of metal halide perovskites," *Chemical Reviews*, vol. 116, no. 21, pp. 12956–13008, 2016. PMID: 27327168.

[150] L. M. Herz, "Charge-carrier dynamics in organic-inorganic metal halide perovskites," *Annual Review of Physical Chemistry*, vol. 67, no. 1, pp. 65–89, 2016. PMID: 26980309.

[151] T. M. Brenner, D. A. Egger, L. Kronik, G. Hodes, and D. Cahen, "Hybrid organic - Inorganic perovskites: Low-cost semiconductors with intriguing charge-transport properties," *Nature Reviews Materials*, vol. 1, no. 1, 2016.

[152] B. Chen, J. Shi, X. Zheng, Y. Zhou, K. Zhu, and S. Priya, "Ferroelectric solar cells based on inorganic–organic hybrid perovskites," *Journal of Materials Chemistry A*, vol. 3, pp. 7699–7705, 2015.

[153] Y. Kutes, L. Ye, Y. Zhou, S. Pang, B. D. Huey, and N. P. Padture, "Direct observation of ferroelectric domains in solution-processed $CH_3NH_3PbI_3$ perovskite thin films," *The Journal of Physical Chemistry Letters*, vol. 5, no. 19, pp. 3335–3339, 2014. PMID: 26278441.

[154] A. A. Medjahed, P. Dally, T. Zhou, N. Lemaitre, D. Djurado, P. Reiss, and S. Pouget, "Unraveling the formation mechanism and ferroelastic behavior of $MAPbI_3$ perovskite thin films prepared in the presence of chloride," *Chemistry of Materials*, vol. 32, no. 8, pp. 3346–3357, 2020.

[155] A. Gómez, Q. Wang, A. R. Goñi, M. Campoy-Quiles, and A. Abate, "Ferroelectricity-free lead halide perovskites," *Energy Environmental Science*, vol. 12, pp. 2537–2547, 2019.

[156] Z. Fan, J. Xiao, K. Sun, L. Chen, Y. Hu, J. Ouyang, K. P. Ong, K. Zeng, and J. Wang, "Ferroelectricity of $CH_3NH_3PbI_3$ perovskite," *The Journal of Physical Chemistry Letters*, vol. 6, no. 7, pp. 1155–1161, 2015. PMID: 26262965.

[157] E. Strelcov, Q. Dong, T. Li, J. Chae, Y. Shao, Y. Deng, A. Gruverman, J. Huang, and A. Centrone, "$CH_3NH_3PbI_3$ perovskites: Ferroelasticity revealed," *Science Advances*, vol. 3, no. 4, 2017.

[158] L. Qin, L. Lv, C. Li, L. Zhu, Q. Cui, Y. Hu, Z. Lou, F. Teng, and Y. Hou, "Temperature dependent amplified spontaneous emission of vacuum annealed perovskite films," *RSC Advances*, vol. 7, no. 26, pp. 15911–15916, 2017.

[159] F. Paquin, J. Rivnay, A. Salleo, N. Stingelin, and C. Silva, "Multi-phase semicrystalline microstructures drive exciton dissociation in neat plastic semiconductors," *Journal of Materials Chemistry C*, vol. 3, pp. 10715 – 10722, 2015.

[160] M. Liu, M. B. Johnston, and H. J. Snaith, "Efficient planar heterojunction perovskite solar cells by vapour deposition," *Nature*, vol. 501, no. 7467, pp. 395–398, 2013.

[161] A. Buin, P. Pietsch, J. Xu, O. Voznyy, A. H. Ip, R. Comin, and E. H. Sargent, "Materials processing routes to trap-free halide perovskites," *Nano Letters*, vol. 14, no. 11, pp. 6281–6286, 2014. PMID: 25296282.

[162] S. T. Williams, C.-C. Chueh, and A. K.-Y. Jen, "Navigating organo-lead halide perovskite phase space via nucleation kinetics toward a deeper understanding of perovskite phase transformations and structure property relationships," *Small*, vol. 11, no. 26, pp. 3088–3096, 2015.

[163] S. D. Stranks, P. K. Nayak, W. Zhang, T. Stergiopoulos, and H. J. Snaith, "Formation of thin films of organic–inorganic perovskites for high-efficiency solar cells," *Angewandte Chemie International Edition*, vol. 54, no. 11, pp. 3240–3248, 2015.

[164] G. E. Eperon, V. M. Burlakov, P. Docampo, A. Goriely, and H. J. Snaith, "Morphological control for high performance, solution-processed planar heterojunction perovskite solar cells," *Advanced Functional Materials*, vol. 24, no. 1, pp. 151–157, 2014.

[165] D. Bi, J. Luo, F. Zhang, A. Magrez, E. N. Athanasopoulou, A. Hagfeldt, and M. Grätzel, "Morphology engineering: A route to highly reproducible and high efficiency perovskite solar cells," *ChemSusChem*, vol. 10, no. 7, pp. 1624–1630, 2017.

[166] G. Niu, X. Guo, and L. Wang, "Review of recent progress in chemical stability of perovskite solar cells," *Journal of Materials Chemistry A*, vol. 3, pp. 8970–8980, 2015.

[167] Y. Han, S. Meyer, Y. Dkhissi, K. Weber, J. M. Pringle, U. Bach, L. Spiccia, and Y.-B. Cheng, "Degradation observations of encapsulated planar $CH_3NH_3PbI_3$ perovskite solar cells at high temperatures and humidity," *Journal of Materials Chemistry A*, vol. 3, pp. 8139–8147, 2015.

[168] T. A. Berhe, W.-N. Su, C.-H. Chen, C.-J. Pan, J.-H. Cheng, H.-M. Chen, M.-C. Tsai, L.-Y. Chen, A. A. Dubale, and B.-J. Hwang, "Organometal halide perovskite solar cells: degradation and stability," *Energy Environmental Science*, vol. 9, pp. 323–356, 2016.

[169] H.-S. Kim, J.-Y. Seo, and N.-G. Park, "Material and device stability in perovskite solar cells," *ChemSusChem*, vol. 9, no. 18, pp. 2528–2540, 2016.

[170] A. Senocrate, T. Acartürk, G. Y. Kim, R. Merkle, U. Starke, M. Grätzel, and J. Maier, "Interaction of oxygen with halide perovskites," *Journal of Materials Chemistry A*, vol. 6, pp. 10847–10855, 2018.

[171] N. Aristidou, I. Sanchez-Molina, T. Chotchuangchutchaval, M. Brown, L. Martinez, T. Rath, and S. A. Haque, "The role of oxygen in the degradation of methylammonium lead trihalide perovskite photoactive layers," *Angewandte Chemie International Edition*, vol. 54, no. 28, pp. 8208–8212, 2015.

[172] L. Ma, D. Guo, M. Li, C. Wang, Z. Zhou, X. Zhao, F. Zhang, Z. Ao, and Z. Nie, "Temperature-dependent thermal decomposition pathway of organic inorganic halide perovskite materials," *Chemistry of Materials*, vol. 31, no. 20, pp. 8515–8522, 2019.

[173] H. Zhou, Q. Chen, G. Li, S. Luo, T.-B. Song, H.-S. Duan, Z. Hong, J. You, Y. Liu, and Y. Yang, "Interface engineering of highly efficient perovskite solar cells," *Science*, vol. 345, no. 6196, pp. 542–546, 2014.

[174] X. Gong, M. Li, X.-B. Shi, H. Ma, Z.-K. Wang, and L.-S. Liao, "Controllable perovskite crystallization by water additive for high-performance solar cells," *Advanced Functional Materials*, vol. 25, no. 42, pp. 6671–6678, 2015.

[175] S. R. Raga, M.-C. Jung, M. V. Lee, M. R. Leyden, Y. Kato, and Y. Qi, "Influence of air annealing on high efficiency planar structure perovskite solar cells," *Chemistry of Materials*, vol. 27, no. 5, pp. 1597–1603, 2015.

[176] Y. Tian, M. Peter, E. Unger, M. Abdellah, K. Zheng, T. Pullerits, A. Yartsev, V. Sundström, and I. G. Scheblykin, "Mechanistic insights into perovskite photoluminescence enhancement: light curing with oxygen can boost yield thousandfold," *Physical Chemistry Chemical Physics*, vol. 17, pp. 24978–24987, 2015.

[177] X. Fu, D. A. Jacobs, F. J. Beck, T. Duong, H. Shen, K. R. Catchpole, and T. P. White, "Photoluminescence study of time- and spatial-dependent light induced trap de-activation in $CH_3NH_3PbI_3$ perovskite films," *Physical Chemistry Chemical Physics*, vol. 18, pp. 22557–22564, 2016.

[178] Y. Yu, S. Wan, D. Hong, and Y. Tian, "Photo-induced dual passivation via usanovich acid base on surface defects of methylammonium lead triiodide perovskite," *Physical Chemistry Chemical Physics*, vol. 20, pp. 28068–28074, 2018.

[179] J. F. Galisteo-López, M. Anaya, M. E. Calvo, and H. Míguez, "Environmental effects on the photophysics of organic–inorganic halide perovskites," *The Journal of Physical Chemistry Letters*, vol. 6, no. 12, pp. 2200–2205, 2015. PMID: 26266592.

[180] H.-H. Fang, S. Adjokatse, H. Wei, J. Yang, G. R. Blake, J. Huang, J. Even, and M. A. Loi, "Ultrahigh sensitivity of methylammonium lead tribromide perovskite single crystals to environmental gases," *Science Advances*, vol. 2, no. 7, 2016.

[181] L. Qin, L. Lv, C. Li, L. Zhu, Q. Cui, Y. Hu, Z. Lou, F. Teng, and Y. Hou, "Temperature dependent amplified spontaneous emission of vacuum annealed perovskite films," *RSC Advances*, vol. 7, pp. 15911–15916, 2017.

[182] Q. Chen, H. Zhou, Y. Fang, A. Z. Stieg, T. B. Song, H. H. Wang, X. Xu, Y. Liu, S. Lu, J. You, P. Sun, J. McKay, M. S. Goorsky, and Y. Yang, "The optoelectronic role of chlorine in $CH_3NH_3PbI_3$ (Cl)-based perovskite solar cells," *Nature Communications*, vol. 6, pp. 1–9, 2015.

[183] C. Ran, J. Xu, W. Gao, C. Huang, and S. Dou, "Defects in metal triiodide perovskite materials towards high-performance solar cells: Origin, impact, characterization, and engineering," *Chemical Society Reviews*, vol. 47, no. 12, pp. 4581–4610, 2018.

[184] G. Xing, N. Mathews, S. S. Lim, N. Yantara, X. Liu, D. Sabba, M. Grätzel, S. Mhaisalkar, and T. C. Sum, "Low-temperature solution-processed wavelength-tunable perovskites for lasing," *Nature Materials*, vol. 13, no. 5, pp. 476–480, 2014.

[185] D. W. DeQuilettes, S. M. Vorpahl, S. D. Stranks, H. Nagaoka, G. E. Eperon, M. E. Ziffer, H. J. Snaith, and D. S. Ginger, "Impact of microstructure on local carrier lifetime in perovskite solar cells," *Science*, vol. 348, no. 6235, pp. 683–686, 2015.

[186] J. Rodraguez-Carvajal, "Recent advances in magnetic structure determination by neutron powder diffraction," *Physica B: Condensed Matter*, vol. 192, no. 1, pp. 55 – 69, 1993.

[187] J. He, W.-H. Fang, R. Long, and O. V. Prezhdo, "Why oxygen increases carrier lifetimes but accelerates degradation of $CH_3NH_3PbI_3$ under light irradiation: Time-domain ab initio analysis," *Journal of the American Chemical Society*, vol. 142, no. 34, pp. 14664–14673, 2020. PMID: 32786790.

[188] R. Brenes, D. Guo, A. Osherov, N. K. Noel, C. Eames, E. M. Hutter, S. K. Pathak, F. Niroui, R. H. Friend, M. S. Islam, H. J. Snaith, V. Bulović, T. J. Savenije, and S. D. Stranks, "Metal Halide Perovskite Polycrystalline Films Exhibiting Properties of Single Crystals," *Joule*, vol. 1, no. 1, pp. 155–167, 2017.

[189] L. Ma, D. Guo, M. Li, C. Wang, Z. Zhou, X. Zhao, F. Zhang, Z. Ao, and Z. Nie, "Temperature-dependent thermal decomposition pathway of organic inorganic halide perovskite materials," *Chemistry of Materials*, vol. 31, no. 20, pp. 8515–8522, 2019.

[190] Y.-K. Ren, S.-D. Liu, B. Duan, Y.-F. Xu, Z.-Q. Li, L.-H. Hu, J. Zhu, and S. Dai, "Controllable intermediates by molecular self-assembly for optimizing the fabrication of large-grain perovskite films via one-step spin-coating," *Journal of Alloys and Compounds*, vol. 705, 01 2017.

[191] R. Caminiti, L. Pandolfi, and P. Ballirano, "Structure of polyethylene from X-ray powder diffraction: influence of the amorphous fraction on data analysis," *Journal of Macromolecular Science - Physics*, vol. 39, 2000.

[192] S. Draguta, S. Thakur, Y. V. Morozov, Y. Wang, J. S. Manser, P. V. Kamat, and M. Kuno, "Spatially Non-uniform Trap State Densities in Solution-Processed Hybrid Perovskite Thin Films," *Journal of Physical Chemistry Letters*, vol. 7, no. 4, pp. 715–721, 2016.

[193] A. Senocrate, I. Moudrakovski, G. Y. Kim, T. Y. Yang, G. Gregori, M. Grätzel, and J. Maier, "The Nature of Ion Conduction in Methylammonium Lead Iodide: A Multimethod Approach," *Angewandte Chemie - International Edition*, vol. 56, no. 27, pp. 7755–7759, 2017.

[194] A. Zohar, I. Levine, S. Gupta, O. Davidson, D. Azulay, O. Millo, I. Balberg, G. Hodes, and D. Cahen, "What is the Mechanism of $MAPbI_3$ p-Doping by I_2? Insights from Optoelectronic Properties," *ACS Energy Letters*, vol. 2, no. 10, pp. 2408–2414, 2017.

[195] D. Meggiolaro, E. Mosconi, and F. De Angelis, "Modeling the Interaction of Molecular Iodine with $MAPbI_3$: A Probe of Lead-Halide Perovskites Defect Chemistry," *ACS Energy Letters*, vol. 3, no. 2, pp. 447–451, 2018.

[196] S. Ivantchev, E. Kroumova, G. Madariaga, J. M. Pérez-Mato, and M. I. Aroyo, "SUBGROUPGRAPH: A computer program for analysis of group-subgroup relations between space groups," *Journal of Applied Crystallography*, vol. 33, no. 4, pp. 1190–1191, 2000.

[197] M. Szafrański and A. Katrusiak, "Mechanism of Pressure-Induced Phase Transitions, Amorphization, and Absorption-Edge Shift in Photovoltaic Methylammonium Lead Iodide," *Journal of Physical Chemistry Letters*, vol. 7, no. 17, pp. 3458–3466, 2016.

[198] F. Capitani, C. Marini, S. Caramazza, P. Postorino, G. Garbarino, M. Hanfland, A. Pisanu, P. Quadrelli, and L. Malavasi, "High-pressure behavior of methylammonium lead iodide ($MAPbI_3$) hybrid perovskite," *Journal of Applied Physics*, vol. 119, no. 18, p. 185901, 2016.

[199] A. Arakcheeva, V. Svitlyk, E. Polini, L. Henry, D. Chernyshov, A. Sienkiewicz, G. Giriat, A. Glushkova, M. Kollar, B. Náfrádi, L. Forro, and E. Horváth, "Pressure-induced transformation of $CH_3NH_3PbI_3$: The role of the noble-gas pressure transmitting media," *Acta Crystallographica Section B: Structural Science, Crystal Engineering and Materials*, vol. 75, pp. 361–370, 2019.

[200] K. A, T. K, S. Y, and M. T, "Organometal halide perovskites as visible-light sensitizers for photovoltaic cells," *Journal of the American Chemical Society*, vol. 131, no. 17, pp. 6050–1, 2009.

[201] Web of Knowledge, "Web of science search for "perovskite solar cell" in 2019 yielded 4,114 hits." www.webofknowledge.com, 2020. Online; accessed 06 December 2020.

[202] J. Feng, "Mechanical properties of hybrid organic-inorganic $CH_3NH_3BX_3$ (B = Sn, Pb; X = Br, I) perovskites for solar cell absorbers," *APL Materials*, vol. 2, no. 8, p. 081801, 2014.

[203] Z. Li, M. Grimsditch, C. Foster, and S.-K. Chan, "Dielectric and elastic properties of ferroelectric materials at elevated temperature," *Journal of Physics and Chemistry of Solids*, vol. 57, no. 10, pp. 1433 – 1438, 1996.

Appendix A

Supplementary Information

A.1 Single Crystal X-ray Diffraction of SE-MAPbI$_3$ - Ambient Temperature

Chemical formula	CNH_6PbI_3
Molar mass, SG, Z, T(K)	619.98, $I4/m$ (87), 4, 300.0(1)
a, b, c () α, β, γ (deg), V(Å^3)	8.87560(10), 8.87560(10), 12.6517(3), 90, 90, 90, 996.65(3)
Radiation source	SuperNova (Mo) X-ray Source, mirror, MoK, 0.71073
Density(g cm-3), μ (mm-1)	4.132, 26.137
Crystal form, colour, dimensions	Multifaceted, dark, 0.13 (max), 0.045 (min), 0.079 (mid)
Diffractometer	Four-circle diffractometer SuperNova, Dual, Cu, AtlasS2 Data collection method scans
Absorption correction	CrysAlisPro 1.171.38.41 (Rigaku OD, 2015) Numerical absorption correction based on gaussian integration over a multifaceted crystal model. Tmin 0.093, Tmax 0.391 Empirical absorption correction using spherical harmonics, implemented in SCALE3 ABSPACK scaling algorithm.
reflections: measured, independent, observed	10920, 947, 801
Criterion for observed	I > 2(I)
Rint, Rsigma,min (o), max (o), full (o)	3.74, 4.58, 3.22, 32.91 (meas. frac. 96.9 %), 25.24 (meas. frac. 99.8 %)
Software	SHELXS, SHELX (2013/14)
R1[F2 > 2(F2)], Rall, wR(F2),S, No. reflections, parameters	3.92, 4.62, 9.93, 1.400, 947, 32
Weighting scheme	(SHELXL) w = 1/[2 (F2o) + (0.0 P)2 + 40.8 P],where P = max(F2o + 2 F2c)/3
(/)max, max, min (e Å-3)	0.022, 1.50, -1.80
Extinction correction	SHELXL, 0.00070(6)

Table A.1 Crystallographic parameters and experimental condition obtained from single crystal X-ray diffraction of the sample SE-MAPbI$_3$ at 300 K. $a = b = 8.8756(1)$ Å and $c = 12.6517(3)$ Å.

A.2 Synchrotron Powder Diffraction - Low Temperature Thermal Annealing

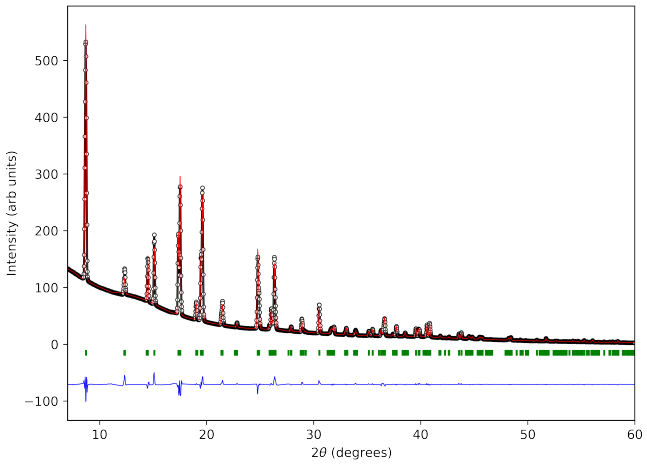

(a)

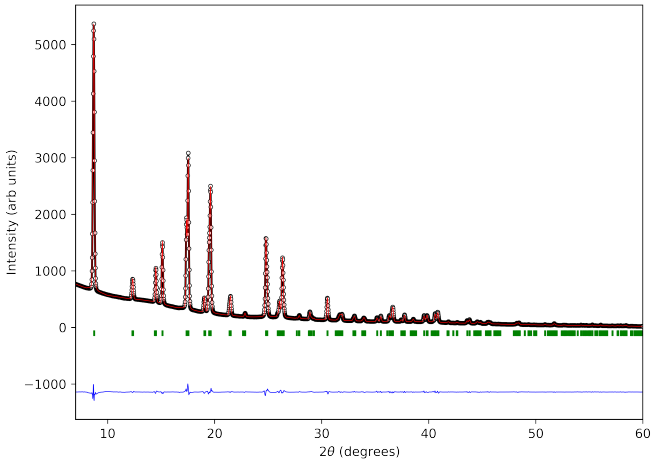

(b)

Fig. A.1 Observed (circles), calculated (solid lines) and difference (blue line) X-ray powder diffraction profile from Rietveld refinement at 300 K for the samples (a) SS-$MAPbI_3$ and (b) AA80-$MAPbI_3$ at 400K. Fit factors for (a) R_p = 11.0 % and R_{wp} = 9.7 %, (b) R_p = 6.10 % and R_{wp} = 5.48 %.

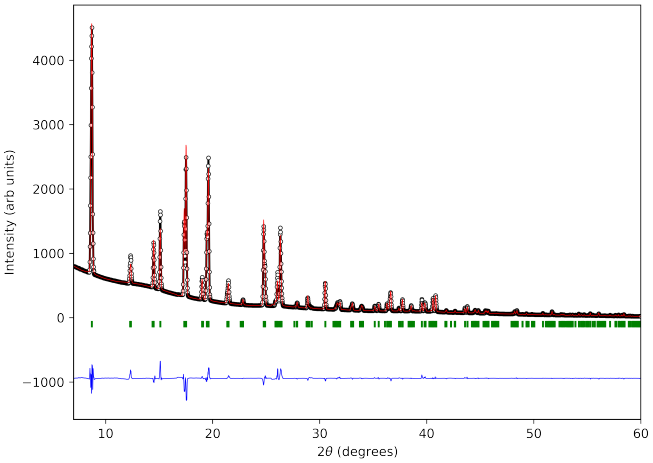

(a)

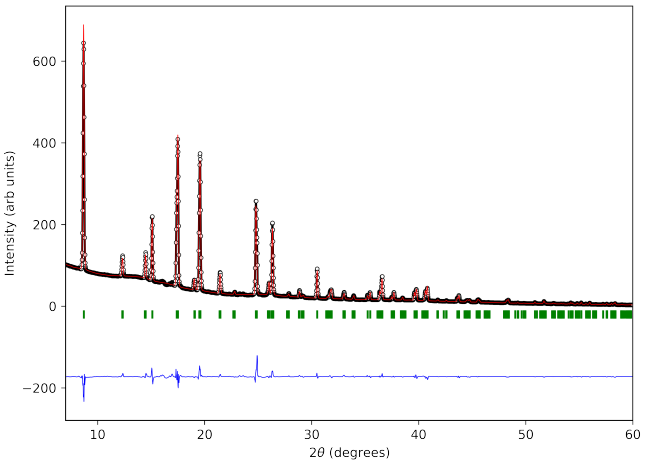

(b)

Fig. A.2 Observed (circles), calculated (solid lines) and difference (blue line) X-ray powder diffraction profile from Rietveld refinement at 300 K for the samples (a) AV80-$MAPbI_3$ and (b) at 400K. Fit factors for (a) R_p = 12.6 % and R_{wp} = 12.4 % and (b) R_p = 13.9 % and R_{wp} = 13.2 %.

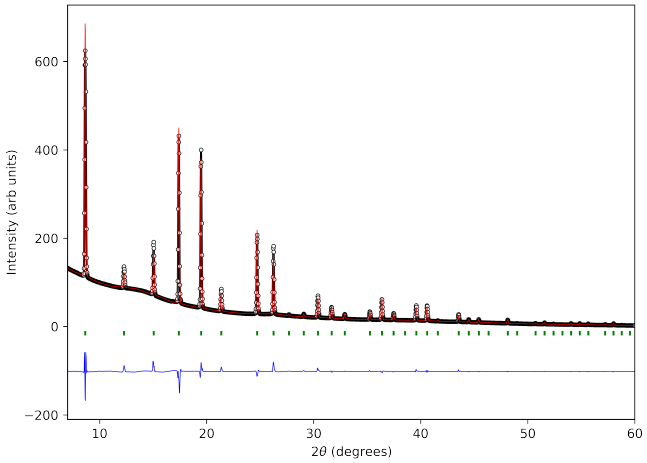

(a)

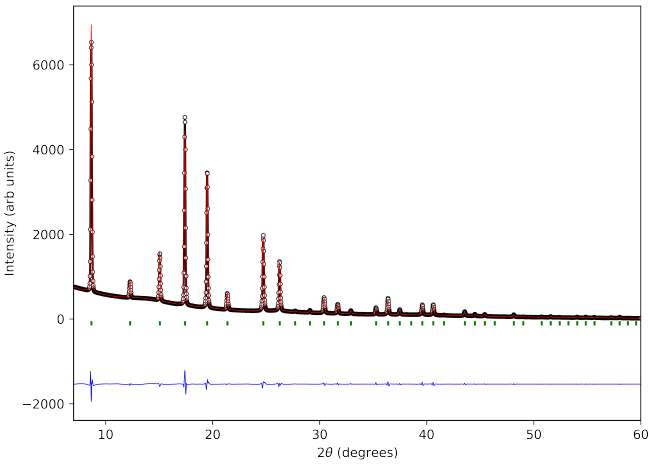

(b)

Fig. A.3 Observed (circles), calculated (solid lines) and difference (blue line) X-ray powder diffraction profile from Rietveld refinement at 400 K for the samples (a) SS-$MAPbI_3$ and (b) AA80-$MAPbI_3$ at 400K. Fit factors for (a) R_p = 15.2 % and R_{wp} = 12.6 %, (b) R_p = 9.67 % and R_{wp} = 8.15 %.

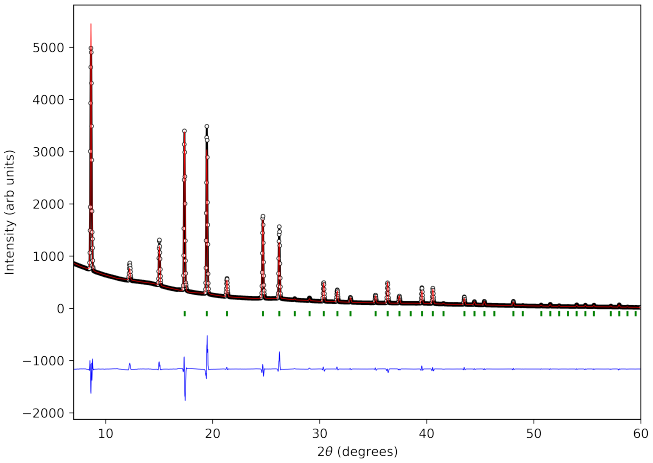

(a)

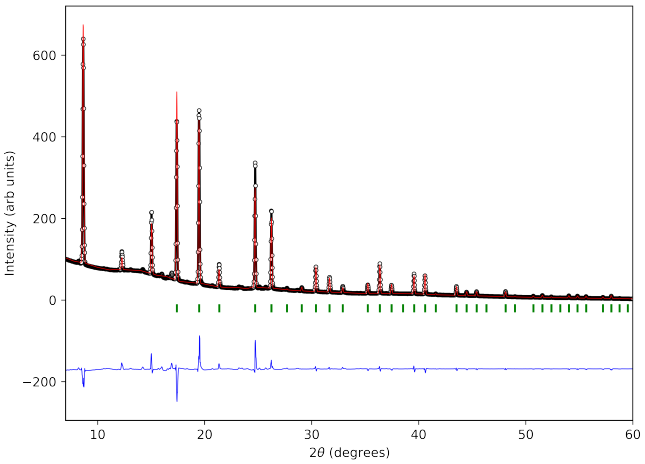

(b)

Fig. A.4 Observed (circles), calculated (solid lines) and difference (blue line) X-ray powder diffraction profile from Rietveld refinement at 400 K for the samples (a) AV80-$MAPbI_3$ and (b) at 400K. Fit factors for (a) R_p = 18.5 % and R_{wp} = 17.7 % and (b) R_p = 27.2 % and R_{wp} = 19.5 %.

A.3 Single Crystal Synchrotron Diffraction of AV80-$MAPbI_3$ - 370 K

Table A.2 and A.3 outlines the details of the refined crystal structure for the sample AV80-$MAPbI_3$ at 370 K. This structure was derived from a synchrotron single crystal diffraction measurement performed using the PILATUS@SNBL diffractometer. The refinement resulted in fit parameters R_1 = 5.18 %, wR_2 = 10.85 %, S = 1.206.

AV80-$MAPbI_3$ - Single Crystal Diffraction Atomic Coordinates at 370 K				
Atom	x	y	z	Occupancy
Pb1	0.50	0.50	0.50	1.00
I1	0.00	0.50	0.50	1.0
C1	0.00	0.00	0.14(2)	0.23(6)
N1	0.00	0.00	0.14(2)	0.23(6)

Table A.2 Refined structural parameters for AV80-$MAPbI_3$ in space group $Pm\bar{3}m$ with lattice parameters $a = b = c$ = 6.2581(3) Å and a cell volume of 245.09(4) $Å^3$.

AV80-$MAPbI_3$ - Single Crystal Diffraction ADPs at 370 K						
Atom	U_{11}	U_{22}	U_{33}	U_{12}	U_{13}	U_{23}
Pb1	0.042(2)	0.042(2)	0.042(2)	0.000	0.000	0.000
I1	0.033(2)	0.177(4)	0.177(4)	0.000	0.000	0.000
C1	0.24(9)	0.24(9)	0.16(12)	0.000	0.000	0.000
N1	0.24(9)	0.24(9)	0.16(12)	0.000	0.000	0.000

Table A.3 Refined atomic displacement parameters for AV80-$MAPbI_3$ in space group $Pm\bar{3}m$ with lattice parameters $a = b = c$ = 6.2581(3) Åand a cell volume of 245.09(4) $Å^3$.

A.4 Single Crystal X-ray Diffraction of AV300-$MAPbI_3$ - Ambient Temperature

An ambient temperature X-ray single crystal diffraction measurement was conducted on a dual wavelength (Cu/Mo) microfocus Rigaku Oxford Diffraction Supernova Diffractometer. A single crystal was selected from the sample AV300-$MAPbI_3$ and mounted onto a goniometer with a loop secured with viscous oil. Data collection was then carried out at 290 K (ambient temperature) with Cu-Kα radiation operating at 50 kV and 50 mA, a full sphere scan was carried out. Subsequent data reduction was carried out using the CrysAlisPro software.

A total of 1953 peaks were observed, of which 1913 (97.95 %) reflections were indexed with a cubic unit cell with lattice constants $a = b = c = 6.297$ Å and $\alpha = \beta = \gamma = 90°$. For data reduction Friedel mates were treated as equivalent and no Laue filter was applied. Multi-faced crystal with Gaussian integration + standard empirical spherical harmonics absorption correction was carried out based on a crystal shape generated through inspection of the crystal movie recorded at the beginning of the experiment. During space group determination systematic absence violations with an I>3σ were observed for all lattice centring options, therefore P type centring was selected. Inspection of the the normalised structure factor values (E), specifically the quantity <|E^2-1|> was found to have a value of 0.6, this value can be cautiously used as justification for a non-centrosymmetric space group. However this would deviate from the published space group $Pm\bar{3}m$ for the cubic phase of prototypical MAPbI$_3$ and without further justification structure determination was carried out for the space group $Pm\bar{3}m$. An initial structure solution generated by directed methods with the program SHELXS was found to be consistent with the high temperature cubic phase of prototypical MAPbI$_3$ reported in the literature. Further structure refinement was carried out using the software package SHELXL. Here, the occupancy of I, C and N atoms were refined along side anisotropic thermal displacement parameters.

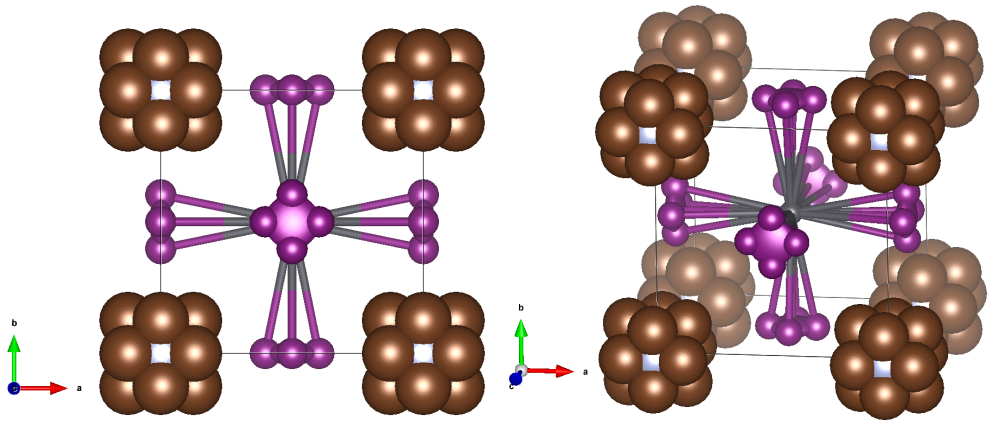

(a) (b)

Fig. A.5 Refined structure for AV300-MAPbI$_3$ annealed at 300 °C obtained from single crystal X-ray diffraction measured at 290 K on the Rigaku Supernova diffractometer with radiation Cu-Kα.

The cubic crystal type and assigned space group the data has been solved for corresponds with that of the high temperature cubic phase I for prototypical MAPbI$_3$ as reported in the literature [47, 48]. However a significant difference was found, an additional iodide site was incorporated into the structural model (labelled I1A) that

is positioned close to the I1 iodide site. This was identified through the presence of a significant peak in the Fourier difference map. This indicates that despite an average Pb-I-Pb bond angle of 180° and therefore the assignment of the cubic crystal type and simple perovskite structure space group $Pm\bar{3}m$, increased disorder in the PbI_6 octahedra is observed. The disorder described above could not be effectively modelled through anisotropic thermal displacements parameters of the I2 site alone, with a significant reduction in the residual fit factors after including the I1A site.

Atom	x	y	z	U_{iso} (^{3})	Occupancy
Pb1	0.5	0.5	0.5	0.043	1
I1	0.5	0.0	0.0	0.133	0.94
I1A	0.398	0.0	0.06	0.019	
C1	0.125	0.125	0.0	0.2	0.31
N1	0.0	0.08	0.0	0.2	0.31

Table A.4 Atomic coordinates of AV300-$MAPbI_3$ annealed at 300 °C and obtained from refinement of a single crystal X-ray diffraction measurement measured at 290 K on the Rigaku Supernova diffractometer. The refinement resulted in agreement factors of 4.42 %, 5.69 % and 1.599 for R_1, wR_2 and S/GooF respectively.

The structural model refined from this measurement for the sample AV300-$MAPbI_3$ differs from the results described in section.4.3.2. The slight suppression of the PbI_6 octahedra tilt observed through powder X-ray diffraction measurements appears to be completely suppressed here, this is reflected in the higher symmetry cubic crystal type for which the single crystal data was solved. Because of this discrepancy, it was decided that the crystal would be remeasured with Mo-kα radiation in order to make use of the different absorption and anomalous scattering contributions of the different radiation type. The same crystal was remeasured under the same experimental conditions except the radiation source was replaced with Mo-Kα. Surprisingly previously reflections unobserved in the Cu-Kα measurement emerged. Figure.A.6 shows the hk1 unwarp layer for both Cu-Kα and Mo-Kα measurements respectively. Specifically, of 4595 observed reflections 4220 (91.84 %) were indexed with a tetragonal type crystal system with lattice constants a, b, c and $\alpha = \beta = \gamma$ of 8.92 Å, 8.92 Å, 12.61 Å and 90° respectively. This crystal system type is consistent with the ambient temperature tetragonal phase II of prototypical $MAPbI_3$, however the relative intensity of the newly emerged reflections were considerably less than those measured for prototypical $MAPbI_3$.

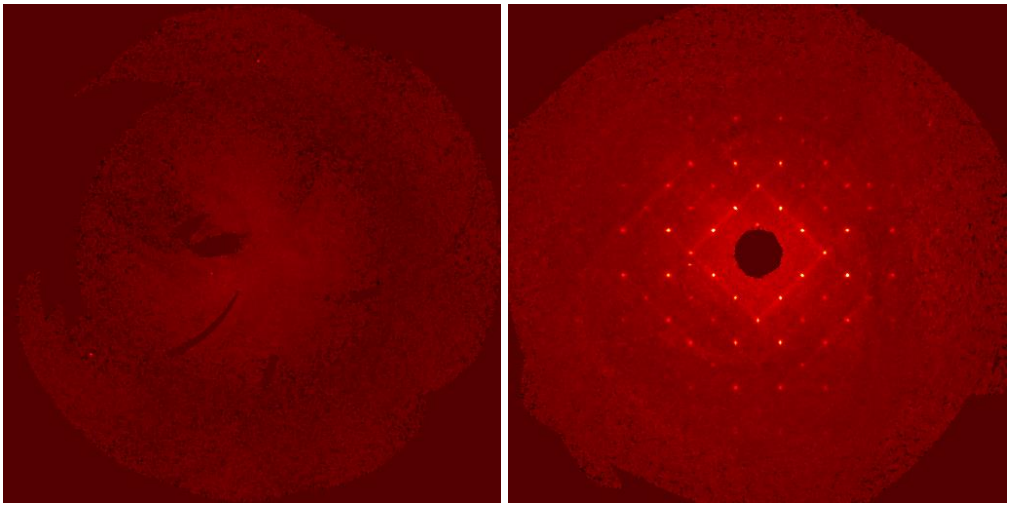

(a) (b)

Fig. A.6 Reconstruction of layer *hk*1 of the diffraction pattern for Cu-Kα (A.6a) and Mo-Kα (A.6b) respectively, both indexed with a tetragonal crystal system with lattice constants a, b, c and $\alpha = \beta = \gamma$ of 8.92 Å, 8.92 Å, 12.61 Å, 90° for comparison purposes.

Data reduction was carried out with Friedel mates treated as equivalent and no outlier rejection filter was applied as with previous refinements. Multifaced crystal with gaussian integration + standard empirical spherical harmanics absorption correction was again carried out based on a crystal shape generated through inspection of the crystal movie recorded before the measurement. During the space group determination process only 20 reflections were found to violate the I centring systematic absences conditions with mean intensity of approximately zero, it should be noted here that these reflections do not correspond to the newly emerged weak reflections observed in this data compared with Cu-Kα measurement. The system was therefore determined to be I centred. The space group used for structure refinement was *I4/m*, this is consistent with previous structural refinements outlined in section 3.3.2. the structure was refined using the software package SHELXL, here anisotropic thermal displacement parameters were refined for all atoms.

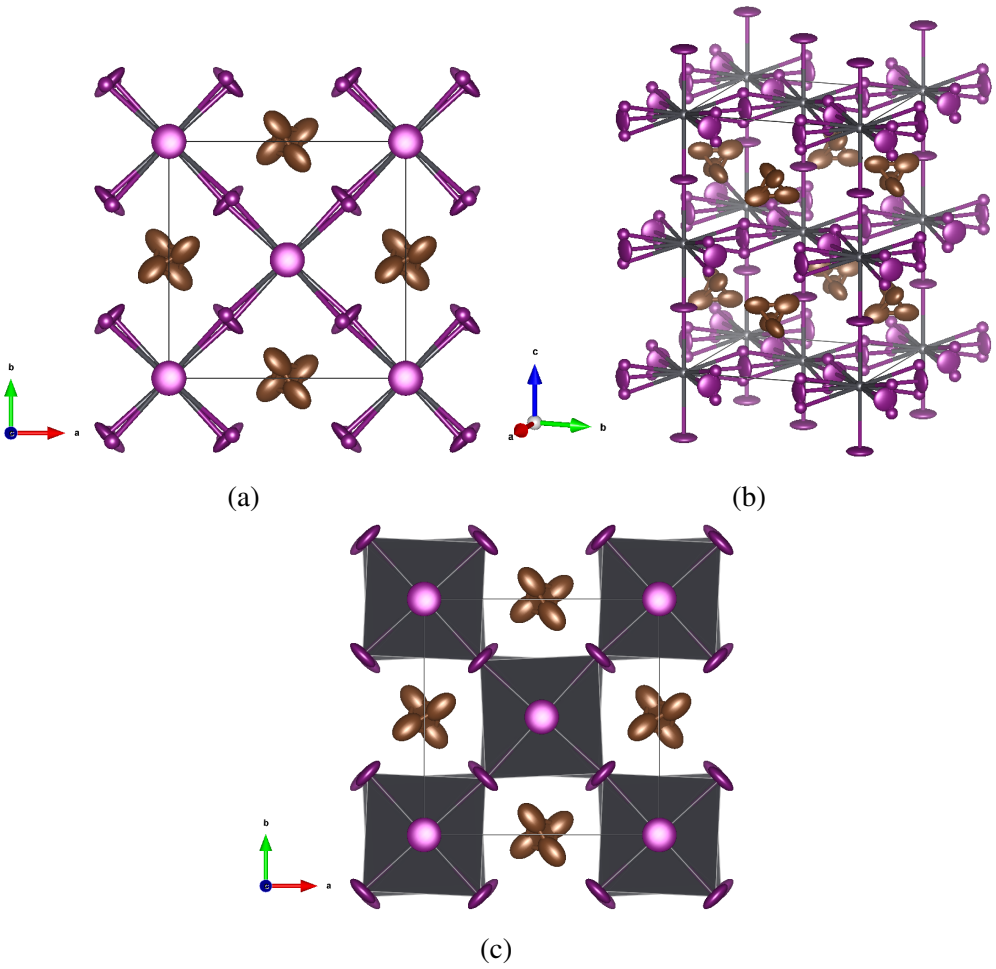

(a) (b)

(c)

Fig. A.7 Diagrams of the refined structure for AV300-MAPbI$_3$ annealed at 300 °C obtained from single crystal X-ray diffraction measured at 290 K on the Rigaku Supernova diffractometer measured with Mo-Kα.

Atom	x	y	z	U$_{iso}$ (Å^3)	Occupancy
Pb1	0.0	0.0	0.0	0.03	1.0
Pb2	0.0	0.0	0.5	0.03	1.0
I1	0.0	0.0	0.2519	0.127	1.0
I2	0.238	0.2611	0.0	0.133	0.94
I2A	0.267	0.241	0.056	0.035	0.04
C1	0.071	-0.457	-0.212	0.113	0.38
N1	0.071	-0.457	-0.212	0.113	0.38

Table A.5 Atomic coordinates ofAV300-MAPbI$_3$ annealed at 300 °C and obtained from refinement of a single crystal X-ray diffraction measurement measured at 290 K on the Rigaku Supernova diffractometer. The refinement resulted in agreement factors of 4.35 %, 11.30 % and 1.453 for R_1, wR_2 and S/GooF respectively.

The MA^+ cation is described by a single carbon and nitrogen atomic sites forming a tetrahedron unit where the positions and thermal parameters are restrained to be equivalent , the centre of mass of for which sits at the centre of the surrounding PbI_6 octahedral framework consistent with prototypical $MAPbI_3$. The PbI_6 octahedral framework is observed to be significantly less tilted compared with prototypical $MAPbI_3$ at the same temperature.

In order to explain the difference in observed reflections between measurements using incident radiation Cu-kα and Mo-kα the linear absorption length for each wavelength was calculated with respect to AV300-$MAPbI_3$. The absorption length was calculated using the Hephaestus software package, here the density of the sample has been calculated from the refined structure above and taken to be 4.2051 g/cm^3 with a chemical formula of $CH_3NH_3PbI_3$. The relative absorption length for Cu-kα and Mo-kα was calculated to be 9.4 and 37.6 micrometers respectively, compared with the diameter of the crystal measured at 56-69 micrometers. This is significant, as it suggests the largest contribution to diffraction originates from the surface structure with a Cu-kα radiation source. Therefore, changes to the average structure for a crystal undergoing vacuum thermal treatment are greater at the surface compared with the bulk crystal, indicating the removal of a chemical species from the sample that is more prominent at the surface. By using the Mo-kα the bulk crystal is measured and therefore a better measurement of the average structure is obtained. Subsequently, future measurements of this compound were carried out with Mo-kα radiation.

A.5 Single Crystal X-ray Diffraction Study of AI200-$MAPbI_3$ Impurity Phases - Ambient Temperature

Table A.6, Table A.7, Table A.8 and Table A.9 outlines the details of the refined crystal structure for two impurity phases NH_4PbI_3 and PbI_2 taken from a sample of AI200-$MAPbI_3$. For NH_4PbI_3 the refinement resulted in fit parameters R1 = 2.03 %, wR2 = 3.69 % and S = 1.096. For PbI_2 the refinement resulted in fit parameters R1 = 9.77 %, wR2 = 25.10 % and S = 1.075.

NH_4PbI_3 - Single Crystal Diffraction Atomic Coordinates at 100 K				
Atom	x	y	z	Occupancy
Pb1	0.66830(2)	0.75	0.55772(2)	1.000(13)
I1	0.47610(4)	0.25	0.61666(2)	0.997(13)
I2	0.84368(4)	0.25	0.48578(2)	1.000(13)
I3	0.81007(4)	0.75	0.71450(2)	0.995(13)
N1	0.9104(6)	-0.250	0.3229(3)	1.23(3)

Table A.6 Refined structural parameters for NH_4PbI_3 in space group *Pnma* with lattice parameters a = 10.2651(4) Å, b = 4.6876(2) Å and c = 17.1646(6) Å and a cell volume of 825.94(6) $Å^3$.

NH_4PbI_3 - Single Crystal Diffraction ADPs at 100 K						
Atom	U_{11}	U_{22}	U_{33}	U_{12}	U_{13}	U_{23}
Pb1	0.01616(13)	0.00950(12)	0.01079(12)	0.000	-0.00143(8)	0.000
I1	0.0151(2)	0.01191(19)	0.00921(19)	0.000	0.00047(13)	0.000
I2	0.0157(2)	0.0103(2)	0.0211(2)	0.000	0.00395(15)	0.000
I3	0.0232(3)	0.0152(2)	0.0140(2)	0.000	-0.00694(15)	0.000
N1	0.059(5)	0.032(3)	0.032(3)	0.000	0.005(3)	0.000

Table A.7 Refined atomic displacement parameters for NH_4PbI_3 in space group *Pnma* with lattice parameters a = 10.2651(4) Å, b = 4.6876(2) Å and c = 17.1646(6) Å and a cell volume of 825.94(6) $Å^3$.

PbI_2 - Single Crystal Diffraction Atomic Coordinates at 270 K				
Atom	x	y	z	Occupancy
Pb1	0.5	0.3323(4)	0.5006(3)	1.00
I1	0.0	0.4984(7)	0.6336(3)	1.00
I2	0.0	0.1650(7)	0.3664(3)	1.00

Table A.8 Refined structural parameters for PbI_2 in space group *Cmc21* with lattice parameters a = 4.5383(8) Å, b = 7.8570(15) Å and c = 13.916(3) Å and a cell volume of 496.20(16) $Å^3$.

PbI_2 - Single Crystal Diffraction ADPs at 370 K						
Atom	U_{11}	U_{22}	U_{33}	U_{12}	U_{13}	U_{23}
Pb1	0.0320(17)	0.0119(14)	0.061(2)	-0.0003(16)	0.000	0.000
I1	0.040(3)	0.020(3)	0.040(3)	-0.001(3)	0.000	0.000
I2	0.044(4)	0.019(3)	0.039(3)	0.000(3)	0.000	0.000

Table A.9 Refined atomic displacement parameters for PbI_2 in space group *Cmc21* with lattice parameters a = 4.5383(8) Å, b = 7.8570(15) Å and c = 13.916(3) Å and a cell volume of 496.20(16) $Å^3$.